LA-4351-MS

C. 3

LOS ALAMOS SCIENTIFIC LABORATORY
of the
University of California

LOS ALAMOS • NEW MEXICO

Status Report of the

LASL Controlled Thermonuclear Research Progran

for 12-Month Period Ending October 1969

UNITED STATES
ATOMIC ENERGY COMMISSION
CONTRACT W-7405-ENG. 36

This LA. . .MS report presents the status of the LASL Controlled Thermonuclear Research Program. Previous annual status reports in this series, all unclassified, are:

LA-3628-MS
LA-3831-MS
LA-4075-MS

This report, like other special-purpose documents in the LA. . .MS series has not been reviewed or verified for accuracy in the interest of prompt distribution.

Printed in the United States of America. Available from
Clearinghouse for Federal Scientific and Technical Information
National Bureau of Standards, U. S. Department of Commerce
Springfield, Virginia 22151
Price: Printed Copy $3.00; Microfiche $0.65

Distributed: February 6, 1970

LA-4351-MS
UC-20, CONTROLLED
THERMONUCLEAR PROCESSES
TID-4500

LOS ALAMOS SCIENTIFIC LABORATORY
of the
University of California
LOS ALAMOS • NEW MEXICO

Status Report of the

LASL Controlled Thermonuclear Research Program

for 12-Month Period Ending October 1969

INTRODUCTION
(J. L. Tuck)

Sherwood activities as a whole at Los Alamos continue to be dominated, as they should be, by Scyllac, the toroidal θ-pinch. This work is going well. The frightening problem of switching 1000 to 3000 high power circuits, simultaneously to within 10 nanoseconds, each with good reliability seems to have been overcome. Although the exact method of stabilization for Scyllac has not been settled on (Ribe, P-15), some of the alternatives, pulsed feedback especially, seem promising. The prevailing climate of thought in P-15 is to hurry on to the full toroidal Scyllac, after the minimum dalliance with the linear Pre-Scyllac.

This decision is forced on us by the combined effects of timetable, staff, and money. It is a pity, nonetheless, for a 15-meter hot θ-pinch would be a very interesting device, both theoretically and experimentally. It even has possibilities as a reactor, in my opinion. (Ribe does not share this view.) For admittedly, a straight θ-pinch of several km length seems impractical, but end stopping by a factor of ten, if achievable, would reduce this to a few hundred meters. The straight θ-pinch reactor also offers a certain simplicity in disposing of the used plasma between pulses, which it is not so obvious how to do for a closed system.

In a single-choice situation, however, the toroidal θ-pinch seems to offer the most direct path to a system with a positive power balance, not excepting Tokamak. By this, I do not mean that Tokamak is not a fine achievement - it is. But the extrapolation to a power producer is far from clear.

For those interested in fundamental theory, the symmetry arguments of Morse and Freidberg (P-18), should be fundamental enough for anybody. The literal interpretation would make stable confinement in any real closed magnetic bottle an impossibility. For of the two possible stable systems, the linear θ-pinch is open, the toroidal z-pinch is MHD unstable. The way out of the impasse, as indicated by Riesenfeld (P-18), seems to be through the long life time of the disassembly of the high-beta region.

The pure z-pinch has now been brought into line with the θ-pinch and apparently has reached thermonuclear temperatures. This was done by applying the fuse-magnetic energy storage trick, as I proposed some years back, and which has been brought into very effective practice by DiMarco and Burkhardt (P-14). The hot z-pinch does seem to be more stable but not greatly so. Results in the experiment are seriously masked by end effects. Extension of the z-pinch studies to a torus are strongly indicated; such a proposal is included by Phillips (P-14).

THETA PINCHES
(Group P-15)

SCYLLA IV-3 EXPERIMENTS

(R.F. Gribble, E.M. Little, W.E. Quinn,
R.E. Siemon, E. L. Zimmerman)

Modification of the Apparatus

Extensive modifications of the Scylla IV θ-pinch have been completed during this report period. The modifications include: (1) a basic change from a 1-m to a 3-m length compression coil; (2) an increase of the primary bank energy storage system from 550-kJ to 830-kJ at 50 kV; (3) the modification of the 324 primary bank spark gaps for operation with the improved Scyllac triggering system; (4) the addition of a Scyllac-type piggy-back crowbar switch to each of the 324 primary start gap switches; (5) the installation of new improved triggering systems for the primary bank start switches, the primary bank crowbar switches, and the preionization bank; (7) the addition of a new collector plate section with cable cartridges to accept the load cables from the added energy storage of the primary bank and of the preionization bank and the installation of a new collector plate section to accommodate exploding foil, solid dielectric, crowbar switches adjacent to the compression coil; (8) the installation of new charge distribution systems for the primary and preionization capacitor banks and the crowbar trigger system which replace the previous fuse-charge resistor systems with liquid resistors; and (9) the assembly and installation of a new vacuum system which utilizes a Vacion pump and a turbo-molecular pump. The various capacitor banks and triggering systems are being checked out at the present time and plasma experiments are beginning.

Parameters of the 3-m Device (Scylla IV-3)

The objective of the 3-m device is to increase the plasma confinement time through a reduction of the plasma end loss rate, while maintaining the device parameters such that a hot collisionless plasma can be produced. The calculated parameters of the modified device with the 3-m length coil are given in Table I.

Table I

Parameters of Scylla IV-3

Coil length	3	m
Coil bore	10.5	cm
W (energy storage)	830	kJ
V (capacitor voltage)	50	kV
C (capacity)	664	μF
No. of capacitor units	324	
No. of start spark gaps	324	
No. of "piggy-back" crowbar gaps	324	
No. of load cables	1944	
Average cable length	18	ft
L (capacitors plus spark gaps	0.23	nH
L ("piggy-back" crowbar gap)	0.28	nH
L (cables)	0.37	nH
L (cable cartridges)	0.12	nH
L (collector plates)	1.72	nH
L (source)	2.44	nH
L (coil)	3.62	nH
L (source + coil)	6.06	nH
L (crowbar source + coil)	6.11	nH
α (transfer efficiency)	0.60	
τ ((period)	12.6	μsec
δ (skin depth of collector plates and coil)	0.52	mm
R (capacitors + spark gaps)	52.5	$\mu\Omega$
R ("piggy-back" crowbar gaps)	10.5	$\mu\Omega$
R (cables)	10.2	$\mu\Omega$
R (collector plates)	116.5	$\mu\Omega$
R (coil)	9.1	$\mu\Omega$
R (start source + coil)	188	$\mu\Omega$
R (crowbar source + coil)	146	$\mu\Omega$
I_{max}	15.7	MA
B_{max}	65.9	kG
$E_{\theta\ max}$ (at tube i.d.)	760	V/cm
L/R (crowbar) min.	42	μsec

The actual decay time of the crowbarred current will be greater than the calculated L/R value of Table I since the resistance of the collector plates and coil were calculated assuming that the current only penetrates the skin depth δ corresponding to the period of the primary bank. An exponential damping factor ($e^{-Rt/2L} = 0.95$) has been used in calculating the current and magnetic field values at the first field maximum. In the operation of the primary bank with the preionization (PI) bank the magnetic field will be less than the 66 kG of Table I due to energy losses to the PI bank.

An estimate of the plasma ion temperature in the 3-m device can be made using the assumption that the heating in the θ-pinch scales as $E_\theta^{\frac{3}{2}}B$; i.e., the initial shock heating is proportional to the azimuthal electric field followed by a 2-dimensional adiabatic compression by the magnetic field, after a time proportional to $E_\theta^{-\frac{1}{2}}$.

$$\frac{T(3m)}{T(1m)} = \frac{E_\theta^{\frac{3}{2}} B(3m)}{E_\theta^{\frac{3}{2}} B(1m)} = \left(\frac{760}{1100}\right)^{\frac{3}{2}} \left(\frac{60}{90}\right) = 0.38.$$

This scaling indicates plasma ion temperatures of 1 to 2 keV in the 3-m device at a filling pressure of 10μ. The plasma confinement time τ can be estimated with the assumption that τ scales as $\ell/T^{\frac{1}{2}}$, i.e., proportional to the ratio of the coil length to the average plasma ion velocity. On the basis of the measured confinement times in the 1-m coil (τ = 3 to 6 μsec), plasma confinement times of 12 to 25 μsec are predicted for the 3-m coil.

Compression Coil

The Scylla IV-3 compression coil has a length of 3-m with a 10.5-cm bore. The coil is made up of 20, 15-cm length sections, each of which consists of an upper and lower "clam-shell" type section.

A photograph of the 3-m compression coil assembled on the collector plates is shown in Fig. 1. An overall view of the front end of the machine and the capacitor banks is shown in Fig. 2.

Discharge Tubes

The initial 3.5-m length discharge tube is 99% alumina made up of 60-cm length sections with lap joints which were joined with a polycarbonate adhesive. After several preionization discharges and a few main bank discharges with plasma, dark rings have developed on the inside of the tube in the vicinity of the joints. The joints were especially designed to eliminate the possibility of the plasma "seeing" the adhesive portion of the joint. However, it appears that the material in the dark ring deposits has in some way come from the adhesive. The polycarbonate adhesive used in this first tube assembly required heating the joint to approximately 300°C. This temperature may have evaporated some material out of the polycarbonate which migrated to the inside of the discharge tube. An attempt was made to discharge-clean this tube. It is important for Scylla IV-3 and the Scyllac device that we achieve workable joints in the ceramic tubes.

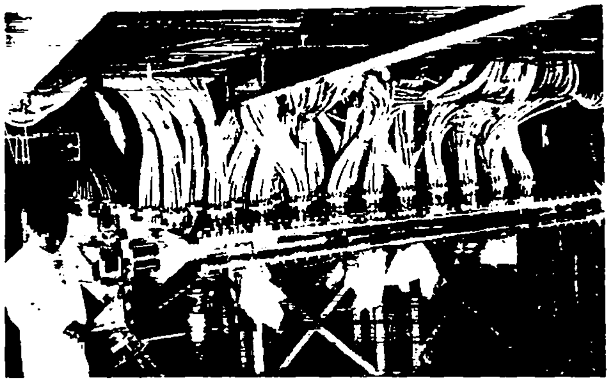

Fig. 1. Photograph of compression coil and front end of the Scylla IV-3 θ-pinch.

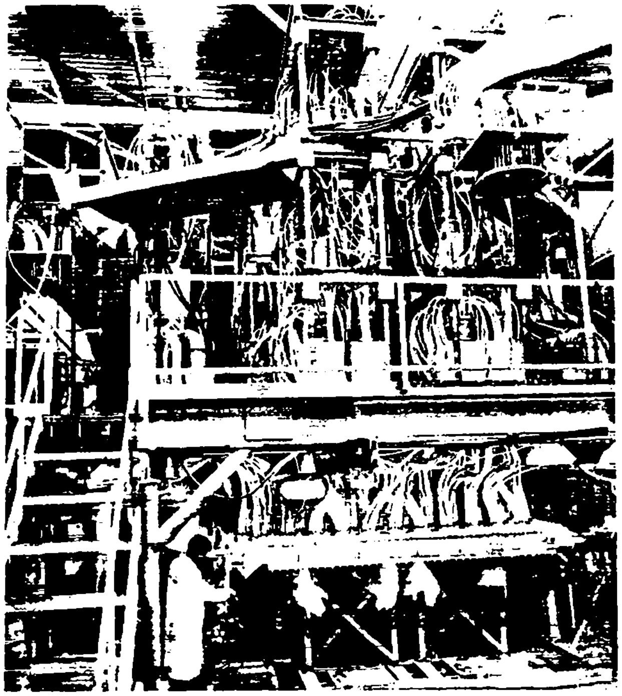

Fig. 2. Overall view of Scylla IV-3.

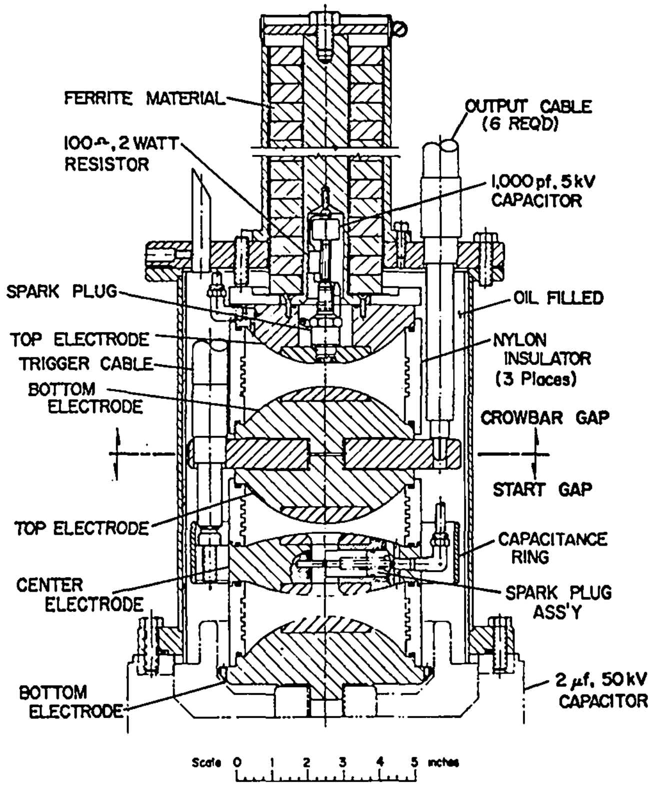

Fig. 3. Assembly diagram of the start-crowbar spark gap for Scylla IV-3.

The alumina ceramic discharge tube was replaced with a 3.5-m length quartz tube in order to obtain plasma data. The plasma properties improved immediately with the installation of the quartz discharge tube, and the data presented in the next section were taken with this tube. Further experiments with ceramic tubes using epoxy joints will be undertaken.

Primary Capacitor Bank System

The primary capacitor bank is divided into 6 modules with 54 capacitor-spark gap units per module. A single submaster trigger gap and charge bus is used for each module. The charge system uses an isolation liquid resistor (0.03% $CuSO_4$ solution) for each group of 6 capacitors.

One of the 324 start and crowbar load spark gap assemblies is shown in Fig. 3. The crowbar gaps are located in the same aluminum housing with the start gaps, directly on top of the 2-μF, 50-kV energy storage capacitors.

The new triggering system for the start spark gaps consists of a single master trigger spark gap and six submaster trigger gaps. A circuit schematic of the triggering system (designed by Gribble) is shown in Fig. 4. Figure 5 shows an assembly view of one of the submaster trigger spark gaps. The lengths of the trigger cables from the submaster gaps to the primary bank load gaps have been chosen such that the total length of the trigger cable, the load cables and the collector plate to coil path is a constant for each of the 324 primary bank capacitors. This should improve the initial rise of the voltage at the coil and consequently improve the dynamics of the implosion phase of the discharge.

The jitter between the firing of the six submaster trigger gaps by the master gap is found to be at most a few nanoseconds. This is a quite encouraging indication for the Scyllac trigger system.

The trigger system for the 324 piggy-back crowbar spark gap switches consists of a master trigger spark gap (Fig. 5) which triggers 18 submaster trigger gap-capacitor units. Each of the submaster gaps triggers 18 crowbar gaps. The trigger capacitors are 1.85-μF, 60-kV units.

Extensive air distribution and exhaust systems have been installed to supply air pressure to the gaps with a static fill and to flush the gaps after a discharge.

The 324 primary bank spark gap capacitor units are connected into the collector plates with 1944 coaxial cables with an average length of 20 ft.

A spark-gap firing monitor system has been constructed by D. Brown of P-1 (cf. page of this report). This system monitors the firing times of each of the 324 start and crowbar spark gaps of the primary bank. This is a prototype of the system to be used on Scyllac. The monitor is being modified to feed directly into the Scyllac computer which is presently installed on Scylla IV-3.

Preionization

The preionization (PI) bank consists of 23 capacitor-spark gap units. The capacitors are

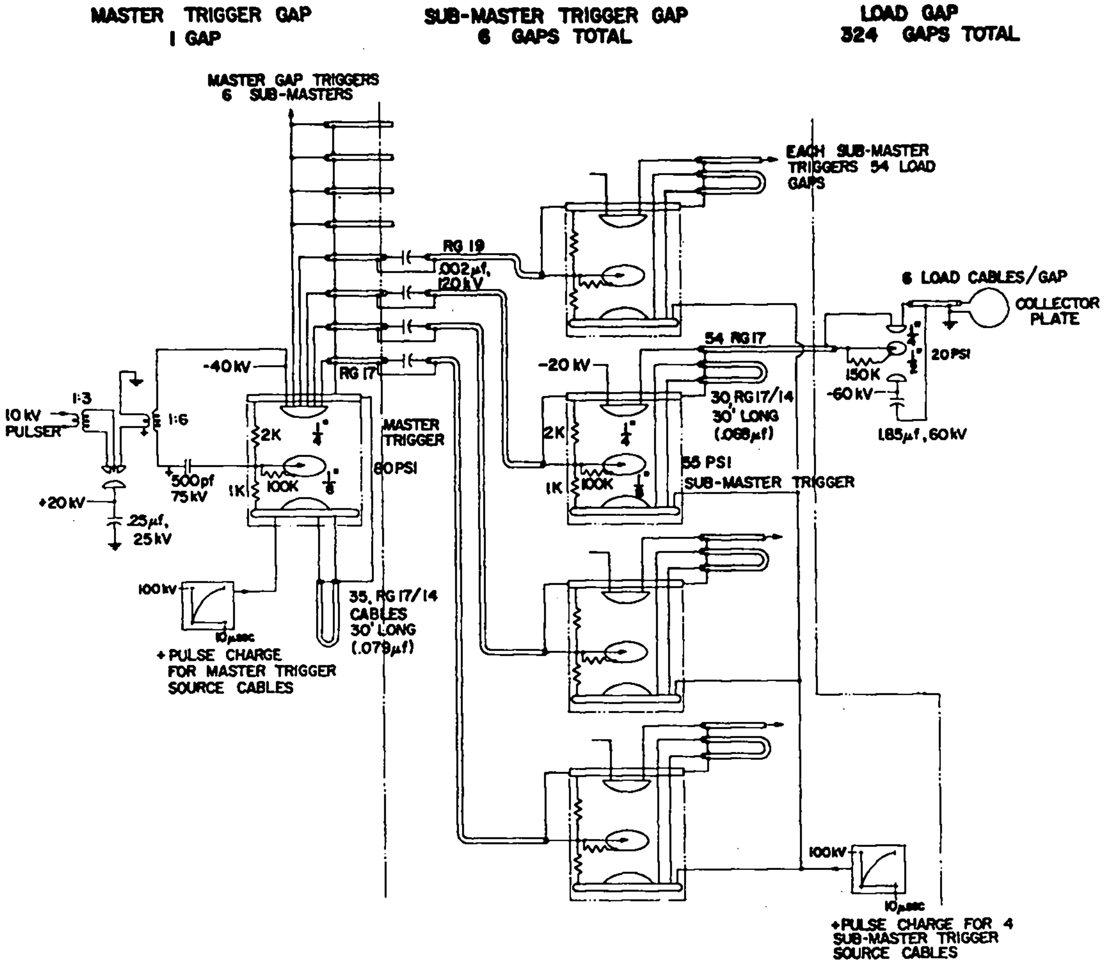

Fig. 4. Schematic diagram of the Scylla IV-3 triggering system.

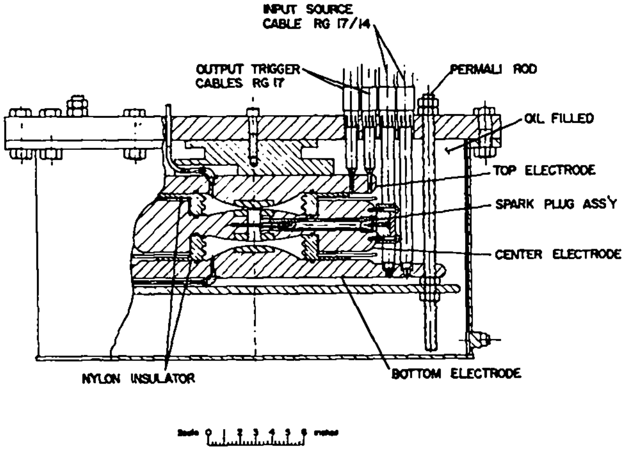

Fig. 5. Scylla IV-3 trigger gap.

a new 0.7-μF, 75-kV capacitor. This bank charged to 50 kV is calculated to produce a maximum E_θ of 290 V/cm and a peak B_z of 6.6-kG at a frequency of 320-kHz in the 3-m length compression coil. The number of capacitor units was chosen to give a compromise between the PI frequency, E_θ and B_z.

A master spark gap similar to that of Fig. 5 is used to trigger the PI bank. Twelve 15-ft cables are used to connect each PI capacitor spark gap unit into the collector plate.

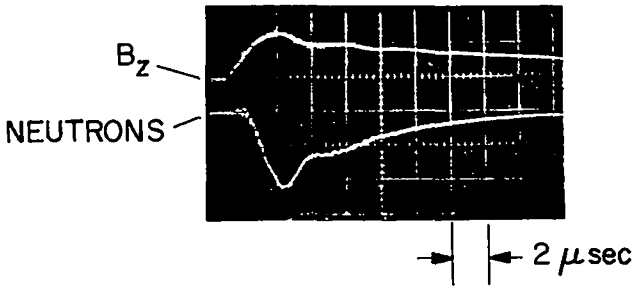

Fig. 6. Magnetic waveform and neutron-emission signal of Scylla IV-3.

Vacuum System

The new vacuum system has been assembled and tested. This system uses a Vacion pump to maintain the base vacuum and a turbo-molecular pump to handle the deuterium gas loads during operation of the machine. Experience gained from the operation of this system has been used in the design of the Scyllac vacuum systems.

Collector Plates

The new collector plate sections, which were added to the front end of the original plates to accept the load cables from the increased energy storage of the primary bank and to adapt to the 3-m coil, have a sufficiently high porosity that they leak SF_6 gas from the cable cartridge regions. These plates were fabricated from Alpase cast aluminum tooling plate. These SF_6 leaks have been minimized; however, aluminum tooling plate should not be used in applications where porosity is not acceptable.

Initial Operation of Scylla IV-3

Magnetic Field Waveform

The crowbarred waveform of the magnetic compression field in the 3-m length, 10.5-cm diameter coil is shown in the oscillogram of Fig. 6. The magnetic field attains a maximum value of 60 kG with a rise time of 3.2 μsec. At the present time, the field decreases by approximately 15% after the field maximum before the crowbar spark gaps become completely effective. Following this sinusoidal decrease in the field, the crowbar system extends the magnetic field with an L/R decay time of 120 μsec. It is estimated that the initial 15% decrease in the field can be appreciably reduced by increasing the crowbar trigger voltage, which requires some changes in the trigger system.

The preliminary results reported below were taken with an initial deuterium filling pressure of 10 mTorr in a quartz discharge tube.

Neutron Emission

The time distribution of the neutron emission at 10-mTorr filling pressure in the quartz tube, as observed with a plastic scintillator-photomultiplier arrangement, is shown with the magnetic compression field in Fig. 6. The neutron emission rate attains a maximum at the peak of the magnetic field and decreases rapidly during its initial decay being quite sensitive to the crowbarred wave form of the magnetic field. The duration of the neutron emission extends to about 12 μsec. The qualitative features of the neutron emission are understood in terms of the magnetic compression field and the plasma end loss. The total neutron yield, measured with silver activation counters, is 10^6 neutrons per centimeter of plasma length. The peak emission rate in the vicinity of the magnetic field maximum is 3×10^5 neutrons/μsec/cm of plasma length.

Plasma Density and Radial Distribution

Double exposure holography has been used to obtain interferograms of the 3-m Scylla IV plasma column. An interferogram taken in ruby laser light at the time of the magnetic field maximum with an initial deuterium gas filling of 20 mTorr is shown in Fig. 7. Such interferograms give the contours of the plasma electron density integrated over the plasma length. The outside diameter of the fringe pattern is 6.9 cm compared with a discharge tube inside diameter of 8.6 cm.

A graph of the plasma fringe shifts or the plasma electron density obtained from the interferogram is shown in Fig. 8. This graph gives the radial profile of the plasma density integrated over the length of the plasma. The density at the maximum of the distribution is

Fig. 7. Interferogram of Scylla IV-3 plasma at first maximum of the compression field.

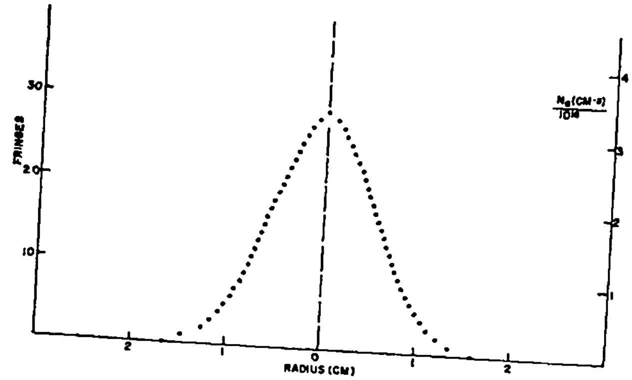

Fig. 8. Density profile corresponding to Fig. 7.

3.3×10^{16} cm^{-3}. A radial integration over the density distribution gives the total number of particles in the discharge, which at the time of the magnetic field maximum is equal within ± 10% to that of the initial gas filling.

Plasma Ion Temperature and Lifetime

An estimate of the plasma ion temperature can be obtained from the absolute neutron yield from the silver-activation counters, the neutron emission rate from the plastic scintillation detectors, and the plasma density and radius from the holographic interferograms. These data, along with the assumption of a Maxwellian velocity distribution, give a plasma ion temperature of 1 keV, which is in agreement with the predicted value obtained by scaling the device parameters from the one-meter coil arrangement. It compares with the value of 1.25 keV obtained in the computation of the next section. The plasma β at the center of the plasma column is estimated to be 0.6 with the assumption that the electron temperature is 300 eV, the same as in the one-meter device. Although the plasma containment time has not been measured as yet, the time distribution of the neutron emission indicates that it is in the range of 10 to 20 μsec as predicted by the scaling from the one-meter device.

CALCULATION OF NEUTRON SIGNAL FROM SCYLLA IV-3

(D.M. Weldon)

From a simple semi-empirical model of Scylla-type plasmas representing plasma density and temperature as a function of time, the neutron yield from Scylla IV-3 has been calculated. In the model, plasma density as a function of time is calculated from the radial ($\gamma = 2$) adiabatic compression determined from the measured magnetic field. Throughout the compression a rigid-rotor profile normalized to the density profile found at peak field is maintained. Plasma loss out the ends as a function of time is taken into account. Temperature is also determined by the adiabatic compression and is normalized to a peak temperature chosen as an input parameter. Account is made of cooling of deuterons through equipartition with electrons after formation of the plasma.

Figure 9(a) is a graph of the magnetic field shape used in the calculation and normalized to the peak magnetic field. Figure 9(b) shows the neutron yield per second per centimeter of plasma column as a function of time for a peak ion temperature of 1.25 keV and peak density of $3 \times 10^{16}/\mathrm{cm}^3$. The time integrated neutron yield is of the order 3×10^5 neutrons/cm, in agreement with the measured yield from Scylla IV-3. The shapes of the calculated neutron yield and the measured

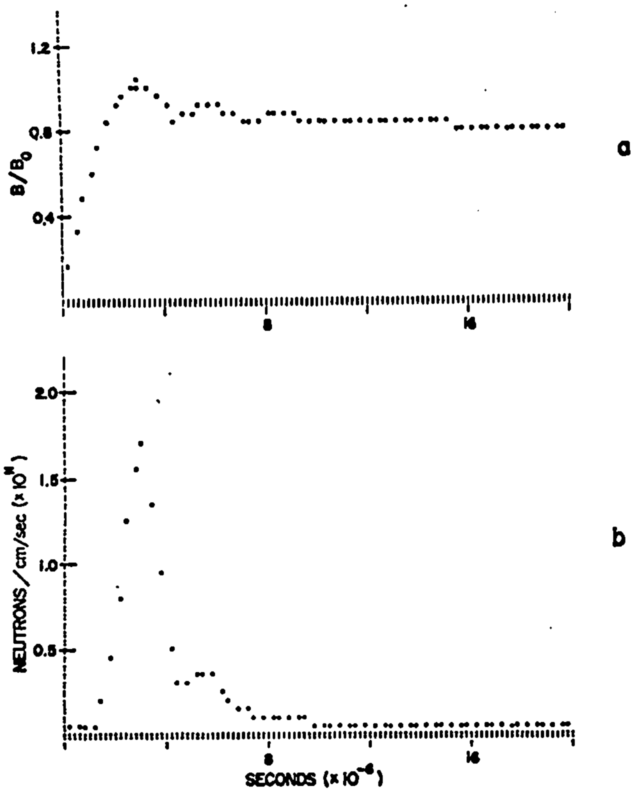

Fig. 9. Graphs of magnetic field and neutron emission computed for Scylla IV-3 at $kT_i = 1.25$ keV.

neutron signal shown in Fig. 6 agree except for the sharper peak in the calculated neutron signal. The exact reason for the discrepancy is not understood, but clearly the model is oversimplified and some important phenomena have been omitted. It is interesting to make an extrapolation of neutron yield to the 10-m Pre-Scyllac device. A yield of the order of 3×10^8/cm is calculated for a peak density of 3×10^{16} and temperature of 6 keV.

SPARK-GAP FIRING MONITOR SYSTEM

(G.A. Sawyer and D. Brown)

A spark-gap firing monitor system has been installed on Scylla IV-3. This system (Fig. 10), which is a prototype of the one to be used on Scyllac, monitors the firing times of each of the 324 start and crowbar spark gaps of the main bank. A single-turn magnetic pickup loop is inserted into the top of each spark gap to sense the gap firing time. A triax cable (Amphenol-21-204) connects each loop to the monitor circuit, which charges the small timing capacitor at a constant rate during the time interval between the submaster trigger and the time each spark gap fires. After the bank firing, an analog-to-digital converter samples the voltage on each capacitor which is proportional to the time delay in gap firing. At the present time, the delays of both start gaps and crowbar gaps are recorded by a printer. However, circuit design is proceeding so that the monitor will feed directly into the SDS Sigma-2 computer now installed on Scylla IV-3.

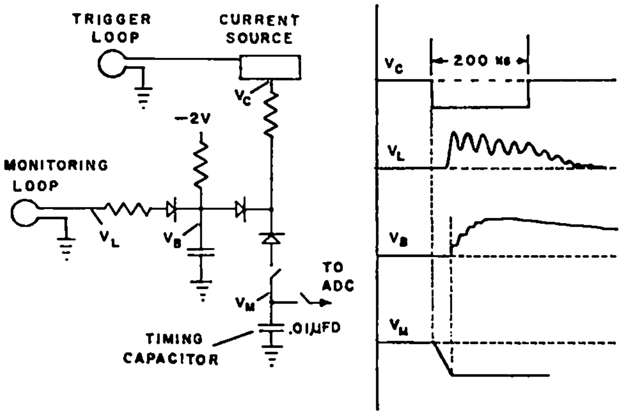

Fig. 10. Schematic diagram of operation of Scylla IV-3 spark gap monitor.

During the short period the monitor has been in operation, it has worked reasonably well and proven to be quite valuable. When the montior indicates a start gap is firing late or a crowbar gap is firing early, these particular gaps are then monitored on oscilloscopes to determine in more detail the nature of the difficulty. A problem exists pertaining to the uniformity and orientation of the magnetic pickup loops in the spark gaps. A more reliable loop fixture is being designed by P-16 for the Scyllac spark gaps.

SCYLLAC COMPUTER

(D. Brow, J. W. Lillberg, G. A. Sawyer, M. Seamons (C-4), D. A. Weldon)

The SDS Sigma-2 computer intended for use with the Scyllac data acquisition system has been delivered and installed in the Scylla IV control room. The central processor, disk storage unit, and teletype have been operational since April 25, and the final element of the computer configuration, the magnetic tape unit, was delivered in May. Early efforts were centered on checkout of the computer hardware and software and on general familiarization with the system, as well as software development for special peripheral devices and checkout of the magnetic tape drive. A character generator and various plot routines have been written for the spark-gap monitor device. The prototype scan converter built by P-15 has also been interfaced to the Scyllac computer. A third special peripheral device being designed for Scyllac, the electronic spark-gap monitor (see Section above), is also being interfaced to the computer after its initial check out on Scylla IV. All essential parts of the computer hardware and software except those pertaining to the magnetic tape unit have been checked out and found to be satisfactory for the Scyllac application.

In checking out the magnetic tape unit a design error was discovered, and the acceptance test of the unit was delayed until an engineering change order could be installed. After installation of the change the tape has performed satisfactorily. Work is progressing on the general data acquisition program for Scyllac.

SCAN CONVERTER DEVELOPMENT

(R. F. Gribble and J. W. Lillberg)

The scan converter system for storing and digitizing oscillograms (see LA-4075-MS, p. 84) is now operational in the Scylla IV control room, although some work remains in order to improve the vertical write amplifiers. The scan converter has been connected to the computer and a sine wave written on its screen and taken into the computer and out to the CRT display. Computer-compatible logic for eight scan converter tubes is designed and construction is under way.

Preparations are being made to produce sixteen scan converter units for initial operation with the 5-m Scyllac toroidal sector. A new scan converter tube with improved screen uniformity is being tested before ordering these for the Scyllac units.

PIGGY-BACK CROWBAR DEVELOPMENT

(R. F. Gribble and D. L. Call)

During this report period the piggy-back crowbar spark gap (see LA-4075-MS, p. 81) has been put into successful operation in the 50-kV capacitor banks of Scylla IA (36 spark gaps) and Scylla IV-3 (324 spark gaps). In both cases low-loss, $\frac{1}{2}$-in. thick, Indiana General Corporation, 0-5 ferrite cores (18 per spark gap) were used. The voltage developed across the ferrite, when it pulses the crowbar switch, is about 40 kV in these systems, and it is hoped to achieve 70 kV in the final Scyllac design. In the diagram of Fig. 3, a 1000-pF, 5-kV capacitor and 100-Ω, 2-W resistor in parallel are shown connected across the spark plug. This combination prevents a premature spark at the plug when the start gap fires. Previously, the fast load voltage rise on the lower electrode of the crowbar gap was capacitively coupled to the ferrite-isolated upper electrode, resulting in a short pulse across the spark plug since the plug pin is tied to ground via the trigger cable impedance.

Considerable development work has been done to improve operation of the crowbar for the 60-kV Scyllac application. Means were devised to measure the trigger current and the voltage across the ferrite. Various trigger configurations were tried in an attempt to optimize the triggering voltage developed across the ferrite. Various ferrite cores were tried, and improved versions of the spark plug were developed.

In the case of the spark plug several different metals and alloys were tried for both the center pin and the outer electrode. "Heavy metal" (tungsten-nickel-copper sintered alloy), nickel, and molybdenum were tried as an outer electrode, and nickel, molybdenum, pure tungsten, thoriated tungsten, and drill rod were tried as the trigger pin. All of the combinations but one resulted in from 5% to 50% crowbar prefires, i.e., crowbar gap breakdown at "start" gap initiation. The only combination that did not result in prefires and also produced the best triggering was that used in the modified Champion plugs installed in Scylla IA and in Scylla IV-3. This is a plug having a nickel center pin and a "heavy-metal" outer electrode. Some ten different plugs of this nature were tested at various times. In about 6000 shots using these plugs there were no prefires for normal gap operating conditions. A slight deterioration of triggering performance of the nickel-"heavy-metal" plug was observed after about 1000 shots; however, the plugs that were run for over 2500 shots on tests were still operating satisfactorily.

In regard to the optimum crowbar triggering arrangement, various trigger capacitors (one for each 18 gaps) have been tried. Triggering is sensitive to the interaction of transients in the trigger cable with the overall waveform of the circuit. Best triggering is achieved with a capacitor which provides a period just long enough for the transients to damp. Scyllac design is 1.5-μF at 75 kV.

Two types of ferrite produced by four manufacturers have been evaluated manganese-zinc, e.g., Indiana-General Corporation type 0-5m, and nickel-zinc, e.g., I.G. Corp. type H.

Mn-Zn material has the advantage of the higher saturation flux of the two types but because of its low, non-linear resistivity (10-100 ohm-cm) cannot be more than ¼-in. thick without loss of voltage through eddy-currents. The Ni-Zn material switches much faster than does Mn-Zn and, because of its relatively high resistivity (400 to 10,000 ohm-cm), can be of a thickness determined by cost considerations. On the basis of these tests, the following qualification specifications have been made for Scyllac ferrite procurement: The material shall be Mn-Zn with a dc bulk resistivity of > 80 Ω-cm and minimum saturation flux of 350 gauss at 25 oersted. Each core will have an o.d. of 2.9 in., an i.d. of 1.54 in., and a thickness of 0.25 in. There will be 40 cores per spark gap.

SCYLLA IA

(K.S. Thomas)

During the period covered by this progress report an experiment was performed to measure B_θ fields outside the coil region. These fields give a measure of the wall shorting currents out the end of the θ-pinch which occur when the plasma is initially formed with radial electrostatic fields. After the shorting of the electrostatic fields, the diamagnetic plasma current is partially transferred from the electrons to the ions. A paper has been published in Phys. Rev. Letters 23, 746 (1969). The total axial current and the radial distribution of the current agree well with values predicted by a theoretical rigid-rotor model.

PLASMA DIAGNOSTICS

(F. C. Jahoda)

Non-Diffuse Subject Illumination Holography

A modification of the holographic interferometry method has given considerably better spatial resolution than previously obtained. The essential difference is that no diffuser is used in this case in the scene beam. This causes the fringes to appear right on the hologram itself (they are just the moiré beats where the fine-scale structure of the grating produced in one exposure is exactly out of phase with the fine-scale structure of the grating produced in the other exposure) and they can be viewed in non-coherent, non-monochromatic light, avoiding the speckle effect produced by reconstruction in laser light. Because there is always a large zero-order term, largely unaffected by the grating structure, the hologram must be viewed at glancing angle. For photographing the result the plus or minus first order of a relatively small diffuse source must be separated with a lens and aperture combination.

The disadvantage of this arrangement is that the reference beam must completely overlap the useful area of the scene beam at the film plane, and all non-uniformities in the film plane (including the gross spatial intensity variations of the laser) are retained in the final product in point-for-point correspondence. On the other hand if the two beams are carefully matched spatially in their overlap at the hologram plane, the ruby laser source coherence requirements are less than for the case with diffuser, which requires both spatial and temporal coherence.

With the use of Agfa-Gevaert 10E75 plates, heavily exposed and then bleached, and a Korad K1Q-H laser, this technique has been used for the Scylla IV-3 interferograms shown elsewhere in this report.

Cine-Holographic Interferometry

We have now successfully adapted the "live fringe" method, the principle of which was discussed earlier in the previous annual report (LA-4075, p. 75). In this case, instead of two consecutive exposures of the hologram emulsion that yield "frozen fringes," the hologram is accurately repositioned after photographic processing following a single exposure. Whenever the original illumination source is again turned on, interference can be observed in real time between (a) the stored virtual image of the scene, reconstructed by the beam that was the reference beam in the hologram recording and (b) the current status of the scene.

A schematic diagram of the experimental arrangement is shown in Fig. 11. Though the absence of a diffuser either before or after the object limits the method to transmission-type objects, it still encompasses all phenomena suitable for the traditional methods of interferometry, e.g., plasma, while retaining the significant holographic advantages that neither high quality optical parts nor precision alignment are required.

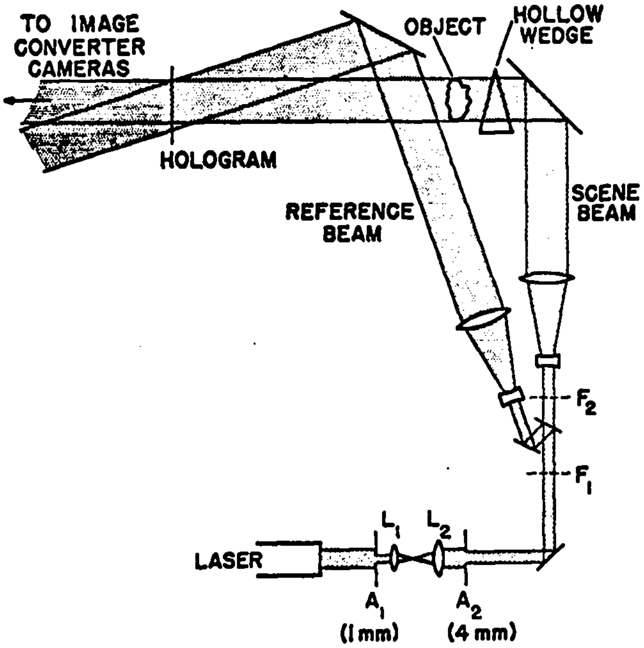

Fig. 11. Schematic diagram "live-fringe" holographic interferometry.

Interference fringes will occur both because of those phase changes in the scene that one wishes to measure and because of inexact repositioning of the hologram. With CW lasers the positioning error can be eliminated by fine adjustment during observation of the unaltered scene through the hologram. With ruby lasers, observations can only be made by camera monitoring of discrete pulses (the reconstruction must be in approximately the same wavelength as the construction to provide "live" fringes) and the fine adjustment procedure is impractical. However, by mounting photographic plates in a repositionable jig that goes through the development process, the residual phase shift due to repositioning error is slight. It is, moreover, small compared to the linear phase shift deliberately introduced into the scene by changing the gas filling in the hollow wedge between exposure and reconstruction. This gives a background of straight fringes and the repositioning error, also linear, only alters slightly the orientation and spacing of the background in a harmless manner.

Holograms have been produced with a rotating prism Q-switched laser (TRG 104) with a resonant output reflector. The combination of a 1-mm pinhole (A_1 in Fig. 11) and near equality in reference beam and scene beam path lengths reduces the source coherence requirements enough so that high quality holograms result without additional mode selection. The laser output energy throughout the pinhole is 5 mJ. With Kodak 031-01 plates (the approximate equivalent of SO 243 film) and a 5-cm diameter for the expanded beams, sufficient exposure can be obtained with an ND3 filter at position F_1 in Fig. 11.

The processed plate is bleached in a chromium intensifier solution in order to enhance the brightness of the reconstructed image. Even with bleaching there remains an intensity imbalance between the reconstructed virtual image and the "live" scene beam which combine to give the interference pattern. To enhance fringe contrast an ND1 filter is placed in the scene beam only at F_2. The use of a filter in one beam only during reconstruction results in some additional phase differences between the interfering beams. By inserting the thin gelatin filter where the beam cross section is small, the variation over the field of view of these phase differences is kept small. It results in a small-scale departure from straightness in the background fringes, but in a time sequence of interferograms this can be recognized as of extraneous origin by its constancy.

For reconstruction the giant pulse ruby laser is replaced with a chilled free-running ruby laser giving 30% modulation but no dead time over a 50-μsec period. Several interferograms can be sliced out during this time by gated image converter cameras focused on the scene through the hologram. This laser, which has its mirrors coated directly onto the ruby, is not used in the hologram construction because its coherence quality integrated over the total pulse length is inadequate to produce high efficiency holograms. Time slices of one microsecond or less, however, have sufficient coherence to give adequate interference fringes. Primarily temporal coherence is required since the reference and scene beams recombine at the hologram plane approximately point-for-point in the way they originated at the beam splitter. If a diffuser were used the relative phase differences across the source aperture would affect every point in the hologram. Besides the greater spatial coherence requirement on each laser individually, any differences across the source aperture between the two lasers would rapidly diminish the fringe contrast. This makes the laser exchange unfeasible for diffuse objects.

It is also possible in the reconstruction to remove pinhole A_1 and lenses L_1 and L_2 (Fig. 11) leaving only the 4-mm diameter aperture A_2 as the effective source aperture. This allows shorter image converter exposures by utilizing a greater portion of the reconstruction laser flux, without sacrificing the better hologram efficiency obtained with the smaller pinhole in the construction. A_1 and A_2 are in the front and back focal planes of the telecentric lenses L_1 and L_2, respectively, and all elements are originally carefully centered on an optic axis with a CW laser alignment beam.

In practice it is useful to insert one or more lenses (not shown in Fig. 11) between the object and the hologram plane. One can thereby reduce the effect of object self-luminosity by an aperture stop in the focal plane of a lens and simultaneously re-image on the shadow projection at the hologram plane rays deviated by refraction in the object. Also, demagnification can increase the flux per unit area at the hologram plane, desirable for reconstruction, without limiting simultaneously the size of the object field. A similar compensating change in the reference beam geometry maintains the reasonably careful spatial overlap of the scene and reference beams at the hologram plane.

Figure 12 shows interference fringes obtained with two image converter cameras at the indicated times after initiation of an air spark. This spark is created by dissipating 1.5 joules between point electrodes spaced 2 mm apart on the 1-cm diameter insulator seen in shadow projection. Two Beckman-Whitley single frame image converters were used. The shorter exposure was obtained with an "S-11, extended red" photocathode, whereas the longer exposure camera had only the regular S-11 photocathode. There is a mirror inversion caused by a beam splitter which enabled both cameras to view the object in the collimated laser beam. The reconstruction laser power was approximately 5 kW through the 4-mm aperture.

After modification of all our four image converters to the "S-11, extended red" photocathode, the "live fringe" method was demonstrated also on Scylla IA. Further, a very significant simplification has resulted from using Agfa-Gevaert 10E75 plates instead of Kodak S0243 plates. This higher-resolution emulsion (about 30 times faster

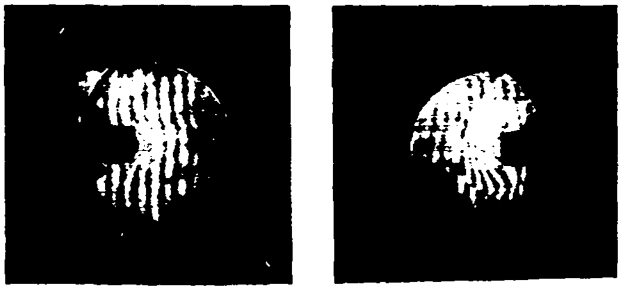

$t = 3 \mu sec$
$\Delta t = 0.1 \mu sec$

$t = 15 \mu sec$
$\Delta t = 1 \mu sec$

Fig. 12. Cine holographic interferograms of an air spark.

than the equivalent high-resolution Kodak 649 emulsion) so improves the bleached hologram diffraction efficiency that the chilled Hughes laser with 4-mm aperture, previously used only in reconstruction, can also be used to construct the hologram.

Figure 13 shows a four-frame sequence together with the image converter sync pulses giving the timing with respect to the magnetic field. The first two frames are of reduced size in order to allow the first (and fastest) image converter frame time to be 5 nsec, whereas the others are all 50 nsec. As before, the image converters are used in pairs, with the beam splitter causing mirror image pairs, as can be seen from the fiducial markers taped to one end window. No plasma structure could be discerned on the fast frame, even when the timing was slightly later than in this example. Unfortunately, to show this much plasma structure at the later times, the density had to be increased from the value that gives a neutron yield. (Current efforts with K. Thomas on a 5-pass geometry have yielded three fringe displacements at peak field in Scylla IA in the normal thermonuclear mode, but the light losses are too large to apply the multiple frame method.)

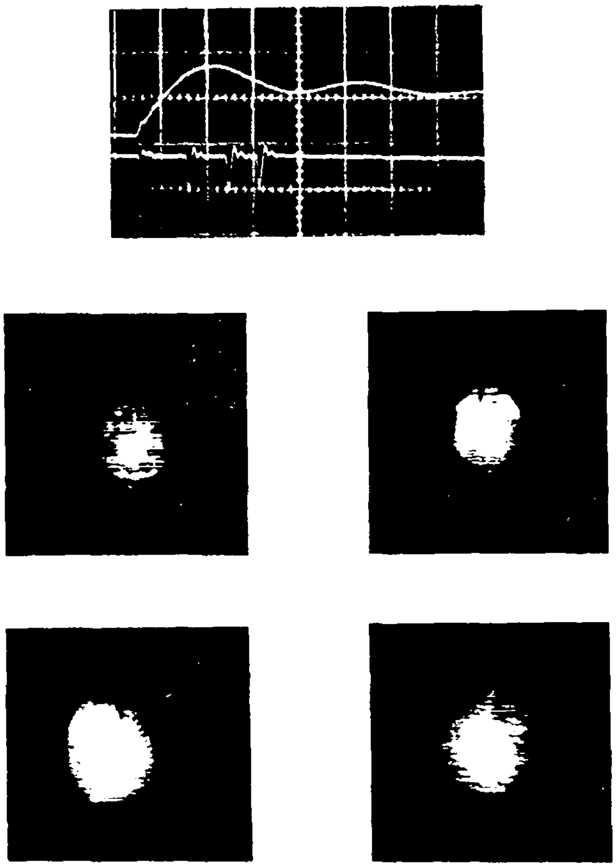

Fig. 13. Four-frame sequence of holographic interferograms in Scylla I-A.

We are exploring two further developments that could simplify this technique even more. One is the use of a single, multiple frame image converter. Indications are that the British Imacon may be adequate if the S-20 photocathode model at high frame rates is of equivalent quality to the S-11 model aleady tried at low frame rates. The second improvement would be an in-place, immediate dry processing photosensitive material to replace the photographic plate. Such techniques already exist, e.g., photopolymers[1] or bismuth films,[2] but in both cases the sensitivity is very marginal. All these considerations point to the fact that the fundamental problem is the lack of a sufficiently intense laser source of several microsecond duration.

Meetings and Publications

1. The cine-holographic interferometry work has been published in Applied Physics Letters 14, 341 (1969) and reported on at the Gordon Conference on Laser Interaction with Matter, Issaquah, Washington, August 1969.

2. A review article on "Optical Refractivity of Plasmas" co-authored with G. A. Sawyer, has been finished for inclusion in Academic Press Volume 9B on Experimental Methods in Plasma Physics, edited by R. Lovberg. The various sections comprise a derivation of the simple dispersion relations, and descriptions of interferometry, schlieren and shadowgraphs, Faraday rotation, the coupled cavity laser interferometer and holographic phase measurement.

3. Some time was devoted to preparation for a NASA committee meeting to review 30 proposals for the OSO-I satellite. This involvement, unrelated to current group effort, came about because of our x-ray work of several years ago, and has been very educational. It is not intended, however, to extend beyond this one-time participation.

References

1. D. H. Close, A. D. Jacobson, J. D Margerum, R. G. Brault, and F. J. McClung, Appl. Phys. Letters 14, 159 (1969).
2. J. J. Amodei, R. S. Mezrich, Appl. Phys. Letters 15, 45 (1969).

FEASIBILITY STUDIES OF PULSED, HIGH-β FUSION REACTORS

(F. L. Ribe)

Introduction

At the Culham Nuclear Fusion Reactor Conference (17-19 September, 1969) a paper[1] was presented with the above title, by G. I. Bell. W. H. Borkenhagen, and F. L. Ribe. This is a sequel to LA-3294-MS and deals with the inner-wall heating problem and lithium blanket breeding for a reactor with a molybdenum coil, lined inside with zirconium-copper to reduce joule heating losses. The conference paper deals with the situation near energy break-even, where the margin of energy

$$M = \text{electrical output energy/energy losses} \qquad (1)$$

is approximately unity. Coil cooling and blanket neutron multiplication are comfortably produced at burning times of 0.01-0.025 sec with duty factors ξ (= time between pulses/burning time) of 20 to 30.

In considering power-producing reactors and their economics, it is necessary to determine how large an energy margin can be achieved, since the fractional circulating power M^{-1} which must be injected to overcome losses (mostly joule heating in this case) largely determines the economics. As we shall see below, it appears that M values of about 4 can be realized. Comparison of the cost factors with those of the standard steady-state reactor[2] allows a simple economic comparison between the steady-state (S.S.) system and the pulsed θ-pinch in terms of the relative costs of the reactor cores consisting of magnetic energy storage and neutron blanket. At a circulating power of ~ 25% the pulsed core must cost about one half as much as the S.S. core. Since the stored energy of the S.S. system is 10 times as large and the blanket twice as large as their pulsed counterparts, there is a reasonable expectation that this factor of 2 can be realized.

Energy Balance at Large M Values

Since the energy balance is basically between thermonuclear output $P_T\tau_T$ (with a significant contribution from α-particle heating and direct conversion) and W_E, the joule heating loss, it is clear that large M values can be achieved by reducing the ratio of magnetic on-time, τ, to burning time, τ_T. In the breakeven studies ($M \approx 1$) the situation of Fig. 14 was assumed, in which for a sinusoidal magnetic pulse, $\tau = 8/3\ \tau_T$. For the longer burning times necessary to give large M values the magnetic pulse can have a rise time much shorter in relation to its average on-time, resulting in the trapezoidal pulse of Fig. 14, for which we can take $\tau \approx \tau_T$. In addition a closer estimate of the copper resistivity can be made on the assumption of a helium cooling cycle at the lowest temperature compatible with avoiding refrigeration. Thus the helium is assumed to

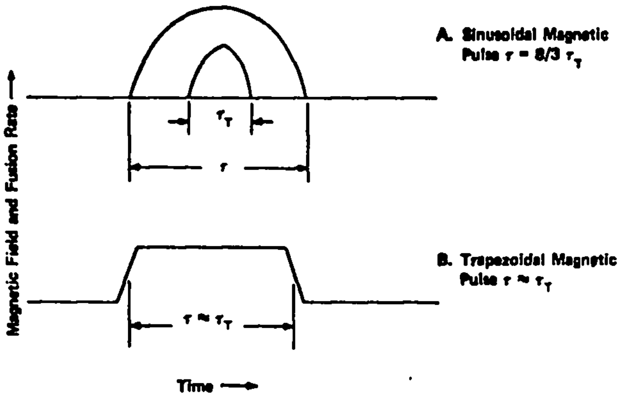

Fig. 14. Illustrating the relationship between burning time τ_T and magnetic on-time τ for sinusoidal and trapezoidal magnetic pulses.

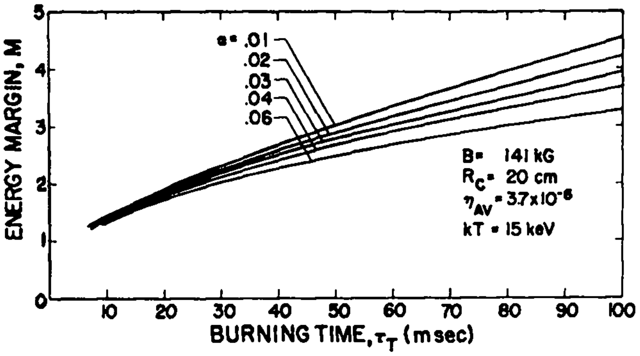

Fig. 15. Fusion energy margin vs burning time for a pulsed θ-pinch reactor at $R_c = 20$ cm. α is the ratio $P_p/\xi P_{To}$, where P_p is the coolant pumping power, ξ the duty factor and P_{To} the thermonuclear power evaluated before burnup.

enter the copper module at 100°C, and the average zirconium-copper temperature in the coil region itself is set by neutron-induced reactions and joule heating during τ_T as 250°C, giving an average Cu resistivity of 4.5×10^{-6} ohm-cm at the inner coil surface. The exit helium from the coil would be taken through the blanket to raise its temperature before use in the turbines. Since the feed has less neutron heating (it decreases as r^{-1} from the plasma axis) the resistivity averaged over the coil and feed slot is 3.7×10^{-6} ohm-cm.

In order to calculate M as accurately as possible we use the complete energy balance

$$\epsilon(P_T\tau_T + P_B\tau_T + W_p + \Delta U + W_E + 1.2\xi\ P_p\tau_T)$$

$$= M(P_B\tau_T + W_p + W_E + 1.2\xi P_p\tau_T - \Delta W), \qquad (2)$$

where the notation is the same as that of Eq. (83) of LA-3294-MS. The following special points are noted:

(1) Oliphant's α-particle heating calculations[3] at kT = 15 keV, $n_o\tau_T \approx 10^{15}$ cm^{-3} sec give an α-energy heat deposition ΔU in the plasma of $0.12\ P_T\tau_T$ and work of direct conversion $\Delta W = 0.070\ P_T\tau_T$. ; From his Fig. 1 the burnup fraction f (and hence the effective $P_T\tau_T$) must be corrected from their values f_o and $P_{To}\tau_T$ at n_o, kT_o by the factor 0.64, to account for rplasma radial expansion by a factor 1.5.

(2) We recalculate the heat transfer in the Cu and Mo for average He coolant at 200°C and 400 psi, for which C = 1.25, $K_c = 0.12$, $\mu = 0.064$, $\rho = 0.28$ in self-consistent British units (compare Table III of Ref. 1). Of particular importance is the fractional pump power α.

With these requirements we find the M values given in Fig. 15 as a function of $n_o\tau_T$, with α as a parameter. The pertinent reactor quantities consistent with helium cooling are given in Table I. The quantity α includes the contributions from both Cu and Mo cooling (0.0125 and 0.0175, respectively). That from joule heating of the feed slot is negligible. The quantity δT = 400°C represents the temperature rise at the inner surface of the copper liner during the burning pulse and limits the value of τ_T which can be used.

In column 3 of Table I are listed for comparison some of the quantities for the steady-state reactor of Carruthers, Davenport, and Mitchell[2] which we take as a standard of comparison in what follows. The quantity $W_M = \pi R_c^2\ B^2/8\pi$ is the magnetic energy in the coil per meter of length.

Ecomonic Considerations

Of the output power P_{out}, a fraction M^{-1} must be injected to provide for reactor losses. The effect of this circulating power P_I on reactor economics has been estimated by Carruthers,[4] for the case where P_I must go through the same thermal/

Table 1

Self consistent reactor quantities for net power production with helium cooling of the compression coil. ℓ_R is the length of a reactor producing 2000 MW(E). W_m is the coil magnetic energy per meter length. See Ref. 1 for notation.

	Pulsed Reactor	Steady-State Reactor	Unit
ϵ	0.4	0.42	
ξ	28		
M	3.8		
α	0.030		
R_c	20	175	cm
B	141	100	kG
ℓ_c	94		cm
ΔR_c	3.4		cm
P_{To}	1660		MW/m
τ_T	0.094	0.6 to 3.5	sec
P_{Th}	66	143	MW/m
P_{out}	20	60	MW(E)/m
ℓ_R	102	34	m
δT_{Tot}	400		°C
W_M	10	1200	MJ/m

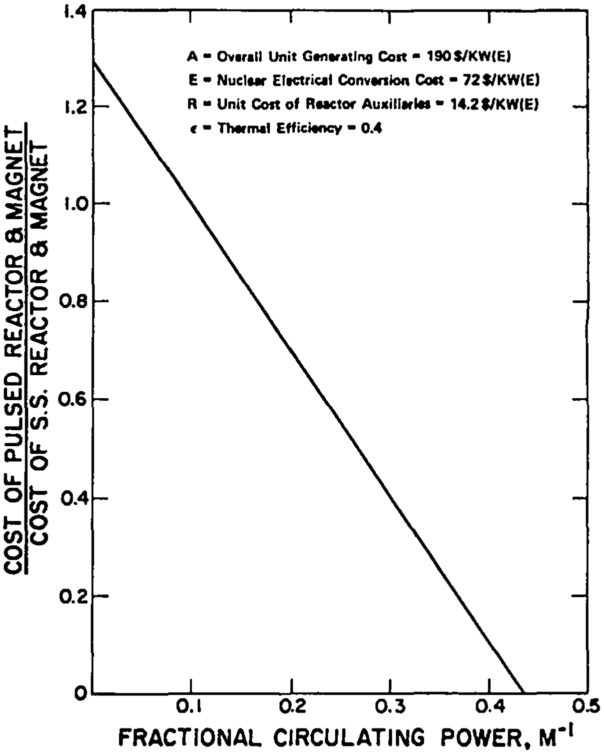

Fig. 16. Cost of pulsed reactor vessel and blanket, plus magnet, relative to that of a steady-state reactor vs fractional circulating power.

electric conversion as does P_{out}, as follows: If I is the cost per kW of P_I and N the cost per kW of P_{Th}, then the capital cost per kW(E) of saleable output is

$$A = \frac{1}{1 - M^{-1}} \left[M^{-1} \eta_I I + N/\epsilon + E \right] , \ \$/\mathrm{kW(E)} \quad (3)$$

where η_I is the efficiency of injection and E the cost per kW(E) of the thermal/electrical conversion, or "conventional plant." The quantity A is fixed by competition with fission plants at \$190/kW(E). Neglecting $\eta_I I$, which means that all elements of our pulsed magnetic storage system must be lumped together, including the elements for varying transfer inductance, this reduces to the necessary cost of the nuclear plant:

$$N = \epsilon \ \left[(1 - M^{-1})A - E \right] , \quad \$/\mathrm{kW(Th)} \qquad (4)$$

where both A and E are in \$/kW(E). From Table II of Ref. 2, we obtain E = 72 \$/kW(E). Since the blanket of our pulsed reactor is small compared to that of the S.S. reactor, we take the lower limit for the cost of reactor auxiliaries and customer "on costs" quoted in Ref. 2, viz. \$14.2/kW(Th). In Fig. 16 we plot N-14.2 = R, the cost of the reactor vessel and blanket plus magnet, normalized to the S.S. value of \$25.7/kW(Th), vs M^{-1}.

Fig. 16 shows that at the value $M^{-1} = 0.26$ of circulating power of Table I the reactor plus magnet must cost ½ as much as that in the S.S. reactor. A precise estimate of this cost for the pulsed case must await a detailed analysis of a particular magnet design for the pulsed system. However, the fact that the attainment of the value ½ is likely is indicated by the following comparisons:

(1) Blanket Costs In Ref. 1 a blanket 1.5-meter thick of slightly poisoned natural lithium was found to suffice comfortably for neutron multiplication. A refinement to include moderating carbon in the blanket reduces its thickness to 1 meter.[5] Comparing volumes on the basis of unit thermal output per meter, we find

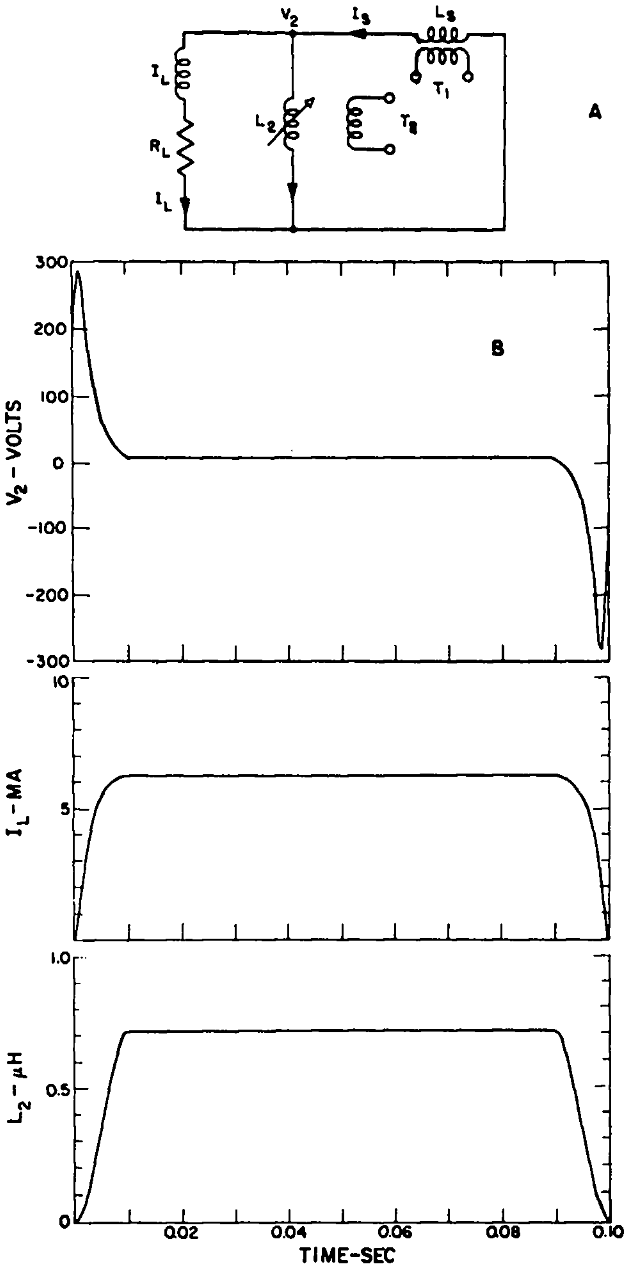

Fig. 17. A. Variable-inductor magnetic energy transfer circuit with losses and circulating-power transformers. B. Waveforms for typical operation on one meter of θ-pinch with a 20-cm coil radius.

$$\frac{\text{S.S. Blanket Volume}}{\text{Pulsed Blanket Volume}} = 2.2.$$

The pulsed reactor blanket requires no thermal insulation to protect a superconducting coil, and the LiH + Pb portion of the S.S. blanket can properly be reduced in the pulsed case, since it is only a biological shield. For the pulsed case it would be reasonable to estimate a reduction of the S.S. blanket cost by the factor 2.2, yielding the figure $4.4/kW(Th) for the pulsed case.

(2) Magnet Cost The small saving in blanket cost has in itself reduced the required magnet cost to 0.91 that of the S.S. reactor. From Table I we see that the relative energy stores in the coils per unit of P_{Th} are in the ratio

$$\frac{\text{S.S. Coil Energy Storage}}{\text{Pulsed Coil Energy Storage}} = 55.$$

This factor must be reduced by another factor of from 5 to 6 to account for the fact that the storage inductor L_s in a pulsed cryogenic system like that of Fig. 17A should store from 4 to 5 times the energy in the coil. Thus the relative energy storages of pulsed and superconducting energy supplies are in the ratio 0.1, while a saving of 45% of the S.S. store must be effected in the pulsed case. This conjunction of figures appears to offer a reasonable probability that the pulsed system will compete economically.

Magnetic Energy Storage Requirements of the Pinch Systems

Both the θ-pinch and programmed z-pinch require pulsed energy storage sources of the order of some thousands of MJ. A 100-meter length of the θ-pinch requires about 5000 MJ, and the programmed pinch requires a like amount. These requirements will almost certainly necessitate magnetic energy storage in order to meet cost requirements. In both cases the current from the magnetic-energy-storage source to the load must rise in a time of the order of 0.01 sec. In the θ-pinch case this is primarily because the rise time must be reasonably short compared to containment time to optimize the (power production/joule resistive loss) ratio. In the programmed-pinch case the rise time is the turbulent heating time and should be kept small in order to reduce possible anomalous losses in the plasma. The short access time to the energy storage appears to rule out the use of rotating machinery of the flywheel-alternator-inverter type.

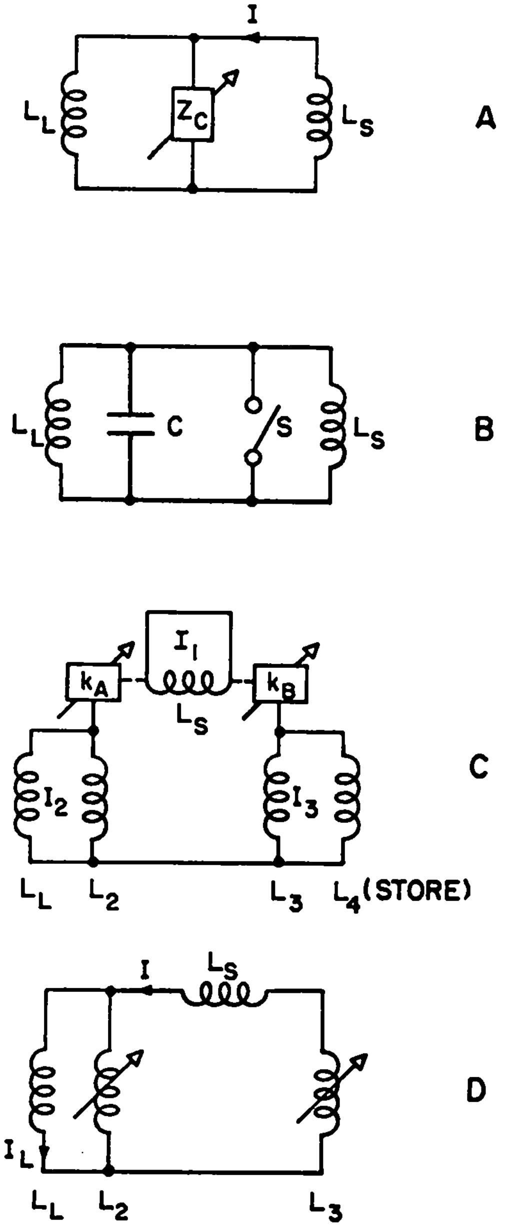

Fig. 18. Magnetic energy transfer circuits.

Cryogenic Alternatives

At the magnitudes of magnetic energy storage necessary, it seems likely that cryogenic magnets will be required. The superconducting magnet (4°K) is the cheapest, but cryogenic aluminum (20°K) and sodium (8.5°K) are only about 15% and 25% more expensive. The time variation of magnetic field places a severe restriction on the use of superconductors. For example, Smith's synchrotron supply[6] requires multiple strands of 10-μ thickness to bring the superconductor losses to an acceptable level at rise times of the order of 1 sec. In some of the variable-inductance cases discussed below the main storage inductor would have constant current for a purely inductive load. However, load resistive losses introduce fluctuations. Thus cryogenic aluminum is probably the best material.

Energy Transfer Elements

Assuming that the current is established in the energy storage inductor L_s, it is necessary to increase the variable impedance Z_c of the common branch, in order to transfer the current to the load inductor L_L (Fig. 18A). The various possibilities for Z_c will be discussed.

(a) Variable Resistor If Z_c is an increasing resistor (usually a fuse across an opening switch) there is an inevitable energy loss in the resistor which is equal to the energy transferred to L_L, or more. In the pinches considered, L_L itself has a resistance which dissipates appreciable energy ($\sim\frac{1}{2} L_L I^2$ for the θ-pinch; less for the programmed pinch) and some loss is acceptable. A cogent objection to resistive switching is that it is irreversible. Thus cyclic operation would require that the fuse be replaceable each cycle or that the resistor not be destroyed.

(b) Capacitive Energy Transfer A capacitor across the transfer switch S (Fig. 18B) can be used to suppress the voltage surge. However, it must store about $\frac{1}{3}$ the energy to be transferred to the load. It is generally considered that capacitors are too expensive for the full energy storage; therefore, even $\frac{1}{3}$ of this storage would also be too expensive, particularly for the θ-pinch case.

It is possible to use an appreciably smaller capacitor energy in the Simon-Bronner scheme,[7] where the current from L_s is inverted to ~ 1-kHz ac, and then fed to L_L through the capacitor. However, the ignitron circuit envisioned by them would be too slow for the pinch application. Solid-state devices offer the possibility of faster inversion, but it is questionable that tens of MA or more can be dealt with.

(c) Variable Inductors P. F. Smith[6] first proposed a system in which variable inductors would be used to transfer energy in a reversible (and therefore easily repetitive) way. As shown in Fig. 18C, inductors L_2 and L_3 have variable coupling coefficients k_A and k_B to the large inductor L_s, the effect being to transfer energy from L_4, through L_1 to L_L, and back again. Mechanical motion is required to change the coupling coefficients, and L_2 and L_3 are on a rotor inside the field of L_1. However, their torques cancel so that no flywheel is necessary to keep the system rotating, and the current I_1 is constant. A disadvantage of this system is that slip rings and brushes must be provided to connect L_2 and L_3 to L_L and L_4. At 10 MA or more this presents a problem which is better avoided.

A variant of Fig. 18C which avoids the moving contact is shown in Fig. 18D. Here variable inductors L_2 and L_3 provide the emf's to switch a major portion of the current I into L_L. L_2 and L_3 are driven off a common rotating shaft with opposite variations so that again there is no torque, and I is constant. If $L_3 = 0$, a flywheel must be attached to L_2.

In Fig. 17A is shown a circuit[8] for furnishing energy to the θ-pinch compression coil, with joule losses represented by the resistance R_L. That portion of the joule losses not supplied by direct conversion from plasma in L_L would best be furnished by an emf in the L_L branch which closely approximated $I_L R_L$. However, such coupling of external energy directly to L_L might be difficult, and two emf's applied through transformers T_1 and T_2 in the other branches of the circuit would perform equivalently. In Fig. 17B are shown typical waveforms[9] of L_2, I_L, and the emf at the branch point necessary to provide energy transfer and circulating power in a circuit typical of one meter of θ-pinch coil, discussed in Table I. The emf from transformer T_2, coupled to L_2, has the same shape as $I_L R_L$, as does that from T_1, during the time when current flows in L_L. The efm's have reverse signs during the time between pulses, giving no dc component. It is seen that the current I_L rises appreciably faster than L_2 does. In the circuit of Fig. 17A, for $R_L = 0$, the ratio of energy transferred to L_L to that stored in L_s before transfer is[9]

$$\frac{W_L}{W_S} = \frac{\left(1 - \frac{L_o}{L_L}\right)^2}{4\left(1 + \frac{L_L}{L_{max}}\right)} , \qquad (5)$$

where L_o and L_{max} are the minimum and maximum values of L_2. Maximum energy transfer occurs at $L_s = L_L/(1 + L_L/L_{max})$.

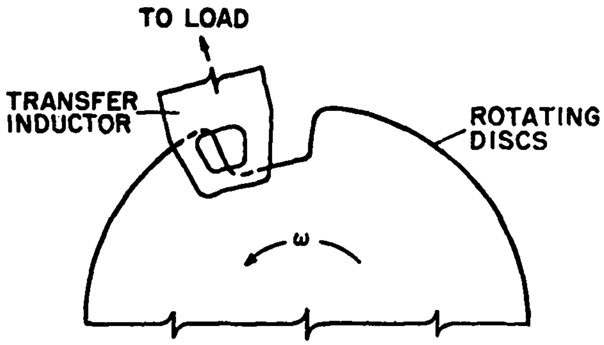

Fig. 19. Conceptual diagram of rotating disk variable inductor.

A suggested manner of realizing the variable inductance L_2 is to build a static coil of 20°K aluminum, consisting of multiple leaves of a few skin depths thickness, through which slots at the peripheries of interleaved disks pass, as indicated in Fig. 19.

The Sustained-Field θ-Pinch

A pulsed system has been proposed[10] for producing θ-pinches with steady compression fields which could be furnished by superconducting magnets outside the coil and neutron blanket. A wave form of the field is shown schematically in Fig. 20. An impulse of magnetic field of duration τ and magnitude $\approx -B$ is applied to the coil volume which is normally filled with magnetic field B. The θ-pinch plasma is formed on the back swing of the negative impulse and held by the steady field B.

The time τ can be quite short and therefore the joule heating in the compression coil negligible. Energy balance occurs at the Lawson

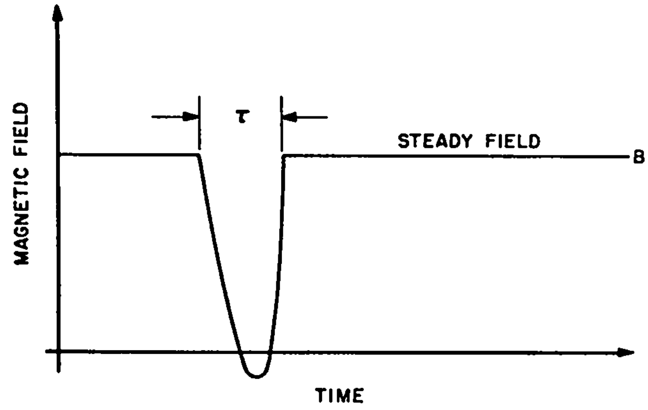

Fig. 20. Magnetic fields in the sustained-field θ-pinch.

nτ value, which is less than the value $n\tau = 1.6 \times 10^{14}$ cm^{-3} at which α-particle heating replenishes the plasma energy. Bodin[11] has suggested that this arrangement might find its best use as a steady-state reactor in which α-heating ignites new D-T fed at the center of a long straight coil with direct MHD conversion of the end-loss plasma. Such a plasma, with 10-msec burning time, might have a length of 2000 meters at a mirror ratio of 2 in order to partially contain the ions against high-β end loss. Its power output would be in the range of tens of thousands of MWE.

The fast pulsed magnetic energy would have to derive either from capacitors or resistively transferred magnetic energy storage. In the latter case energy-balance nτ would rise since the magnetic energy would appear as a loss, and the length of the reactor would increase considerably. Capacitor energy storage, even where the energy is only about one percent that of the superconducting coil, is too expensive. Thus the exploitation of this attractive idea is limited by the energy source.

References

1. G. I. Bell, W. H. Borkenhagen and F. L. Ribe, Paper 33, Culham Conference Proceedings. Also Los Alamos Scientific Laboratory Report LA-DC-10618.
2. R. Carruthers, P. A. Davenport, and J. T. D. Mitchell, Culham Laboratory Report CLM-P85 (1967).
3. T. A. Oliphant, Paper 37, Culham Conference Proceedings.
4. R. Carruthers, Culham Laboratory Report CMC/SPSC(67) 13 (1967).
5. G. I. Bell, private communication.
6. P. F. Smith, Proceedings, International Conference on Magnet Technology, Oxford, 1967 (Rutherford Laboratory, 1967), pp. 589-598.
7. Simon and Bronner, IEEE Trans. on Nucl. Sci. 14, 3, 33 (1967).
8. F. J. Edeskuty, E. F. Hammel, H. L. Laquer, J. Marshall, J. D. Rogers, and F. L. Ribe, Los Alamos Scientific Laboratory Report LA-4195-MS (1969).
9. D. A. Baker, private communication. We are indebted to Dr. Baker for deriving Eq. (5) and performing the computations necessary to produce the graphs of Fig. 17B.
10. W. F. Westendorp and H. Hurwitz, Jr., General Electric Research Laboratory Report No. 63-RL-(3254E). (Revised) (Nov. 1963).
11. H. A. B. Bodin, private communication.

SCYLLAC HELICAL $\ell = 1$ EQUILIBRIA WITH FEEDBACK STABILIZATION

(F. L. Ribe)

Introduction

During the past year further studies[1,2,3] of the sharp-boundaried, high-β Stellarator equilibria proposed by Grad and Weitzner[4] at Novosibirsk have indicated that this is an attractive possibility for Scyllac. This is because the $\ell = 1$ case is nearly neutrally stable to the m = 1 mode and equilibria with no shift of the plasma ring from the minor toroidal axis are possible if small admixtures of $\ell = 0$ or $\ell = 2$ fields are introduced. An unstable displacement ξ signals its presence by $\ell = 0$ and $\ell = 2$ fields which can be compensated in a feedback system to provide stabilization.

Summary of the Theory

One considers a sharp-boundaried theta-pinch plasma column of major radius of curvature R (minor radius a) in the presence of helical transverse fields whose scalar potential is of the form

$$\chi = (B_0/h)\left[C_\ell I_\ell(hr) + D_\ell K_\ell(hr)\right] \sin(\ell\theta - hz). \qquad (1)$$

In zero order the plasma column is straight with external longitudinal field B_0 and internal field

$\sqrt{1-B}\, B_o$, directed along z. Corresponding to the first-order coefficient C_ℓ, the maximum component of radial magnetic field in vacuum is

$$B_r^V(a) = C_\ell I'_\ell\,(ha). \tag{2}$$

The first-order excursion δ_ℓ of the plasma radius about r = a is given by

$$r = a + \delta_\ell \cos(\ell\theta - hz), \tag{3}$$

where, for $ha \ll 1$ (the case to be considered here) and $\ell \neq 0$,

$$\delta_\ell = B_r^V(a)/B_o ha\,(1-\beta/2). \tag{4}$$

For the special case $\ell = 0$, $1-\beta >> \frac{1}{2}\gamma(ha)^2$ (γ is Euler's constant), treated earlier by Haas and Wesson[5] and Morse, Riesenfeld, and Johnson,[6]

$$\delta_o = B_r^V(a)/B_o ha\,(1-\beta). \tag{5}$$

With a single ℓ value the third-order curvature effects, proportional to $1/R$, cause the plasma to shift inward by an amount

$$\bar{\xi} = 2\,[h^2 a R \delta_\ell^2 G_\ell\,(\beta, ha)]^{-1}, \tag{6}$$

where

$$G_o(\beta, ha) = 2\,(1-\beta)(3-2\beta)/(2-\beta) \tag{7}$$

$$G_1 = [(2-\beta)(4-3\beta)/4\,(1-\beta)]\,(ha)^2 \tag{8}$$

$$G_\ell = (2-\beta)(\ell-1)\cdot \ell > 1 \tag{9}$$

The effect of a conducting wall at some large radius has been neglected.

To second order the effect of major curvature is not observable, and a straight plasma column subject to a Stellarator field is unstable to displacements, given in lowest order by $\xi(m,k) = \xi_o \cos[m\theta - kz]$. Following recent experimental results on the $\ell = 0$ system[7,8,9] which show the presence only of the $m = 1$ mode (as would be predicted from the effects of finite Larmor radius on the plasma dynamics) we limit consideration to $m = 1$. The instability growth rates γ_ℓ are given by

$$\gamma_\ell^2 = \tfrac{1}{2}\beta\, G_\ell\, \delta_\ell^2\,(hv_A)^2 - (2-\beta)(kv_A)^2, \tag{10}$$

where $v_A = B_o/(4\pi\rho)^{\frac{1}{2}}$ is an "Alfvén" speed and ρ is the plasma density. The case $\ell = 1$ has an especially low growth rate, owing to the presence of the small factor $(ha)^2$ in Eq. (8). In the Scyllac ordering[2] under consideration here, these growth rates also apply in the presence of curvature.

Control of Equilibrium and Stability by Means of Combinations of Helical Field

The energy principle calculation[1] shows that a first-order $m = 1$, $k \approx 0$ displacement ξ_o gives rise to $(\ell \pm 1)$ helical distortions of the plasma column in next higher order which account for the instability. To first order in ha these are:

$$\delta_{\ell\pm1}^{(2)} = \tfrac{1}{2}(\ell - 1 \pm 1)\,\delta_\ell\,\xi_o/a \qquad \ell \neq 0 \tag{11}$$

$$\delta_{\pm1}^{(2)} = \tfrac{1}{2}\,\frac{2-\beta\,(3\mp1)}{2-\beta}\,\delta_o\xi_o/a. \tag{12}$$

This effect was noted earlier for the $\ell = 0$ system by Ribe and Riesenfeld.[10] In the $\ell = 1$ case the $\delta_{\ell\pm1}^{(2)}$ are equal and opposite to first order in ha, leading to neutral stability. To next higher order in ha, $\delta_2^{(2)}$ and $\delta_0^{(2)}$ take on additional terms in $(ha)^2$ which are responsible for the weak instability of Eqs. (8) and (10).

Such distortions can also be produced by second-order $\ell \pm 1$ external fields of strengths $C_{\ell\pm1}^{ext}$. According to Eqs. (2) and (4) the second-order distortions are

$$\delta_{\ell\pm1}^{ext} = C_{\ell\pm1}^{ext}\;/\;(2-\beta)(ha)^2 K_{\ell\pm1}\,(ha), \tag{13}$$

with the special case

$$\delta_o^{ext} = C_o^{ext}/2\,(1-\beta). \tag{14}$$

(Here the modified Bessel functions $K_{\ell\pm1}$ are to be evaluated in the limit $ha << 1$). The effect of the $\delta_{\ell\pm1}^{ext}$ is to give an "interference" of the ℓ and $\ell \pm 1$ components, producing an asymmetrical distortion of the plasma column. In the direction of largest distortion there is a force per unit length given by

$$F^{ext}_{\ell,\ell\pm1} = \left[\beta(2-\beta)/8\right] B_o^2 h^2 a^3 \delta_\ell \delta^{ext}_{\ell\pm1} \tag{15}$$

$$F^{ext}_{1,0} = \left[\beta(3-2\beta)/8\right] B_o^2 h^2 a^3 \delta_1 \delta_o^{ext} \tag{16}$$

$$F^{ext}_{0,\pm1} = \left[\beta(3-2\beta)/8\right] B_o^2 h^2 a^3 \delta_o \delta^{ext}_{\pm1} \tag{17}$$

A toroidal equilibrium with zero shift $\overline{\xi}$ can be produced by means of external $\ell\pm1$ fields. The effect of toroidal curvature can be represented by a radial force

$$F_R = \beta B_o^2 a^2/4R \ . \tag{18}$$

The balance of forces $F_R + F^{ext}_{\ell,\ell\pm1} = 0$ yields the following equilibrium conditions for $\overline{\xi} = 0$.

$$\delta_\ell \delta^{ext}_{\ell\pm1} = -2/(2-\beta)h^2 aR \tag{19}$$

$$\begin{cases} \ell \neq 0 \\ \ell, \ell-1 \neq 1,0 \end{cases}$$

$$\delta_1 \delta_0^{ext} = -2/(3-2\beta)h^2 aR \tag{20}$$

$$\tfrac{1}{2}\delta_o \left(\delta_1^{ext} + \delta_{-1}^{ext}\right) = -2/(3-2\beta)h^2 aR. \tag{21}$$

The last condition corresponds to that derived by Morse, Riesenfeld, and Johnson[6] for the "M and S" torus[11] of large aspect ratio.

The distortions produced by a destabilizing displacement produce similar interference forces which can be expressed as follows:

$$F_\ell = (\beta/8)B_o^2 (ha)^2 G_\ell \delta_\ell^2 \xi_o \ . \tag{22}$$

The equation of motion of the m = 1, $k \approx 0$ mode,

$$\pi a^2 \rho \ddot{\xi}_o - F_\ell = 0, \tag{23}$$

with $\xi_o \propto \exp \gamma_\ell t$, yields the expressions for γ_ℓ^2 given by the first term of Eq. (10).

In view of the equivalence of the distortions (fields) produced by destabilizing displacements and by external fields, the latter can be used to control the instability. The displacement ξ_o must be sensed and used to control the $C^{ext}_{\ell\pm1}$. In the simplest systems $\delta^{ext}_{\ell\pm1}$ becomes proportional to ξ_o:

$$a\delta^{ext}_{\ell\pm1} = g_{\ell\pm1}\xi_o. \tag{24}$$

As an example we consider feedback stabilization of the weakly unstable $\ell = 1$ system with an $\ell = 2$ external field. One might also consider an $\ell = 0$ field; however an $\ell = 2$ field seems simpler to produce. The new equation of motion is obtained by subtracting (15) from (23), and the stabilization condition is

$$g_2 = \frac{4-3\beta}{(1-\beta)}(ha)^2\delta_1 \ . \tag{25}$$

Realization of the Helical Fields

The C_ℓ and $B_r^v(a)$ of Eqs. (1) and (2) can be produced by means of helical longitudinal multipole conductors inside the θ-pinch compression coil, as shown in cross section of Fig. 21. In this case[4]

$$B_r^v(a)/I = (0.4)(2\mu_o/\pi\ell)h^2 b K'_\ell(hb) I'_\ell(ha) \ , \tag{26}$$

where the factor 0.4 accounts for the image currents in the coil and is measured by modeling. For a = 1 cm, b = 5 cm with $0.1 \leq h \leq 0.3$ we obtain $B_r^v(a)/I = 0.034$ and 0.013 G/A, for $\ell = 1$ and $\ell = 2$, respectively.

Another method of producing the helical perturbations in a θ-pinch is shown in Fig. 22, where the compression coil inner surface is shaped as a flux surface of the helical field, by means of rectangular grooves of depth Δ, providing an approximation to the sinusoidal amplitude

$$\delta_\ell(b) = (\Delta/2b)(1 - \Delta/2b). \tag{27}$$

It is easily shown that the excursions on the plasma at r = a and on the wall at r = b are related as follows:

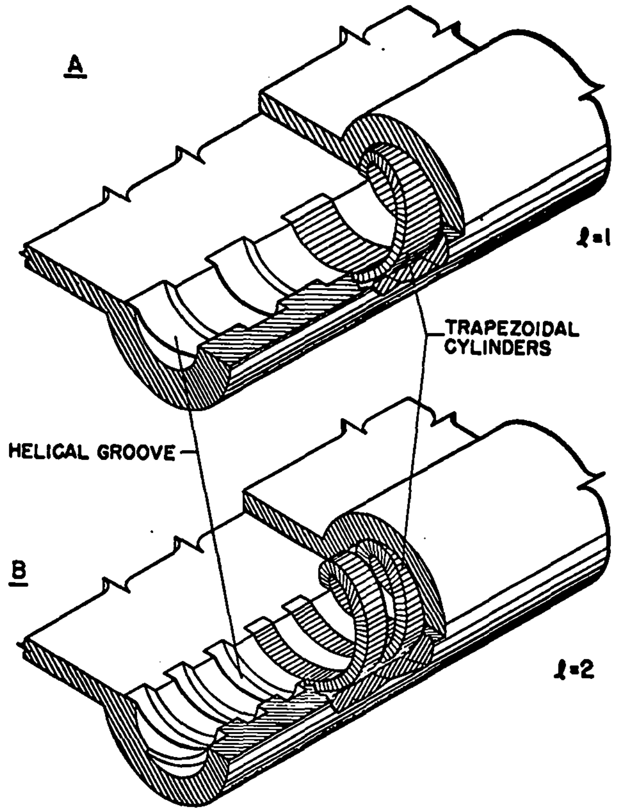

Fig. 21. Production of $\ell = 1$ and $\ell = 2$ helical fields by helical conductors inside a θ-pinch coil.

$$\frac{\delta_\ell(a)}{\delta_\ell(b)} = \frac{(b/a)I'_\ell(ha)/I'_\ell(hb)}{1 + \beta haI_\ell(ha)K'_\ell(ha)} \approx \begin{cases} \dfrac{b/a}{1 - \beta/2} & \ell = 1 \\ \dfrac{1}{1 - \beta/2} & \ell = 2 \end{cases} \qquad (28)$$

In practice it seems preferable to use grooves like those of Fig. 22, to provide the main toroidal equilibrium and to use conductors only for correcting the equilibrium and for feedback stabilization. The skin effect of the hollow trapezoidal cylinders in Fig. 22 provides a time delay of the penetration of magnetic lines into the helical grooves so that the symmetry of the θ-pinch implosion is not disturbed.

To evaluate the $\ell = 2$ current typically necessary for feedback stabilization we set $\delta_1 = \beta = 0.5$ and $ha = 0.2$ in Eq. (25) and $\xi_0 = a$ in Eq. (24). The result is $\delta_2^{ext} = 0.025$. For $B_o = 100$ kG, Eq. (4) yields $B_r^v(a) = 0.375$ kG, and Eq. (26) yields the current pure wire, $I_2 = 29$ kA.

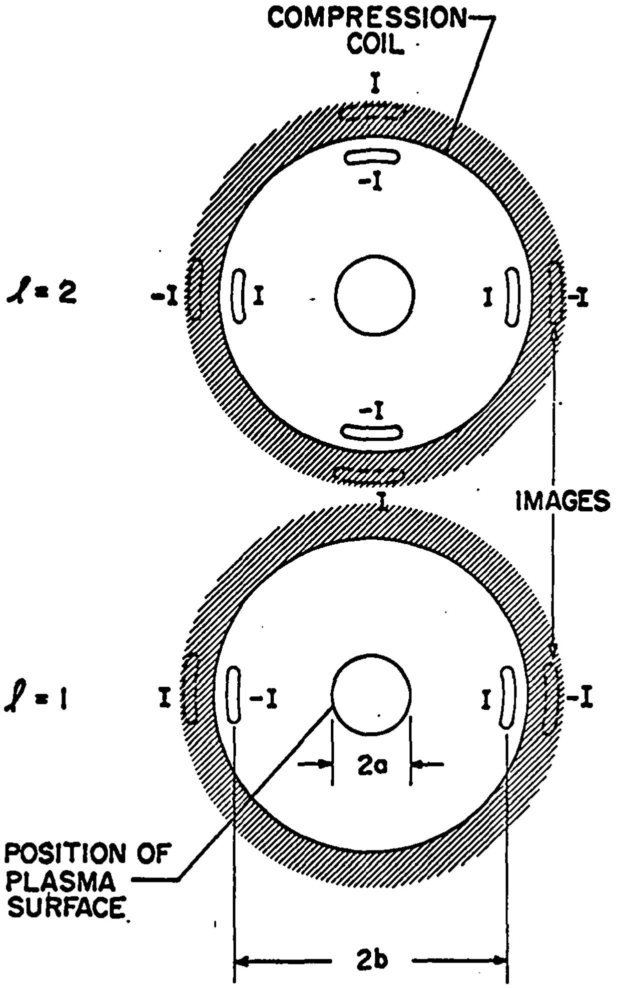

Fig. 22. Illustrating the production of $\ell = 1$ helical fields by flux shaping the inner surface of a θ-pinch coil.

The maximum k value to be stabilized is given by Eq. (10) with $\gamma_\ell = 0$. For the $\ell = 1$ system

$$k_{max} = \left[\beta(4 - 3\beta)/8(1 - \beta)\right]^{\frac{1}{2}} h^2 a \delta_1. \qquad (29)$$

For the above parameters the corresponding minimum wavelength is 5.7 meters.

Discussion

The application of the methods discussed in this paper to the Scyllac toroidal theta pinch[12] depends on the exact degree of instability, as described by Eqs. (8) and (10), which indicate that the $\ell = 1$ system lies close to neutral stability, at least in the present analytical approximation. In addition both equilibrium and stabilization depend on the validity of the force $F_{\ell,\ell\pm1}$ of Eqs. (15) through (17). Critical experiments can be done on a long straight θ-pinch plasma with a basic quasi-static helical ℓ-type field, in order to observe stability, and an additional set of $\ell \pm 1$ conductors to produce the sideward force.

The heuristic treatment given in this paper makes use of the approximation $ha \ll 1$, for which the mathematical expressions are simple. A more complete derivation without such approximation is given in Ref. 3.

Acknowledgment

In a recent conversation with M. N. Rosenbluth it became clear that essentially the same method of feedback stabilization presented here had occurred to him independently. Discussions with H. Weitzner on related material are also acknowledged.

References

1. M. N. Rosenbluth, J. L. Johnson, J. M. Greene, and K. E. Weimer, Phys. Fluids 12, 726 (1969).

2. H. Grad and H. Weitzner, Phys. Fluids 12, 1725 (1969).

3. F. L. Ribe, Los Alamos Report LA-4098 (1969).

4. A. A. Blank, H. Grad, and H. Weitzner, Plasma Physics and Controlled Nuclear Fusion Research, Novosibirsk Conference Proceedings 1968 (I.A.E.A., Vienna, 1969). Vol. II, p. 607.

5. F. A. Haas and J. A. Wesson, Phys. Fluids 10, 2245 (1967).

6. R. L. Morse, W. B. Riesenfeld, and J. L. Johnson, Plasma Phys. 10, 543 (1968).

7. H. A. B. Bodin, J. McCartan, A. A. Newton, and G. H. Wolf, Plasma Physics and Controlled Nuclear Fusion Research, Novosibirsk Conference Proceedings 1968 (I.A.E.A., Vienna, 1969). Vol. II, p. 533.

8. E. M. Little, A. A. Newton, W. E. Quinn, and F. L. Ribe, Plasma Physics and Controlled Nuclear Fusion Research, Novosibirsk Conference Proceedings 1968 (I.A.E.A., Vienna, 1969). Vol. II, p. 555.

9. E. Fuenfer, J. Junker, M. Kaufmann, J. Neuhauser, and V. Seidel, Bull. Am. Phys. Soc., 13, 1552 (1968).

10. F. L. Ribe and W. B. Riesenfeld, Phys. Fluids 11, 2035 (1968).

11. F. Meyer and H. V. Schmidt, Z. Naturforsch. 13a, 1005 (1958).

12. E. L. Kemp, W. E. Quinn, F. L. Ribe, and G. A. Sawyer, Bull. Am. Phys. Soc. 12, 1161 (1967).

THEORY
(Group P-18)

MHD STABILITY OF THE LOS ALAMOS QUADRUPOLE

(D. A. Baker and L. W. Mann (T-5))

General

We have made a stability analysis of finite beta equilibria obtained numerically for the geometry corresponding to the Los Alamos quadrupole injection experiment. The equilibrium is calculated with the idealizing assumptions of azimuthal symmetry and perfectly conducting boundaries.[1] The calculation was made by numerical application of the energy principle in the form developed at Princeton[2,3] to an azimuthally symmetric system having no poloidal currents.

After an energy minimization with respect to perturbations in the field and azimuthal directions, the total energy change can be written in the form

$$\delta W = \int \delta w(\psi) d\psi$$

where ψ is the stream function for the equilibrium magnetic field $\vec{B}$. This feature allows one to study the stability of each flux surface separately. If any $\delta w(\psi) < 0$ the system is unstable since a perturbation localized there will give a total $\delta W < 0$. The final minimization of $\delta w(\psi)$ with respect to displacements normal to flux surfaces reduces the stability problem to determining the existence of solutions for negative eigenvalues Λ of an Euler equation of the form

$$\frac{d}{d\ell}\left(\frac{1}{r^2 B}\frac{dX}{d\ell}\right) + \left(\frac{\Lambda - p'D}{B}\right) X = K \oint \frac{DX}{B} d\ell \qquad (1)$$

where D and K are functions which are determined from the equilibrium solution and $p' = dp/d\psi$ where p is the pressure as a function of ψ. Periodic solutions $X_\psi(\ell)$ of this equation represent the product of rB and the component of the perturbation in the $\vec{\nabla}\psi$ direction (as a function of arc length ℓ along the field line) which minimizes the energy $\delta w(\psi)$. If such solutions exist for $\Lambda < 0$ they correspond to displacements from equilibrium which can make $\delta W < 0$ and the system is unstable.

Fortunately one can determine the existence of solutions with negative eigenvalues from the solutions of a simpler equation obtained from Eq. (1) by setting Λ and the right hand side to zero. This simplification stems from the fact that Eq. (1) is a linear equation with periodic coefficients and is subject to the Floquet theorem. Related types of problems arise in the stability analysis of orbits in particle accelerators. The required solutions were obtained by numerical integration of the differential equation along the equilibrium field lines. Unlike the usual stability analysis using low-β expansions, our numerical procedure is valid for arbitrary β. It is limited only by the inaccuracies introduced by the finite difference approximations. The details of the techniques used and results for the LASL device will be given in a Los Alamos report now in preparation. We give here only a brief summary of some of the results we have obtained.

Equilibrium Properties

The geometry used in the computation is shown in Fig. 23. To obtain the equilibrium solutions, one must specify how the plasma pressure is distributed over the magnetic flux. We have studied pressure profiles which peak on the separatrix and go continuously to zero at the plasma edge. Three functions have been used: a half-cycle cosine, a full-cycle displaced cosine, and a truncated and displaced gaussian. The half-cycle and gaussian profiles give a finite pressure gradient at the plasma edges while the full-cycle cosine is arranged to produce a pressure which goes to zero with zero slope at the plasma boundaries.

One characteristic of the equilibria is that as the peak pressure is raised, for a given width of the pressure profile (distance between plasma boundaries in flux units), the separatrix departs from its vacuum flux value to lower values nearer the current rings. Corrections were made during the computation to keep the plasma pressure peaked on the separatrix. When this procedure is

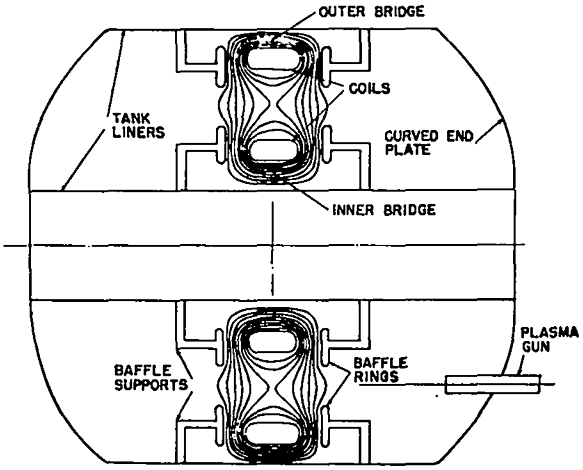

Fig. 23. Geometry used to compute equilibria and stability of an azimuthally symmetric version of the Los Alamos quadrupole injection experiment.

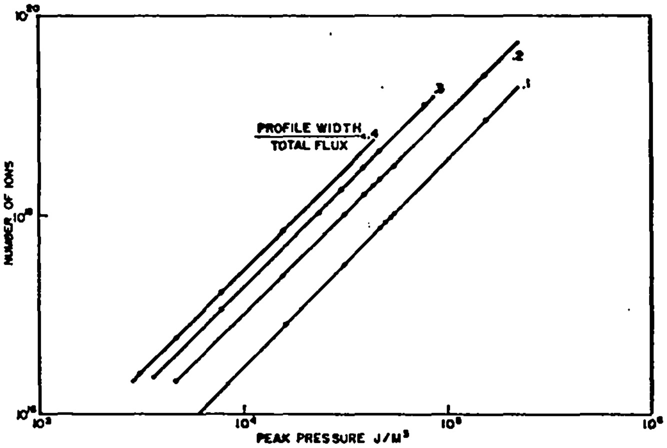

Fig. 24. Plot showing the variation of the number of ions (for T_i = 2.5 keV) contained in a half-cycle cosine pressure profile $p(\psi)$ as a function of the peak pressure for various profile widths.

followed it is found that the total amount of plasma varies linearly with the peak pressure as shown in Fig. 24 over the range of pressures calculated. This dependence shows that the equilibrium adjusts itself to remain essentially of constant volume. Evidently over this pressure range, the spatial widening of the flux tubes near the separatrix as the pressure increases is compensated by the narrowing of the tubes nearer the plasma edges and the shortening of the field lines as the separatrix shifts its position inward.

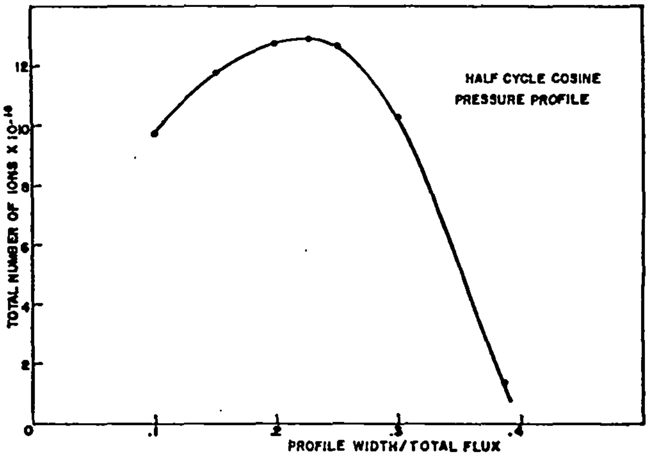

Fig. 25. Curve showing the number of ions at T_i = 2.5 keV contained at the MHD stability limit vs the width of a half cosine pressure profile.

MHD Stability Properties

A study was made to see how much plasma at the design ion temperature of 2.5 keV can be introduced into the containment field before onset of MHD instability. For a specified width of a given pressure profile it is found that there is a definite limit to the peak pressure above which the system becomes unstable. It was found, moreover, that there is an optimum width which yields the maximum amount of plasma at the MHD stability limit. This effect is evident in Fig. 25 which shows the amount of plasma, i.e., the number of contained ions for kT_i = 2.5 keV and T_e negligible, at the stability limit versus the width of a half-cycle cosine pressure profile. The optimum width of 22.5% of the total flux corresponds to 1.3 x 10^{19} ions which roughly are comparable to the number of energetic ions expected to be produced by the coaxial plasma gun. The corresponding critical $\beta (\beta \equiv p/(B^2/2\mu_0))$ values are low in the inner and outer bridges, 0.1% and 2.5%, respectively. The β values naturally become high in the weaker field regions.

An example of an eigenfunction $X_\psi(\ell)$ corresponding to a negative eigenvalue is shown in Fig. 26. This solution represents the lowest energy $\delta w(\psi)$ perturbation for a half cosine pressure profile at a value of ψ where the pressure is 10% of the pressure maximum. As expected, Fig. 26

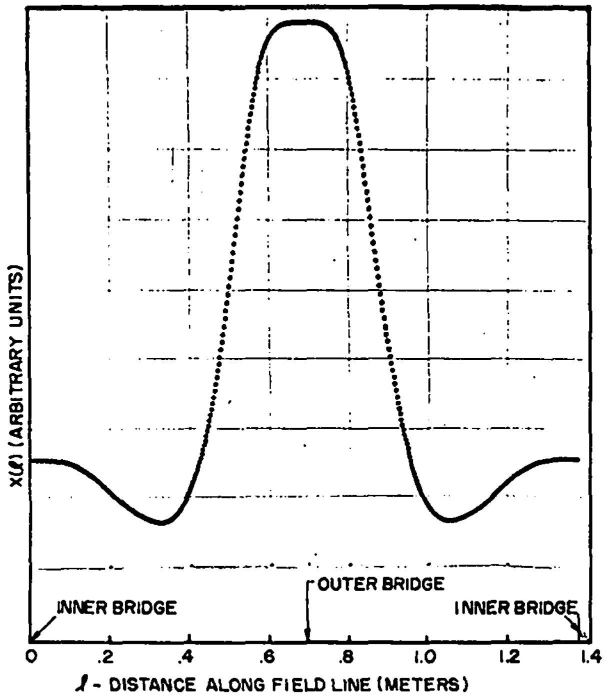

Fig. 26. Sample energy minimizing perturbation which yields $\delta w(\psi) < 0$ (instability).

shows that this unstable perturbation arises from large displacements (ballooning) in the bridge regions where the field line curvature is unfavorable and is much greater for the outer bridge where the field is weaker.

An investigation was made to see to what extent the amount of plasma contained at the stability limit might be increased if an asymmetric profile is used. For the same pressure distribution outside the separatrix as the optimum described above, but with a wider cosine dependence inside (nearer the current rings) extending inside over more flux by a factor of 1.7 we find that the amount of plasma at the stability limit increases 23%. One is able to load some plasma stably anywhere in this inside region where the average curvature is good. Outside the separatrix, however, no plasma can be stably contained away from the walls beyond the flux surface where $\oint d\ell/B$ reaches a minimum.

References

1. D. A. Baker and L. W. Mann, LASL Report LA-4075-MS (October 1968) p. 110.

2. I. B. Bernstein et al., Proc. Roy. Soc. (London) A244 17 (1958).

3. J. M. Green and J. L. Johnson, Adv. In Theor. Phys. 1 195 (1965).

PLASMA SIMULATION

(D. Dickman (C-4), J. P. Freidberg, B. Marder, R. L. Morse, C. W. Nielson, T. A. Oliphant, L. Rudsinski (C-4), and C. R. Shonk (J-10))

During this last year, numerical simulation methods have been applied to new and extended areas of plasma physics, and some new methods have been developed. In the first category of further applications of already developed methods are multi-dimensional beam plasma studies, the related subjects of electrostatic anomalous resistivity and electrostatic shock wave formation, velocity space instabilities of high-β plasmas (in axisymmetric systems), including relativistic beams in electron ring accelerators, and deposition of laser energy in dense, inhomogeneous plasmas.

In the second category are two new simulation techniques which are variations of the particle-in-cell concept. Methods have been developed for introducing the effect of weak binary collisions into PIC codes and for doing linear stability analysis of systems which are too complex for analytic methods.

Beam Plasmas

Previous numerical simulations of two-beam electron distributions (fixed positive background), ranging from two equal beams to bump-on-tail form, in one dimension have shown most such problems to be dominated by persistent strong single mode structure and the corresponding phase space vortices.[1] When such mode structure persists, the electrostatic field energy settles down to the self-consistent super thermal level, after an initial overshoot. In order to determine the relevance of all of this to real life, several of the cases previously treated in one dimension have been done in one, two, and three dimensions with all other conditions held fixed so that the effect of dimensionality could be clearly seen. The result found was that while the single mode with greatest linear growth rate still dominates the early development in two and three dimensions, all modes damp away after saturation leaving only "thermal" fluctuations in the electrostatic field.[2] Hence the much discussed vortices are apparently of no real significance in magnetic field-free plasmas.

Anomalous Resistivity

The development of the ion-electron two-stream instability has been simulated in one dimension with the hydrogen mass ratio, i.e., $m_i/m_e = 1836$. Several cases have been studied ranging from the strongly unstable two-beam limit to the ion-acoustic regime. Nothing resembling a dc resistivity has been found, but such was not expected. Instead, the current flow increases under an externally imposed electric field until instability develops, then the current levels off while the thermal velocities increase, and then the pattern repeats. This sequence of plateaus in the current is more pronounced for higher external fields and hence more unstable plasmas. The results are consistent with published experimental results, but close quantitative comparisons are difficult because experimenters are unable to give good estimates of initial electron temperatures. These results have been reported at Stanford[3] and will be published soon.

Collisionless Electrostatic Shocks

The study of strong collisionless shocks is important to the understanding of the earth's bow shock and the heating of plasmas in Sherwood devices and is well-suited to study by numerical simulation (as well as being virtually inaccessible to analytic plasma turbulence methods). The formation of a collisionless shock has been simulated in two dimensions under the assumption that the crucial interaction between ion streams is electrostatic and therefore acts through the presence of warm electrons. These electrons must, therefore, be treated microscopically along with the ions. Because of anticipated development of important unstable modes oblique to the shock front, it makes no sense to do this problem in one dimension. Computations to date have shown the formation of the shock to be essentially laminar and dominated by a small forward-breaking ion component.[4] The interaction of this breaking component with the plasma ahead of the shock is seen from linear estimates to be unstable to the oblique modes mentioned above in a way which is expected to be significant for longer-time behavior. This study is continuing.

Axisymmetric High-β Plasmas

A class of codes has been developed for studying axisymmetric charge-neutral high-β plasmas and has previously been used to study mirror instabilities in θ-pinches and rotational and tearing modes in Astron-like cylindrical sheet pinches.[5] One of these codes has now been used to treat fire hose modes ($T_{\parallel} >> T_{\perp}$) in a cylindrical sheet pinch. Because of the symmetry, this locally hose-like mode has the overall appearance of the wrinkled bellows of a concertina. Unlike the mirror and tearing modes which lead to persistent long wavelength structure after repeated coalescing from shorter wavelengths, the hose instability seems to develop toward shorter wavelengths after which the plasma returns to a uniform but thicker sheet pinch form with a modified velocity distribution. This is a qualitatively new development in strong turbulence theory. A more complete discussion of this result will be published soon.[6]

Electron Ring Simulation

As an outgrowth of the axisymmetric high-β work above, a code has been developed which simulates similar systems but with charge separation, multiple species and relativistic particle motion. This work was initiated at the request of Andrew Sessler, Lawrence Radiation Laboratory, Berkeley, for the purpose of supporting the electron ring accelerator work there and has been carried on in collaboration with Jackson Laslett and Al Garren from that laboratory.

The first physical results, which have been obtained in the last month, show containment of a pure electron ring in a focussed field, space charge disassembly of a pure electron ring in a straight field and self-pinched containment of a partially ion-neutralized ring in a straight field. This behavior was anticipated and indicates progress with the simulation techniques. These cases are being checked further for various types of errors before we proceed to study questions about which the experimenters are concerned.

Laser Heating of Plasma

Codes have been written for studying the propagation in one and two dimensions of an electromagnetic wave into an inhomogeneous plasma. Relativistic effects and binary collisions have been included in the basically collisionless treatment. This is a qualitatively new physical application and progress to date has consisted of getting a feeling for the relative importance of different aspects of the problem.

Binary Collisions

In view of the fact that many Sherwood experiments, as well as anticipated CTR devices, operate in a regime where binary collisions cannot be completely neglected and the realization that weak collisions (less than a full right angle collision on average during a time of interest) can have a profound effect on plasma turbulence, a method has been developed for introducing multiple small-angle collisions into basically collisionless PIC codes. The method considers local densities and temperatures to obtain local collision rates and then modifies particle velocities according to a Monte Carlo procedure which conserves overall momentum and energy, cell by cell. This method has been checked against a Fokker-Planck code by comparing time evolution of a non-Maxwellian velocity distribution of a homogeneous plasma and found to give excellent results. Subsequently the method has been applied to the simulation of mirror instabilities in a θ-pinch. This problem, which uses the same basic code discussed above in connection with fire hose modes in an axisymmetric sheet pinch, provides a good test of the method because it naturally requires two-dimensional spatial inhomogeneity as well as the full three-dimensional velocity space. A range of scalings, i.e., mean collision rates, have been tried. The results show that somewhat less than a full collision in the time required for full development of instability and some coalescing causes a considerable shift of the wave spectrum to longer wavelengths, in agreement with experimental observation. A wide range of applications of this method is anticipated. A first paper on the method and the application to the θ-pinch mirror instabilities has been submitted to the Physics of Fluids.

Linear Stability Studies

A numerical method has been developed for determining linear instability of collisionless plasma equilibria, regardless of the kind of complex field geometries, density inhomogeneities and unusual velocity distributions which make analytic approaches impossible.[7] The method is a direct linearization of the particle-in-cell method, including a differential version of the usual area weighting. Like linear analysis, the method takes advantage of symmetries in initial equilibria to reduce the effective number of dimensions in a problem by Fourier analyzing perturbations with respect to the corresponding degrees of freedom. The method has only been tested on simple problems but a considerable number of useful applications is expected.

Cooperative Program

In the last year, LASL has assumed responsibility for making numerical plasma simulation techniques available to other AEC contractors. Collaborations and some transfer of software have taken place or are in progress with CTR groups at ORNL, the University of Houston, the University of Texas, and Stevens Institute of Technology. In addition, preliminary discussions have taken place with several other groups, including those at the University of Wisconsin and Yale.

References

1. R. L. Morse and C. W. Nielson, Phys. Fluids 12, 2418 (1969).
2. R. L. Morse and C. W. Nielson, Phys. Rev. Letters 23, 1087 (1969).
3. R. L. Morse and C. W. Nielson, "Particle-In-Cell Simulation of Counter-Streaming Electron and Ion Beams," Proceedings of the Third Annual Numerical Plasma Simulation Conference, September 2-5, 1969, Stanford University, Stanford, California, Paper No. 9.
4. C. R. Shonk and R. L. Morse, "Two-Dimensional, Two-Species PIC Simulations of Collisionless Shocks," Paper 9A5, Bull. APS (November, 1969).
5. D. O. Dickman, R. L. Morse, and C. W. Nielson, Phys. Fluids 12, 1708 (1969).
6. R. L. Morse, "Multi-Dimensional Plasma Simulation by the Particle-In-Cell Method," Vol. 9, Methods in Computational Physics, Interscience Publishers.
7. J. P. Freidberg, R. L. Morse, and C. W. Nielson, Paper 10E10, "Numerical Method for Studying Linear Stability of Highly Inhomogeneous Plasmas," Bull. APS (November, 1969).

VARIATIONAL APPROACH TO VLASOV PLASMAS

(H. R. Lewis)

The application of Hamilton's variational principle to Vlasov plasmas has expanded considerably during the past year. It now includes computer simulation with a finite number of point particles, nonlinear analysis of the cold two-stream instability with a continuum of particles, and linearized analysis of one-dimensional electrostatic oscillations. Work on the linearized analysis of a rotating theta pinch with this method has begun in collaboration with J. Freidberg (P-18). The variational principle is proving to be an effective tool for numerical analysis of Vlasov plasmas, both in the nonlinear and the linear regimes. It also appears that some analytical understanding of the time-asymptotic development of the two-stream instability may result from this work. A general feature of the approximation schemes implied by the variational principle is that they possess an exact energy theorem.

A detailed description of the variational method with some applications to nonlinear problems has been prepared for publication as a chapter in Vol. 9 of Methods in Computational Physics (Los Alamos Scientific Laboratory preprint LA-DC-10775). The introduction to this book chapter is reprinted below. A short article on this subject is to be published in the Journal of Computational Physics.

Computer Simulation with Point Particles

When the variational principle is applied to simulation with a finite number of point particles, the equations obtained are the equations of motion for the particles along with a specific numerical approximation scheme for computing the scalar and vector potentials. The approximation scheme is determined uniquely by the functional forms that are chosen for parameterizing the potentials. For example, if the potentials are represented by linear combinations of local basis functions of position, then a specific generalized finite-difference scheme is obtained from the variational principle. In the case of electrostatic problems, choosing the local basis functions to be those appropriate to a piecewise linear approximation of the scalar potential leads to the particle-in-cell method used by Morse and Nielson.

The details of the generalized finite-difference schemes implied by the variational principle in the general case, including magnetic interactions, will be worked out soon. It is expected that they will prove useful in practical simulation computations. Also, it has now been recognized that the variational principle can be used to derive finite-difference schemes for solving the particle equations of motion.

Two-Stream Instability

The investigation of the cold two-stream instability using a continuum of particles has continued during this year, and progress has been made toward an understanding of the time-asymptotic development. To begin with, for the problems that have been tried it has been observed that certain quantities are insensitive to the number of basis functions used. In particular, the peak value of the electric energy, the time of occurrence of this peak value, and the velocity distribution at long times have been insensitive to the number of basis functions. After the time of peak electric energy, the numerical computations become increasingly time-consuming because definite integrals appearing in the differential equations become more difficult to evaluate. At least in some cases, the increasing complexity of the integrands finally becomes an asset because the integrals can then be evaluated by an asymptotic method, and it is conjectured that this is true in all cases. The asymptotic evaluation has suggested the use of a quite different set of parameters for representing the particle position as a function of the initial conditions and time. In terms of them it seems to be possible to describe the long-time development in a simpler way. The next step is to investigate the use of the new parameters. The numerical work on this problem has been in collaboration with J. Melendez (C-4).

Linearized Analyses

By appropriate use of the variational principle, the linearized description of Vlasov plasmas has been formulated in terms of a system of ordinary second-order differential equations in time with constant coefficients and time-dependent driving terms. This system of equations is particularly suitable for numerical computations of the linearized behavior of even complicated physical situations. The constant coefficients of the homogeneous part of the equations depend on the equilibrium distribution functions, but they do not depend on knowledge of the equilibrium particle orbits. The time-dependent driving terms depend on the perturbations of the equilibrium distribution functions and on some knowledge of the unperturbed orbits. Therefore, to compute the linear eigenfrequencies, no integration along unperturbed orbits is required. To do the complete initial value problem, some knowledge of the unperturbed trajectories is required as would be expected.

This method has been applied with considerable success to the problem of one-dimensional electrostatic oscillations with an arbitrary equilibrium velocity distribution. With a modest number of basis functions, Landau damping has been accurately predicted for a Maxwellian equilibrium, and the bump-on-tail instability has been observed for a bounded equilibrium velocity distribution. A particular solution of the basic equations has been found for an arbitrary equilibrium velocity distribution. It also appears simple to identify the effects that are a result of truncation of the number of basis functions and which would disappear with a complete set of basis functions. The numerical work on this problem is being done in collaboration with J. R. Neergaard (C-7), B. Buzbee (C-4), and G. Golub (C-Division consultant).

Because of the encouraging results with the one-dimensional electrostatic problem, the method is being applied in collaboration with J. Freidberg (P-18) to the rotating theta pinch.

Description of the Variational Method

Here we reprint the introduction to the chapter that was prepared for Vol. 9 of Methods in Computational Physics (Los Alamos Scientific Laboratory preprint LA-DC-10775):

The problem of obtaining useful numerical descriptions of the behavior of high-temperature plasmas is currently of intense interest, for example in the field of controlled-thermonuclear-fusion research. For sufficiently high temperatures it is appropriate to use the Vlasov approximation, in which the particles can be represented by time-dependent distribution functions, one for each particle species. These distribution functions are functions of position and velocity in a single-particle phase space, and they satisfy collisionless Boltzmann equations in which the electromagnetic field due to the particles is approximated by the so-called "self-consistent" field. A completely equivalent way to represent the particle motion is to specify the trajectories of the points in the single-particle phase space for each species. The trajectories, which are the characteristic curves of the Boltzmann equations, are the solutions of the single-particle equations of motion that are satisfied for each particle when the electromagnetic field due to the particles is replaced by the "self-consistent" field. This latter method of describing the particle motion, that of specifying particle trajectories instead of distribution functions, is being used with increasing favor, especially for numerical work.

In this chapter we present a general method for deriving numerical approximation schemes within the framework of the trajectory approach, a method based on an exact Lagrangian description of plasmas in the Vlasov limit. The functions to be determined in this Lagrangian formulation are the scalar and vector potentials, $\phi(\vec{r},t)$ and $\vec{A}(\vec{r},t)$, as functions of position $\vec{r}$ and time t, and functions $\vec{R}_k(\vec{r}',\vec{v}',t)$ that describe the particle trajectories as functions of initial conditions and time.[2] The vectors $\vec{r} = \vec{R}_k(\vec{r}',\vec{v}',t)$ and $\vec{v} = \dot{\vec{R}}_k(\vec{r}',\vec{v}',t)$ where the dot denotes differentation with respect to t, are the position and velocity vectors, respectively, of that particle of species k whose initial position and velocity vectors were, respectively, $\vec{r}'$ and $\vec{v}'$. We consider arbitrary approximations of these functions that can be represented in terms of time-dependent parameters. For example, $\phi(\vec{r},t)$ could be approximated by its time-dependent values at the points of a finite spatial mesh together with a method for interpolating between the mesh points. A more general possibility, which includes this as a special case, would be to approximate $\phi(\vec{r},t)$ by a sum of linearly independent functions of position with time-dependent coefficients. The dependence of the approximation to $\phi(\vec{r},t)$ on the time-dependent parameters could also be highly nonlinear. In general, we allow any approximations of $\phi(\vec{r},t)$, $\vec{A}(\vec{r},t)$, and $\vec{R}_k(\vec{r}',\vec{v}',t)$ of the form

$$\phi(\vec{r},t) \simeq \Phi[\vec{r},t,\{\alpha_n(t)\}],$$

$$\vec{A}(\vec{r},t) \simeq \vec{\mathfrak{a}}[\vec{r},t\{\beta_m(t)\}],$$

and

$$\vec{R}_k(\vec{r}',\vec{v}',t) \simeq \vec{\mathfrak{R}}_k[\vec{r}',\vec{v}',t,\{\gamma_{k\ell}(t)\}], \tag{1}$$

where Φ, $\vec{\mathfrak{a}}$, and $\vec{\mathfrak{R}}_k$ are arbitrary specified functions, and the dependence on t of the sets of parameters $\alpha_n(t)$, $\beta_m(t)$, and $\gamma_{k\ell}(t)$ is to be determined.

Once specific functions Φ, $\vec{\mathfrak{a}}$, and $\vec{\mathfrak{R}}_k$ have been chosen, we must still choose a principle that determines the time dependence of the parameters. By using different principles, it is nearly always possible to derive infinitely many different systems of equations for the time-dependent parameters starting from the exact equations of motion. The crux of our approach is to use Hamilton's variational principle to choose one of these systems of equations. The system of equations implied by Hamilton's principle is unique and is obtained by substituting Eqs. (1) into the exact Lagrangian and then satisfying the variational principle exactly for those variations of ϕ, $\vec{A}$, and $\vec{R}_k$ allowed by the approximation. The only difference between deriving the exact equations and deriving the equations for the time-dependent parameters is that the variations are carried out within a restricted class of functions in the latter case. These equations for the time-dependent parameters should be optimal in some useful sense.

An important consequence of the variational method of deriving equations for the time-dependent parameters is that there is an exact energy theorem for these equations no matter what choice of Φ, $\vec{\mathfrak{a}}$, and $\vec{\mathfrak{R}}_k$ is made. As an example, if there is no <u>explicit</u> time dependence of these functions, and if the physical system is energy-conserving, then the equations for the time-dependent parameters also conserve energy exactly.

Because of the complexity of the behavior of Vlasov plasmas, the great freedom allowed in the choice of Φ, $\vec{\mathfrak{a}}$, and $\vec{\mathfrak{R}}_k$ is highly desirable. These functions can be chosen so as to take account of knowledge or intuition concerning the behavior of the plasma for the problem at hand, and they can be modified as the knowledge or intuition improves. For each choice, the variational principle implies a unique system of equations for the time-dependent parameters. Furthermore, the variational principle can be adapted to include the imposition of auxiliary approximations that are appropriate to a given physical problem. The great generality inherent in the variational approach should be advantageous in obtaining numerical solutions to the problems encountered in experimental research.

The simplest application of Hamilton's principle is to approximate the continuum of particles envisioned in the Vlasov limit by a finite number of particles and the potentials by some class of continuous functions. Some approximation schemes that are obtained in this way are closely related to numerical methods currently in use. For example, if magnetic effects are ignored and if a piecewise bilinear approximation is used for the scalar potential, then a finite-difference formula for the scalar potential is obtained that includes the "area-weighting" procedure used in particle-in-cell (PIC or CIC) calculations (Morse and Nielson, 1968; Birdsall and Fuss, 1968, 1969). Hamilton's principle also prescribes a specific difference scheme for Poisson's equation in this representation, and a specific way of calculating the electric field, such that energy conservation is preserved. The variational approach with a finite number of particles is directly applicable in three dimensions with the full Maxwell equations and external fields, so that a class of schemes can be derived which are energy-conserving generalizations of the particle-in-cell method.

Hamilton's principle can also be applied to cases in which a continuum of particles is represented approximately in terms of a finite number of parameters. A particular instance of this, in which the cold two-stream instability is considered, is under investigation by the author (Lewis and Melendez, 1968), and it appears that some quasi-analytical understanding of the asymptotic state of the cold two-stream instability may emerge from this work. Probably the most attractive long-range aspect of the variational method is the possibility of learning how to describe a continuum of particles usefully in terms of a small number of parameters.

Hamilton's principle is relevant to numerical analyses of Vlasov plasmas when the particles are represented by their trajectories--for a finite number of particles and for continua. To further place the method in perspective, we compare it briefly to methods that involve time-dependent distribution functions. A major difficulty that is encountered in numerical analyses of Vlasov plasmas when the particles are represented by time-dependent distribution functions is that the distribution functions for initially unstable plasmas tend to become ever more convoluted in phase space as time goes on. This effect is the most severe limitation of the applicability of a method involving time-dependent distribution functions, be it a finite-difference scheme for the Boltzmann equation, an expansion method (Armstrong, Harding, Knorr, and Montgomery, 1969), or the "water-bag" model (Berk and Roberts, 1969). (The "water-bag" model uses time-dependent distribution functions, even though the motion of boundaries in phase space is calculated by means of particle equations of motion.) The observation that representing the particles by their trajectories is quite different in detail from using time-dependent distribution functions, and that it may allow useful numerical approximations for longer times, is an important reason for pursuing various trajectory approaches.

There is a superficial similarity of the variational formulation to those methods that represent a time-dependent distribution function as a linear combination of a finite number of basis functions of position and velocity with time-dependent coefficients. The similarity is simply the common use of a parametrization in terms of time-dependent quantities. However, the similarity ends there. In the variational formulation, we do not parametrize time-dependent distribution functions; we parametrize the solution of the particle equations of motion as a function of initial conditions and time. The two procedures are equivalent only if each is carried out exactly.

In Section II we present the Lagrangian description of Vlasov plasmas in detail. The formulation includes the possibility of nonelectromagnetic potentials that can be velocity-dependent. It also includes the description of material media that exhibit a certain type of nonlinear polarizability or magnetizability. Although no specific application to plasma physics involving nonlinear material media is proposed, there may be useful applications to the numerical study of nonlinear optical phenomena. The derivation of approximation schemes from Hamilton's principle is discussed in Section III. Both Lagrangian and Hamiltonian formulations are presented, and the energy theorem is derived. In Section IV we specialize the method to the consideration of a finite number of particles, and thereby obtain classes of energy-conserving generalizations of the particle-in-cell method. The application of the variational method to the cold two-stream instability with a continuum of particles is described in Section V.

FUEL BURNUP AND DIRECT CONVERSION OF ENERGY IN A DT PLASMA

(T. A. Oliphant)

Numerical solutions to the Fokker-Planck equation with applications to the α-particle heating problem were discussed in last year's annual report.

One of the approximations used was the replacement of the actual electron and fuel ion distribution functions by parameterized Maxwellians. This approximation is far more suspect for fuel ions than for electrons. A special numerical program was set up which included calculation of the actual fuel ion distribution function. Although this program consumed much more machine time, the improvement in accuracy was found to be negligible, thus justifying the previous use of parameterized Maxwellians.

Another approximation involves the fact that the Fokker-Planck equation ignores the effects of large angle collisions. A simple analytic estimate of this effect was presented in the February 1, 1969 to April 30, 1969 quarterly report. The analytic result was verified by a more detailed numerical computation. The conclusion was that this effect is also small enough to be ignored in the numerical calculation. This was also seen to be a fortunate result since otherwise considerably more machine time would be required to run the full program.

One very important effect which was added to the computation and which does not take much additional machine time is the effect of the expansion of the plasma against the external magnetic field. The plasma is heated by the alpha particles, but cooled by the expansion as well as by the energy extracted in doing work against the external field. The effect of this expansion on the fuel ion and electron temperatures is shown in Fig. 27 for an initial density of 5 x 10^{16} ion/cm^3 and an initial temperature of 15 keV. This lowering of temperature along with the decrease in density resulting from expansion reduces the thermonuclear reaction rate. Thus the burnup fraction increases less rapidly, as illustrated in Fig. 28. These effects influence each other and the problem necessarily involves a fairly complex, nonlinear, computation.

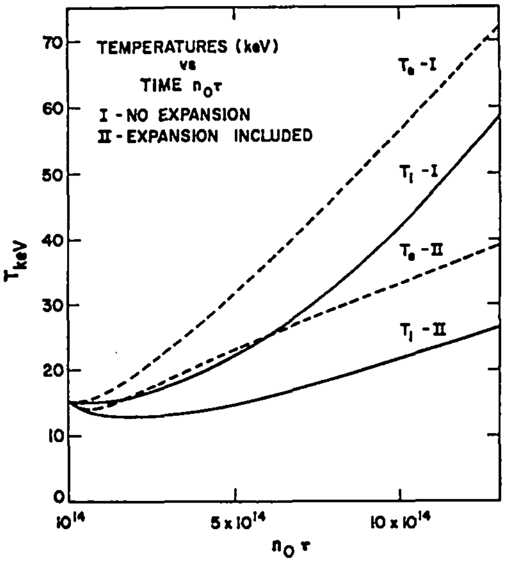

Fig. 27. The electron temperature T_e and the ion temperature T_i are plotted versus $n_0\tau$ for Cases I (no plasma expansion) and II (plasma expansion allowed).

These results were discussed in considerable detail at the Nuclear Fusion Reactor Conference held during 17-19 September 1969 at the Culham Laboratory in England.

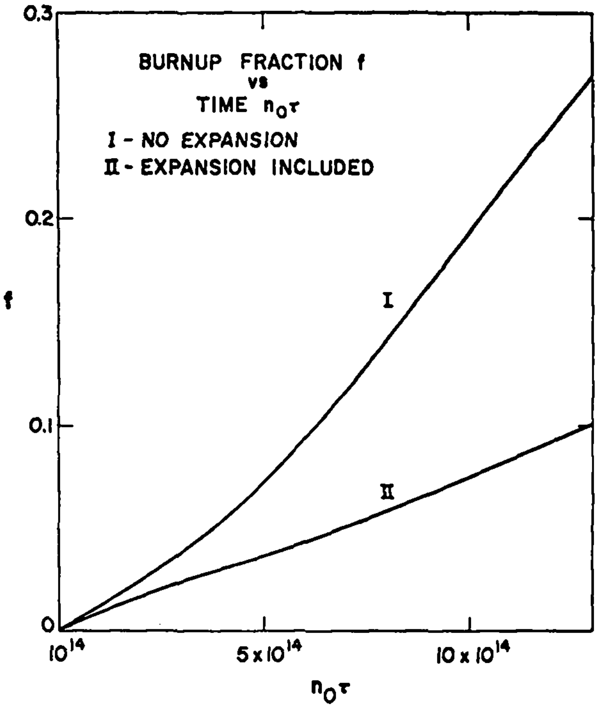

Fig. 28. The burnup fraction f is plotted versus $n_0\tau$ for Cases I and II.

SYMMETRY VIOLATION AND TIME DEPENDENCES IN A TOROIDAL THETA PINCH

(W. B. Riesenfeld)

In a recent research note[1] Morse and Freidberg express a conjecture which may correlate a considerable body of experimental data; their hypothesis is that a collisionless Vlasov plasma has a large anomalous resistivity (presumably generated by microinstabilities) unless the equilibrium is in some sense close to a so-called collisionless drift equilibrium, i.e., a rigid translator or rotator. Such equilibria are self-consistent solutions of the Vlasov equations for arbitrary beta, depend only on global constants of motion, and are Maxwellian in the drift frame so that they remain invariant under like particle collisions.

Classical statistical mechanics provides a plausibility argument that stationary solutions of the Liouville equation should indeed be functions only of the global constants of motion (energy and conserved linear and angular canonical momenta). These solutions reflect the maximum information content normally available from experiment, including total linear and angular kinetic momenta of the system. Such stationary ensembles are, of course, more general than the rigid drift equilibria, but in any case it is essential that there be an appropriate spatial symmetry to lead to a needed conserved canonical momentum.

A theta pinch is confined by a diamagnetic B_z field coupled to a self-consistent j_θ current density. The latter is nonzero only for distribution functions depending on the canonical P_θ angular momentum, which thus must be a constant of motion. Consequently we require symmetry about the pinch axis. For a toroidal theta pinch, however, the toroidal curvature breaks this symmetry; the only remaining global constants of motion (for a system symmetric about the major toroidal axis) are the energy and the canonical momentum in the toroidal direction. If the distribution function depends on the latter, we obtain electric currents in the toroidal direction and poloidal magnetic fields, i.e., we wind up with a toroidal z-pinch (which, by the way, is entirely confined by the poloidal field since any toroidal component must be a vacuum field). Thus for theta-pinch geometry we are left with only the energy as a constant of motion, leading to a nonconfinement or at best electrostatic confinement. We conclude that stationary Vlasov equilibria for a toroidal theta pinch, satisfying either the Morse-Freidberg requirement or the more general statistical mechanical assumptions, do not exist.

Instead, the description of such a system involves the solution of an initial value problem, in which the initial distribution function is specified to resemble that for a theta pinch bent into a torus. The time evolution, as governed by the Vlasov equation, then yields fast single-particle drift losses in the outer region of the pinch (where beta is low) due to toroidal curvature and gradient effects; these are assumed to be compensated by first-order correction fields, precisely as in the toroidal MHD case. There remains, however, a longer-term time dependence in the distribution function reflecting time-dependent perturbations of the diamagnetic current density due to the symmetry-violating toroidal terms. The time scales for these effects have been estimated by use of perturbation theory, based on a toroidally modified rigid-rotor solution as the initial state. In addition to a number of periodicities, a secular time scale was found which corresponds to an average hydromagnetic wave propagation time azimuthally around the device. It is to be noted that this effect depends on the simultaneous presence of toroidal curvature, nonzero beta, and finite gyration effects for the ions.

Numerical calculation of the ion orbits in the toroidally modified self-consistent magnetic field shows, interestingly enough, that individual particles are perfectly contained in the high-beta region, notwithstanding the excursions in the diamagnetic current. These calculations extended over many orbital periods, i.e., over times long compared with the secular shift time of the diamagnetic current. Evidently the solution describes a confined system which is steady-state in its gross features, yet has time-dependent fine structure. As such, it differs radically from the usual time-independent solutions of the Vlasov equations, yet it corresponds to a physically acceptable confined plasma state. Examination of the orbits shows that it is precisely the high-beta diamagnetic field gradient which tends to confine individual particles, in spite of the fluctuations introduced into the diamagnetic current and other moments of the distribution function.

These calculations were performed in collaboration with Jacob Enoch, visiting staff member from the Department of Physics and Astronomy of the University of Kansas.

Reference

1. R. L. Morse and J. P. Freidberg, Rigid Drift Model of High Temperature Plasma Containment, Research Note to appear in Phys. Fluids, January 1970.

STABILITY OF PINCH TYPE DEVICES

(J.P. Freidberg)

During the past year, theoretical calculations have been performed on the stability of the $m = 1$ mode for various pinch configurations, using both Vlasov and MHD models. The results at the present time are as follows.

Rotating θ-Pinch

It has been a generally accepted result that the $m = 1$ mode of a rotating θ-pinch is neutrally stable in the MHD limit. This result was based on several different calculations, although each of these was done for the case $k_\parallel = 0$. These calculations have been extended to the case $k_\parallel \neq 0$ and it was found that the plasma was $m = 1$ unstable for $0 < k_\parallel < k_{critical}$. If the ions carry the current, then the rotation due to this motion leads to an extremely fast growth rate of the order $\gamma \approx .01\ \omega_{ci}$. If the electrons carry the current, the growth rate is much slower and is of the order $\gamma \approx .01\ (m_e/m_i)\omega_{ci}$.

Ion Drift Wave Instability

In connection with the above calculation, it was decided to investigate this instability using the Vlasov equations. Because of the complexity, the calculation was done in a slab geometry with an artificial gravity, g, to simulate rotation. Conventional theory predicts that for $k_\parallel = 0$, finite Larmor radius effects stabilize the flute mode for $k_\perp^2 V_D^2 > 4g/L$ where V_D is the diamagnetic drift, and L is the density scale length. The effects of $k_\parallel \neq 0$ were again considered and it was found that a resonant particle instability driven by ions was present for any $k_\parallel$ in the range $0 < k_\parallel < k_{critical}$ where $k_{critical}$ is identical to the MHD value of $k_{critical}$. Hence the Vlasov mode does not completely eliminate the gravitational interchange instability by finite Larmor radius effects as might have been expected from the $k_\parallel = 0$ calculation. Instead, resonant particle instability persists, up to the MHD limit, with however a smaller growth rate. The work described in the above two paragraphs was done in collaboration with J. Wesson of the Culham Laboratory, England.

Screw Pinch Stability

The MHD stability of the $m = 1$ mode of a diffuse screw pinch was studied in order to explain certain experimental observations on Scylla IV. These observations indicated that experimental growth rates were slower by a factor of 9 than those predicted by sharp boundary theory. The calculations for the diffuse profile indicated that the growth rate and threshold current are fairly sensitive to the B_θ profile. By spreading the J_z current density over an area of approximately 2 plasma radii, it was found that theory and experiment were now in agreement to within 20 percent.

Rigid Drift Model

A model was proposed in order to explain certain experimental results in high temperature heating and confinement experiments. The model proposes that many plasma configurations must eventually evolve to a distribution function of the rigid drift type. The reason for this is that rigid drift, and only rigid drift, distribution functions are isotropic and have no velocity shear. Hence any configuration which is not a rigid drift type will probably be unstable to some high frequency instabilities which will cause the distribution function to evolve to a rigid drift function. At present, the model has been applied only to a few experiments and further study is required.

RIGID DRIFT EQUILIBRIA

(R. L. Morse)

A general review of high temperature finite-β plasma containment experiments indicates that by far the most successful in terms of $n\tau$ are high symmetry devices in which equilibria based solely on exact constants of particle motion are allowed. Further evidence indicates a preference for exact equilibria of the "rigid drift type," i.e., distributions of particle velocities, the local mean values of which are spatially distributed like the velocity field of a rigid body. This has led to a conjecture that such equilibria are less vulnerable to some important anomalous loss process than are other equilibria.[1,2]

References

1. "Rigid Drift Model of High Temperature Plasma Containment," J. P. Freidberg and R. L. Morse (to be published in Phys. Fluids, January, 1970).
2. "Equilibria of Collisionless Plasma," LA-3844, Pts. I and II.

Z PINCHES
(Group P-14)

COLUMBA

(J. A. Phillips, P. R. Forman, A. Haberstich, H.J. Karr, A.E.Schofield)

The feasibility of dynamic stabilization methods as applied to the Columba pinch device is being investigated. A number of theoretical and experimental studies[1-4] have appeared in the literature describing methods of stabilization of the magnetohydrodynamic instabilities characteristic of the pinch by means of high frequency magnetic fields. In the Columba program, two of these methods are being investigated as possible modifications to the initial system: (a) high frequency transverse magnetic fields provided by longitudinal multipole conductors (similar in geometry to Ioffe bars), and (b) high frequency oscillations of the B_z magnetic field. The stabilization tests have been made with modest z-pinch current discharges with the ultimate objective of extending the stabilization methods to the confined θ- and z-pinch in the Columba experiment. Investigations of the first method have been completed. Experiments with the second method have been started but only preliminary and inconclusive results have been obtained and will not be included in this report.

Theory

It is well known that the pinch plasma column is unstable to perturbations which tend to distort its form. The objective of this experiment is to stabilize the bending or kink m = 1 instability which is one of the most dangerous, a rapidly growing deformation that destroys the simple unstabilized z-pinch. The destabilizing force driving each harmonic component of the kink instability is given by[1]

$$F_1 = \left(\frac{2\pi I_z}{c\lambda}\right)^2 \ln\left(\frac{\lambda}{\pi a}\right)\xi , \qquad (1)$$

where ξ is the displacement amplitude, λ is the axial wavelength of the perturbation, and a is the pinch radius. An additional force is developed by the interaction of the discharge current, which is assumed to have a uniform surface current density, with the magnetic field of the longitudinal stabilizing conductors, which are located near the outer surface of the discharge tube. The magnetic field at the surface of the plasma is comprised of the field due to the longitudinal pinch current, I_z, the field due to the quadrupole array, and that due to the diamagnetic surface currents in the plasma associated with the distortion of the plasma cross section under the influence of the quadrupole field. The vector potential outside the plasma is

$$A_z = \frac{4I_Q r^2}{cb^2}\cos 2\theta + \frac{\phi}{r^2}\cos 2\theta + \frac{2I_z}{c}\ln r, \qquad (2)$$

where the first term is the contribution of the vacuum quadrupole system, the second, the diamagnetic currents in the plasma, and the third, the pinch current. The constant, b, is the radius at which the line currents of the quadrupole (I_Q) are located. The parameter ϕ is evaluated by assuming that the plasma surface has the form

$$r = a\,(1 - \delta_2 \cos 2\theta),$$

and requiring the plasma boundary to be a surface of constant B^2 and constant flux. If $\delta_2 << 1$, the theta component of the magnetic field at the surface of the plasma due to the combined quadrupole and plasma diamagnetic currents is, to first order,

$$B_\theta = \frac{8I_Q}{cb^2}\left[r - \frac{3a^4}{r^3}\right]\cos 2\theta, \qquad (3)$$

and

$$\delta_2 = 8\left(\frac{a}{b}\right)^2 \frac{I_Q}{I_z} . \qquad (4)$$

If the plasma column is subjected to a kink perturbation such that

$$r = a\,(1 + \epsilon \cos\theta \cos kz), \qquad (5)$$

the resulting force per unit length is

$$F_z = 20 \frac{I_Q I_z}{c^2} \frac{a}{b^2} \epsilon \cos kz. \tag{6}$$

Combining the forces yields the equation of motion:

$$\pi a^2 \rho \frac{d^2\xi}{dt^2} = \left[\frac{I_z^2}{c^2} \left(\frac{2\pi}{\lambda}\right)^2 \ln \frac{\lambda}{\pi a} + 20 \frac{I_Q I_z}{b^2 c^2} \right] \xi. \tag{7}$$

If the quadrupole current is oscillatory at a frequency ω such that

$$I_Q = I_Q \cos \omega t, \tag{8}$$

and the following definitions are made

$$Z = \frac{\omega t}{2} \qquad M = \pi a^2 \rho$$

$$\alpha = \frac{-4 I_z^2}{M \omega^2 c^2} \left(\frac{2\pi}{\lambda}\right)^2 \ln \frac{\lambda}{\pi a} \tag{9}$$

$$q = \frac{40}{M \omega^2 c^2 b^2} I_Q I_z ,$$

the equation of motion becomes the Mathieu equation in its canonical form:

$$\frac{d^2\xi}{dz} + (\alpha - 2q \cos 2z)\, \xi = 0. \tag{10}$$

Figure 29 is a plot of the first stable region of the Mathieu equation in which the parameters α and q are abscissa and ordinate, respectively. The magnitude of the frequency and current in the quadrupole circuit necessary for stabilization are obtained from the bounds of the stable region. The system lies below the upper bound of the first stable region for $q < 1$ and the lower bound is given approximately by $\alpha = -q^2/2$. These limits lead to the stability condition

$$\frac{4\sqrt{2\pi I_z}}{\omega \lambda c} \sqrt{\frac{\ln\left(\frac{\lambda}{\pi a}\right)}{M}} \leq \frac{40\, I_Q I_z}{\omega^2 c^2 b^2 M} < 1. \tag{11}$$

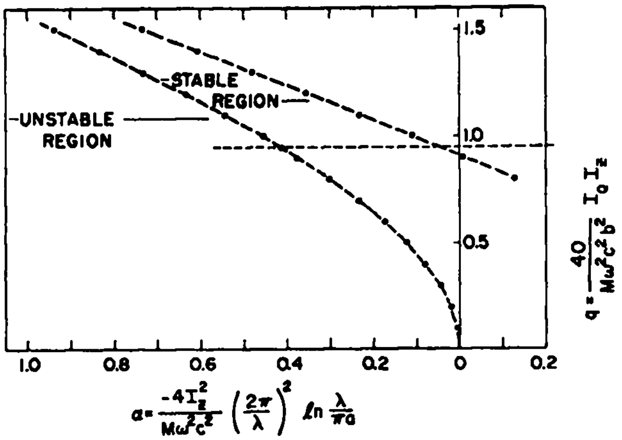

Fig. 29. Plot of the first stable region of the Mathieu equation.

These conditions for the frequency and amplitude of the stabilizing current are similar to those given by Osovets,[1] but differ by a constant factor since the additional contribution of the plasma diamagnetic currents arising in the free boundary plasma model is used here but is not included in the earlier theory.

It should be noted the value of the ordinate, q, in the Mathieu diagram depends on the experimental parameters I_Q, I_z, ω, b, and M. For typical experimental values, $I_z = 25$ kA, $\omega = 4.6 \times 10^7$ rad/sec, b = 3.7 cm, $M = 5 \times 10^{-7}$ g/cm of D_2, $I_Q = 13.7$ kA per conductor, the ordinate is indicated by dashed horizontal line through the stable region in Fig. 29. From the values of the abscissa at the end points of this line ($\alpha = -.425$ and $\alpha \approx 0$), it is implied that kink wavelengths of $\lambda > 20$ cm should be stabilized under these experimental conditions. MHD theory[5] predicts that the shorter wavelengths of the order of the pinch diameter are the most dangerous and grow most rapidly. However, the reported results of other experiments[1-3] are very encouraging even though the stabilizing frequencies and field magnitudes are in the range used here, and the wavelengths that were theoretically predicted to be stabilized were as long or longer. In fact, the hypothesis has been advanced[2,3] that the longer wavelengths appear first and, if they are stabilized, the shorter ones do not develop. However, a later report[4] by the same group now discredits this hypothesis. As shown below, our experimental results also show that the shorter wavelengths develop first and grow most rapidly.

In order to compare this theory with the experiment it was necessary to obtain the growth rates for the condition that corresponds to regions in the unstable zones of the Mathieu diagram. This was done by determining the exponential factor of the Floquet solutions of the Mathieu equation. The general solution for the Mathieu equation can be written in the form

$$\Gamma(z) = \psi(z)e^{i\mu z} + \psi(-z)e^{-i\mu z}, \tag{12}$$

where $\psi(z)$ and $\psi(-z)$ are periodic functions of period π. If the solution is to be unstable, i.e., unbounded, then the exponent μ must be imaginary or complex. The growth rate for the solution will be the imaginary part of μ. By numerically integrating the Mathieu equation subject to the initial condition that $\Gamma(0) = 1$ up to $z = \pi$, one obtains

$$\Gamma(\pi) = \frac{e^{i\mu\pi} + e^{-i\mu\pi}}{2} \quad . \tag{13}$$

If $|\Gamma(\pi)| \leq 1$ the solution is stable. If $|\Gamma(\pi)| > 1$ the growth rate is given by

$$\mathrm{Im}|\mu| = \frac{\mathrm{arc\,cos\,h}\ (\Gamma(\pi))}{\pi} \quad . \tag{14}$$

Figure 30 is a plot of the kink growth rates with and without dynamic stabilization. The conditions used are those of the "typical experimental values" specified for Fig. 29.

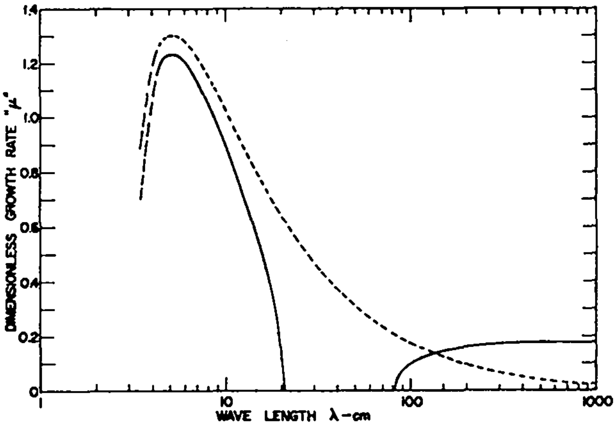

Fig. 30. Kink growth rate: dashed line without dynamic stabilization; solid line with dynamic stabilization.

Table I

Z-Pinch Circuit:	
Inside diameter of the Pyrex discharge tube	6 cm
Distance between hollow electrodes	43.5 cm
Capacity	90 μF
Voltage	7 kV
D₂ initial gas filling	75 mTorr
Initial $\dot{I}$	2×10^{10} kA/sec
Period	30 μsec
Stabilizing Circuit:	
Number of bars	4
Distance between diametrically opposite bars	7.6 cm
Length of bars	28 cm
Width of bars	1.5 cm
Ringing frequency	740 kHz
Peak current per bar	13.7 kA
B_z Bias Circuit:	
B_{zo} magnetic field	≤ 275 gauss
Inside diameter of the B_z coil	12 cm
Length of the B_z coil (single turn)	28 cm

Experimental Apparatus

The experiment consists of three principal circuits; the z-pinch circuit, the quadrupole stabilizing circuit, and an optional B_z bias circuit. Dimensions and electrical parameters are summarized in Table I. The discharge tube is a Pyrex glass cylinder with hollow electrodes at the ends with a separation of 43.7 cm. The B_z bias field was applied through a single turn coil of perforated metal of 6-cm radius and the quadrupole stabilizing field was obtained from four metal straps along the outer surface of the tube. The return conductors in the z-pinch consisted of eight rods at 8-cm radius. This arrangement made it possible to obtain both axial and radial high speed photographs of the pinch discharge behavior and axial density measurements with a Mach-Zehnder interferometer. The pinch current was measured by Rogowski loops around the return conductors.

Two single turn loops (of 3-cm diameter) were placed around the Pyrex tube approximately 3.5 cm above and below the midplane to observe ϕ_z flux changes during the discharge. A small B_z probe ($nA \approx 0.5\ cm^2$) was placed at the outer wall of the tube at the midplane to observe local flux density variations during the pinch cycle. As indicated by the stability condition of Eq. (1), the required frequencies and stabilizing currents increase with the pinch current. The feasibility of this stabilization method can be tested more readily at modest pinch currents ($\lesssim$ 50 kA). Most of the observations were made with pinch currents in the range of ~ 15 to ~ 30 kA through deuterium gas at ~.075 mTorr initial filling pressure.

A damped z-current preionized the gas approximately 20 μsec before the z-pinch was fired. Two auxiliary spark gaps located inside the two hollow electrodes of the z-pinch connected to ground through 2000 μμF initiated the PI discharge when the voltage was applied to the electrodes. This avoided breakdown of the main z-pinch spark gaps due to voltage doubling on the electrodes. The shadows of the two PI spark gaps can be seen in the Mach-Zehnder photographs.

The quadrupole stabilization circuit is triggered through an electronic delay so that the stabilization field can be initiated at the optimum time relative to the pinch discharge. The importance of this timing is discussed in a later section. The supply consists of two 0.23 μF capacitors which are discharged through triggered spark gaps to produce a damped oscillatory current of 13.7 kA per rod at the first current peak at a frequency of 740 kHz. The e-folding damping period was 4.5 μsec. The conductors are connected so that currents in adjacent rods are in opposite directions. The current distributes equally through the four bars of the quadrupole due to the relatively high external inductance of the circuit. The magnetic induction produced by the quadrupole, assuming filamentary currents rather than strap conductors, is

$$B_r = \frac{8}{c} \frac{I_Q r(1 + (r/b)^4) \sin 2\theta}{b^2 \left[(1 + (r/b)^4)^2 - 4(r/b)^4 \cos^2 2\theta \right]}$$

$$B_\theta = \frac{8}{c} \frac{I_Q r(1 - (r/b)^4) \cos 2\theta}{b^2 \left[(1 + (r/b)^4)^2 - 4(r/b)^4 \cos^2 2\theta \right]} ,$$

where b = radius of quadrupole conductors, I_Q = current per conductor, and θ = azimuth angle with θ = 0 through a conductor. In vacuum, this field has an approximately linear positive gradient for r << b rising from 0 at the tube axis to ~ 4000 gauss at the tube wall at the peak current of 13.7 kA per stabilizer bar. Experimental measurements with a magnetic field probe (in the absence of plasma) show the field magnitude follows the theoretical values within a few percent from r = 0 to r ≈ 2.5 cm. Tests at 90° intervals proved that the currents were equal and opposite in successive conductors. Further probe measurements of the B_θ field were made to determine the variation with axial distance along the ~ 30-cm length of the quadrupole. At a fixed radius the field is flat within ~ 5% for ~20 cm over the central region and then falls approximately linearly to ~ 40% of the central region magnitude at the ends of the coil.

The computed combined fields of the pinch discharge (I_z = 25 kA), B_z = 200 G, the quadrupole (I_Q = 13.7 kA), and the induced diamagnetic plasma currents (assuming the free plasma solution) are plotted in Fig. 31 at the time of the first peak of the stabilization field. The lines of force (constant $\vec{A}_z$) are shown at the left and the contours of constant magnetic pressure (or mod. B surfaces) are shown at the right with field magnitudes in gauss in the margin. The approximate theoretical plasma surface contour is shown by the cross-hatched region and is in first order agreement in form and size with that observed from image converter photographs for these field conditions and with the plasma density contours obtained with the Mach-Zehnder interferometer described in a following section. The lines of force around the

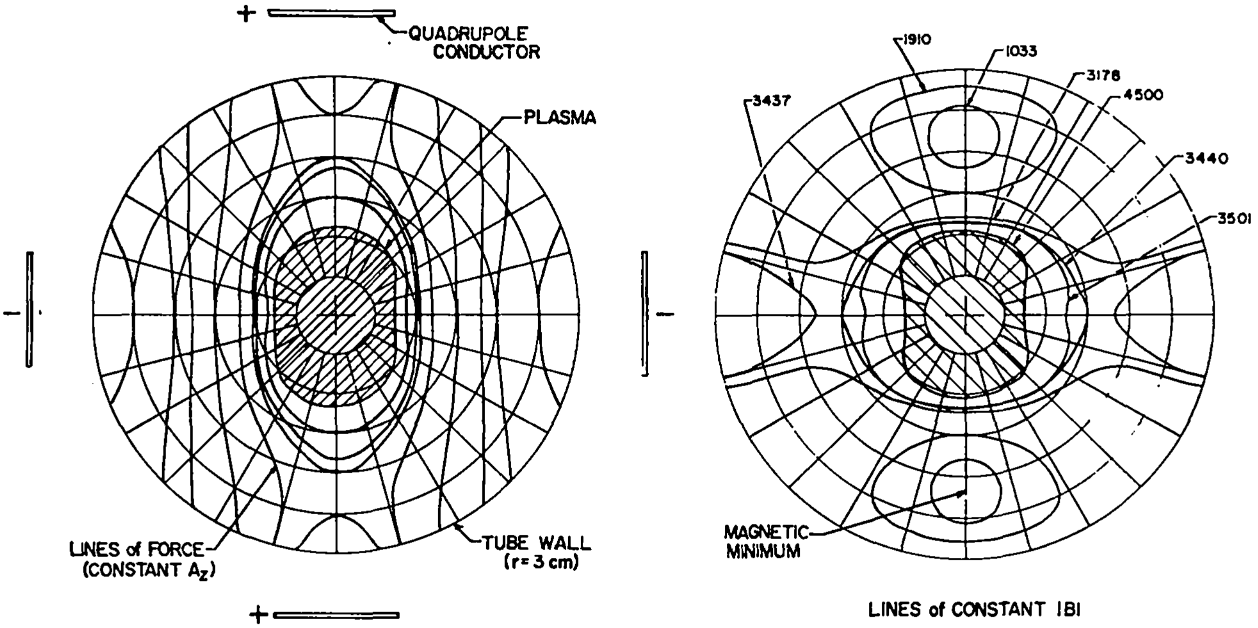

Fig. 31. Computed fields at first peak of stabilization fields.

pinch in Fig. 31 are roughly elliptical instead of circular as in the simple z-pinch. As the quadrupole field and the induced magnetic currents vary in time, the plasma surface will oscillate as the field lines go from the elliptical shape shown to circular when the quadrupole field goes through zero and then becomes elliptical in the transverse direction at the peak of the next half cycle of the stabilization field. In Fig. 31, the direction of the fields is such that the pinch column is theoretically stabilized in the horizontal direction and is unstable in the vertical direction. During the next half cycle the situation is reversed if the concept of "average stability" is valid and, if the stability criteria for frequency and field magnitude are satisfied, the theory predicts that the system should attain average stability over the plasma column as each part of it is stabilized momentarily at some phase of the time-varying field.

In the model used for the stability theory and field computation, only first order terms are included. It is observed experimentally, however, that the growth rates of the m = 0 instability are reduced along with the m = 1 modes even in the absence of applied B_z field. This effect is believed to be due to generation of B_z fields by the Hall currents and drift currents generated by the high frequency, high gradient quadrupole field not included in the first order theory used. Probe measurements in a similar system reported by Borzunov et al[4] have shown the presence of such quasistationary B_z fields of a complex, azimuthally periodic nature due to the quadrupole field.

Experimental Results

High Speed Photography

Figure 32b shows pictures of the plasma taken at selected times during the discharge with an image converter camera. Each 0.1 μsec exposure shows two radial views of the pinch. The upper view of each picture is taken along a tube diameter through the space between a pair of stabilizer bars. The other view is centered on a diameter through a stabilizer rod at 70 degrees in azimuth from the first. This view of the discharge is largely obscured by the rod until instabilities cause the plasma to diverge past the angle subtended by the bar. Figure 32a shows the z-pinch and stabilization current wave forms. The exposure times of the photographs of Fig. 32b are indicated by the letters on the time axis.

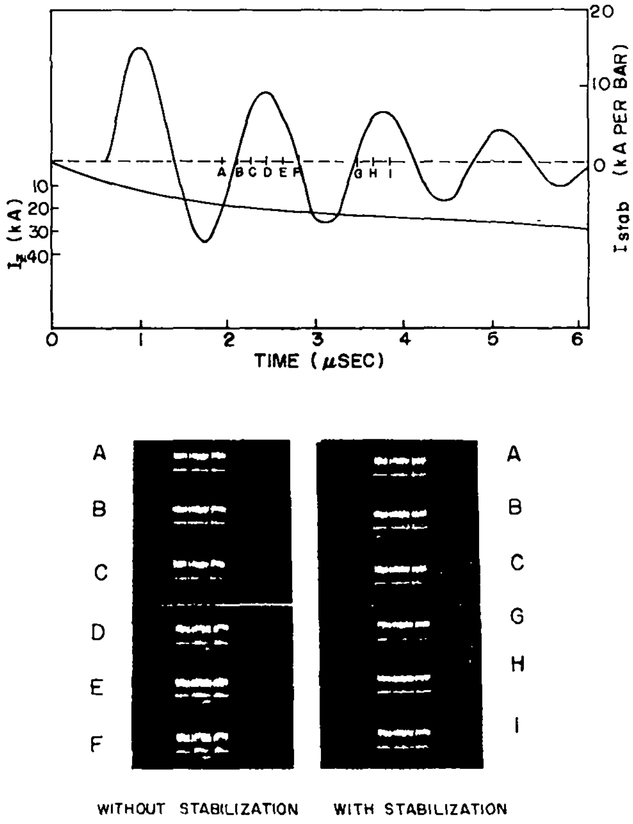

Fig. 32. Current wave forms (a, above) and photographs of pinch (b, below) at times as shown.

The discharge is pinched to a well-defined plasma column of approximately 1-cm radius within 1.25 μsec after the initiation of the discharge. Without stabilization, the column becomes visibly unstable at about 2 μsec. The instability is clearly evident in the kinking and curling of the pinch. At this time the wavelength of the m = 1 instability is ~ 9 cm. The amplitude of the instability is observed to grow and the discharge reaches the tube walls (Picture F) at approximately 2.7 μsec. The wavelength is reduced to ~ 6 cm at the time of blowup.

The effect of dynamic stabilization on this simple z-pinch is shown in the photographs at the right of Fig. 32b. Although the perturbations, both m = 0 and m = 1, are visible in the photographs, their growth rate is noticeably reduced and the pinch is still contained away from the tube walls at 3.8 μsec (Picture I). From shot to shot there are variations in the growth rates, and in the form of the m = 0 and m = 1 instabilities. Wavelengths over the range ~ 6 to ~ 12 cm are observed. From comparison of photographs of equal instability amplitudes, with and without stabilization, it is estimated that the growth rates are reduced by approximately 30%. At higher pinch currents, the reduction in growth rate of the instabilities is smaller. For example, for a 40% increase in the pinch current the average growth rate reduction falls to ~ 20%.

To obtain the results shown in Fig. 32, the stabilization field was initiated at ~0.7 μsec after the start of the pinch current and a stabilization current of 13.7 kA per rod was used. These were determined to be within the optimum range of firing times and field magnitudes. It was found that firing the stabilization ≥ 1.5 μsec after the start of the pinch current resulted in no observable stabilizing effect. Apparently the instabilities are well established by this time so that the multipole field has no effect. On the other hand, if the stabilization field is initiated too early (≤ 0.5 μsec after I_z), the strong electric fields associated with the high frequency stabilization distort the pinch in its initial stages of formation. Any magnetic fields trapped by imploding z-pinch cause further deformation of the pinch. The stabilization field is very effective in preionizing and breaking down the gas when applied alone to the system without the z-pinch. The luminous plasma forms spectacular patterns with the cyclic variations of the quadrupole field. If the stabilization field is initiated before the z-pinch, these effects should disturb the pinch formation.

End Effects Observed

Photographs show an instability growing axially from the cathode end of the discharge tube. If the instability is enhanced or triggered by end effects, the observed growth rates may be altered by such effects occurring in the unstabilized region near the electrodes. Possible explanations are (a) a propagating m = 0 instability (as an apparent shock wave) as observed by Folkierski et al[6] or (b) a "Polytron" effect as described by Dangor et al[7] which would predict a propagating m = 1 instability.

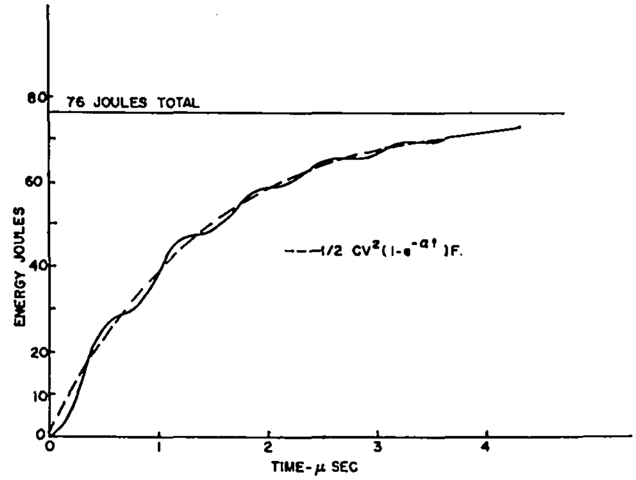

Fig. 33. Time integral of energy loss.

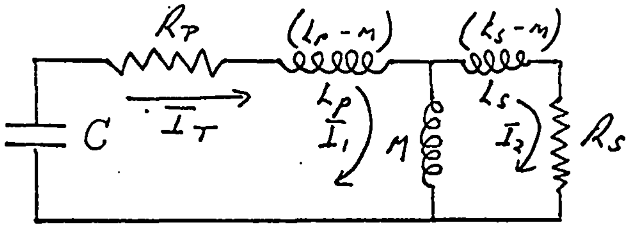

Fig. 34. Circuit equivalent to situation at wall breakdown.

Current and Voltage Measurements

Examination of the stabilization current waveforms with and without a z-pinch discharge show that the logarithmic decay is appreciably more rapid in the presence of the discharge. The period (1.34 μsec) remains constant within ~ 2% but the effective resistance of the circuit determined from the damping rate increases from 0.046 Ω with vacuum (R_v) to 0.074 Ω with the z-pinch (R_ρ). The increase in energy dissipation is given by

$$W_\rho = \int_0^{*} (R_\rho - R_v)\,(I_0 \sin \omega t e^{-R^*/2L})^2 \, dt .$$

This time integral of the energy loss is plotted in Fig. 33. From this figure, it is seen that the energy loss is large and in the first quarter cycle of the stabilization current, 17 joules of the 200 initial bank energy are transferred to the discharge and the energy transfer reaches ~ 76 joules by the end of the discharge. Plasma heating was initially considered as an interesting possible explanation for this effect but this was discarded both from pressure balance considerations and calculations of the electromagnetic coupling of the quadrupole circuit to the pinched discharge.

An attempt to explain this loss in energy assumes a breakdown along the inside of the discharge tube wall with the equivalent circuit shown in Fig. 34.

With the maximum mutual inductance that exists between the inside of the discharge tube and the axis, ~ 3.0 joules per bar can be deposited in the secondary discharge through a resistance of 0.5 Ω in a time of one-quarter cycle. The inductance of the secondary circuit Ls is assumed equal to M; the discharge current runs parallel and close to the bar and returns down the axis. This resistance is compatible with a current sheath 1 cm wide, ~ 2 mm thick and 4 eV temperature. A source of gas would be that absorbed on the glass surface. The peak induced voltage by the quadrupole circuit along this plasma column would be ~ 4.4 kV with a length of ~ 20 producing an electric field of ± 220 V/cm which is comparable with the 5 kV and 120 V/cm of the z-pinch. Light from this plasma is not observed close to the bars in the side-on photographs. Such a wall breakdown, however, would explain the influx of additional plasma into the discharge tube volume seen by interferometry as described below. Incidentally the L/R time constant is sufficiently short to allow penetration of the quadrupole magnetic field inside the tube.

Flux Loop Measurements

Loops were placed around the Pyrex tube to observe ϕ_z flux changes during the pinch. When helical instability modes (m > 1) develop in the plasma, axial magnetic fields are generated producing signals in the loops. The change in onset time and rate of rise of the signal when the stabilizing field is applied is a measure of the effectiveness of the method as shown in Figs. 35 and 36. With stabilization the onset is delayed from ~ 2.3 to ~ 2.6 μsec (20 kV stab) to ~ 2.9 μsec

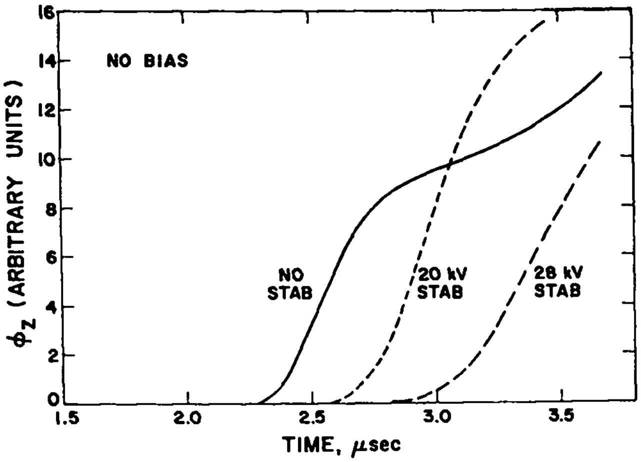

Fig. 35. Effect of stabilization field on time of onset of instability.

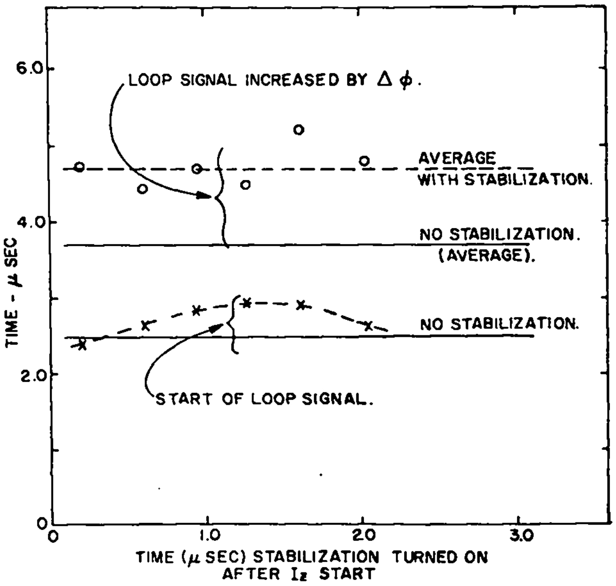

Fig. 36. Effect of stabilization field on growth rate of instability.

(28 kV stab); the higher the stabilization current, the longer is the instability delayed.

In Fig. 35 is the time in μsec at which the loop signals indicate the onset of an m = 1 instability versus the time at which the stabilization field was turned on after the start of the z-pinch. Here the bias field is ~ 200 gauss. With no stabilization the instability starts at ~ 2.5 μsec. This time is delayed to ~ 3.0 μsec when stabilization is turned on ~ 1.3 μsec after the z-current. If stabilization is turned on earlier or later the time is earlier. Stabilization may then be said to delay the onset of this instability by ~ 0.5 μsec or ~20% but does not suppress it.

To obtain a measure of the growth rates the time for the instability to increase the ϕ_z flux through the loop by an arbitrary fixed amount $\Delta\phi$ was determined for a number of cases. With no stabilization a time of ~ 3.7 μsec is measured which is increased to ~ 4.7 μsec with stabilization. Again from the onset times and times to grow to the same amplitude we can say that the growth rates of the instability have been reduced by 27%.

Mach-Zehnder Interferometry

Interferometry was used to obtain (1) the distortion of the pinch channel by the rods and (2) the total number of electrons in the discharge tube.

Radial density profiles were made by overlaying interferograms taken with plasma over one taken with vacuum (Fig. 37). The total number of electrons in the discharge tube as a function of time is shown in Fig. 38 for the three cases. In the interval 1-1.5 μsec, the number of electrons is almost equal to the number in the initial gas filling. At ~2 μsec this number increases for all cases with a more rapid rise the higher the stabilization voltage. Examination of the fringe pattern indicates that this rise is not primarily due to plasma released from the electrodes.

We have suggested in the discussion above on the losses in the stabilization circuit that a current breakdown adjacent to the bars could explain the increased resistance. Presumably gas absorbed on the discharge tube could therefore be involved; gas is ionized and enters the z-current channel.

The eccentricity of the discharge was determined by measuring the major and minor axes, A and B, and calculating a δ by

$$\delta = \frac{A - B}{A + B}$$

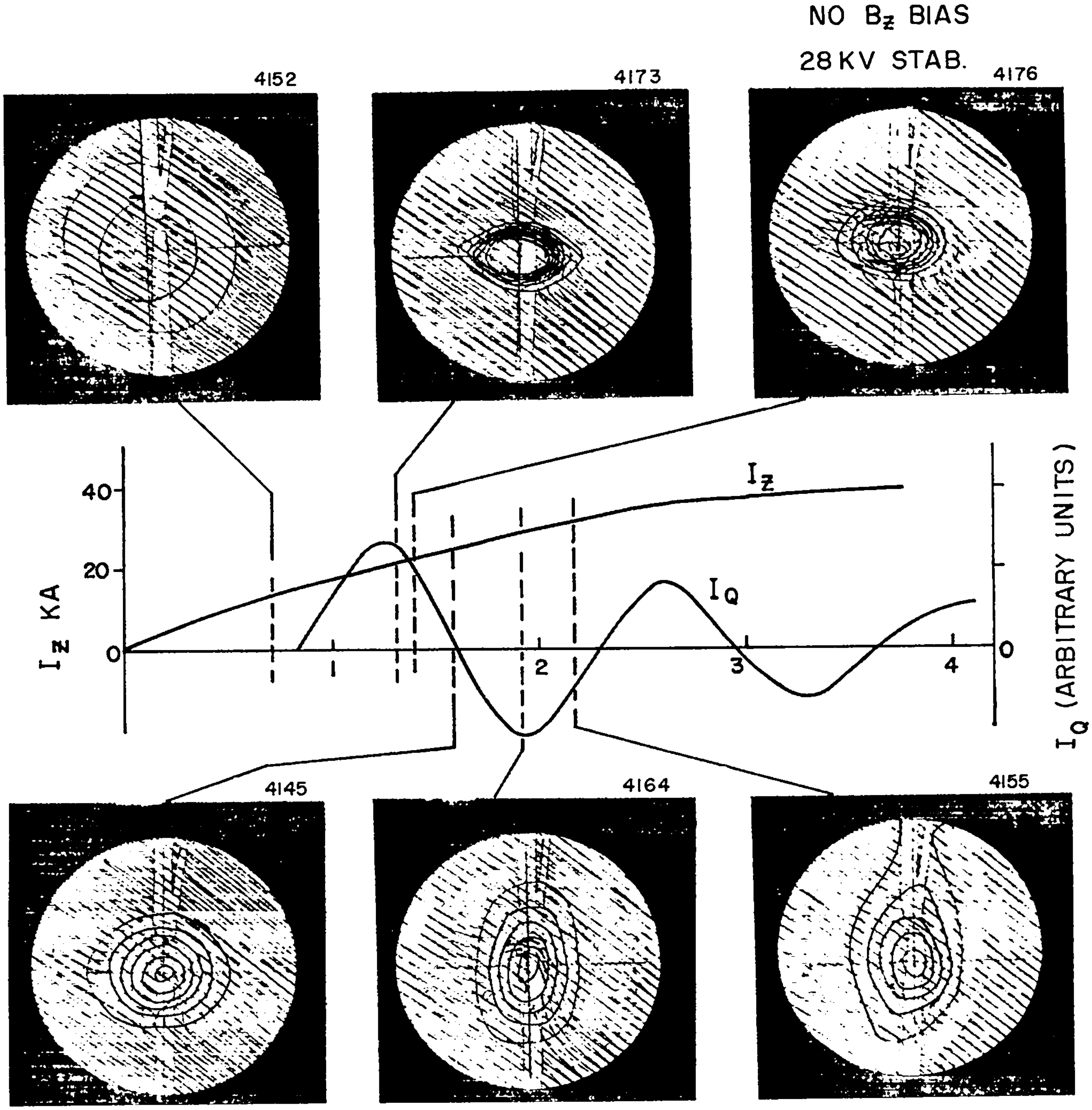

Fig. 37. Radial density profiles of plasma.

following the definition of Morse and Ribe.[8] The results for the three cases as a function of time are shown in Fig. 39. With no stabilization the discharge is symmetric within experimental error. With 20 kV stabilization δ is small, ~ 0.12 over the first half cycle, increases to ~0.15 cm the second and is ~0.10 cm the third. We plot for comparison δ as calculated[8] by

$$\delta = 8 \left(\frac{a}{b}\right)^2 \frac{I_Q}{I_z}$$

where a is the mean plasma radius, b the distance of the bars from the axis, and I_Q and I_z the

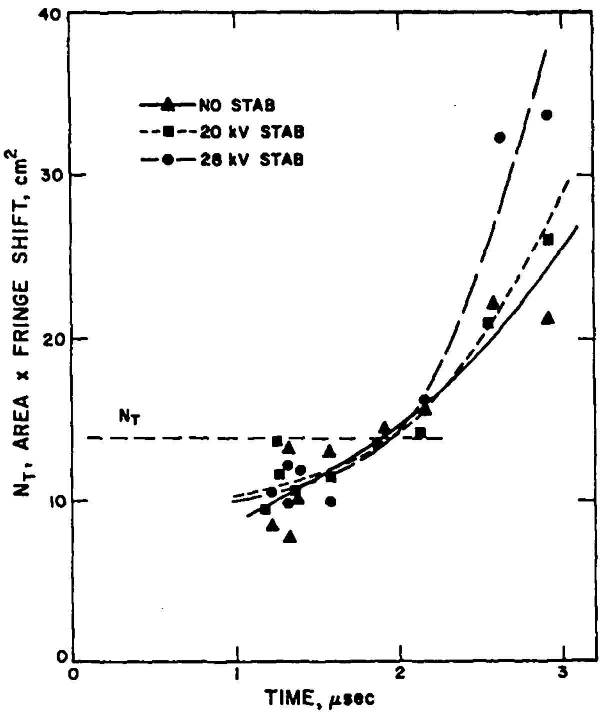

Fig. 38. Number of electrons in discharge tube vs time.

currents in the bars and pinch, respectively. Two cases are shown, (1) the values for δ with a_p assumed constant at 1 cm and (2) δ with a pinch radius determined by the z-pinch current inductance. In all cases on the first half cycle the experimental values of δ are smaller than calculated, approach the theoretical values on the second or become so large (28 kV stabilization) that the discharge strikes the wall.

These results show that the pinch column is set into oscillation in an elliptical mode whose amplitude increases with time.

Simple Z-Pinch with Small Bias B_z Field

With a bias field (~ 270 G to reduce growth rate of m = 0 instability) the general characteristics with stabilization are similar to those without B_z field as, for example (1) fluctuations in the z-current are seen as driven modulations in an elliptical mode, and (2) an increase in the total number of electrons in the discharge tube at ~ 2.2 μsec.

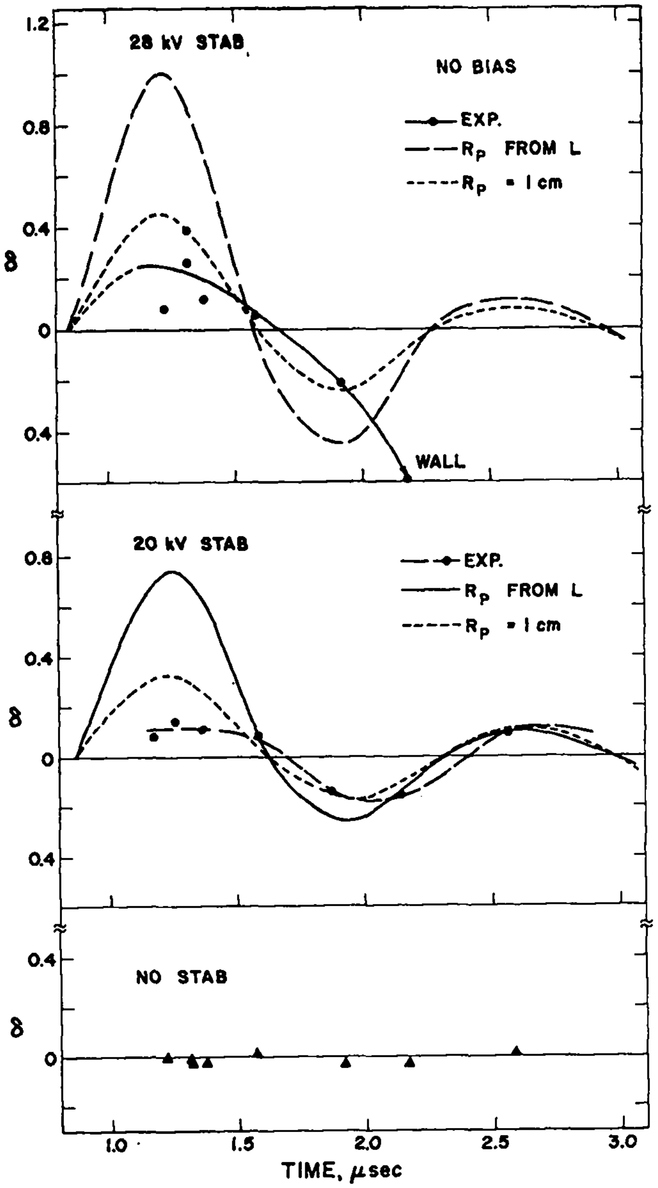

Fig. 39. Eccentricity of discharge vs time

Further information can be gained from the ϕ_z flux loops with the bias field, Fig. 40. Without stabilization the ϕ_z flux first increases with time as the z-pinch contracts towards the axis, compresses the enclosed B_z flux, and allows further flux outside the discharge tube to fill in the region behind it. As the increase in flux is ~ 2.5 times the starting flux and at most a flux change of 2.0 is expected from area considerations, we assign "paramagnetism" to the discharge. Although the total current through the B_z coil is

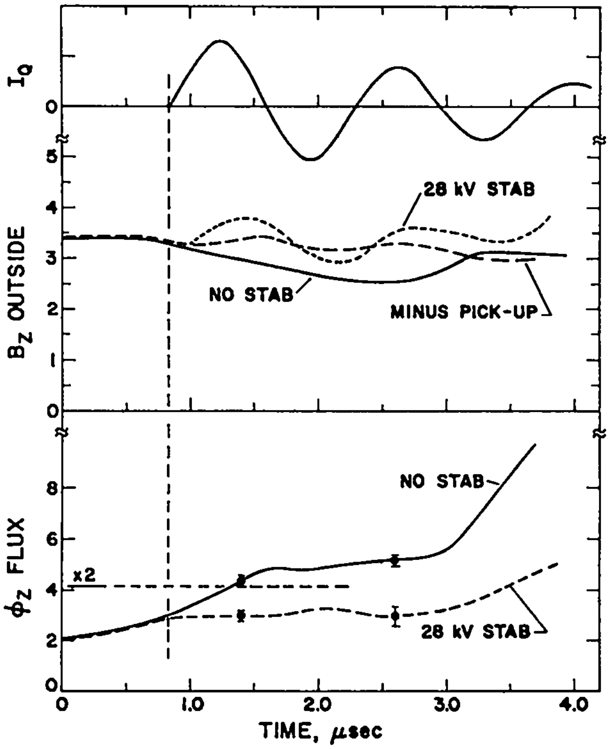

Fig. 40. B_z flux outside discharge tube and ϕ_z flux vs time.

constant (measured to be constant to $\leqslant 3\%$) the return flux from the new lines created in the z-pinch reduces the B_z outside the discharge tube, Fig. 40.

When the stabilizing current is turned on there is no further increase in ϕ_z flux through the loops, Fig. 40. The total B_z flux in the discharge tube sharply ($\leqslant 0.1$ μsec) becomes fixed and remains constant for ~ 2.5 μsec. We must therefore invoke some mechanism as the following:

1. A shorted turn immediately forms inside the discharge tube which prevents the inward flow of B_z flux. The creation of such a current sheath is unlikely in that we know that magnetic fields from the bars penetrate this region as seen by the distortion of the current channel.

2. The stabilization circuit on closure of the spark gap creates a shorted turn about the discharge tube for B_z flux. A test of penetration of the B_z field with the stabilizing spark gaps closed shows this to be unimportant.

3. The discharge remains approximately constant in radius and there is no further flow of B_z flux into the discharge tube. Side-on image converter photographs tend to support this hypothesis. Two possible mechanisms have been proposed.

   a. The plasma pressure is increased by joule heating by the stabilizing circuit. A fraction of the 17 joules of energy lost by the stabilizing circuit during the first quarter cycle could be deposited into the pinch column.

   b. The radial B_r fields from the quadrupole magnetic fields from the bars induce Hall currents in the plasma which in turn produce B_z fields inside the plasma column, as seen in the Polytron (Dangor, et al.[7]) and suggested by Borzunov.[4]

Conclusions

In spite of the early experimental results which indicated that this method would have considerable value in helping to stabilize the z-pinch there are a number of rather definite statements that can be made.

1. Theory predicts that long wavelengths will be stabilized but the growth rates for short wavelengths are only decreased. Experimentally we find agreement in that the growth rates are decreased as the bar currents are raised while wavelengths of the order two to three times the diameter of the discharge tube are the most dangerous.

2. Transfer of energy from the stabilizing circuit to the plasma or z-pinch circuit is high with the energy appearing as (a) hydromagnetic oscillations in the plasma column, (b) ionization of additional gas outside the z-pinch, and (c) joule heating.

3. The mass density of the z-pinch increases with the application of the stabilizing fields. Additional gas is introduced into the plasma column by the bars.

4. The amplitude of the hydromagnetic oscillation driven by the stabilizing bars as seen by the eccentricity of the pinch channel increase

with time until the plasma column intersects the tube walls.

With these experimental observations and the theoretical prediction that short wavelengths cannot be controlled, we conclude that this method of stabilization as examined in this experiment will not be practical for stabilizing a z-pinch for the times of interest in CTR.

References

1. S. M. Osovets and U. I. Sinitsyn, JETP 21, 4, 715 (1965).
2. E. I. Pavlov and U. I. Sinitsyn, JETP 24, 1, 59 (1967).
3. U. Y. Morozov and D. V. Orlinskii, A.E.C.-tr-7003.
4. N. A. Borzunov, et al., MATT-Trans-74 (Oct. 1968) of CN-24/J-12 Novosibirsk Meeting on Controlled Thermonuclear Reactions 1968.
5. R. J. Taylor, Proc. Phys. Soc. 70, 31 (1957).
6. A. Folkierski, P. G. Frayne, R. Latham, Nuclear Fusion, Pt. II 627, 1962 Supplement.
7. A. Dangor, G. Parkinson, R. Dunnett, M. Haines, R. Latham, Paper CN-24/B-7, Plasma Physics and Controlled Nuclear Fusion Research, Novosibirsk, 1968.
8. F. L. Ribe, LA-4081-MS.

ONE-DIMENSIONAL MHD CODE

(A. Haberstich)

A one-dimensional MHD code based on the work by Oliphant[1] has been written for the computation of azimuthally as well as axially symmetric pinches. The code makes use of a Lagrangian coordinate system and includes axial as well as azimuthal magnetic fields.

The calculation includes a classical or anomalous electrical resistivity tensor, radial electron and ion heat conductivities, an electron-ion equipartition time, and the usual Richtmyer-Von Neumann artificial viscosity. A typical implosion using 41 mesh points takes about 3 minutes computer time on the CDC 6600.

The code has been used to determine the detailed behavior of the shock-heated plasma in our fast linear z-pinch experiment. The results were found to be in general agreement with the available data.

Other applications of the code include calculations of the achievable temperature in a proposed toroidal pinch, penetration of the oscillating B_z-field in a dynamically stabilized z-pinch and paramagnetic effect in a biased z-pinch described in detail below.

Reference

1. T. A. Oliphant, Jr., Los Alamos Report LAMS-2944.

PARAMAGNETIC EFFECTS IN A BIASED Z-PINCH

(A. Haberstich)

As mentioned elsewhere in this report, B_z-flux loops have been used to detect the onset of m = 1 instabilities in the dynamically stabilized Columba experiment. Large flux increases were observed, following the application of the z-current and, presumably, before the onset of the instabilities. These fluxes are too large to be attributed to the compression of the bias field and the question arises whether they could be due to paramagnetic effects caused by an anisotropy of the plasma resistivity.

Steady State Plasma

We first consider the paramagnetism caused by anisotropies of the electrical resistivity in a steady state cylindrical plasma. The calculation is one-dimensional in the sense that we assume axial as well as azimuthal symmetry.

The plasma is assumed to have resistivity $\mu^{ij}(r)$, to contain a magnetic field $\underline{B} = (0, B_\theta(r), B_z(r))$ and to be of radius r_a. Maxwell's equations then reduce to:

$$-\mu^{\theta z}\frac{dB_z}{dr} + \mu^{\theta\theta}\frac{1}{r}\frac{d}{dr}\, r\, B_\theta = C_1$$

$$-\mu^{zz}\frac{dB_z}{dr} + \mu^{z\theta}\frac{1}{r}\frac{d}{dr}\, r\, B_\theta = 0, \qquad (1)$$

where C_1 is a constant and where:[1]

$$\mu^{\theta z} = \mu^{z\theta} = -\mu\,\delta\mu\,\frac{B_z B_\theta}{B^2}$$

$$\mu^{\theta\theta} = \mu\left(1 + \delta\mu\,\frac{B_\theta^2}{B^2}\right) \qquad (2)$$

$$\mu^{zz} = \mu\left(1 + \delta\mu\,\frac{B_z^2}{B^2}\right),$$

with

$$\mu = \mu_\parallel$$

$$\delta\mu = \frac{\mu_\perp - \mu_\parallel}{\mu_\parallel},$$

and:

$$B^2 = B_\theta^2 + B_z^2 .$$

$\mu_\perp$ and $\mu_\parallel$ are the components of the resistivity perpendicular and parallel to the magnet field.

Equations (1) can be normalized by means of the following variables:

$$Z(\rho) = \frac{B_z}{B_z(r_a)} \qquad kT(\rho) = \frac{B_\theta}{B_\theta(r_a)}$$

$$M(\rho) = \frac{\mu}{\mu(r_a)} \qquad \beta = \frac{C_1}{\mu(r_a)}\,\frac{r_a}{B_z(r_a)},$$

where

$$\rho = \frac{r}{r_a} \qquad k = \frac{B_\theta(r_a)}{B_z(r_a)} .$$

Defining $\gamma = \delta\mu/(1 + \delta\mu)$, equations (1) become

$$\frac{dZ}{d\rho} = -\gamma\,\frac{B}{M}\,\frac{ZkT}{Z^2 + (KT)^2}$$

$$\frac{1}{\rho}\frac{d}{d\rho}\,\rho kT = \frac{\beta}{M}\left(1 - \gamma\,\frac{(kT)^2}{Z^2 + (kT)^2}\right) . \qquad (3)$$

While M is assumed to be a known function of ρ, β is determined by the boundary conditions

$$Z = Z(0),\ kT = 0$$

at the origin and

$$Z = 1,\ kT = k$$

at $\rho = 1$.

Numerical solutions of Eqns. (3) are shown in Fig. 41 for M = 1 and k = 10 for several values of $\mu_\perp/\mu_\parallel$. The cases $\mu_\perp/\mu_\parallel = 2$ and $\mu_\perp/\mu_\parallel = \infty$ correspond to the results of Bickerton[2] and Kadomtsev[3], respectively.

Knowing $Z(\rho)$, one can calculate the relative increase in B_z-flux due to paramagnetism

$$\frac{\phi_\gamma}{\phi_{\frac{1}{2}}} = \int_0^1 Z(\rho)\, d\rho^2,$$

and the relative increase of B_z-field on axis

$$\frac{B_z(0)}{B_z(r_a)} = Z(0).$$

Calculated values of $\phi_\gamma/\phi_{\frac{1}{2}}$ are plotted in Fig. 42, for several ratios $\mu_\perp/\mu_\parallel$. A very large paramagnetic effect is seen to be possible for $\mu_\perp/\mu_\parallel >> 1$.

Dynamic Pinch

Depending on the temperature of the plasma, the magnetic field distribution may be relatively slow to reach a steady state. The increase of the B_z-flux in a biased z-pinch must therefore be expected to be somewhat smaller than predicted for a steady state plasma.

Use was made of the MHD code described elsewhere in this report to investigate this situation. The discharge parameters were chosen as follows:

Radius 3.175 cm Length 36 cm Return radius 4 cm
Gas D_2 at 70 μHg Initial temperature 1 eV
C_z 90 μF L_z 0.25 μH V_z 7 kV
B_z bias 270 G

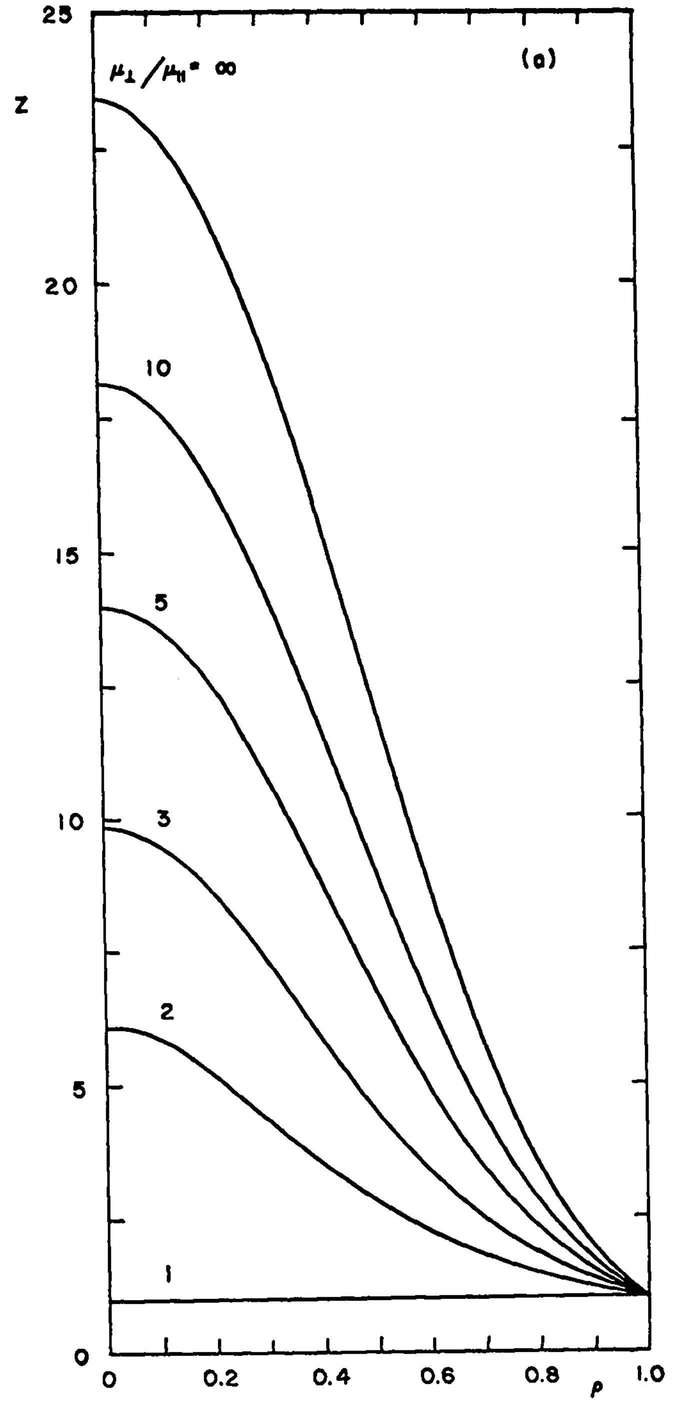

Fig. 41a. Normalized (a) axial and (b) azimuthal magnetic field distributions in a steady state plasma for M = 1, k = 10 and several ratios $\mu_\perp/\mu_\parallel$.

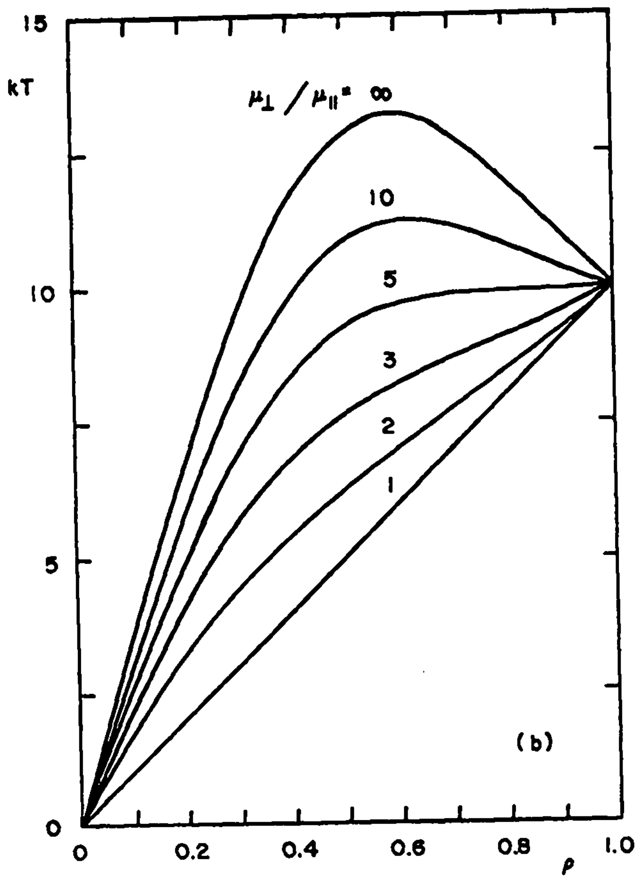

Fig. 41b.

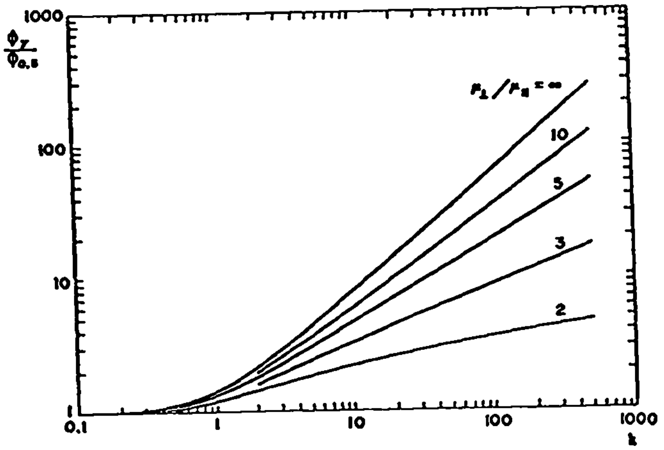

Fig. 42. Increase in B_z-flux, ϕ_γ/ϕ_1, in a steady state plasma for M = 1 and several values of $\mu_\perp/\mu_\parallel$ as function of k.

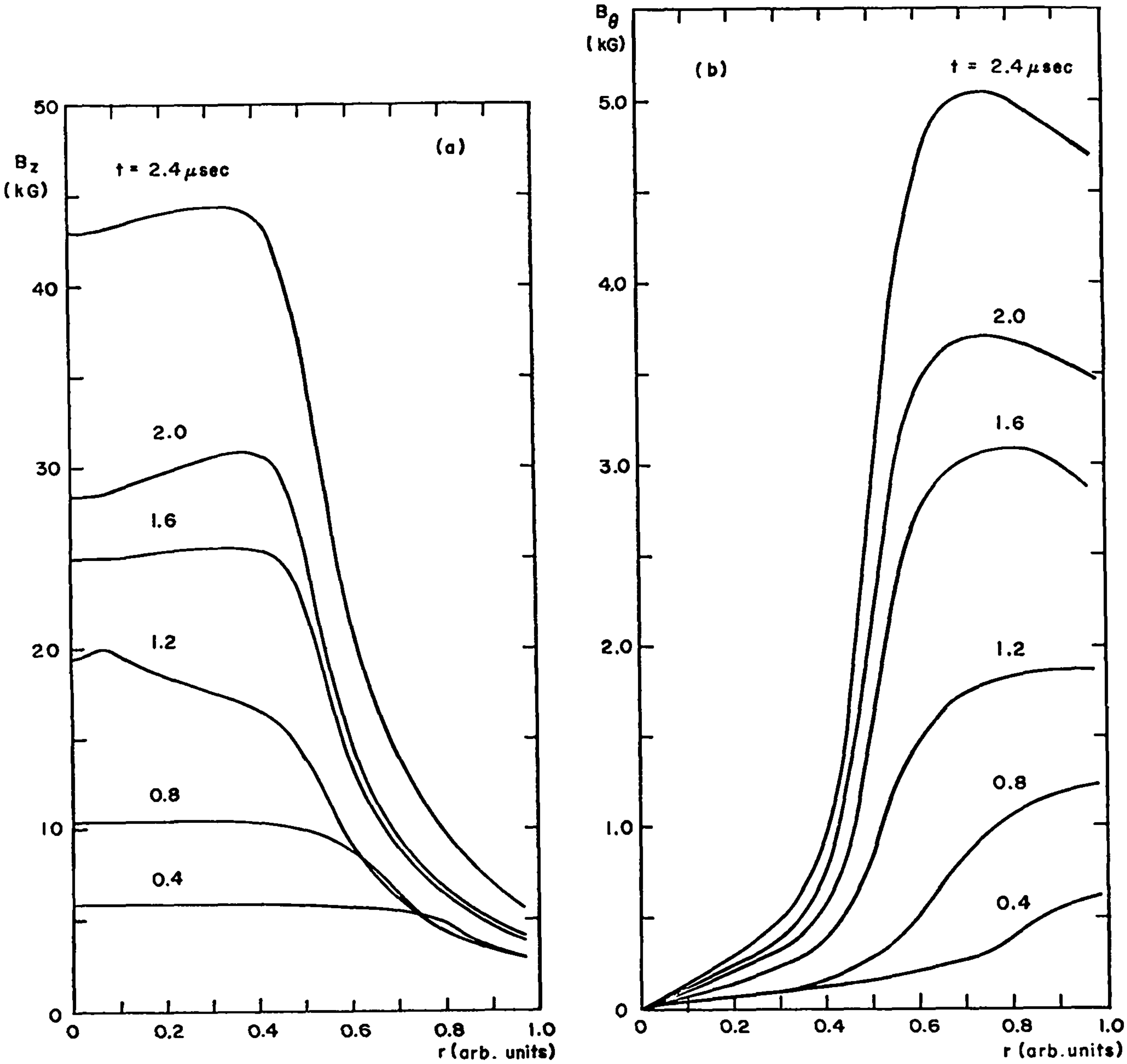

Fig. 43. Axial (a) and azimuthal (b) magnetic field distributions calculated with the MHD code, for several times in the discharge.

In Fig. 43 are shown radial profiles of B_z and B_θ at several times in the discharge, for a ratio $\mu_\perp/\mu_\parallel = 10$. The radial position r has been normalized to the radius of the plasma.

In Fig. 44 are plotted B_z distributions for a uniform steady state plasma, for a steady state plasma having the temperature distribution calculated at time 1.6 μsec in the discharge, and for the field calculated with the MHD code. The flattening of the B_z-field is seen to be due both to the temperature profile and slow diffusion.

In Fig. 45 are shown B_z-fluxes integrated over an area corresponding to the inner radius of the discharge tube. The fluxes are plotted as functions of time for several values of $\mu_\perp/\mu_\parallel$. The actual value of $\mu_\perp/\mu_\parallel$ is not known. For a

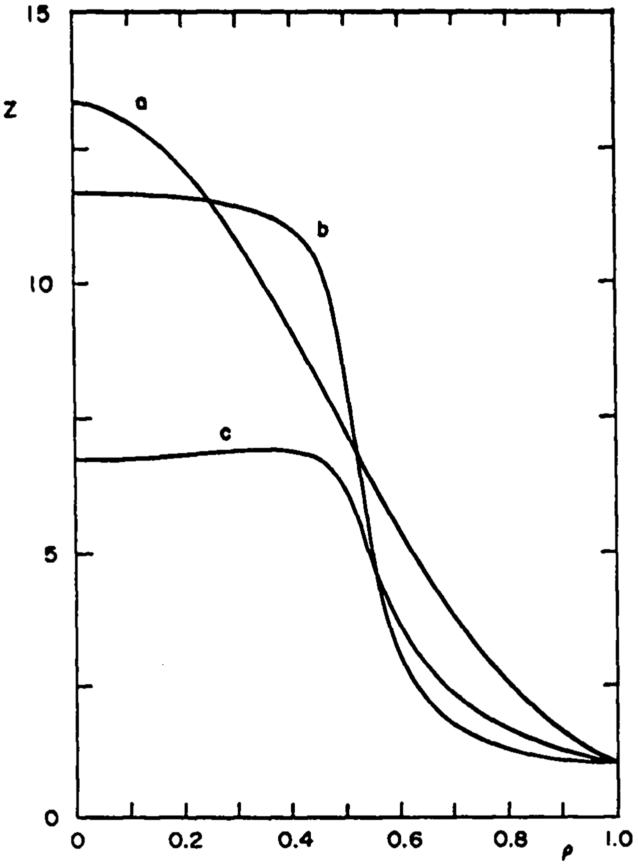

Fig. 44. Normalized azial magnetic field distribution (a) for a steady state uniform plasma, (b) for a steady state nonuniform plasma, (c) as calculated with the MHD code.

quiescent plasma, one would expect $\mu_\perp/\mu_\parallel = 2$,[4], while in a microscopically unstable plasma $\mu_\perp/\mu_\perp$ may be considerably larger.[3] A ratio of 25, for example, does not seem unreasonable under such conditions.[5]

Also in Fig. 45 is plotted the flux observed with the B_z-flux loop under conditions approximating the ones used in the calculation within 10 percent. The measured flux is seen to rise very slowly initially, suggesting an initially classical plasma that becomes anomalous later in the discharge.

Similar MHD calculations have been carried out for initial temperatures of 5 and 10 eV. The ratios $\mu_\perp/\mu_\parallel$ fitting the data at times ≥ 1.2 μsec then become larger than 20.

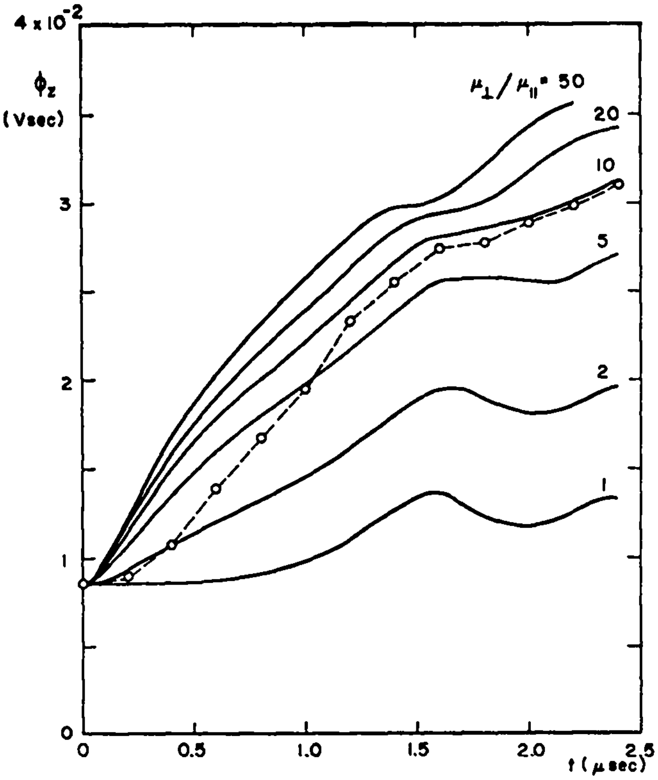

Fig. 45. B_z-fluxes as functions of time, (solid lines) calculated with the MHD code for several ratios $\mu_\perp/\mu_\parallel$, (dashed line) measured on Columba.

In conclusion, the observed large flux increases can be accounted for by a ratio $\mu_\perp/\mu_\parallel$ of the order of 10. This then implies that the plasma becomes microscopically unstable about 0.5 μsec after initiation of the discharge.

References

1. K. Hain, AERE Report R 3383.
2. R. J. Bickerton, Proc. Phys. Soc. Lond. 72, 618, 1958.
3. B. B. Kadomtsev, AEC-tr-5589 of CN-10/227, Salzburg Meeting on Plasma Physics and Controlled Thermonuclear Fusion (1961).
4. Lyman Spitzer, Jr., Physics of Fully Ionized Gases, New York, 1962.
5. D. J. Lees and M. G. Rusbridge, Proceedings of the Fourth International Conference on Ionization Phenomena in Gases, Uppsala, Vol. 2, 954, 1959.

FAST Z-PINCH

(J. N. DiMarco and L. C. Burkhardt)

Introduction

This experiment is being performed in an attempt to achieve a high temperature (keV) z-pinch. Heating is accomplished by driving a strong shock through the plasma. It is therefore required that the z-pinch be driven by a system capable of supplying a few thousand joules in a time scale faster than the sonic transit time, which is of the order of 0.5 μsec. Accordingly, a low inductance energy source is utilized employing the technique of magnetic energy storage.[1] This system is capable of supplying current at a rate of 2×10^{12} A/sec with voltages of the order of the order of 60 kV and peak currents of the order of 200 kA.

With an initial deuterium filling pressure of 20 mTorr, shock velocities of 4×10^7 cm/sec are measured. The plasma temperature, as determined by pressure balance, is ~ 1 keV, in agreement with the value predicted by shock theory.

Background

In the previous work with z-pinches, one of the limitations has been the low plasma temperature of a few hundred electron volts. Scaling between hot θ-pinch experiments and z-pinch experiments was attempted in terms of the electric field, which indicated that comparable temperatures (keV) should have been achieved. This section points out the difficulty with the previous scaling laws and presents the appropriate experimental parameters for the production of a hot z-pinch.

Numerical calculations of shock heating have been performed by A. Haberstich and are presented elsewhere in this report. The result indicates that there is no inherent limitation to heating in a z-pinch. Temperatures of several keV are predicted by the model for both z- and θ- pinches having comparable starting conditions. One of the important parameters is the initial rate of change of the magnetic field on the surface of the plasma. The requirements placed upon this parameter can be developed by considering the plasma sheath to be the "piston" that is driving the shock through the plasma. Using the snowplow model, it can be shown[1] that the initial piston acceleration is proportional to $\dot{B}/\sqrt{\rho}$, where $\dot{B}$ is the rate of change of magnetic field on the surface of the sheath and ρ is the initial plasma density. If it is now required that the piston achieve sonic velocity after it has moved some fraction of the discharge tube radius, the minimum initial $\dot{B}$ is specified.

Most of the experiments on z- and θ-pinches have approximately the same discharge tube dimensions. It therefore seems reasonable to consider $\dot{B}/\sqrt{\rho}$ as a scaling parameter. When compared to the θ-pinch experiments the z-pinch experiments did not achieve comparable $\dot{B}/\sqrt{\rho}$. There are two exceptions: One[2] achieved high sheath velocity in a discharge tube 1 cm in diameter and 2 cm long and thereby rendered diagnostics almost impossible. The other experiment[3] experienced difficulty with secondary breakdown on the wall of the discharge tube after the first pinch had formed. Our use of a magnetic energy storage system has eliminated this problem, as detailed in the section on experimental results.

Since the relationship between the initial $\dot{B}$ and the electric field is geometric, the difficulty in using the electric field as a scaling parameter can be realized. Two z-pinches can have the same initial $\dot{B}$ (the same initial shock heating), but, depending upon the geometry of the discharge tube, can have different electric fields.

The electric field can be calculated by measuring the voltage applied to the discharge tube and dividing by its length. However, the thickness of the discharge tube wall as well as any additional inductance between the voltage probe and the discharge tube must be included in the calculation. When attempting to scale among experiments one finds that the literature usually does not include all the required geometric information. However, the current waveform, or even $\dot{I}$, and the discharge tube radius are usually available, from which $\dot{B}$ can then be calculated. If the attempt is made to minimize the geometric differences by allowing the pinch to form, the resulting electric field is developed too late in the

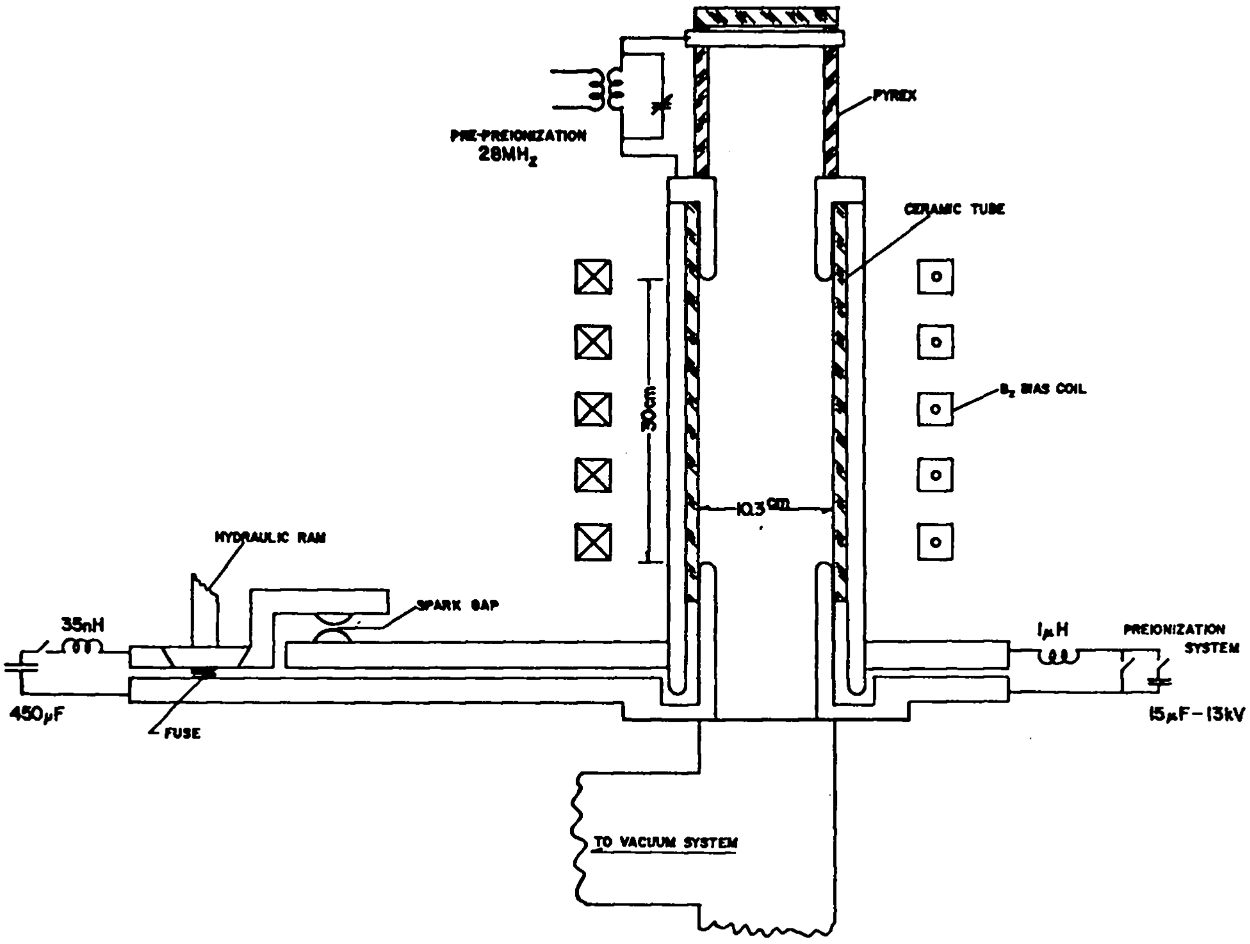

Fig. 46. Schematic of fast z-pinch experiment.

pinch history to generate strong shocks. The experiment described in this report, therefore, is designed to produce strong shock heating of a plasma in a z-pinch having sufficient access for the required diagnostics.

Description of Experiment

A schematic representation of the experiment is shown in Fig. 46. Deuterium gas flows continuously through the vacuum system. Preionization of the deuterium gas is caused by a 28-MHz, 300-W oscillator. The level of ionization is increased by means of a 25 kA axial current pulse of half-period 13 μ-sec. This current is removed from the pinch by means of a crowbar applied at the end of the first half cycle. The rapid current transfer is timed so as to occur approximately 3 μsec after the end of the first half cycle of the preionization current pulse. A description of the operation of a magnetic energy storage system is given elsewhere.[1] The experiment described in this report utilizes a 450-μF capacitor bank, typically charged to 12.5 - 14 kV, as the primary energy storage.

The energy is transferred into the 35-nH storage inductance. This inductance occurs in the capacitors, coax cables, headers, and parallel plate transmission line, although the majority of the inductance is associated with the parallel plate transmission line so as to isolate the capacitor bank from the high voltage generated across the fuse. The fuse construction was detailed previously. It consists of a copper foil 1-mil thick, 14-cm wide, and 15-cm long. Conductor-fuse interface continuity is maintained by a 9-ton hydraulic press which holds the short section of transmission line located on top of the fuse. An illuminated air gap switch is used to transfer the current from the storage inductance into the z-pinch. It operates at atmospheric pressure and the gap is illuminated by a current-limited (~ 0.1 amp) discharge located within the top electrode. The switch is not triggered but rather is allowed to break down spontaneously. The breakdown voltage is found to be very reproducible (~ 5%).

The discharge tube is made of 99.8% Al_2O_3 and has a wall thickness of 0.47 cm. Electrodes are made from 304 stainless steel with a wall thickness of .635 cm. Optical access is achieved by using tubular electrodes. The return conductor is made from an aluminum cylinder of wall thickness 1.27 cm. Assembly is achieved by splitting the cylinder along the axis and clamping the halves together with stainless steel clamps. These clamps then serve as flux conservers during the lifetime of the z-pinch, but allow the slow B_z bias field to penetrate the 0.3-cm gap in the return conductor. The bias magnetic field is produced by a solenoid external to the discharge tube, and has a half period of 3 msec.

The voltage is measured with a resistance probe located on the parallel plate transmission line adjacent to the z-pinch discharge. It consists of 10-1 kΩ, 2 watt resistors within an oil-filled coaxial return conductor. Its frequency response is 3DB down at 15 MHz. The z-pinch current is measured with a Rogowski probe located at the base of the discharge tube and constructed[4] so as to have a rise time of 5 nsec. In agreement with the calculated rise time is the measured frequency response fall-off of less than 2 DB at 80 MHz. Magnetic probes are typically 8 turns on a 1-mm diameter form placed in a 99.8% Al_2O_3 tube of 0.954-cm outer diameter having a wall thickness of 0.318 cm. This large tube is required to eliminate breakage and loss of vacuum which occurs when the z-pinch discharge takes place and a 0.159-cm wall thickness is used. The probes have a measured rise time of ~5 nsec and are electrostatically shielded.

Experimental Results

The experimental parameters that apply to all of the data discussed below are: main bank capacitance 450 μF, operating at 12.5 kV; storage inductance 35 nH; preionization bank capacitance 15 μF, operating at 13 kV. The filling gas is deuterium at a pressure of 10-133 mTorr.

The crowbar is installed in the preionization circuit in an attempt to produce reproducible behavior of the main z-pinch discharge. It is observed that the onset of an instability is delayed by about 7 μsec for approximately 50% of the discharges. Since the preionization pinch (30 kA) is unstable and a B_z field is produced in the plasma in a rather random manner, the conjecture was made that this B_z field is reducing the growth rate of the instability. Accordingly, the crowbar was installed in the preionization circuit in an attempt to generate only a single pulse of preionization current. The effect is shown in Fig. 47. The sweep time is 5 μsec/div. A crowbar is applied ~11 μsec after the start of the discharge and reduces the current in the second half by 1/4. In addition, the formation of a pinch does not occur and magnetic probes do not measure trapped magnetic field in the plasma. The fast current transfer is delayed with respect to the start of the preionization current by 21 μsec. An instability is observed to occur on every firing within 1 μsec of the start of the fast current transfer. Evidently, the stable behavior observed previous to crowbarring the preionization current is due to the B_z field in the plasma. The data that follow in this report were obtained with the preionization current crowbarred unless otherwise noted.

Typical voltage, current, and $\dot{I}$ are displayed in Fig. 48. The bias B_z field is zero. The sweep of the $\dot{I}$ signal is deliberately displaced with respect to the top traces in order to emphasize that the sweep rate is different. The general behavior of the transfer is displayed in that peak voltages of 40-60 kV are generated across the discharge. The rate of rise of current is such that 80% of the current is transferred in a time of ~0.1 μsec.

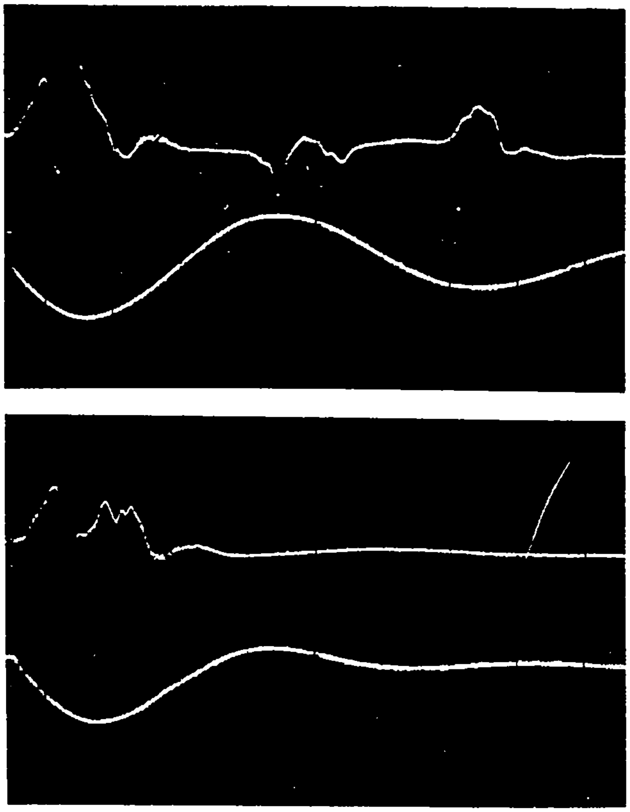

Effect Of Crowbar On Preionization
UPPER: Without Crowbar
LOWER: With Crowbar
TOP SIGNAL: B_θ r = 2.5 cm, 800 G/div
BOTTOM SIGNAL: I, 26 kA/div

Fig. 47. Effect of crowbar on preionization.

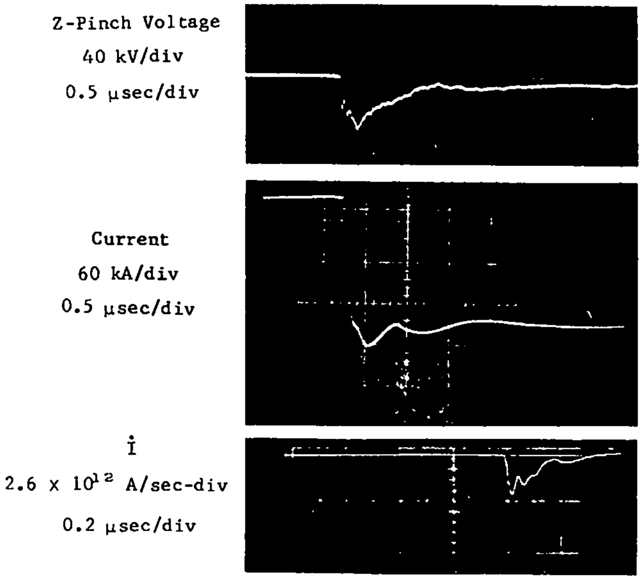

Deuterium at 26 μ of Hg.

Fig. 48. Typical voltage, current, and $\dot{I}$ values.

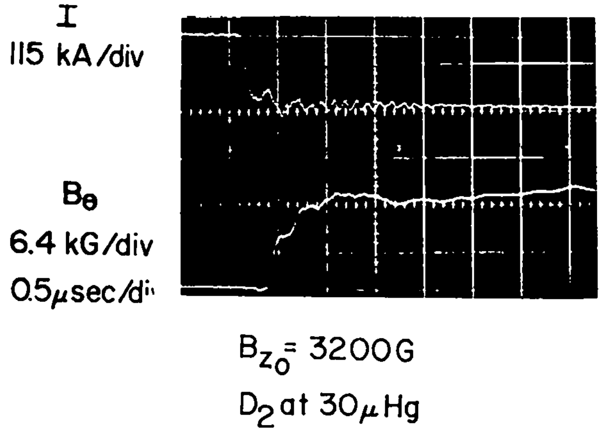

Fig. 49. Current and B_θ signal vs time.

It must be determined whether the current sheath moves away from the discharge tube wall and forms a pinch under these conditions of high rate of current transfer. A magnetic probe positioned to measure B_θ is inserted axially into the discharge and located at the midplane between the electrodes. The radial position is 2.5 cm from the axis. Figure 49 displays the current and B_θ signal. The fact that the current sheath moves off the wall is evident from the B_θ-probe signal. In addition, from the probe calibration and position, the total current enclosed by the probe can be calculated assuming a symmetrical current distribution, giving the result that at least 90% of the current is flowing in the pinch at this radius. Current "hang-up" on the wall is evidently not taking place.

Evidence for the generation of shocks is obtained from smear photographs which show luminous fronts propagating, with velocities as high as 4.2×10^7 cm/sec, through deuterium at an initial density of 20 mTorr. This corresponds to an Alfvén Mach number of ~ 3 at 3000 G bias field. These velocities are in general agreement with the

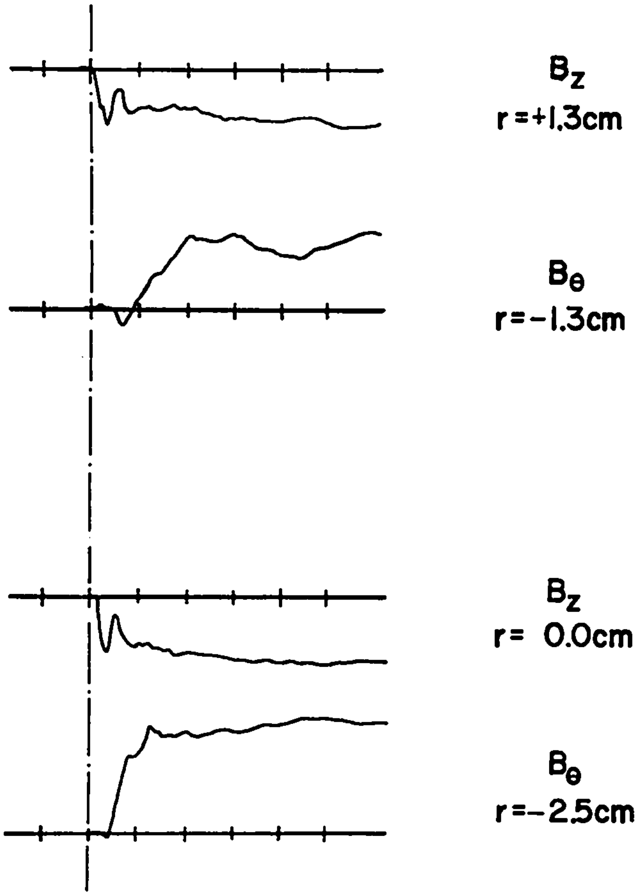

Fig. 50. B_z and B_θ from magnetic probes.

predictions of the theory[1] based on the snowplow model. In addition, hydrodynamic shock theory predicts that shocks of this magnitude should produce ~1 keV plasma temperatures. Experimental existence of a shock structure is shown in Fig. 50 which presents the B_z and B_θ signals obtained on a different shot. The B_z pulse of ~0.1-μsec duration is identified as resulting from the passage of the shock across the probe. The second increase of the B_z magnetic field results from the compression of the field inside the z-pinch by the B_θ field. In the lower set of signals the B_z probe is located at the axis of the system but the time at which the shock passes the position of the B_θ probe is calculated from the measured shock velocity. The relation of the shock front and piston can be observed from the time history of the signals. B_z probes placed beyond the position of the sheath show only a single pulse caused by the passage of the shock and lack the increase due to flux compression by the plasma current sheath.

In previous[3] fast z-pinches driven by capacitor banks, a secondary discharge is observed along the wall of the tube. This isolates the pinch from the energy source and prevents further heating of the hot plasma. Figure 51 shows the voltage and current as a function of time. The voltage traces clearly show the bouncing of the plasma column in the presence of a B_z magnetic field and the change in the bounce frequency with mass density. If a secondary breakdown had taken place along the wall of the discharge tube, it would have prevented flux from escaping from the pinch tube and the voltage oscillation would not be observed. In addition, the streak pictures do not indicate any bright secondary discharges taking place on the wall of the tube.

Figure 52 presents the current (I_z) obtained, by calculation, from the B_θ signals of two probes placed on a diagonal and equidistant from the axis, at 2.5 cm. If the z-pinch current is symmetrical then the signals should be mirror images of one another. Also plotted is the total current in the z-pinch as measured with the Rogowski probe. At the low value of bias (B_z) field the symmetry is lost within 1 μsec of the formation of the pinch. At the next two higher values of bias field the signal amplitudes vary out of phase with one another for ~4 μsec, and tend to lose amplitude after this time. At the highest value of bias field symmetry is maintained for at least 8 μsec. At the two intermediate values of bias field, the signals could be interpreted as arising from a current distribution that is centered off-axis and is rotating around the axis with a period of approximately 3 μsec. The displacement of the current from the axis increases until most of the current is flowing in the vicinity of the walls. This behavior could then be considered to be a slow-growing kink instability that is rotating around the axis of the discharge tube.

Figure 53 presents the same information as Fig. 52 for the case of 30 mTorr D_2 and 3200 G. Current symmetry is maintained for times of the

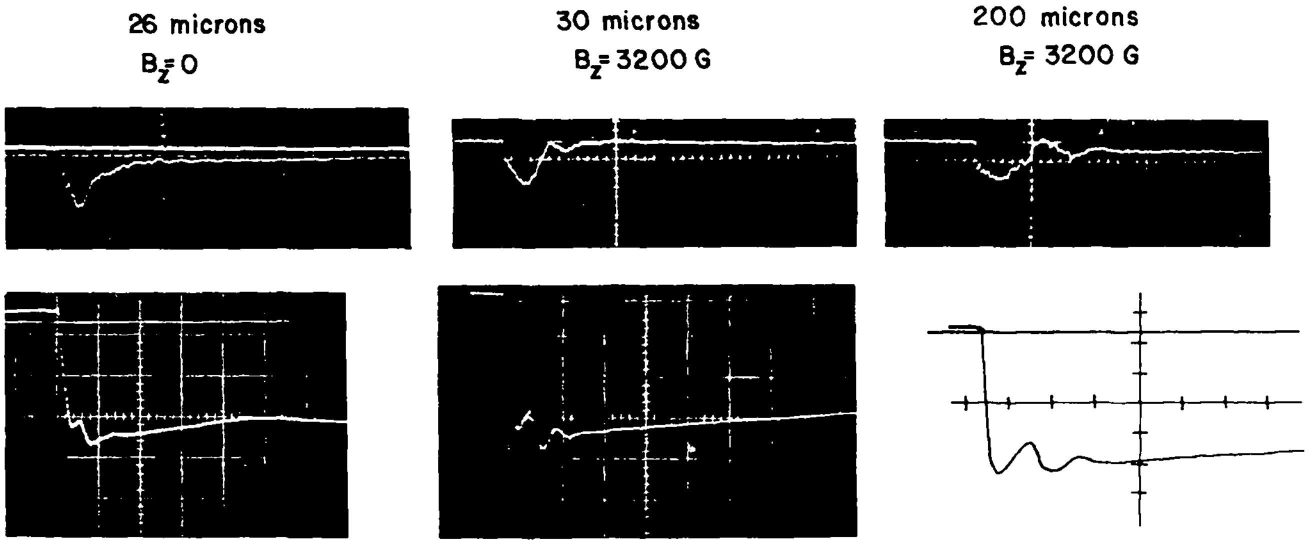

Z-Pinch Voltage And Current

Voltage: 49 kV/div, Current: 60 kA/div

Sweep Time: 0.5 μsec/div

Fig. 51. Voltage and current vs time.

order of 8 μsec. In these figures, the B_θ probe signals were integrated by means of 10 μsec passive RC integrators. The displayed results have not been corrected for the effect of the integrator. Figure 54 presents the same information as Fig. 53, but the B_θ-probe signals are obtained with 100-μsec integrators. Figure 55 presents the data obtained under the same experimental conditions as the previous data except that the filling density is increased by a factor of 6.6 to 200 mTorr. Because of the increased mass density of the plasma, it is expected that the growth rate should be reduced. This was noted on earlier low temperature experiments. However, it can be seen from the figure that the current symmetry is lost in times $\leqslant$ 5 μsec.

Discussion

The results presented in Fig. 49 show that a magnetic energy storage system can be used to drive a z-pinch. Energy transfer from storage inductance to the z-pinch is of the order of 20%. There are some aspects of this technique that make it an ideal method for coupling into the z-pinch, namely, it provides a constant current source. This advantage will be specified when the prevention of a secondary breakdown is considered.

Under the conditions outlined in the previous section, all of the current moved away from the wall and formed a pinch. It should be noted that under some conditions only partial "pull-off" is achieved. If the rapid transfer of the current into the z-pinch takes place sometime during the first ~ $\frac{3}{8}$ cycle of the preionization current, only $\frac{1}{3}$ of the total I_z current is detected by the B_θ probes. By causing the transfer to occur at the end of the first $\frac{1}{2}$ cycle or later, all of the current formed a pinch.

In previous experiments[3] with fast z-pinches driven by capacitor banks, a secondary

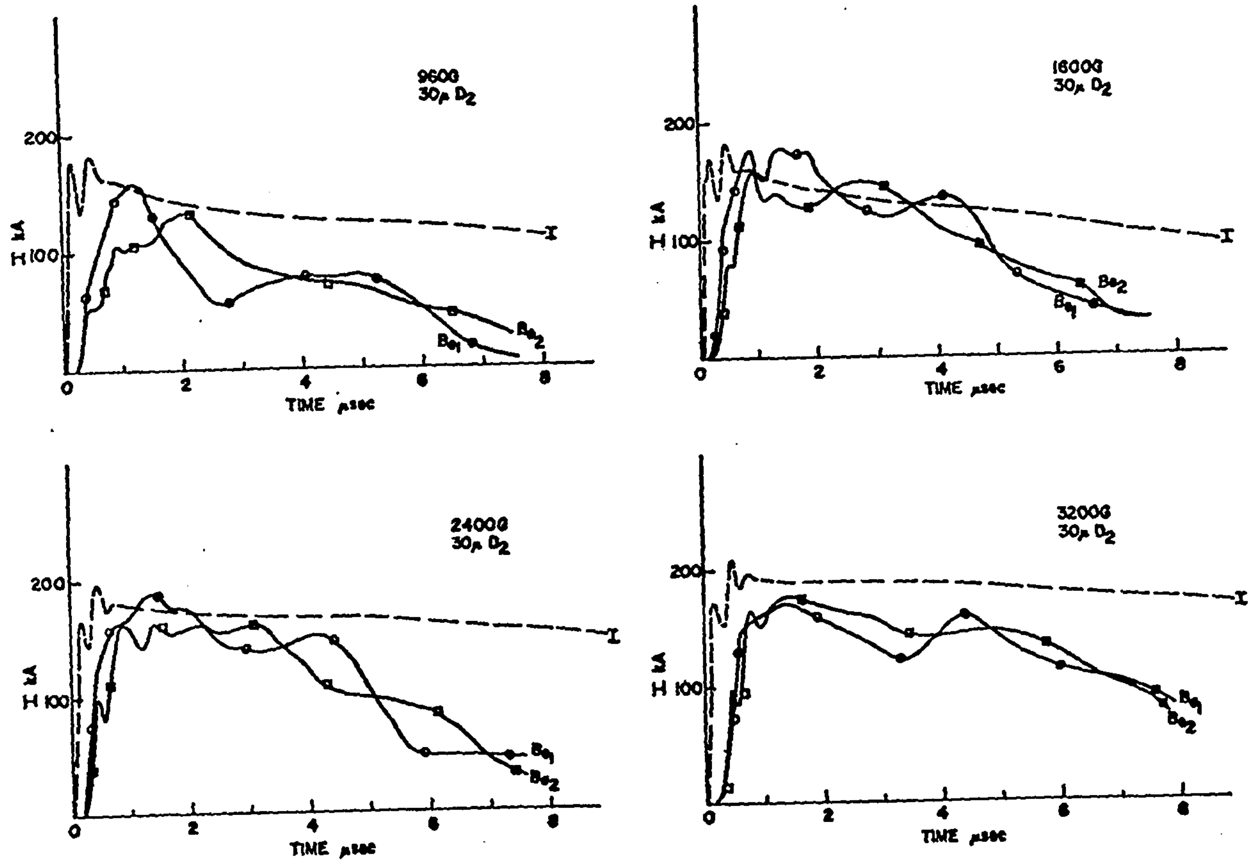

Fig. 52. Calculated I_z vs time.

discharge has been observed along the wall of the discharge tube, which isolates the pinch from the energy source. This secondary breakdown does not take place in this experiment: streak and framing pictures do not show any bright secondary discharge taking place on the wall of the discharge tube. In addition, the voltage and current traces in Fig. 51 clearly show the bouncing of the plasma column in the presence of a B_z magnetic field and the change in the bounce frequency with mass density. If a secondary breakdown had taken place along the wall of the discharge tube, it would have prevented flux from escaping from the pinch tube and the voltage oscillation would not be observed. By considering the fact that the voltage across the pinch tube is given by $L\dot{I}$ + $\dot{L}I + RI$, the lack of a secondary breakdown can be explained. The source tries to maintain a constant current so the $L\dot{I}$ voltage is small, the $\dot{L}I$ voltage is also small at the time of peak

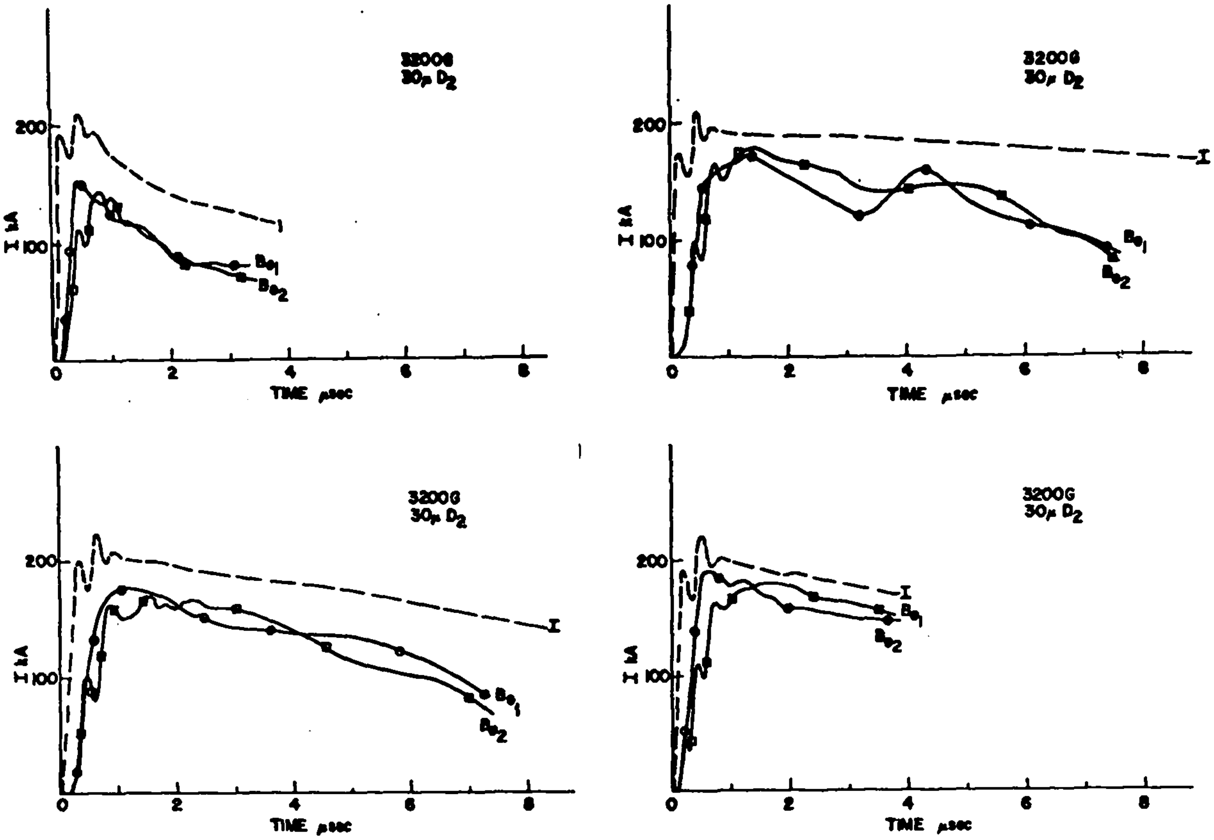

Fig. 53. Calculated I_z vs time.

compression where $\dot{L} = 0$. Therefore, the total voltage across the pinch is low. If a low-inductance capacitor bank is used to drive the z-pinch, however, the pinch inductance is a maximum at the time of maximum compression, and the voltage developed across the pinch is then almost the full capacitor-bank voltage. The discharge tube is then required to hold off a high voltage while being exposed to the intense radiation produced by the hot pinched plasma--which it evidently cannot do.

The temperature of the plasma can be calculated from the observed shock speeds, using an MHD numerical code. The predicted ion temperature for the case of a 10 mTorr filling pressure is of the order of 1 keV. Pressure balance measurements at 2 μsec after the implosion yield plasma $(T_i + T_e)$ temperatures of ~750 eV which is in general agreement with the theory. However, more work is needed to verify that a high temperature plasma is being produced.

The stability of the pinched plasma column can be examined by referring to Figs. 52, 53, 54, and 55. Figure 52 shows that by increasing the magnetic field the stability of the plasma in a column is enhanced. This effect is opposite to what may be expected since the growth of an instability should scale as the Alfv̆en speed. This speed increases with magnetic field, yet the growth rate decreases. Also, decreasing the density increases the sound speed so at the low density the growth rate should be faster than at the high density. Yet the data in Figs. 53, 54,

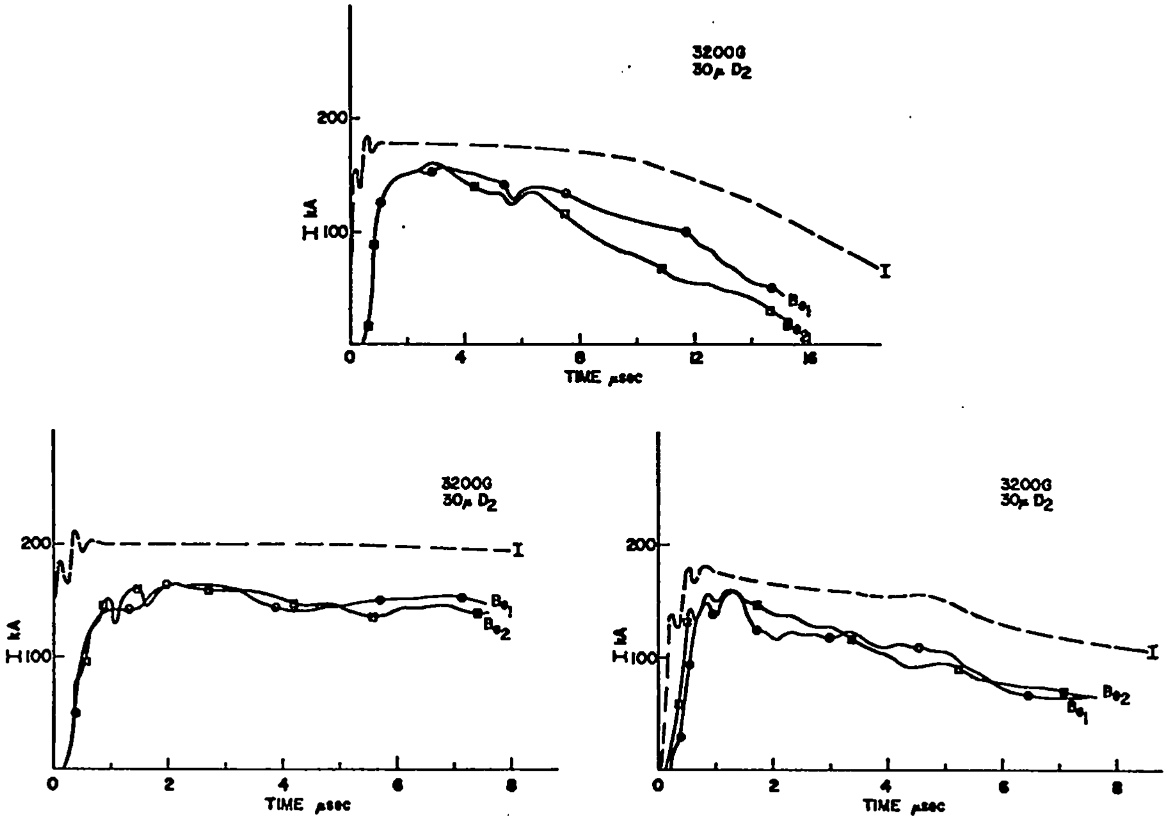

Fig. 54. Calculated I_z vs time.

and 55 show that current symmetry is maintained for a longer period of time at the lower density. Some of these results can be fitted into the MHD^{5,6} stability theory. The theoretical model has restrictions that limit its application to the experiment, but the general trend and amplitude of the parameters predicted by the theory(to yield stability)is in agreement with the data. For the observed equilibrium position of the plasma of 2.5 cm, the theory predicts absolute stability for an initial bias magnetic field >2100 G. The data show a gradual reduction in the growth rate for magnetic fields in this range. The effect of the density of the plasma on the stability is not resolved by the theory, for it predicts that instabilities should scale as the Alfvén speed.

An approach that can be taken to fit the data into the theory is to consider that the low density plasma might be a better approximation to the assumed thin sheath model. Figure 56 shows that approximately the same amount of energy is delivered to the plasma independent of the initial filling density. Assuming that the magnetic field distribution is the same for the different densities, then the temperature must decrease with increasing density. A higher temperature is also predicted by hydrodynamic shock theory. The conductivity, being a function of temperature and not density, then increases as the temperature increases. The higher-temperature plasma should therefore maintain a thin current sheath for a longer period of time. Since the model requires an infinitely thin sheath, damping mechanisms must be invoked to prevent instability growth with a thick sheath. The question of how thick a sheath may be tolerated is unresolved.

Conclusion

It has been demonstrated that a magnetic energy storage system is an effective technique

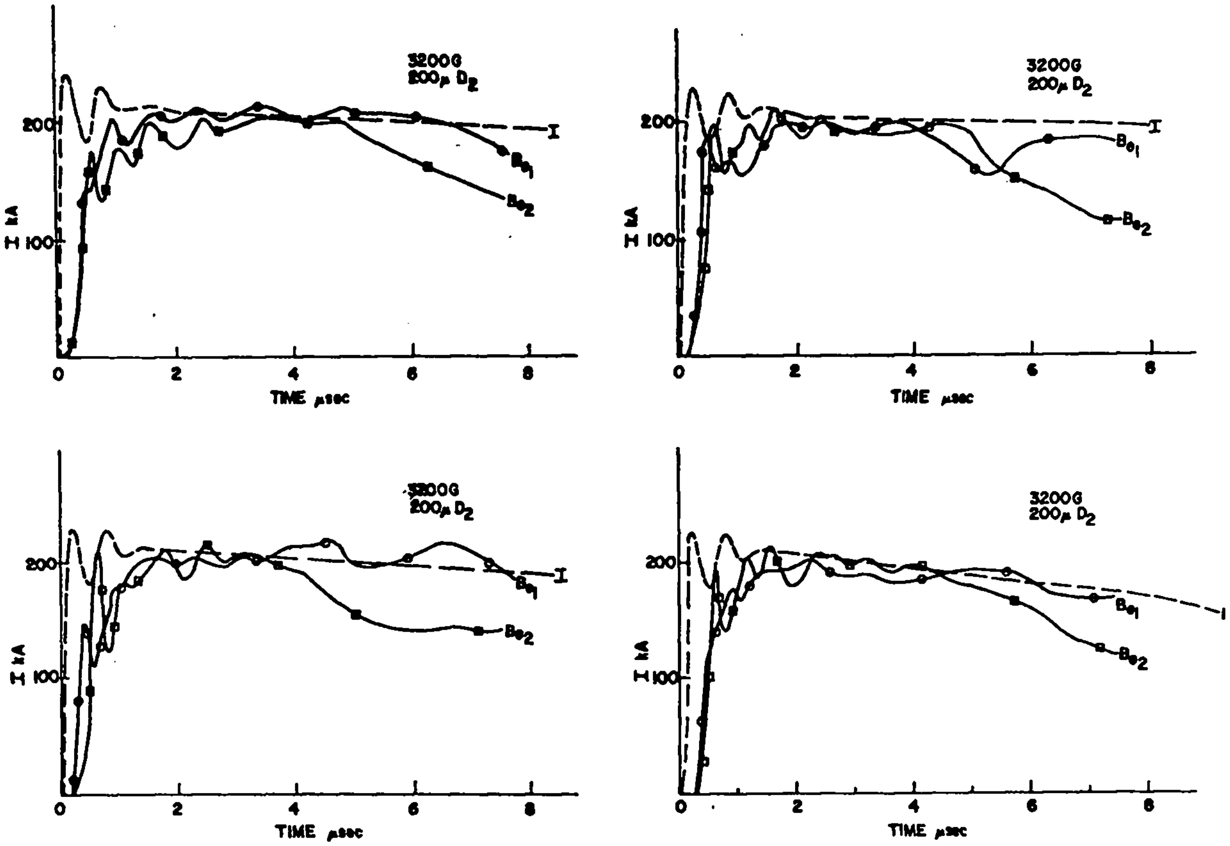

Fig. 55. Calculated I_z vs time.

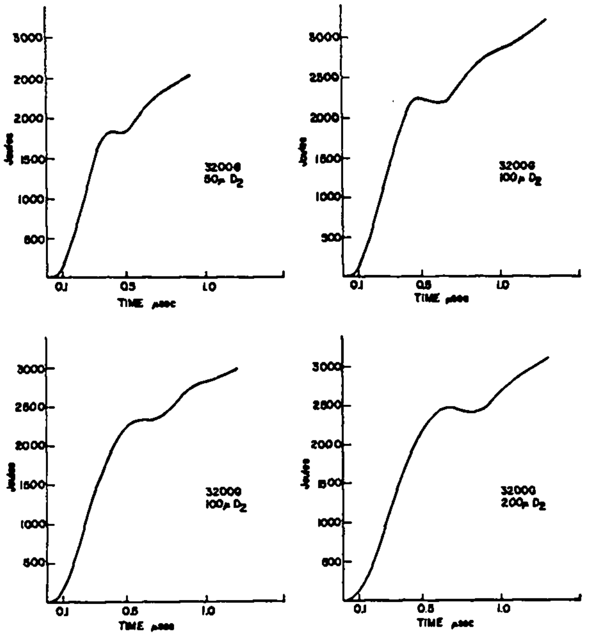

Fig. 56. Energy vs filling density.

for transferring energy into a z-pinch. The phenomena of wall "hang-up" and secondary breakdown can be prevented. The observed shock velocities and pressure balance measurements are indicative of the production of a keV plasma. The stability results show a general agreement with MHD theory. In addition, there is some evidence that the stability of the z-pinch is dependent upon the plasma temperature.

References

1. LASL Controlled Thermonuclear Research Program, LA-4075-MS, 1968, p. 3.
2. L. D. Heflinger and S. L. Leonard, Phys. Fluids, 4, 406 (1960).
3. H.A.B. Bodin, A.A. Newton, and N.J. Peacock, Nuclear Fusion 1, 54 (1960).
4. J. Cooper, Plasma Physics (Journal of Nuclear Energy Part C), 5, 285 (1963).
5. R. J. Tayler, AERE-L104 (1959).
6. M. D. Kruskal, et al., Phys. Fluids 1, 139 (1958).

A SHOCK HEATED TOROIDAL Z-PINCH EXPERIMENT

(J. A. Phillips et al.)

We are planning a high temperature toroidal z-pinch experiment.[1] The fast linear z-pinch experiment (see elsewhere this report) indicates that a stable plasma with a peak temperature ~ 1 keV has been produced in a z-pinch. These results lead us to take the next step to the toroidal geometry to eliminate end effects.

In the proposed experiment the main heating mechanism is a strong shock driven by the B_θ magnetic field of the fast-rising axial current. The magnetic energy storage technique as developed for the linear experiment will be used. The B_θ magnetic field subsequently confines the plasma. MHD stabilization is provided by a conducting wall and an internal B_z magnetic field. The B_z field outside the pinch is small or zero. The experiment will be designed to permit the addition of programmed profiles of B_z and B_θ radial distributions if found necessary for MHD stability.

Each quadrant of the torus will approximate the dimensions and electrical characteristics of the present linear experiment and will be energized by a somewhat larger magnetic energy storage system. Iron cores couple the primary current to the secondary plasma current. Design parameters are shown in Table I.

Table I

Major diameter	~ 76 cm
Minor diameter	~ 11 cm
Rate of rise of plasma current	~ 3×10^{12} A/sec
Peak plasma current	~ 300 kA
Number of feedpoints	4
Max. voltage per feedpoint	~ 80 kV
Primary energy source	~ 2500 μF at 20 kV
Longitudinal bias B_z field	$\leqslant$ 6 kG

Reference

1. LASL report in preparation.

PLASMA GUNS

(Group P-17)

PULSED PLASMA GUN PROGRAM

(I. Henins, J. Marshall)

While most of the effort in the gun program has gone into the "Birdseed" experiment, some has gone into preparations for further work on the continuous-flow pinch. Present plans are to study plasma flow over the end of a large-diameter center electrode so that a system of this kind can be investigated in greater detail than heretofore, and to investigate effects of electrical polarity on plasma flow in a coaxial system. Since almost none of this work has progressed far enough to include actual plasma experiments, it will not be discussed further here.

The Birdseed experiment is an extension of auroral work and high altitude barium release experiments which have been carried out elsewhere in the laboratory. While it is not of direct interest for controlled thermonuclear research, it makes possible the investigation of gun behavior under conditions which would ordinarily be quite impossible because of lack of funds, facilities, and personnel. It is a cooperative effort among a number of organizations with general responsibility for the overall program in LASL Group J-10. We reproduce here that part of a report written for Birdseed that deals with the plasma gun.

Among the conclusions which can be drawn from the Birdseed shots and related experiments are:

1) Efficiency: A coaxial gun is a very efficient device. Seventy percent or more of the electrical energy flowing in to the terminals is delivered through the gun muzzle so as to be recoverable as heat. Most of this, in the case of hydrogen isotopes, is kinetic energy of plasma flow. With heavy gases, of the order of half of the energy is in vacuum ultraviolet radiation, while the remainder is in kinetic energy.

2) Collimation: In the case of a heavy gas, the muzzle pinch forms a very tightly

collimated jet of plasma. With hydrogen or deuterium, the plasma jet fills a much larger solid angle. This is probably because of the effect of line radiation which reduces the electron temperature in the jet. The result is reduced plasma pressure and hydromagnetic flow which is more convergent because of resistive flux annihilation in the pinch.

PAYLOAD DEVELOPMENT FOR A HIGH ALTITUDE PLASMA INJECTION EXPERIMENT

(Deleted Version)

(R. S. Caird, C. M. Fowler, W. B. Garn, I. Henins, R. A. Jeffries, D. M. Kerr, J. Marshall, D. B. Thomson, and J. C. Ingraham, EG&G, Inc.)

Introduction

The Birdseed experiment is designed to inject an optically traceable neon plasma into the ionosphere in order to investigate the dynamic interaction of a high energy plasma with the upper atmosphere and the earth's geomagnetic field. The experimental objectives require that the plasma be injected at velocities in excess of 10^7 cm/sec--the minimum speed for which charge exchange and ionization cross sections are greater than momentum transport cross sections--in a quantity sufficient to allow collective effects to be significant. To meet these objectives, it is proposed that a coaxial plasma gun powered by high-explosive current generators be fired to altitudes between 210 and 230 km by a STRYPI rocket. The groups involved in the Birdseed experiment include: J-10, general responsibility for the overall program; P-17, plasma gun; GMX-6, high-explosive generators; Sandia Laboratories, Albuquerque, rocket hardware, telemetry, and launch; and EG&G, field diagnostics support. Laboratory measurements of the plasma produced by an explosive generator-powered coaxial gun are described in this [version of the] report.

Plasma Gun Operation

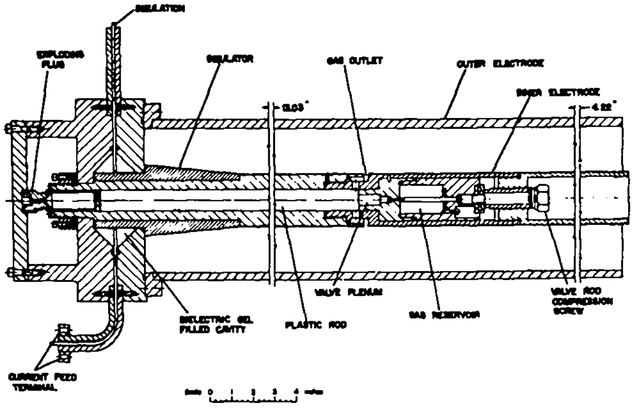

Fig. 57. Rocket borne plasma gun design.

The design of the coaxial plasma gun, which is operated in the continuous flow pinch mode[1] for these experiments, is shown in Fig. 57. With this device a neon plasma is produced and accelerated to a high velocity in the following manner. The gun is initially filled with neon gas released into the interelectrode volume by a fast-acting valve.[2] The gas valve derives its opening motion from energy stored elastically in an axially compressed polycarbonate plastic rod. This compression is released suddenly and controllably by exploding a supporting plug. After about 1.2 msec, by which time the gas has expanded throughout the gun, a negative high voltage is applied to the center at the electrical terminals of the gun. Initial breakdown occurs near the gas outlet ports, roughly half-way along the gun barrel, where the gas density is highest. Plasma current spreads toward the muzzle as a result of $\vec{J} \times \vec{B}$ forces and in the direction of the electrical terminals as the result of additional breakdown into a region already magnetized by the existing current. As the current sheath advances to the muzzle, plasma is displaced radially toward the outer electrodes and is left behind magnetized and carrying current by processes which are not now fully understood.

By the time the current sheath has reached the muzzle, the entire gun volume is filled with magnetized plasma with the B_θ field near the gun terminals larger than that near the muzzle. This gradient in magnetic pressure accelerates the plasma axially from the gun into a region where the radial confining forces provided by the electrodes are no longer present. Here the combination of magnetic and kinetic pressure allows some of the plasma to expand radially, but more importantly, these pressures cause a large fraction of the plasma to be compressed into a pinch just beyond the gun muzzle. As a consequence of lower plasma density and higher magnetic field near the inner electrode than near the outer, the flow inward to the pinch has higher Alfvén and plasma flow velocities than the outwardly directed flow and is therefore more energetic. In addition, resistive annihilation of magnetic flux[3] at the pinch axis appears to enhance further the inward flow and to produce a cylinder of demagnetized heated plasma which expands axially, much like gas from a rocket nozzle.

The current at the gun terminals persists for some time (> 100 μsec) after the applied voltage at that point has dropped to zero. This indicates the presence of magnetic flux in the gun barrel which gradually decreases as the magnetized plasma flows out through the muzzle. Very little, if any, plasma in the pinch flows backward into the open end of the center electrode, presumably because of momentum acquired within the gun. The plasma expands primarily in the axial direction as it moves away from the gun muzzle. The radial expansion is much less because of the confining magnetic field. Although this field decreases with distance from the gun muzzle, the plasma cools as it expands and therefore requires lower magnetic fields for confinement. Excellent collimation of the plasma is observed optically for the full length of the vacuum tank (~ 2.7 m), while ablation damage at the end of the tank implies that a major portion of the jet is contained within a solid angle of 3×10^{-3} steradians.

A theoretical treatment of the continuous-flow pinch performed by Morozov[4] predicts the formation of a pinch in steady-state plasma flow through the conversion of magnetic energy to random and/or directed plasma kinetic energy, as is observed experimentally. These results have also been verified by recent particle-in-cell computer calculations.[5]

It should be mentioned that a pinch produced by a plasma gun filled with neon is smaller in radius than that observed using deuterium. This tighter pinch is formed because ionized neon emits copious line radiation and therefore cools more rapidly than ionized deuterium which can radiate only through bremsstrahlung. The cooler plasma can then be more highly compressed by the magnetic field.

Explosively-Driven Power Supply

The design of the power supply is fixed by several requirements: an appropriate minimum energy needed to drive the plasma gun (250 kJ); a maximum weight allowance (< 250 kg) for the power supply (based on the total rocket payload weight); a specified initial voltage to start the plasma gun (~ 5 kV); and a current waveform that reaches peak in a few tens of microseconds and remains crowbarred for several tens of microseconds. Because of the low energy-to-weight ratio of capacitors (< 220 J/kg), the only way to achieve these electrical requirements within the weight allowance is to use explosively driven generators in the power supply, thus utilizing a part of the large energy density available in high explosives (4 MJ/kg).

The two generators used here, shown schematically in Fig. 58, are both of the spiral-wound type. An initial current is established in a solenoid wound concentric with and outside of a hollow conducting cylinder called the armature. The armature is filled with high explosive which when detonated causes it to expand and make electrical contact with the solenoid. As the detonation wave travels down the armature axis, the inductance of the solenoid is forcibly reduced with a resulting increase in solenoid current. The circuit current increases, and energy is transferred to the series load with an efficiency which depends on the load impedance.

Because of time limitations, the design[6] chosen here made use of previously tested

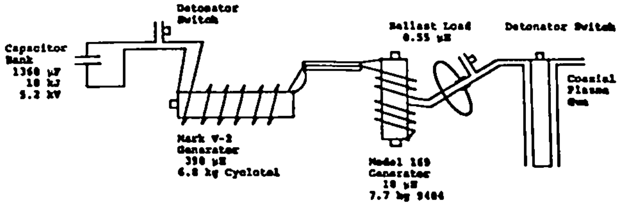

Fig. 58. Schematic diagram of explosive power supply.

components and techniques wherever possible. Previous experience[7] with the Sandia Model 169 generator led to its selection as the output stage. An intermediate generator, the LASL Mark V, was designed to supply the necessary input current (~65-70 kA) for the Model 169. A small bank of high energy-to-weight ratio Maxwell capacitors (1360 μF, rated at 6 kV, 18 kJ, 240 lb weight) is used to supply the initial current (~ 8000 A) to the Mark V generator.

The present design of this power supply is shown schematically in Fig. 58. All switching is accomplished with detonator-activated solid-dielectric switches. The ballast load shown at the output of the Model 169 is used to complete the circuit prior to firing the switch to the plasma gun. After the switching, the ballast load shares the output current. The inductance of the ballast load, together with the switching time, determines the initial voltage applied to the gun. Since the ballast load has a greater impedance than the plasma gun, most of the energy is delivered to the gun. The optimum ballast load inductance and output switch timing have been determined by thorough testing at the explosive firing site.

All the components used in the power supply design were chosen with an eye to meeting the stabilizing spin and takeoff acceleration requirements of the rocket. Preliminary spin and acceleration tests have been conducted at LASL, and complete tests are being conducted by the Sandia rocket group.

Framing camera pictures of the Mark V armature under explosive drive have shown that the Mark V generator, fired 100 μsec ahead of the Model 169, will not mechanically interfere with the 169 in the rocket configuration. Subsequent shots at the firing site, with the two generators in rocket configuration, have confirmed this.

Fears that the explosive jet formed by the colliding detonation waves in the Model 169 generator might harm the plasma gun before it stopped accelerating plasma were laid to rest by measurements on two tests. Studies of the jet motion gave its time of arrival at a point 30 cm from the generator as 202 μsec after the 169 fire signal; its velocity at this point was 1.8 mm/μsec. Since the plasma flow from the gun lasts for only about 100 μsec and is complete by 150 μsec after the 169 fire signal, placing the 169 generator 30 cm from the gun without special blast protection should present no danger to the gun's performance.

In its final explosive test prior to use with the plasma gun, the power supply described in Fig. 58, delivered 500 kJ into a passive 0.11-μH mock-gun load, at a peak current of 3 MA and peak voltage of ~ 27 kV.

Experimental Results

Prior to the Birdseed experiments, plasma gun research had involved only capacitor-energized devices. Preliminary investigations indicated, however, that the peak power levels experienced in explosively energized plasma guns were about five times greater than the highest obtained with capacitor power supplies. Furthermore, the time duration of the power pulse from an explosive power supply is about half that from a capacitor source of comparable energy. With these obvious differences in the two systems in mind, a program of extensive testing of the explosively driven coaxial gun has been undertaken and is now nearing completion. These tests have allowed optimization of the performance of the explosively driven gun, and equally important, have provided pertinent diagnostic information about the plasma jet produced under these conditions. Data of the latter type are essential to the determination of optical diagnostic parameters for the field experiment and to the subsequent quantitative analysis of the results obtained.

The 1.5-m diam. by 3-m long vacuum tank used in the testing is shown schematically in Fig. 59 together with the positioning of the plasma gun, the location of the generated plasma jet, and the arrangement for the diagnostic instrumentation. A massive sandbag wall separated the explosive generators and the vacuum tank and protected the tank and nearby instrumentation from all but minor blast damage during the experiments. The current from the generators to the plasma gun was transmitted by a parallel-plate line 0.915-m wide and 4.88-m long which passed through the wall.

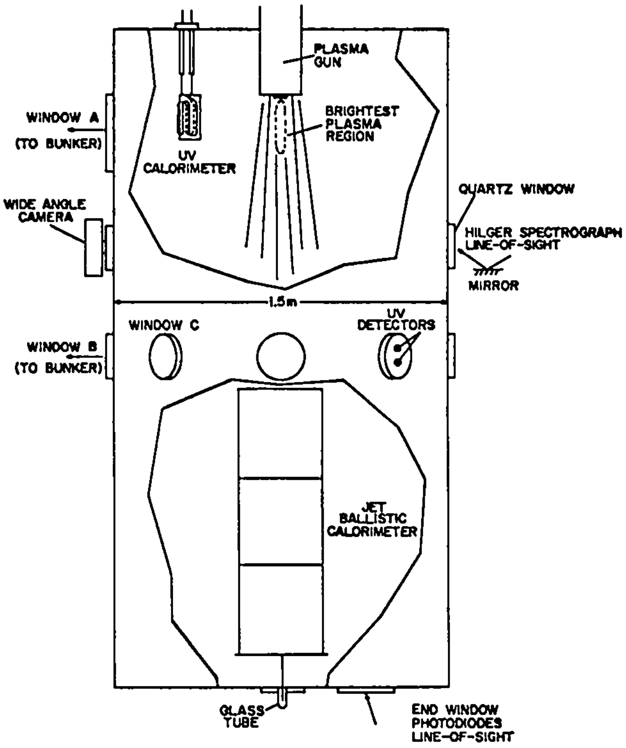

Fig. 59. Schematic of vacuum tank.

Optical diagnostic instrumentation allowed streak photography of the plasma jet, multiple-exposure image converter photography, time-integrated photography, time-integrated spectroscopy, and visible photometry. Most of this instrumentation was housed in the concrete bunker beneath the firing table and the light was transmitted to that location by a train of mirrors and beam splitters.

Electrical diagnostics comprised current and voltage measurements at various points in the power supply circuit including the gun terminals, plus a flux signal obtained by passive integration of the voltage across the gun terminals. Other diagnostic equipment included calorimeters, a ballistic pendulum, and vacuum ultraviolet photometers. A more detailed description of each of the diagnostic instruments and their arrangement is contained in the Appendix to this report.

A summary of the salient data obtained in the plasma gun experiments performed to date is presented in Table I. Birdseed shots I-IV were pure power-supply development shots and were all successful. Shots V, VII, and IX failed to produce plasmas because of systems difficulties. With one exception, the details of the explosive power supply and the plasma gun were identical for each of these shots. The plasma gun of Birdseed VI differed from those used later in that the inner electrode was aluminum alloy flame-sprayed with copper, while the outer electrode was aluminum alloy. While this gun apparently performed adequately, a rather low plasma velocity was observed, and both electrodes showed mechanical damage. As a result, the electrode material was changed--the inner to drawn copper and the outer to copper--and subsequent experiments gave consistently higher plasma velocities for comparable experimental parameters with little or no damage to the electrodes.

The data presented in Table I point to the rather curious fact that the total energy actually delivered to the plasma gun terminals--as well as the peak current, voltage, and power--were all independent of the amount of neon injected into the gun. The data also suggest that the plasma flow velocities increase as the gas load is decreased; however, because the shot-to-shot variation in velocity for the same experimental conditions (c.f. XI and XII) is comparable with the velocity differences that could be associated with changes in gas load (c.f. VII and XII), this conclusion is in some doubt. Additional design and testing would be required to achieve optimum matching of the explosively driven power supply to the plasma gun, but the results of Table I indicate that the minimum design requirements have been met with energy to spare.

A typical example (from VII) of the streak-photographic and image converter records that have been obtained is presented in Fig. 60. Here the image converter photographs with 2-μsec exposures have been time-indexed with the streak record and illustrate the temporal character of the plasma pinch. The streak record suggests that the plasma is ejected in a series of "blobs" rather than in a truly continuous flow. The brightest plasma region recorded on the image converter

Table I. Birdseed Shot Data

Shot	VI	VII	X	XI	XII
Date	6/24/69	7/31/69	9/5/69	9/17/69	10/3/69
Neon load (mg)	63.8	63.8	84.2	43.2	43.2
Peak current (MA)	1.84	1.53	1.72	1.62	1.53
Peak voltage (kV)	25.8	23.8	24.1	25.4	25.0
Peak power (GW)	42.6	35.6	40.4	39.0	37.9
Energy (kJ)	346	310	324	337	348
Flux (Wb)	0.28	0.289	0.265	0.295	0.263
Peak velocity (cm/μsec)	8	19.2	-	28	24.2
Velocity spread	-	3.8:1	-	3.5:1	4.65:1

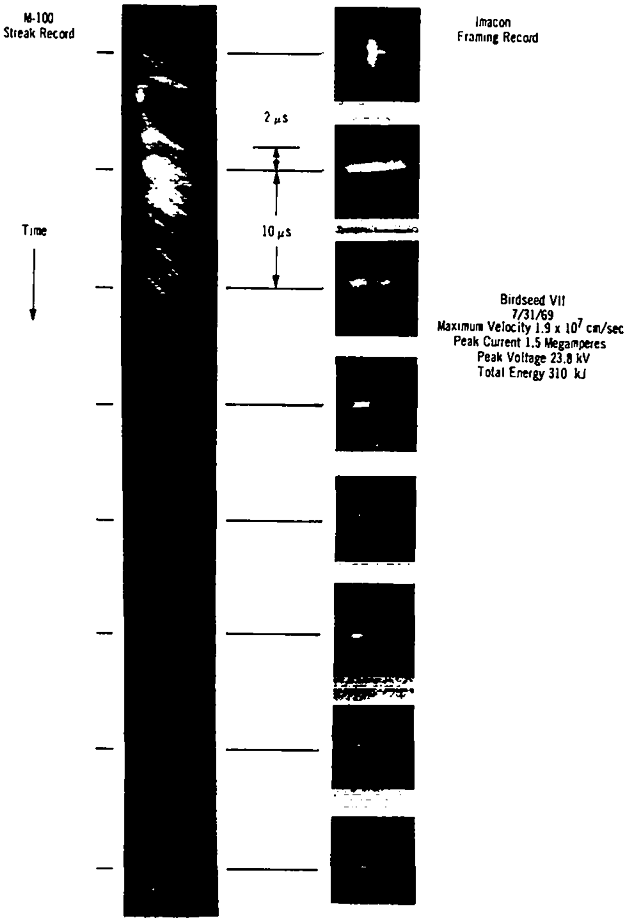

Fig. 60. Streak photographs and image converter records from Shot VII.

photographs, the pinch, is a cylindrical volume centered on the gun longitudinal axis with an approximate diameter of 4 cm and extending about 30 cm beyond the muzzle. The brightness of other plasma regions, excepting the open gun muzzle itself, is less than that of the pinch; this observation is further verified by the time-integrated photographs of the muzzle pinch similar to that presented in Fig. 61. Streak-camera records like that of Fig. 60 provide the information on the plasma velocity in the region of the pinch. Records from an image converter camera operating in the streak mode and viewing the plasma at a distance of 120 cm from the muzzle show that the plasma does not accelerate between the points 30 cm and 120 cm from the gun muzzle.

In the two earliest experiments, stigmatic and time-integrated spectrograms of the visible radiation emitted by the plasma near the gun muzzle were obtained with a Hilger quartz-prism spectrograph. The spectra of these plasmas were quite similar but were substantially different from those routinely observed in capacitor-energized gun experiments.

When activated by a 2800-μF bank charged to 15 kV, the neon-filled gun consistently produces line radiation characteristic of the Ne, Ne^+, and Ne^{++} species and these species alone. The time-integrated spectrograms of the Birdseed plasmas, however, have superposed on the neutral and

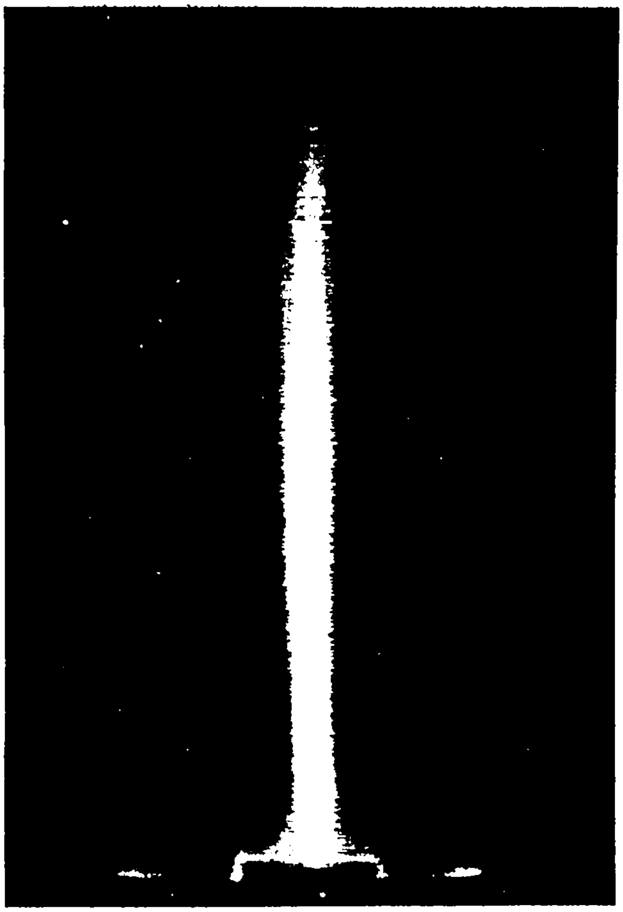

Fig. 61. Time-integrated photograph of muzzle pinch.

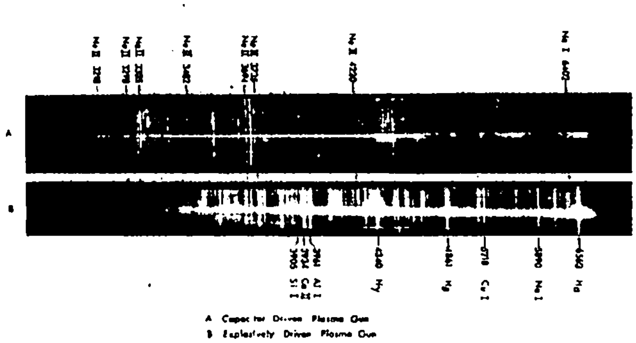

Fig. 62. Time-integrated spectra from the plasma gun.

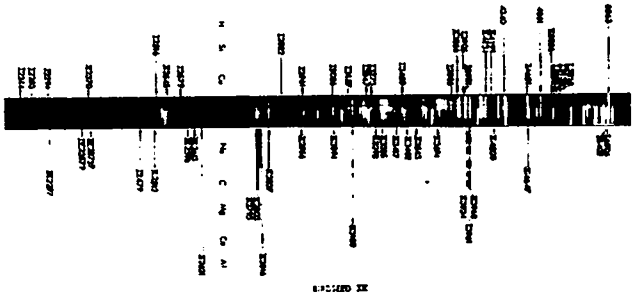

Fig. 63. Time-integrated spectrum over visible and ultraviolet regions from Shot XII.

ionized neon lines a highly exposed impurity spectrum comprising radiation from H, C, Al, Ca^+, Na, Si, Si^+, Mg, and Cu. The apparent sources of these impurities are the gun electrodes and electrical insulator and the tank wall. Examples of the time-integrated spectra obtained with both capacitor- and explosive-powered (from VI) plasma guns are presented in Fig. 62. Spectrograms of this type also show that the line radiation superposed on the bright continuum in the plasma pinch is characteristic of the same species that are observed exterior to the pinch, although relative line intensities may well vary between these two regions.

Following the second Birdseed experiment, the time-integrated prism spectrograph was rearranged to allow spectroscopy of the plasma pinch in the ultraviolet region. The spectrograms so obtained in later experiments were similar throughout the visible region to the two previously discussed but, in addition, allowed a positive identification of the Ne^{++} and a possible identification of Ne^{+++} in the plasma spectrum; no radiation was observed from other species not previously mentioned. A spectrogram of this later type (from XII), obtained with an astigmatic spectrograph, is shown in Fig. 63.

A second time-integrating spectrograph viewed the visible radiation from the plasma at a location about one meter from the gun muzzle. Spectra from this location were quite similar to those from near the muzzle, although the intensity of the Ne lines relative to the remainder of the spectrum appeared to be greater at the more distant position; such an observation would be consistent with the idea of a recombining plasma.

The diagnostic observation of the plasma in experiment XII were by far the most successful and extensive to date. The following discussion will therefore be directed mostly to the quantitative

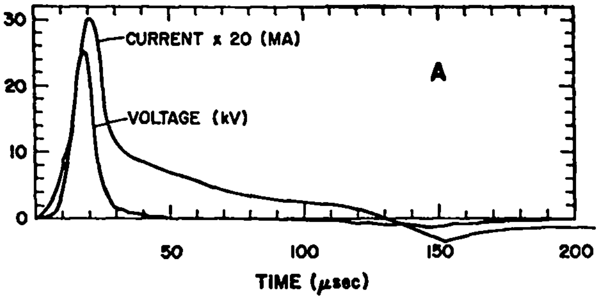

Fig. 64a

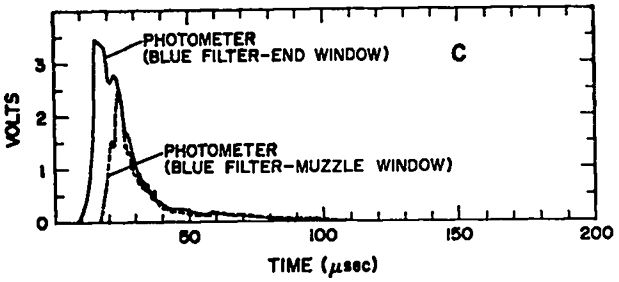

Fig. 64c

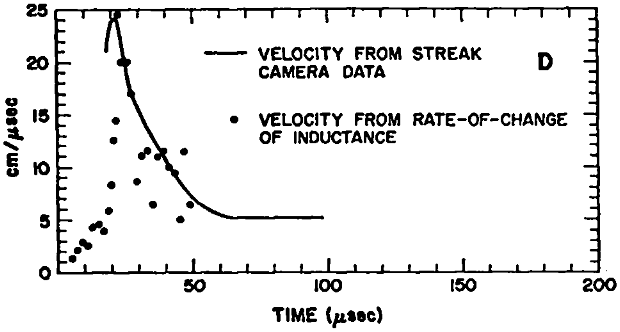

Fig. 64d

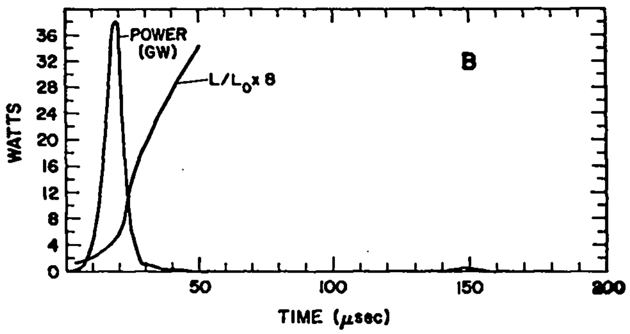

Fig. 64b

Fig. 64. Composite plots of parameters vs time on Shot XII; (a) voltage and current; (b) power and inductance, (c) photometer signals, and (d) plasma flow velocity.

data obtained for that shot from electrical, photometric, and calorimetric instrumentation. A compsite plot of several of the parameters measured during XII as a function of time is presented in Fig. 64. Comparison of the two plots of 64a shows the plasma gun voltage peaking about 1 μsec before the current,arelationship observed in each experiment. On this shot, as well as on XI, a late-time (150 μsec) current and voltage signal of polarity opposite to the initial signal was also observed. Such a signal could be generated if the Model 169 generator did not remain shorted and developed an open circuit at this time, thereby causing the ballast load current to flow with reversed polarity through the gun. As discussed earlier in this report, the long current tail observed between 30 and 120 μsec corresponds to the period when magnetic energy stored in the gun is converted into additional plasma kinetic energy.

The power flowing into the gun terminals and a calculated quantity corresponding to a gun inductance are plotted in Fig. 64b. This quantity, an equivalent inductance, is computed by dividing the magnetic flux generated within the gun, $\int Vdt$, by the current; it is a measure of the flux area emcompassed by the mean longitudinal position of the current through the plasma in the absence of flux annihilation. For the purposes of this plot, the equivalent inductance has been scaled by L_o, the inductance of the coaxial gun in vacuum. Thus at the point where the ratio of $\int Vdt/I$ to L_o is unity, the axial positional mean of the radial current flow is at the gun muzzle. It is significant that this ratio reaches unity some 5 μsec after plasma is first observed by photometry to exist from the muzzle. Note also that a continued increase of the scaled equivalent inductance to values greater than one, such as that actually observed here,

Table II. Total Energy and Peak Power Flux of Visible Radiation from Plasma of Birdseed XII

	Muzzle Photometer (216 cm)		End Photometer (290 cm)	
Wavelength Range (Å)	Total Energy Flux (μJ cm^{-2})	Peak Power Flux (W cm^{-2})	Total Energy Flux (μJ cm^{-2})	Peak Power Flux (W cm^{-2})
4075-4590	76	6.5	142	12.6
5030-5560	41	3.6	77	6.0
6150-6960	32	2.6	84	6.3
4000-7000	245	21	505	38.0

would be expected to follow emergence of a resistance-free plasma from the muzzle and the expansion of the flux into the space beyond. Previous experiments, however, have shown that the major part of the flux emerging from the gun, is, in fact, resistively annihilated in the pinch. This implies that interpretation of the quantity $\int Vdt/I$ as an inductance is incorrect at late times.

The signals originating at two photometers viewing the plasma from different directions are compared in Fig. 64c. The muzzle photometer accepted light emitted from the bright plasma region immediately adjacent to the muzzle in a direction normal to the gun axis, while the end photometer looked back at the gun muzzle and plasma pinch from an angle 10° off the gun axis. The muzzle photometer signal provides an indication of the time the plasma first left the gun (17 μsec) and the time of the peak light output (24 μsec—5 μsec after peak electrical power). The end photometer signal shows that light is emitted from the interior of the gun and has a temporal behavior similar to that of the power at the gun terminals.

In Fig. 64d the variation of the plasma flow velocity with time as determined from streak-camera data is presented. The qualitative features of this plot have been the same for each shot: (1) the peak velocity occurs a few microseconds after the plasma first leaves the gun almost simultaneously with the peak in electrical power, and (2) the velocity then decreases uniformly with time for the next 25 μsec and thereafter remains constant to the end of the film record. Figure 64d also shows a velocity calculated from the relationship between the velocity of the positional mean current and the time-derivative of the inductance for a coaxial transmission line with constant conductor radii. The equivalent inductance discussed above has been used for numerical solution. This model appears to have little applicability to the plasma gun after the plasma begins to leave the gun muzzle, but it is interesting to note how well the late-time calculated velocities agree with the streak-camera measurements.

Additional data of a quantitative nature obtained from the photometric measurements of XII are summarized in Table II. The values of total energy and peak power flux are reported for the distances that separated the muzzle and end photometers from the gun muzzle (216 and 290 cm, respectively) and have been corrected from the raw data to reflect certain geometric factors. The muzzle photometer field-of-view included only about half the bright plasma region; therefore the actual measurements have been increased two-fold. The end photometer measurements have been increased by a factor of 1.33 for similar reasons. An equivalent, total energy radiated isotropically in the visible spectrum has been calculated to be 140 J by using the muzzle photometric measurements, this is about 0.16% of what is thought to be the total energy radiated from the pinch region (determined by a total radiation calorimetric measurement and with certain assumptions about the geometry of the source).*

---

*For comparison, the total isotropic radiation was 105 kJ for X, 97 kJ for XI, and 84 kJ for XII.

An indirect estimate of the plasma mass flow may be obtained by using velocity data previously discussed together with measurements of energy and longitudinal momentum. For the latter of these measurements, a calorimeter can was positioned to collect the plasma leaving the gun within a solid angle of 0.066 steradians about the gun axis (9.25° half-angle) and was suspended to act as a ballistic pendulum. In XII the measured energy was 135 kJ and the impulse was 2.53 kg-m/sec. For the purpose of calculation, the velocity behavior was approximated by a function linearly decreasing with time for the first 30 μsec and staying constant at that level for the remainder of the plasma flow. The mass flow calculated using these data and assumptions was 8.2 mg during the first 30 μsec and 25.1 mg in later times. The total mass flow collected by the calorimeter can was therefore 33.3 mg, which may be compared with the total injected neon mass of 43.2 mg. The average plasma velocity computed from the total energy and mass is 9.0 cm/μsec.

A second quantity of importance is the azimuthal distribution of the mass and energy flow within the jet. A limited inference can be made from the calorimeter can data, since the can is formed of four thermally separated sections (three hollow cylindrical wall sections and the end plate). Numbering these sections consecutively, beginning with the one nearest to the gun muzzle, the solid angle, Ω, subtended at the gun muzzle and the energy, E, collected by each are as follows: $\Omega_1 = 0.026$ ster, $E_1 = 24.65$ kJ; $\Omega_2 = 0.0132$ ster, $E_2 = 23.4$ kJ; $\Omega_3 = 0.0072$ ster, $E_3 = 60.7$ kJ; and $\Omega_4 = 0.0192$ ster, $E_4 = 26.55$ kJ. The jet also creates an ablation damage area upon the end plate with an average diameter less than six inches and a solid angle less than 0.003 ster, indicating that a significant but unknown fraction of the jet energy is within a 0.003 ster cone about the gun axis. It appears that the value of E_3 exceeds E_4 by a large amount because the ablated material carries most of the energy away from the end plate, and a large portion of this material is then condensed on cylinder section 3. Following this model, crude estimates indicate that 40-50 kJ were deposited originally on the 0.003 ster damage area. Further refinements in the measurement of the angular energy distribution are planned. Note that caution is necessary if one attempts to use the values of E_1, Ω_1, etc., to determine an angular energy distribution since the plasma generally does not necessarily give all its energy to the first object it strikes.

It should be noted that the 87 kJ deposited into 0.034 ster on shot XI is in fair agreement with the total of 87.3 kJ deposited into $\Omega_3 + \Omega_4 = 0.0263$ ster on shot XII.

The data from the experiments completed to date suggest that the mass loading for the field experiment should be 62 mg or about 2×10^{21} neon atoms. This intermediate loading is indicated in spite of the higher velocities observed with lower neon concentrations because the rocket-borne gun will be more closely coupled electrically to the high-explosive generators. Therefore, the energy delivered to the plasma for a given loading should exceed that of the ground-based experiments. Furthermore, optical observation of the field experiment is improved with an increased number of neon atoms injected into the ionosphere.

References

1. A. A. Newton and J. Marshall, Bull. Am. Phys. Soc., 13, 878 (1968).
2. I. Henins and J. Marshall, Rev. Sci. Instr., 40, 875 (1969).
3. A. A. Newton, J. Marshall, and I. Henins, Bull. Am. Phys. Soc., 13, 1544 (1968).
4. A. I. Morozov, Sov. Phys. - Tech. Phys. 12, 1580 (1968).
5. T. D. Butler, J. L. Cook, and R. L. Morse, "MHD Simulation of Coaxial Plasma Flow," Proceedings of the APS Topical Conference on Numerical Simulation of Plasmas, Sept. 18-20, 1968, Los Alamos, N.M., LA-3990.
6. C. M. Fowler, D. B. Thomson, K. J. Ewing, R. S. Caird, and W. B. Garn, "High Altitude Pulsed Plasma Power Supply," Symposium on Engineering Problems of Fusion Research, Los Alamos, N.M., April 8-11, 1969, Paper DI-10, LA-4250.
7. R. A. Damerow, J. C. Crawford, D. B. Thomson, R. S. Caird, K. J. Ewing, W. B. Garn and C. M. Fowler, "Use of Explosive Generators to Power the θ-Pinch," Symposium on Engineering Problems of Fusion Research, Los Alamos, N.M., April 8-11, 1969, Paper DI-9, LA-4250.

Appendix - Description of Diagnostics

This section gives a description of the diagnostic techniques utilized in the Birdseed experiment, and is applicable in detail to the most recent experiment, Birdseed XII. Table I gives information on the quantities measured in earlier experiments. Figure 65 (supplementing Fig. 59), is an end view of the tank looking toward the gun muzzle. Figures 66 and 67 show the optical paths from windows A and B, respectively, to the bunker, and the equipment contained therein. Table III is a tabulation of the optical path lengths for all of the optical diagnostics; it also gives pertinent film and exposure data.

Located at window A are: (1) a 1-m focal length open shutter camera, (2) an Imacon framing camera making a 2-μsec exposure every 10 μsec, (3) a continuous writing Mod-100 streak camera which views an on-axis region extending to

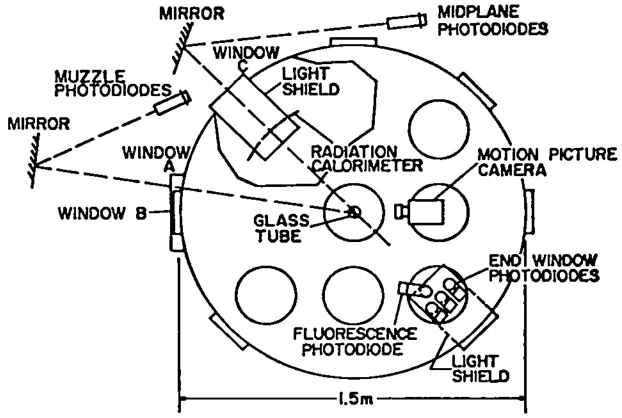

Fig. 65. Layout of diagnostics, and view of tank looking toward muzzle.

Table III. Optical Data

	Distance from Tank Center to:	Other Distances	Film	Exposure Data f-number	ND Filter
WINDOW A					
1-meter camera	Input lens-6m		Super XX	f/302	ND 0.3
Imacon framing camera	Input lens-6.7m		Royal X Pan	f/16	ND 0.3
Mod-100 streak camera	Lens A-6.65m	Lens A to Slit-0.85m	2484	f/19 to f/22	ND 0
Streak Spectrograph	Lens B-7.34m	Lens B to Lens C-0.27m; Lens C to Slit-0.32m	Royal X Pan	--	ND 0.3
Muzzle Photodiodes	Input Lens-2.16m				
WINDOW B					
Auroral Spectrograph	Slit - 5.56m		103a-F	f/8	ND 1.0
TRW Streak Camera	Input Lens-6.17m		Royal X Pan	f/22	ND 1.0
Mid Plane photodiodes	Input Lens-1.95m				
QUARTZ WINDOW					
Hilger 1-meter quartz spectrograph		Bright plasma region to slit-1.14m	103a-F	f/15	ND-step wedge
END WINDOW					
End window photodiodes		Bright plasma region to input lens-2.74m			
Fluorescence photodiode		Darkened copper sheet to input lens-0.61m			
SIDE WINDOW					
Wide angle camera	Input lens-0.89m		Panatomic	f/32	ND 1.6

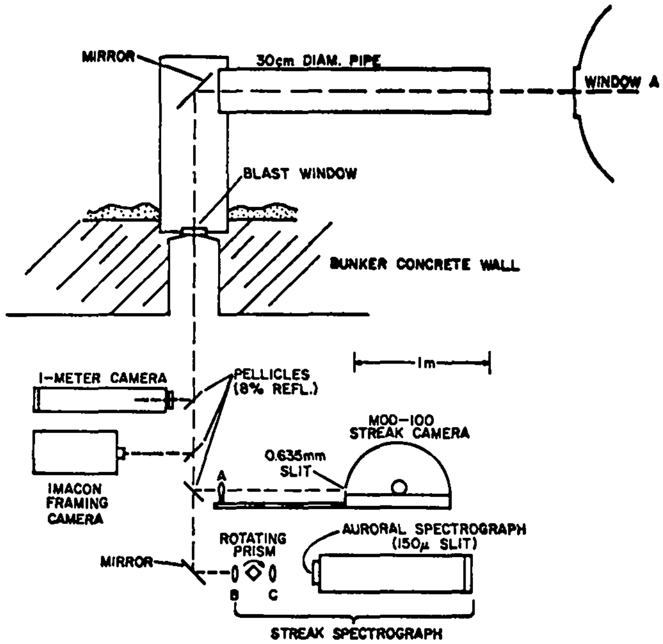

Fig. 66. Optical path from window A to bunker, and equipment.

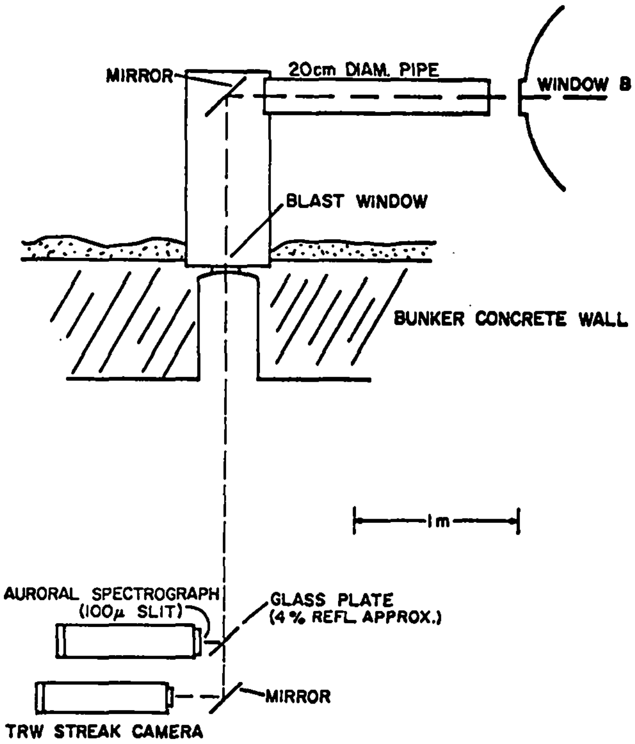

Fig. 67. Optical path from window B to bunker, and equipment.

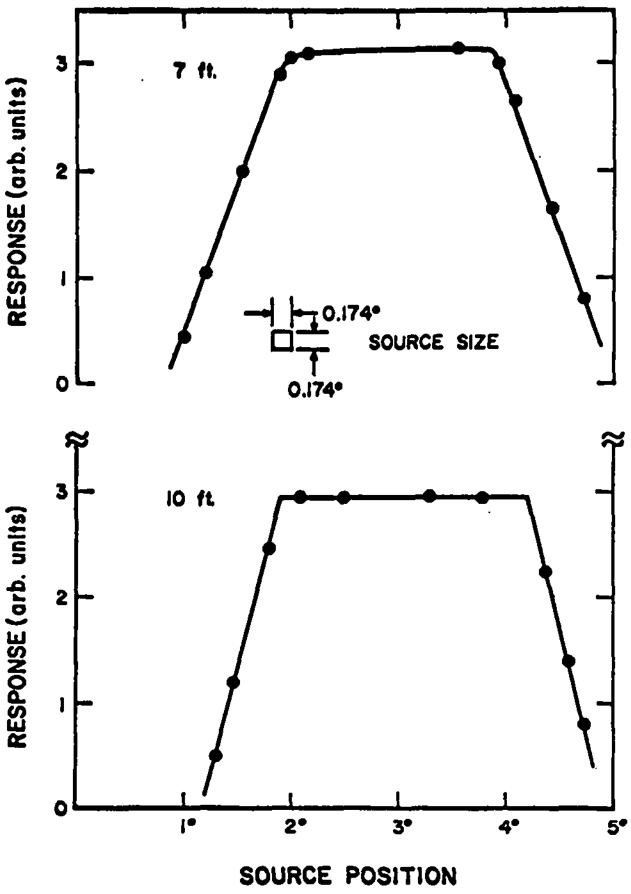

Fig. 68. Field of view of tricolor photometers.

30 cm in front of the gun muzzle and with a diameter of 0.5 cm, and (4) a time-resolving streak spectrograph consisting of an open shutter auroral spectrograph with a rotating prism at its input.

At window B is located an open shutter auroral spectrograph and a TRW image converter camera with a 10-μsec duration streak. Pellicle (8% reflection) or glass plate (4% reflection) beam splitters are used to divide the beam among the diagnostics.

Three tri-color photometers view the plasma from windows A and C and an end-window in the tank. Each photometer consists of a set of three SGD-444 silicon photodiodes in a double lens mounting designed to give a 2° field-of-view for an object at infinity. The lens system has not been modified for objects at finite distances, but the field-of-view has been measured with a small light source, 0.28 cm square, for object distances of seven and ten feet. The results are shown in Fig. 68.

Table IV. Photodiode Calibration

Mean Range (Å)	Bandwidth (Å)	Sensitivity (Measured) $\frac{\text{volts-cm}^2}{\text{watts}}$		Sensitivity (Nominal) $\frac{\text{volts-cm}^2}{\text{watts}}$
		Muzzle	End Window	
4075-4590	515	0.9	0.847	0.928
5030-5560	530	1.74	1.753	2.68
6150-6960	810	4.23	4.95	4.69

The three photodiodes of each set are fitted, respectively, with red (W-29), green (W-61), and blue (W-47B) Wratten color separation filters. A 6-mm thickness of KG-3 heat absorbing glass is used with each photodiode to block the infrared. To prevent saturation, the muzzle and end-window photodiodes have ND 1.4 filters.

The sensitivities of the photodiodes have been measured using a standard tungsten-filament lamp. The $1/r^2$ law is obeyed by the detectors at distances of seven, ten, and fifteen feet, and the calibrating source illuminated about thirty percent of the photocathode area. The calibration factors are presented in Table IV, and for comparison are shown a set of factors calculated from nominal photodiode data supplied by the manufacturer. The output voltage of the photodiodes is measured across a 50-Ω load resistor. The wavelength sensitivity of each photodiode is assumed constant over the mean wavelength range specified in the table. Thus, the sensitivity is a measure of the total power per cm² incident on the input lens of the photodiode in the specified wavelength range.

The muzzle photodiodes are located about seven feet from the center line of the tank and measure emission from a region about three inches in diameter centered about five inches from the end of the muzzle. Thus they sample the center of the brightest plasma region as shown in Fig. 59. The field-of-view of the end window photodiodes encompasses the entire bright region. The line-of-sight of these photodiodes forms an angle of 10° with the tank axis. The mid-plane photodiodes view a region approximately three inches in diameter centered 45 inches from the gun muzzle. A light shield at window C shades the window from direct illumination from the bright region. An identical shield is located at the window diametrically opposed to window C. Also located at the end window is a photodiode that does not view the plasma light directly but which detects light scattering and fluorescence from the end window itself.

A Hilger quartz spectrograph having a 10-μ slit is located immediately outside the tank and views the bright plasma region through a quartz window which transmit ultraviolet radiation down to a wavelength of 2100 Å.

Two vacuum photoelectric ultraviolet detectors with a wide acceptance angle which includes the bright plasma region are located at a midplane window. One detector is sensitive to all wavelengths below 1500 Å and the other, with a lithium fluoride filter, is sensitive to the 1050 to 1500 Å wavelength region only.

Two calorimeters are located within the vacuum tank. One of these is located 0.5 m to the side of the bright plasma region and detects primarily radiated energy from this region since the plasma leaves the gun muzzle with a forward-directed momentum component. This calorimeter is cooled by a 1-liter/min flow of water. A thermistor monitors the outlet water temperature which, combined with the flow rate, yields the total energy deposited in the calorimeter. The second calorimeter is a copper can, 38 cm diameter by 122 cm long, positioned to receive all of the plasma jet contained in a solid angle of 0.06 steradians. The calorimeter is formed of three cylindrical segments each 40 cm long, and an end plate, all thermally insulated from one another. Ten thermocouples monitor the temperature of the parts of the calorimeter. In addition the calorimeter is suspended by pendulum supports to allow free recoil of the calorimeter from the jet momentum. A motion picture camera records the motion of a flag attached to the back end of the tank. The pendulum supports are 70-cm long; the total calorimeter mass is 20.73 kg. The measured period of oscillation is 1.5 sec, less than the calculated value for a simple pendulum, 1.68 sec, because of additional restoring force supplied by the thermocouple leads.

A wide angle camera located at a side window 63.5 cm from the gun muzzle produces an open-shutter picture of the plasma jet from the gun muzzle to the mouth of the ballistic pendulum calorimeter.

One current measurement is made with a Rogowski loop which encircles the center conductor of the gun. A 1000:1 resistive voltage divider measures the center conductor voltage. Additional electrical measurements are made to monitor the generator power supply performance. These include various types of current probes which measure input currents to both generators and the output current both before and behind the detonator switch as well as voltage dividers to monitor the gun breech voltage.

QUADRUPOLE INJECTION EXPERIMENT

(J.E.Hammel, A.R.Sherwood, R.W.Kewish (P-16))

Our efforts this year on the Quadrupole Injection Experiment concerned mainly the fabrication and assembly of the apparatus. This phase has been completed and the machine is now ready for a plasma. There are, however, still a couple of assembly steps that might be done should the experiments indicate they would be advantageous. For example, we have all the parts for the exploding foil crowbar switches, but at present only the old ignitron crowbar switches are in use. Also the quadrupole coils have been installed without an electrostatic shield to protect the plasma from the ohmic electric fields of the coil.

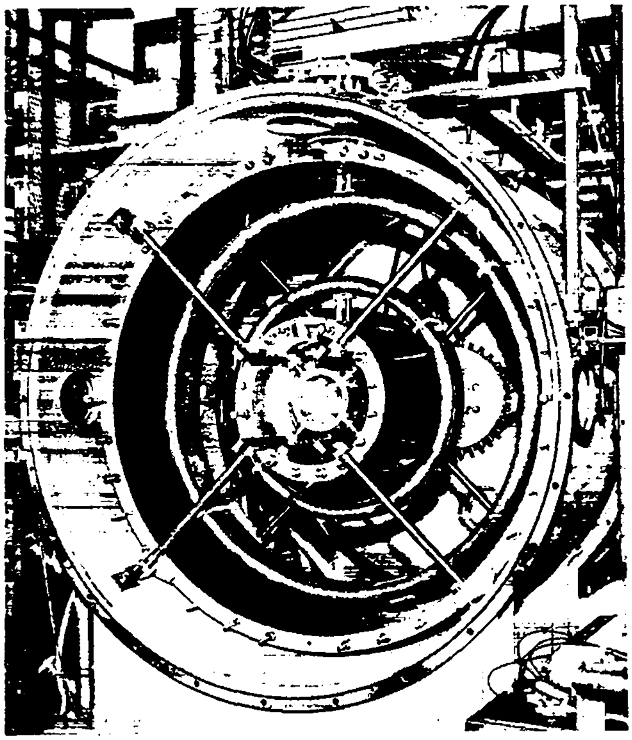

Fig. 69. Quadrupole injection apparatus near end of assembly procedure.

Figure 69 shows the apparatus near the end of the assembly procedure. The end of the vacuum tank is removed, of course, and the photograph was taken before the baffle rings were installed. (The baffle rings are parasitically-driven, field-shaping conductors which are located near the coils and tend to block them from view.) Starting from the outside, the various circular and cylindrical structures that one sees in the photograph are as follows: the vacuum tank, the outer liner, the outer quadrupole coil, the inner quadrupole coil, the inner liner, and finally a cylinder associated with the coaxial current feed to the inner coil. The diameter of the vacuum tank is about seven feet. The radial members (four in front and four in the rear) are the spokes which support the inner liner and the inner coil from the outer liner. They are located well outside of the plasma region. The inner coil is fed from the rear and the outer coil is fed in parallel with it from the top. The magnetically guarded dipole current feeds by which the currents are led through the plasma volume to the coils can be seen just above the top of the outer coil and just below the top of the inner coil. The obvious port in the vacuum tank at the left is a pumping port.

Lengthy, frustrating delays were experienced during the construction of the experiment because of fabrication problems with each of the quadrupole coils. Both of these coils have two turns and are made of aluminum. There is a very critical region where the crossover between the two turns of the coil is located which is also where the coil current feeds are located. Because of strength problems in the crossover region, it was necessary to use a special high-strength aluminum alloy (7039-T64) for the inner coil. The outer coil arrived first but was considerably delayed from its expected delivery date because (among other things) the vendor ran into difficulties during the heat-treatment process. When it did arrive it was unsatisfactory because it did not meet our stated tolerance requirements in the critical crossover region. As we received it, there was not enough space for the necessary electrical insulation in this region. After further negotiations with the vendor the coil was reworked under our supervision in the main LASL shop.

Meanwhile the same vendor had been unable to demonstrate his ability to make high-strength welds in the special aluminum alloy to be used for the inner coil. Eventually, on the basis of the various weld samples submitted by the vendor, we concluded that he was not qualified to make these welds. The Kaiser Aluminum Company agreed to do the welding and heat-treatment for us in their metallurgical lab. The weld samples supplied to us by Kaiser that had been done at the same time the coil was welded and that underwent the same heat-treatment as the coil proved to be satisfactory. Because the outer coil had been unsatisfactory, the machining of the inner coil by the vendor was done under much closer supervision than for the outer coil and the crossover region turned out to be acceptable (but not perfect). However, after the final machining of the inner coil somehow one turn of the two-turn coil became sprung into an elliptical shape rather than being circular. This necessitated considerable further effort on our part to reshape it back to within tolerance.

Each coil is enclosed in a 0.010-in. split copper shroud, the purpose of which is to smooth out magnetic field perturbations arising from the two-turn structure of the coil and to enclose the epoxy-fiberglass coil insulation. The necessary insulation between the two turns of the coil and between the coil and the shroud was provided by filling the space with fiberglass and epoxy. Thus the epoxy insulator itself became the means for attaching the shroud to the coil and the shroud became the vessel for the epoxy pour. To insure complete penetration of the epoxy throughout the insulator region, this pour was done under vacuum conditions. The large size of the outer coil necessitated doing this vacuum potting in the same vacuum tank as is used in the experiment. Thus the coil delays held up even the first assembly steps because the vacuum tank was needed for the coil potting.

Our first attempt at the potting of the outer coil (following the potting procedure employed successfully some time ago on the small prototype coil) failed because during the actual pour large leaks developed along the joints between the shroud and its micalex insulators at the splits in the shroud. In effect, the vessel that was to hold the epoxy had ruptured. We had to remove the shroud and the fiberglass wrap, disassemble the coil, and clean off the (uncured) epoxy in order to save the coil. Several improvements were made in our technique, and the second pour was successful. The inner coil was potted with the improved technique without incident.

We were concerned about possible unbalance forces on the coils due to their not being in exact equilibrium position. These forces could arise from the fact that the conductors are not really uniform (e.g., the outer liner isn't actually round in cross section, or even cylindrical, the coil shrouds are not exactly round, etc.) so that a first guess at the equilibrium positions might not be quite correct. The coils are supported at only one place each by the potted-in dipole elements; we wanted to avoid mechanical failure of these somewhat weak supports at all costs. Therefore the capacitor bank was temporarily connected to the coils and the coils were instrumented with light beams to detect possible pendulum-type motions or twisting motions. In addition, piezoelectric probes were placed at various places on the surfaces of the coils and the liners and especially on the dipole feed elements in order to detect motions at these various places.

Using these detectors we measured small displacements of the coils when they were pulsed, and we adjusted the coil positions to minimize these observed displacements. We tested the coils at 4 kV on six shelves of the capacitor bank, which put a current of about 270 kA through the inner coil. This is just less than one-half of design current and so about one-fourth of the maximum expected forces. (It is not anticipated, however, that we will run at full design current in the first plasma experiments.) At this current level with the coils in their final position we observed a pendulum-type oscillation of the outer coil towards the baffle rings with an amplitude of less than $\frac{1}{4}$ mm. The inner coil motions were even smaller. The piezoelectric probes gave impulses comparable to a light tap from a plastic-handled screwdriver. The largest signals were from the probes attached to the dipole feed elements.

By the end of the period the final assembly of the apparatus had just been completed.

ENGINEERING
(Group P-16

SCYLLAC ENGINEERING

(E. L. Kemp)

The design of the Scyllac system is complete. The new Scyllac building is essentially complete and will be occupied in January 1970. The design of the energy system and the experiment has proceeded in three phases: component development, system development, and system design. Component development, which included the capacitor, the coax cable, the spark gap and the cable cartridge, was done by G. P. Boicourt, D. L. Call, K. W. Hanks, and R. F. Gribble.

The major energy storage component is a 60-kV, 1.85-μF capacitor. This development which was a joint effort between LASL and the U.S. capacitor industry and was led by Boicourt. The capacitor shown in Fig. 70 is 11 in. x 14 in. x 25 in. high with a low-inductance header that was designed to match the Scyllac spark gap. The capacitor uses tissue paper and aluminum foil and is impregnated with castor oil. The life of this unit is over 50,000 shots ringing with 85% reversal. This is completely adequate in the actual crowbarred Scyllac application. Over 3500 of these capacitors will be installed in the system.

Scyllac will use over 500,000 feet of low-inductance, coaxial cable. This cable development was a joint effort between LASL and the U.S. cable industry and was also led by Boicourt. The cable shown in Fig. 71 has a foamed polyethylene center, an inner and outer conductor of braided copper, and extruded polyethylene insulation with extruded conductive plastic screens to protect the insulation from sharp points on the braids. This cable has an inductance of 45 nH per foot and a resistance of 1.1 mΩ per foot. It operates satisfactorily in an unterminated 60-kV pulsed system.

The Scyllac spark gap combines the start gap and the crowbar gap into one low-inductance

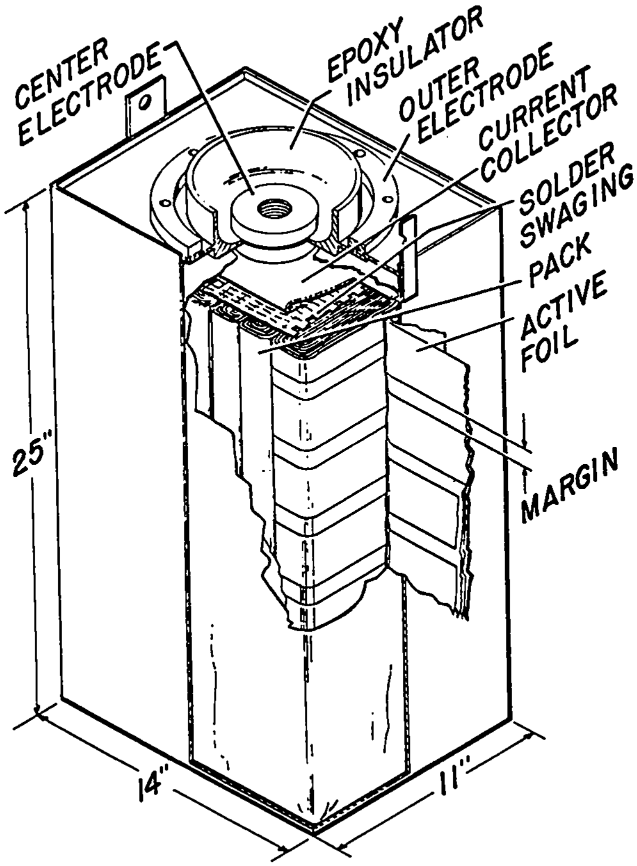

Fig. 70. Scyllac capacitor.

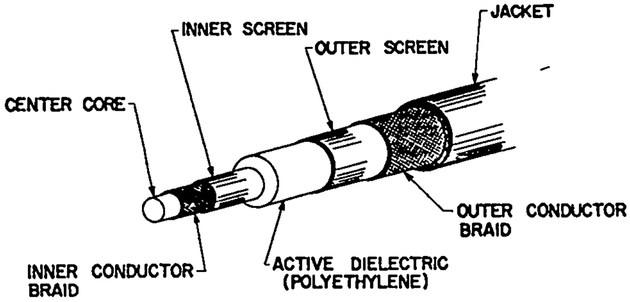

Fig. 71. Scyllac low-inductance coaxial cable.

geometry. It was developed by Gribble and Call and is described in another part of this report.

The coaxial cables from each spark gap are connected to the collector plate by a low-inductance cartridge. Four cartridges were developed by Hanks and Boicourt. Figure 72 shows the top surface model. The cable center conductors are terminated with male plugs, and the outer conductors are terminated with plug-in connectors.

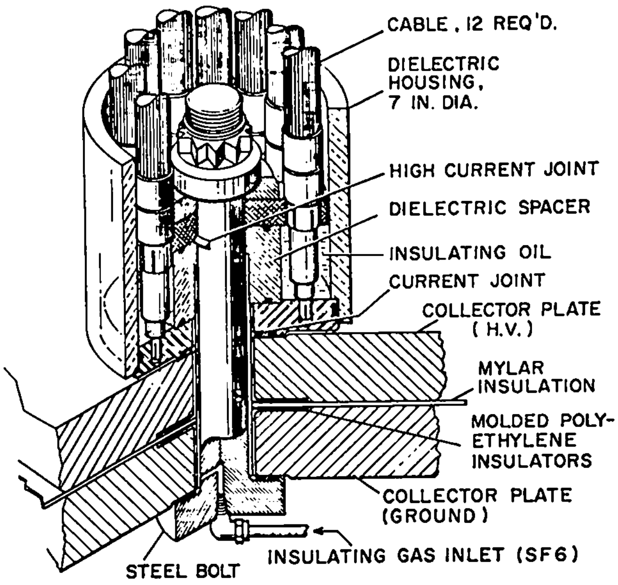

Fig. 72. Top-surface model of connector cartridge.

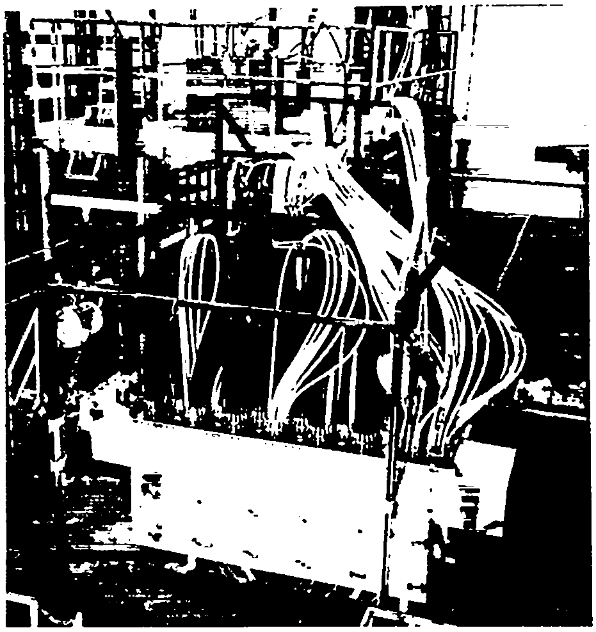

Fig. 73. Prototype Scyllac energy storage and transfer system.

The cable terminations are immersed in insulating oil and the insulation cavity between the plates is flooded with SF_6 at 80 psi. The steel bolt, 1.5-in. diameter, is prestressed to contain the magnetic forces between the plates. The inductance of this cartridge assembly is 22 nH and it carries 120 kA reliably without sparking. One other top mounting cartridge and two inverted cartridges were also developed.

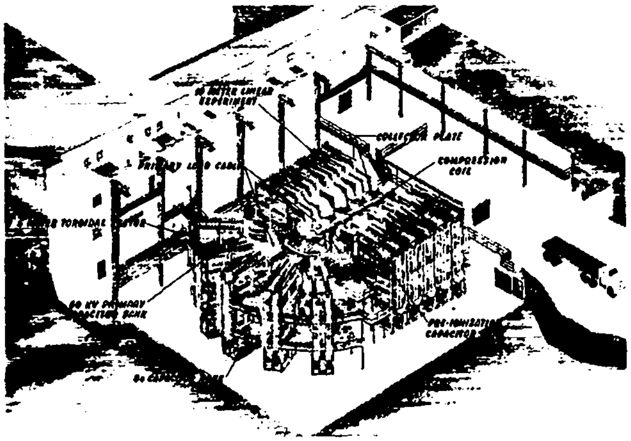

Fig. 74. Initial layout of Scyllac system.

The first phase in the development of a component consisted of designing it, building it, and testing one or more models to destruction or until it operated satisfactorily. The second phase of the development was to install a significant number of the components in a prototype Scyllac system. The prototype system, shown in Fig. 73, was designed and operated by C. F. Hammer and later by H. W. Harris. It consisted entirely of Scyllac developmental components and circuits. It contained 72 capacitors and spark gaps, 10,000 feet of coaxial cable, the Scyllac charge system and trigger system, and other miscellaneous components and circuits. The prototype system evaluation usually showed some modest design deficiencies and in one case a cartridge had to be redesigned and reevaluated before it could be reinstalled in the prototype. All components were certified in the prototype before the design was released for Scyllac procurement.

The Scyllac design team, under W. A. Bradley, consisted of J. D. Allen, J. J. Banta, and R. A. Haarman. Because of the developmental nature of the hardware the design changed several times before it was completed. Figure 74 shows the layout of the system as it will be installed initially. The 5-m toroidal sector will be installed first and will be put into operation during 1970. The 10-m linear hardware will also be installed but will not become operational until late in 1971. The 10-m hardware will ultimately be moved to turn the 5-m sector into a 15-m toroidal system. All the hardware for the 5-m sector and much of the 10-m equipment has been ordered and received. The remainder of the 10-m system will be ordered as soon as the final funds are released.

Component reliability is expected to be the major problem in the operation of Scyllac. Every capacitor, spark gap and cable in the system is being pretested to minimize the early failure problem. This preinstallation testing is being led by J. A. Meissner and J. D. Wing. All capacitors are tested to 1500 shots in a ringing application after which a Scyllac spark gap is attached. The gap and capacitor are then operated about 200 shots during which the jitter of the gap is monitored to determine when it becomes acceptable for the system. Every cable is pulsed for 10,000 shots in a voltage-enhancing application.

The design of Scyllac is almost identical to the 50-kV Scylla IV system except that Scyllac will operate at 60 kV. Many of the Scyllac designs such as the trigger system and the spark gap crowbar system have been incorporated into Scylla IV. The evaluation of these new designs by W. E. Quinn, E. M. Little, and R. F. Gribble in an operating theta-pinch system has been invaluable in identifying deficiencies and suggesting design corrections.

PLASMA PHYSICS

(Group P-13)

SUMMARY OF FUNDAMENTAL PLASMA GROUP ACTIVITIES

(H. Dreicer)

After an initial period devoted to the development of the necessary equipment, the Fundamental Plasma Group now is actively involved in two main experimental programs to study plasma phenomena on well-understood plasma columns.

In line with our earlier contention that resonant charge exchange can represent an important cross-field diffusion mechanism, we have proceeded in the alkali Q-machine with the measurement of the charge exchange cross section. This work utilizes an unusual radioactive tracer technique, new to plasma physics, which has yielded interesting cross section results.

Our use of resonant charge exchange as a means of converting radioactive atoms to radioactive ions inside of a plasma suggests the possibility of doing autoradiography on these test ions. A proposal for such an experiment is contained in this report.

During the past year measurements were obtained on the angular distribution of atoms emitted by an atomic beam nozzle. This study is important in connection with the programmed injection of neutrals into our Q-machine. We expect to complete the acquisition of these data on a representative set of nozzles during the early part of the coming year.

Experiments continued on our second experimental plasma device in which a collisionless plasma column is produced by the application of a modest amount of microwave power close to cyclotron resonance. Studies made with Langmuir probes and a diamagnetic pickup coil indicate that reasonable agreement exists among the measured plasma density, average electron energy, absorbed microwave power, and neutral gas density, as is required by the conservation laws for steady state operation.

The task of improving our dc magnet power supplies was carried out steadily throughout the past year, but it is now about one year behind schedule because of various engineering problems that were encountered, and a severe lack of manpower. Nevertheless important modifications have been made that already permit us to make much better use of our magnets. We hope that our original goals will be achieved during 1970.

D. Ignat joined the group on a postdoctoral appointment during the past summer, and is working on the design of an electron beam injector which we hope to use for synchrotron radiation plasma studies. Messrs. N. Gardner and A. Mondragon have provided expert assistance in all phases of the group's experimental activities.

Measurement of the Resonant Charge Exchange Cross Section in a Potassium Q-Machine Plasma Column (H. Dreicer, D. B. Henderson, D. Mosher, F. E. Wittman, and K. Wolfsberg (J-11))

When the charge exchange reaction of an ion in its parent gas occurs in a magnetic field, it contributes to the ion cross-field diffusion because the initial and final ions do not possess the same center of gyration. The cross section for this process is expected to become large with decreasing energy; this is borne out by data available for potassium and cesium down to about 6 eV. No measurements exist at lower energies, but an estimate based upon extrapolation of high energy data to Q-machine energies yields values clustered about the average value $\sigma = 2 \times 10^{-13}$ cm^2 for cesium.[1] This large cross section, when combined with the very large mean square diffusion step across the magnetic field ($M/m = 2.4 \times 10^5$ times larger than for electron-ion encounters), produces an important cross-field diffusion flux which can exceed that due to electron-ion encounters. We have investigated the role played by this loss mechanism and have found it to place more severe restrictions on the vacuum tank wall temperature for cesium Q-machines than are generally satisfied. Analysis[1] of Q-machine diffusion and ion loss measurements[2] show that it is necessary to include charge exchange diffusion losses to account for the results reported there.

Principle of the Experiment

To measure the charge exchange cross section we intersect a relatively cold (630°K) atomic potassium beam with a potassium plasma column produced by contact ionization on a 2500°K hot plate. A uniform static magnetic field oriented perpendicular to the hot plate guides the plasma to a cold collector (denoted as No. 2 on Fig. 75), and confines the plasma in the cross-field direction. Of the potassium atoms which traverse the plasma, a small fraction will charge-exchange or collide elastically with potassium ions. In the first instance, the newly formed colder ion must gyrate around magnetic field lines and be eventually condensed on collector 2. Those newly formed ions which move unimpeded by ion-ion encounters towards the hot plate after charge exchange make one reflection on the electrostatic sheath in front of it and are also condensed on this collector. In the second instance, there is no charge exchange involved, and the atom is simply deflected out of the atomic beam. Whether or not it reaches collector 2 is now determined by the differential cross section for elastic scattering, $\sigma_e(\theta)$, and the solid angle subtended by this collector at the interaction volume. The total cross section can be measured if the atoms originally in the neutral beam are tagged and their relative number subsequently condensed on collectors 1 and 2 is determined. A suitable tagging technique utilizes radioactive potassium tracer in the atomic beam and nonradioactive potassium atoms in the formation of the plasma.

The radioactivities R_1 and R_2 due to the condensed tracer atoms on collectors 1 and 2 are related to the current I_o of radioactive atoms which enter the plasma column and the current I_x of radioactive charge-exchange ions which reach collector 2:

$$\frac{R_2}{R_1} = \frac{\int I_x dt}{\int I_o dt} .$$

The ratio of these two currents is related to the cross section by

$$\frac{I_x}{I_o} = \frac{\langle \sigma_x v_{rel} \rangle}{\langle v_{atom} \rangle} \int n(x)dx,$$

provided $I_x \ll I_o$. It follows that

$$\frac{R_2}{R_1} = \frac{\langle \sigma_x v_{rel} \rangle}{\langle v_{atom} \rangle} \int n(x)\,dx,$$

provided that the velocity distributions of the ions and atoms as well as their densities remain constant during the collection time.

In these equations, v_{rel} is the relative speed $|v_{ion} - v_{atom}|$ between ions and atoms, and $\langle\rangle$ denotes the appropriate average over ion and atomic beam velocity distributions. The quantity $\int n(x)dx$ is the integral of the ion density along the undisturbed atomic beam path, and I_o is the current of radioactive atoms which enters the plasma column. The corresponding current, I_e, of elastically scattered radioactive atoms which reach collector 2, given by

$$I_e = I_o \int_{\Omega} \frac{\langle \sigma_e(\theta)\, v_{rel} \rangle}{\langle v_{atom} \rangle} d\Omega \int n(x)dx ,$$

is expected to be much smaller than I_x since $\int \frac{d\Omega}{4\pi} \approx 7 \times 10^{-4}$ and $\theta \approx \pi/2$. In any case, I_x and I_e can be separated experimentally by altering the angle subtended by collectors 1 and 2 at the interaction volume and by altering the total solid angle Ω subtended by collector 2.

The effect of ion-ion encounters when the mean free path for this process, ℓ_{ii}, is less than the distance L between the radioactive atomic beam and collector 2 or the hot plate is not expected to

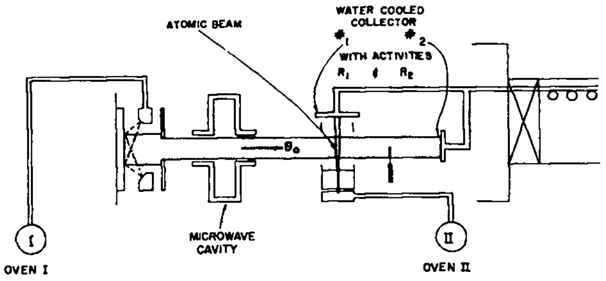

Fig. 75. Schematic of experimental setup.

be serious for several reasons. First of all, ion-ion encounters do not result in simple radial diffusion, and electron-ion encounters are not very effective, because the ions produced at the hot plate are condensed on collector 2 before a significant radial diffusion can occur. Secondly, the effect of rapid ion-ion encounters is to entrain the radioactive ions in the ion distribution which drifts from the hot plate to collector 2. In the intermediate range, where $\ell_{ii} \approx L$, it appears possible for some radioactive ions to change their direction of motion and gain sufficient energy from a single or several encounters to surmount the repelling sheath at the hot plate. Subsequently, these would undergo recombination on the hot surface. Although a fraction of these is again contact-ionized, most of the rest will not be condensed on collector 2. To avoid this problem, it is necessary to study the variation in the branching ratio R_2/R_1 with plasma density. It is also instructive to study the effect of inclining the radioactive atomic beam with respect to the applied magnetic field so that the newly formed radioactive ions all start their motion either towards or away from collector 1.

Experimental Arrangement

A 2.5-cm-diam, 155-cm-long potassium plasma column is produced by single-ended operation of a standard Q-machine as shown in Fig. 75. The plasma, contact-ionized at the hot plate and defined by a 2.5-cm-diam limiter, is accelerated toward the 5-7.5-cm-diam water-cooled collector 2 by the electrostatic sheath in front of the hot plate. The strength of that sheath is a function of the hot plate temperature and of the neutral flux. Plasma particles condensed on collector 2 are replenished from a multi-hole atomic beam nozzle which is fed from an oven located outside of the vacuum chamber. Commercially available potassium, which contains the naturally occurring mixture of its isotopes (93% ^{39}K; 7/ ^{41}K), serves as the source material for the plasma.

Ion density is monitored by a 2 GHz microwave resonator system. A motor-driven Langmuir probe operated in the ion saturation current region and movable in a plane perpendicular to the plasma column is used to measure the density profile.

From this information, the measured hot plate temperature, and the current-voltage characteristic obtained with collector 2, we infer the ion temperature and drift speed. Figure 75 shows a schematic view of the microwave resonator. It is provided with circular holes in its end plates through which plasma flows. With these holes protected against microwave leakage by cylindrical waveguides operated below cut-off, the resonator retains a loaded Q of about 20,000 in the TM_{010}-like mode without plasma in the resonator. A self-tuning oscillator technique[3] is used for monitoring the cavity's resonant frequency continuously. This information is then related to the average electron density by means of a modified perturbation formula.[4] An analysis of the self-tuning technique is given elsewhere in this report.

The cross-beam oven is charged with 500 mg of natural potassium which is first irradiated in the Los Alamos Omega West Reactor.[5] Through the $^{41}K(n,\gamma)^{42}K$ reaction, about 0.5 millicurie ($\approx 10^{12}$ atoms) of the 12.4-hour half life isotope ^{42}K is produced. The activity of the ^{40}K is completely negligible. Of the total oven charge, only 0.1% leaves the cross-beam nozzle to traverse the plasma. The remainder is collected on water cooled beam-defining diaphragms. Most of this beam is undeflected and is condensed on the water cooled collector 1. A small fraction charge-exchanges and is eventually condensed on collector 2. Both collectors are rigidly mounted on a trolley which can be withdrawn into a second vacuum chamber separated from the main vacuum chamber by a gate valve. This arrangement allows removal and replacement of these collectors without raising the gas pressure in the main vacuum chamber which operates at a background pressure of 1-6 x 10^{-6} Torr as read at the ion pump when the machine is in operation.

The condensed potassium is washed from each collector with water and dilute hydrochloric acid. It is eventually precipitated as $KClO_4$ and mounted in standard geometry for β-counting.[6] The process results in 98.1 ± 0.7% recovery of the ^{42}K. The final uncertainty, which includes counting statistics, is only ± 3% for the branching ratio R_2/R_1.

Experimental Results

Our results to date are based upon five experimental runs, four made with plasma, one without plasma, in order to check for cross-talk between collectors 1 and 2. The total ion flux reaching collector 2 in the plasma runs ranged from 0.5 to 2.0 mA, and was used to deduce the ion drift velocity. In runs made at high magnetic field values ($\approx$ 7500 gauss), the ion flux collected on the down-stream side of the microwave cavity with a movable shutter was 10% larger than the ion flux collected on collector 2. These collection points are 118 cm apart.

The spot size of condensed potassium on the two collectors indicated a 2.5-cm plasma diameter with a reasonably sharp boundary and a cross-beam diameter of about 0.6 cm as expected from design. The branching ratio, R_2/R_1, varied from 0.01 to 0.02. With plasma absent, R_2/R_1 was found to be 10^{-4}, indicating that scattering from diaphragms and background neutrals is not a serious problem. A separate experiment showed that surface migration of radioactive atoms is entirely negligible on cool collectors.

Reduction of Data

The charge exchange cross section, given by

$\sigma_x = (A - B\log v_{rel})^2$, where A & B are constants,

according to quantum theory,[7] changes very little over the range of ion and atom velocities involved in the experiment. For this reason, we replace $<\sigma_x v_{rel}>$ by $\sigma_x < v_{rel}>$. The average relative speed is obtained numerically for an assumed ion velocity distribution and a Maxwellian atomic beam velocity distribution. A separate section of this report is devoted to the subject of the ion velocity distribution. As is indicated there, considerable information about the distribution is obtained from a knowledge of the drift velocity. To evaluate it from the ion flux collected, as well as to evaluate the line integral $\int n(x)dx$ and the relationship between the electron density and the resonator frequency shift, requires a measurement of the plasma density profile. In the first two plasma runs, the movable Langmuir probe was not available for this measurement. Thus, the cross section deduced from these runs on the basis of profile assumptions (although reasonable) will not be described further here. Table I summarizes the conditions of the last two plasma runs for which profiles were measured. The values of σ_x given in this table depend upon the further assumption that the ion drift velocity is independent of radial position in the plasma.

Table I

Run	A	B
Maximum density from microwaves - cm^{-3}	6.8×10^9	6.9×10^9
Magnetic field-gauss	7524	7567
Ion drift velocity-cm/sec	1.10×10^5	1.17×10^5
$<v_{rel}>$ - cm/sec	1.51×10^5	1.68×10^5
$\frac{1}{2}M<v_{rel}>^2$ - eV	0.47	0.57
R_2/R_1	1.23×10^{-2}	1.96×10^{-2}
σ_x-cm^2	3.6×10^{-13}	5.1×10^{-13}

Our tentative cross section values are larger than the values obtained by extrapolating high energy data to the 0.5 eV range. For example, use of the quantum theory result, $\sigma_x = (A - B\log v_{rel})^2$, and the data obtained by Kushnir, Palyukh, and Sena[8] above 6 eV yields a cross section at 0.5 eV which is 6 to 8 times smaller than our measured value. Moreover, our measured values are 15-20 times larger than the value predicted by Rapp and Francis[7] for potassium using a hydrogen-like theory.

Q-Machine Ion Distribution Function (D. B. Henderson, H. Dreicer)

The charge exchange cross section, σ_x, depends implicitly upon the relative collision speed $v_{rel} = |v_{ion} - v_{atom}|$, and explicitly upon the velocity space average of v_{rel}. For this computation, knowledge of the ion velocity distribution F_i is required. We have begun a study of the collisionless

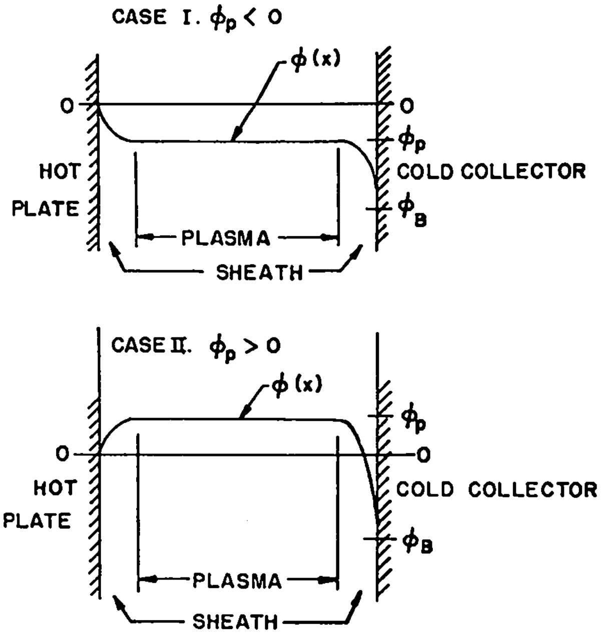

Fig. 76. Potential profiles.

distribution described by the Vlasov equation for linear slab geometry.

We assume the potential to be either monotonic (case I) or to have a single maximum (case II) as shown in Fig. 76. In all cases we take the potential, φ_B, on the cold end plate to be negative, and large compared with kT/e. In case I both the ion and electron distribution function, F_e and F_i, are uniquely determined by the Maxwellian velocity distribution function boundary condition assumed on the hot plate. In this case we find for F_e and F_i inside of the plasma at potential $\varphi < 0$,

$$F_e(v) = \begin{cases} F_{eo} \exp\left(\frac{e\varphi}{kT} - \frac{mv^2}{2kT}\right), & -\sqrt{\frac{2e(\varphi-\varphi_B)}{m}} \le v \le \infty \\ 0, & -\infty \le v < -\sqrt{\frac{2e(\varphi-\varphi_B)}{m}} \end{cases}$$

$$F_i(v) = \begin{cases} F_{io} \exp \frac{-e\varphi}{kT} - \frac{Mv^2}{2kT}, & +\sqrt{\frac{-2e\varphi}{M}} \le v \le \infty \\ 0, & -\infty \le v < +\sqrt{-\frac{2e\varphi}{M}} \end{cases} .$$

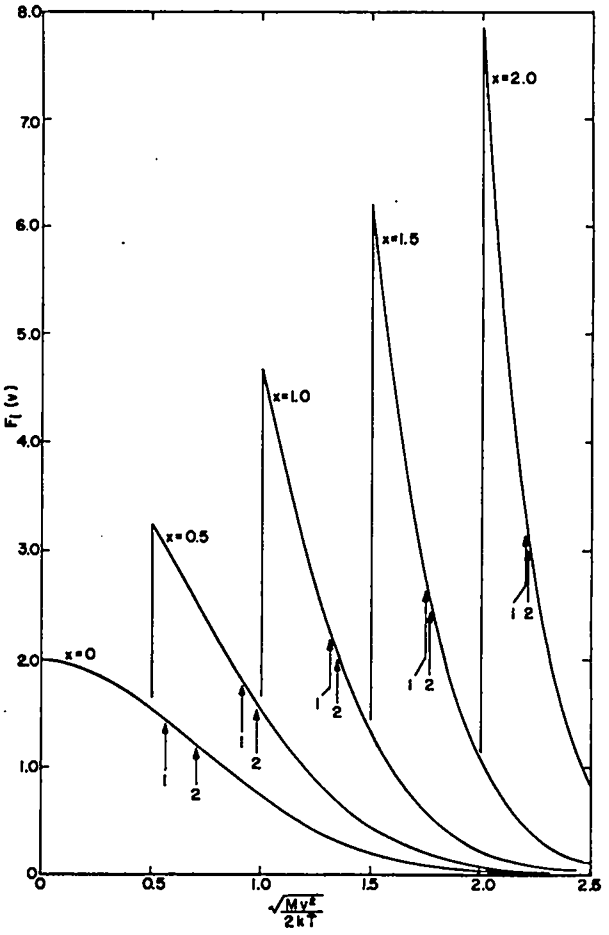

Fig. 77. Ion velocity distribution function as a function of normalized speed with the square root of the normalized potential as parameter.

The normalizations F_{eo} and F_{io} are given by the Richardson current at the hot plate ($\varphi = 0$),

$$F_{eo} = \frac{m}{kT} j_R(T) = \frac{m}{kT} AT^2 e^{-W/kT} ,$$

by the neutralinjected flux S, and by the probability of ionization $\beta(T)$,

$$F_{io} = \frac{M}{kT} \beta(T) S,$$

$$\beta(T) = \left[1 + \exp\left(\frac{E_I - W}{kT}\right)\right]^{-1}$$

where E_I is the atom's ionization potential and W is the work function of the metal. Case 1 corresponds most closely to the sheath conditions under which our alkali Q-machine has been operated. Figure 77 shows the ion distribution for this case as a function of normalized speed with the quantity

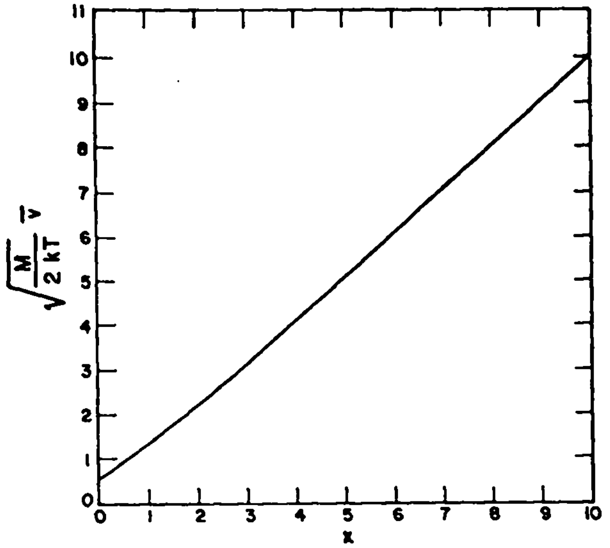

Fig. 78. Normalized drift velocity as a function of the square root of the normalized potential.

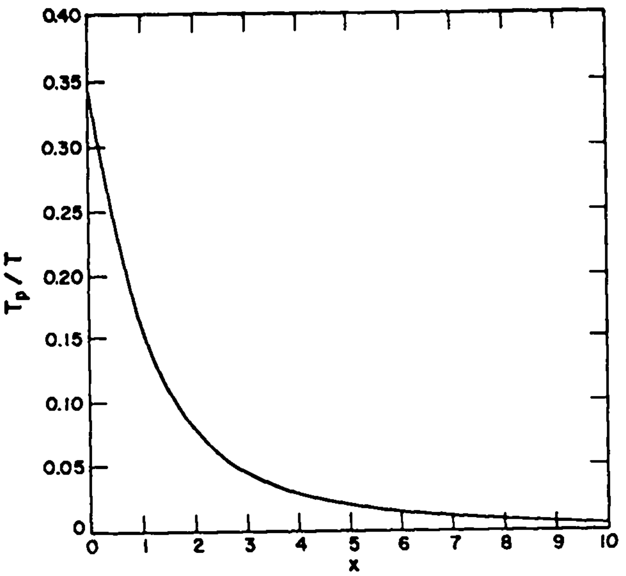

Fig. 79. Normalized thermal spread as a function of the square root of the normalized spread.

$x = \left(\frac{-e\varphi}{kT}\right)^{\frac{1}{2}}$ as a parameter. For each x the vertical arrows marked 1 and 2 denote the location of the normalized ion drift velocity, $\sqrt{\frac{M}{2kT}}\;\bar{v}$, and the normalized root mean square ion velocity, $\sqrt{\frac{M}{2kT}\;\overline{v^2}}$. Figure 78 gives the relation between ion drift velocity $\bar{v}$ and x. A measure of the thermal spread in the ion distribution is obtained from the relation

$$\frac{T_p}{T} = \frac{M}{kT}\left[\overline{v^2} - (\bar{v})^2\right],$$

which is shown in Fig. 79 as a function of x.

For case II ($\varphi > 0$), there may be trapped electrons whose distribution we identify with the subscript t. This trapped distribution is not determined by boundary conditions at the hot or cold plates and can be any function of the energy.

$$F_e(v) = \begin{cases} F_{eo}\exp\left(\frac{e\varphi}{kT} - \frac{mv^2}{2kT}\right), & +\sqrt{2e\varphi/m} \le v \le \infty \\ F_t(e\varphi - mv^2/2), & -\sqrt{2e\varphi/m} < v < +\sqrt{2e\varphi/m} \\ F_{eo}\exp\left(\frac{e\varphi}{kT} - \frac{mv^2}{2kT}\right), & -\sqrt{2e(\varphi-\varphi_B)/m} < v \le -\sqrt{2e\varphi/m} \\ 0 & , -\infty \le v \le -\sqrt{2e(\varphi-\varphi_B)/M} \ . \end{cases}$$

Again by considering the Pichardson current we have

$$F_{eo} = \frac{m}{kT}\, j_R(T) = \frac{m}{kT}\, AT^2 \exp(-W/kT).$$

The Vlasov equation allows the trapped electron distribution to be any function of $(e\varphi - mv^2/2)$; we have taken it to be

$$F_t = \alpha F_{eo} \exp\left(\frac{e\varphi}{kT} - \frac{mv^2}{2kT}\right) ,$$

where $0 \le \alpha \le 1$.

For $\alpha = 1$ the trapped distribution fills in the untrapped distribution so that it becomes a complete Maxwellian.

The ion distribution for Case II has no gap:

$$F_i(v) = \begin{cases} F_{io} \exp\left(\frac{-e\varphi}{kT} - \frac{Mv^2}{2kT}\right) & , 0 \le v \le \infty \\ 0 & , -\infty \le v < 0. \end{cases}$$

The normalization F_{io} is determined by equating the ion current leaving the hot plate with β times the sum of the neutral injection flux and the reflected flux,

$$F_{io} = \frac{M}{kT}\,\beta(T)S\left\{1 - \beta(T)\left(1 - \exp\left(\frac{-e\varphi}{kT}\right)\right)\right\}^{-1} .$$

Integration of these distribution functions over all velocities leads to the following electron and ion densities in the plasma. For case I($\varphi < 0$):

$$n_e = A\sqrt{\pi m/2k}\;T^{\frac{3}{2}}\cdot$$

$$\exp\left(\frac{e\varphi}{kT} - \frac{W}{kT}\right)\left[1 + \mathrm{erf}\left(\sqrt{e(\varphi-\varphi_B)/kT}\right)\right]$$

$$n_i = S\,\beta(T)\sqrt{\pi M/2kT}\cdot$$

$$\exp\left(\frac{-e\varphi}{kT}\right)\left[1 - \mathrm{erf}\left(\sqrt{e(-\varphi)/kT}\right)\right]$$

and for case II ($\varphi > 0$):

$$n_e = A\sqrt{\pi m/2k}\;T^{\frac{3}{2}}\exp\left(\frac{e\varphi}{kT} - \frac{W}{kT}\right)$$

$$\times\left\{1 - 2\,(1-\alpha)\,\mathrm{erf}\left(\sqrt{e(\varphi)/kT}\right) + \mathrm{erf}\left(\sqrt{e(\varphi-\varphi_B)/kT}\right)\right\}$$

$$n_i = S\,\beta(T)\sqrt{\pi M/2kT}$$

$$e^{-e\varphi/kT}\left\{1 - \beta(T)\left[1 - \exp\left(\frac{-e\varphi}{kT}\right)\right]\right\}^{-1} .$$

In either case we may require net neutrality ($n_e = n_i$) and thus determine φ:

$$\varphi = \varphi\,(T,S;\;W,E_I,\varphi_B,\alpha).$$

With φ determined we may solve for the desired integrals of the distribution function such as the plasma density and the net electric current. We remind the reader that of the various parameters, W and E_I are physical constants determined by the material, ($-\varphi_B$) is an applied voltage which is usually effectively infinite, and the parameter α gives the fraction of trapped electrons.

The resulting curves $\varphi(T,S)$ with W for tungsten, E_I for potassium, φ_B = -20V, and α = 0,1 are shown in Fig. 80. The double-valued result for $\varphi < 0$ was previously obtained by Gurevich, Salimov, and Buchel'nikova.[1] To understand why φ may be double valued, consider the point at which $\varphi = 0$. This is just that point at which the density of electrons obtained from the Richardson current and moving with the electron thermal speed, $n_e = j_R(T)/\sqrt{2kT/\pi m}$, precisely equals the density of ions (due to incident neutral flux) moving away with ion thermal speed, $n_i = \beta(T)\,S/\sqrt{2kT/\pi M}$. The parameters S and T are such as to give $n_e = n_i$ with no sheath. But with the same S and T there is another solution for some small $|\varphi|$, $\varphi < 0$. At this φ the electron current is attenuated ($\sim e^{-|\varphi|}$), so the electron density is smaller. The ions are accelerated (at the same current) so the ion density is also smaller ($\sim 1/\sqrt{|\varphi|}$), allowing a second solution. The third solution at small positive

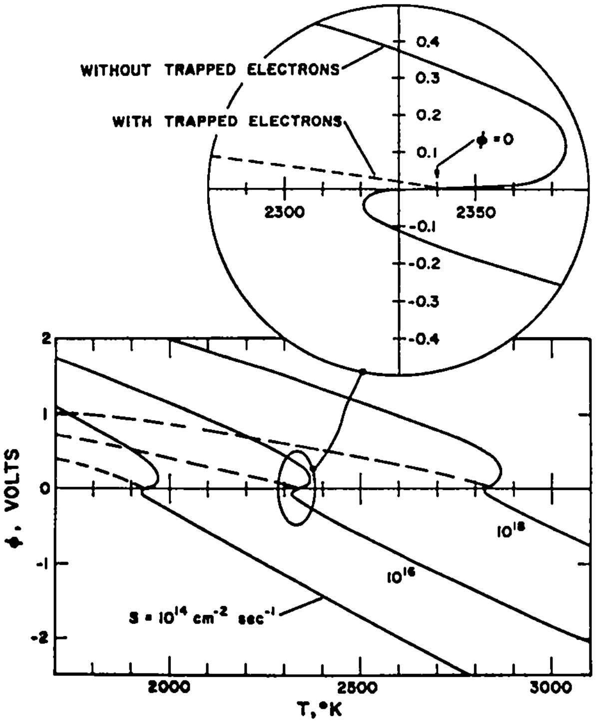

Fig. 80. Plasma potential as a function of hot plate temperature with neutral flux as parameter.

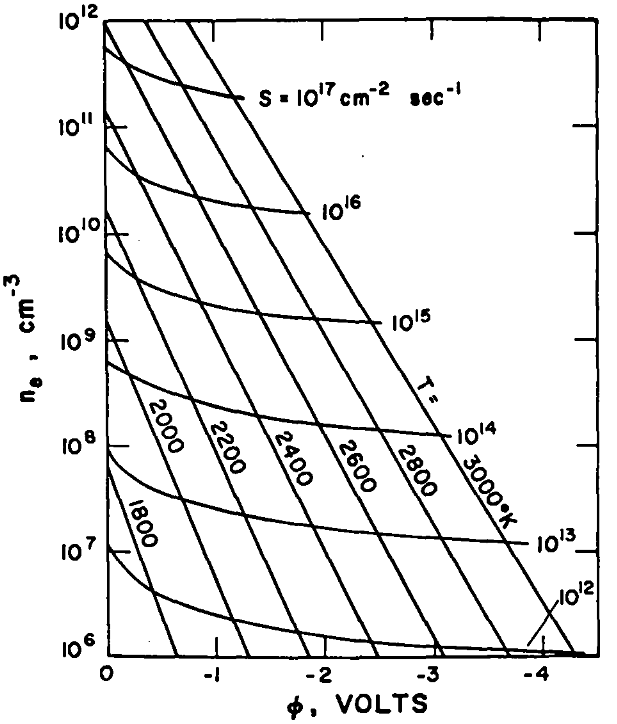

Fig. 81. Electron density as a function of plasma potential with hot plate temperature and neutral flux as parameters.

φ for the $\alpha = 0$ case is analogous. For $\alpha = 1$ there is no drop in density due to acceleration and hence no additional solution.

With $\alpha = 1$, the range of multiply defined $\varphi(T)$ is only comparable to kT/e or less; with $\alpha = 0$, it is several kT/e. One may thus speculate that if the $\alpha = 0$ condition were to prevail the plasma might jump between the different states and show noise. This last possibility is indicated by Gurevich, et al.[1]

A map of possible operating points for $\varphi < 0$ (accelerated ions) is shown in Fig. 81. The computed φ and n_e are plotted against the parameters S and T. One sees that the greatest range in φ with changing T occurs at low fixed S (and low n_e). It is therefore desirable to work at low density in which case the collisionless assumption is justified. Practically speaking one is limited in T by the melting point of tungsten and in n_e by the limiting sensitivity of density measurement. Different hot plate materials offer lower work functions but also lower temperature limits. Thus the available range of $|\varphi|$ is not greatly different than it is for tungsten.

Reference

1. Gurevich, Salimov, and Buchel'nikova, Preprint 208, Institute of Nuclear Physics, Novosibirsk, 1968. No published reference available.

Analysis of the Self-Tuning Oscillator Method for Measuring Electron Density (H. Dreicer and J. McLeod)

Following a technique used by R. B. Hall[1], we have constructed a self-tuning oscillator system for measuring electron density in the potassium Q-machine. It consists of a broadband microwave traveling wave tube amplifier (TWT) arranged in series with an open ended TM_{010} microwave cavity which resonates at 2 GHz. The latter has a transmission loss of about 25 db and a loaded Q of about 20,000 in the absence of plasma. A self-tuning oscillator is constructed from these components by connecting the resonator output to the TWT input, and the TWT output to the resonator input. Such a system will be unstable to oscillations at the frequency f_n provided the net phase shift around the loop at this frequency is $2\pi n$ (n = integer), and the net gain of the system exceeds unity. We have tested this system in the following way: with the resonator by-passed, a spectrum analysis of the closed loop oscillations shows a large number of sharp signals (corresponding to various n) within the bandpass of the TWT. The integer n corresponding to f_n is now easily determined from the phase shift around the loop measured without the cavity. This phase shift, denoted by ϕ_p, is given by

$$\phi_p = -\frac{2\pi f_n L}{c} - 2\pi f_n T = -2\pi n,$$

and the integer n can be determined from

$$\Delta f_n \left(\frac{L}{c} + T\right) = \Delta n$$

by measuring f_n and Δf_n for $\Delta n = 1$. Here L represents the length of the transmission line (≈ 110 feet in our setup) and T is the equivalent transit time for the microwave radiation in passing

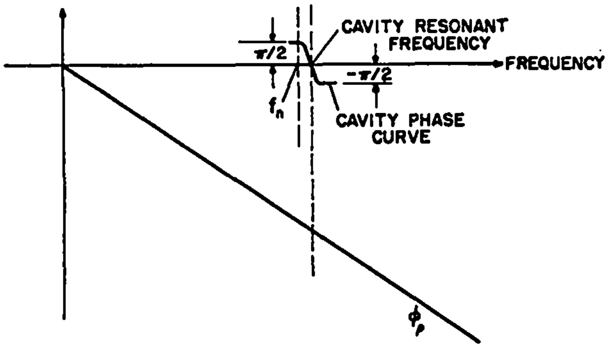

Fig. 82. Phase vs frequency.

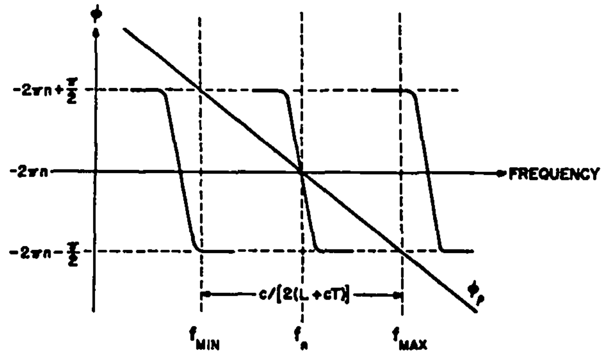

Fig. 83. Magnification of the phase vs frequency relationship near the cavity resonant frequency.

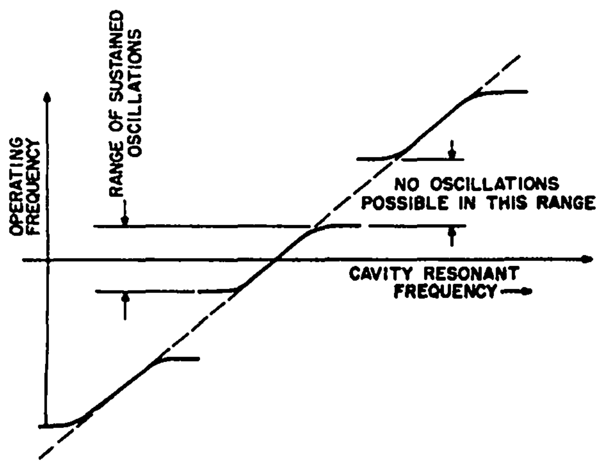

Fig. 84. Operating frequency vs cavity resonance frequency.

through the TWT. For our system we found $\Delta f_n \simeq 5$ MHz and $n \approx 400$ at $f_n \approx 2$ GHz. With the microwave resonator reconnected in the line the total phase shift around the loop changes by a maximum of $\pm\pi/2$ since the resonator behaves exactly like a resonant circuit near its resonance. Consider next the variation of phase with frequency for the entire system. Figure 82 shows the two contributions we have just discussed. By magnifying the region near the cavity resonant frequency we can concentrate on the useful portion of Fig. 82. This is done in Fig. 83 which shows that the maximum frequency range around f_n over which self oscillation is possible, i.e., $(f_{max} - f_{min}) = \frac{c}{2(L+cT)}$, corresponds to a range of phases $-2\pi n-\frac{\pi}{2} < \phi_p < -2\pi n + \frac{\pi}{2}$ over which the cavity phase can compensate for the difference between ϕ_p and $(-2\pi n)$. For example, at f_{max}, $\phi_p = -2\pi n-\frac{\pi}{2}$ and the cavity operates off resonance so that $\phi_p + \frac{\pi}{2} = -2\pi n$, as it must if oscillations are sustained. Similarly if the system oscillates at $f = f_n$, this means that f_n is the resonant frequency of the cavity. These arguments are applicable provided the TWT gain is large enough to sustain oscillations at any frequency for which the phase condition with a definite integer n is satisfied without at the same time sustaining oscillations at another frequency characterized by a different integer n'. In practice we find that oscillations can be sustained over nearly the entire bandwidth $f_{max} - f_{min}$. Unless a mechanically or electrically controlled phase shifter is inserted into the transmission line and used to compensate deviations from $-2\pi n$ which exceed $\pm\pi/2$, this self-tuning system can at most track over one-half of the available frequency spectrum. Even in this allowed frequency range only one-half of the frequency spectrum corresponds to frequencies within the bandwidth, f/Q, of the cavity. Thus, unless the shift in cavity resonant frequency is large compared to $(f_{max} - f_{min})$, it will be necessary to determine what the difference actually is between the operating frequency and the resonant frequency of the cavity. This situation may be understood with the help of Fig. 84, which gives a plot of operating frequency versus cavity resonant frequency (as determined by the electron density.) If the TWT gain is large but limited, the system can be operated in only one of the branches shown, at a time.

Reference

1. Richard B. Hall, Boeing Scientific Research Laboratories Document D1-82-0688, March 1968. See also R. C. Amjera and H. Lashinsky, Applied Phys. Letters 13, 96 (1968).

AUTORADIOGRAPHY WITH RADIOACTIVE TEST IONS - A NEW TECHNIQUE FOR MAKING PLASMA MEASUREMENTS

(H. Dreicer)

Our recently proven ability to charge-exchange a small fraction of a radioactive atomic beam passing through a plasma column suggests the possibility of utilizing autoradiography as a new plasma diagnostic technique. To understand this proposal consider the magnetized plasma column shown in Fig. 85. The radioactive atomic beam, which intersects it at $z = z_0$, consists of neutrals which when ionized by charge exchange become radioactive ions that are equivalent to the plasma ions except for their radioactivity and velocity distribution. An examination of the relationship between the velocity of the radioactive atom before the charge transfer and the velocity of the resulting radioactive ion just after the charge transfer shows it to be highly deterministic provided the process is resonant. This will always be the case for ions traveling through their parent gas, and, in particular, it is true for the case of charge transfer from K to K^+. Under these circumstances an electron is exchanged between the colliding partners at impact parameters for which the scattering angle is predominantly very small. For relative energies between 0.25 and 0.5 eV, almost all charge exchange encounters in potassium occur with scattering angles less than 10°. This result insures that such radioactive test ions can be produced with controlled initial velocities simply by controlling the velocity of the original radioactive atom. Moreover by using atomic beams of small cross section it is possible to produce these test ions in a controlled fashion anywhere inside of a plasma and thus predetermine their initial spatial coordinates as well.

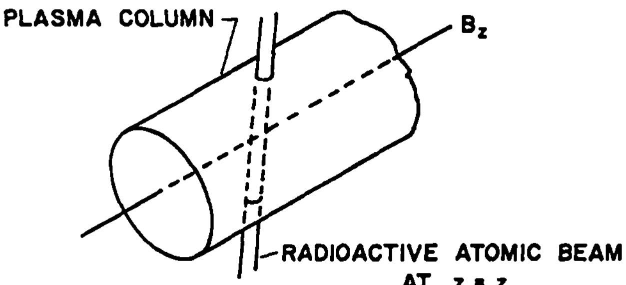

Fig. 85. Plasma column intersected by a radioactive atomic beam.

Radioactive test ions produced with given initial conditions will diffuse and drift in space in a manner determined by collisions, and by ac and dc electric and magnetic fields. At later times they will be found in other locations where they can be identified by radioactive detection schemes.

As a simple example of the autoradiography technique, consider the experimental setup used in the charge exchange experiment described above. Photographic film placed on collector 2 (Fig. 75) which intercepts plasma drifting along magnetic field lines, will be exposed wherever ^{42}K ions are condensed. If these are introduced into the plasma in a fine pencil beam we expect radial space charge electric fields to induce an azimuthal ExB drift which will rotate the pencil beam in some (possibly complicated) way. The exposed photographic film will provide evidence of such rotation, and thus permit the radial space charge field to be determined. Moreover, from the diffusive spreading of the pencil beam the effect of collisions could be deduced.

An investigation of the sensitivity of film to the ^{42}K beta-ray spectrum* indicates that the experiment just described should be feasible with the setup available from the charge exchange experiment.

---

* S. Stone, J-10 Los Alamos, provided all of the information about the sensitivity of photographic emulsions to beta rays.

THE ANGULAR DISTRIBUTION OF ATOMS EMITTED BY ATOMIC BEAM NOZZLE

(D. B. Henderson)

Proper design of atomic beam nozzles for the injection of neutrals into a Q-machine requires a knowledge of the distribution of efflux from a single nozzle. Such knowledge is unavailable from either experiment or theory in the range of physical dimensions and fluxes used in Q-machines. We have therefore measured the angular distribution of cesium efflux as a function of the driving pressure (or reservoir temperature) for various nozzles.

Figure 86 is a photograph of those parts of the apparatus which are inside the main vacuum chamber. The alkali vapor is generated in a constant-temperature oven on the outside and is fed in through heated pipes, marked "A," to a heated pillbox assembly, "B," the top of which rotates. The nozzle, "C," is mounted on a tower on the top of the pillbox. In this way the nozzle is rotated about its tip, thus keeping constant the distance to the detector and the solid angle subtended by it at the nozzle. From the nozzle the atoms pass through a liquid-nitrogen-cooled tube, "D." which reduces background pressure. They pass through a rotating chopping wheel, "E," and through the detector aperture to strike the positively biased detector filament. Here they are evaporated as ions and after acceleration are condensed by the liquid-nitrogen-cooled cathode which surrounds it. The modulated filament-to-cathode current is then detected by a phase-sensitive detector locked to the reference signal from a co-rotating chopping wheel outside the vacuum tank. The electronic measurement circuit is sketched in Fig. 87. The shielding reduces ac hum to 5 μV, which is roughly equal to the input white noise of the preamplifier. With the lock-in amplifier this circuit provides a sensitivity of a few picoamperes as is evident from the data.

A surface ionization detector of this sort may be analyzed through an extension of the work of Langmuir and Kingdon.[1] Briefly, one must account for the effects of partial coating of the filament with cesium. Langmuir and Kingdon

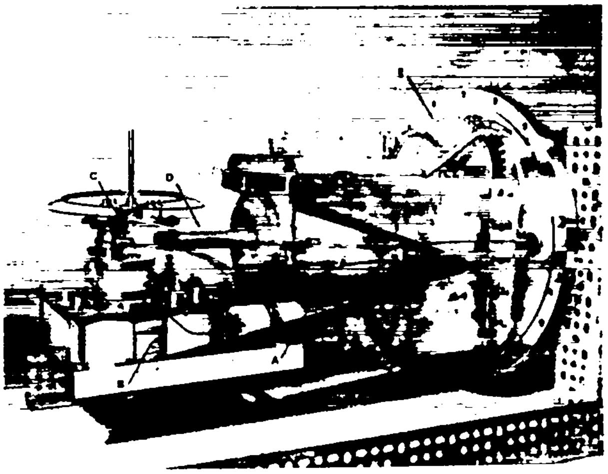

Fig. 86. Apparatus.

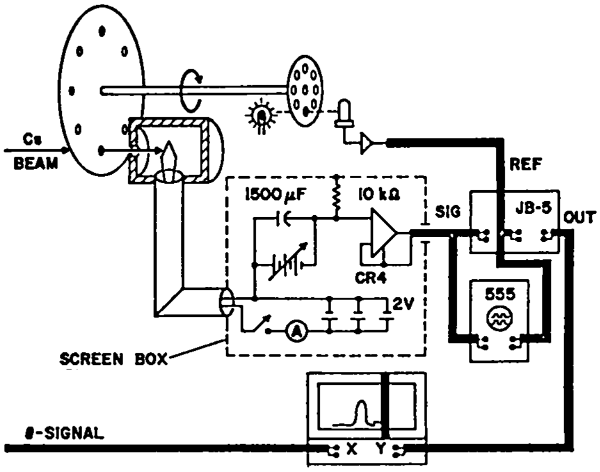

Fig. 87. Circuit.

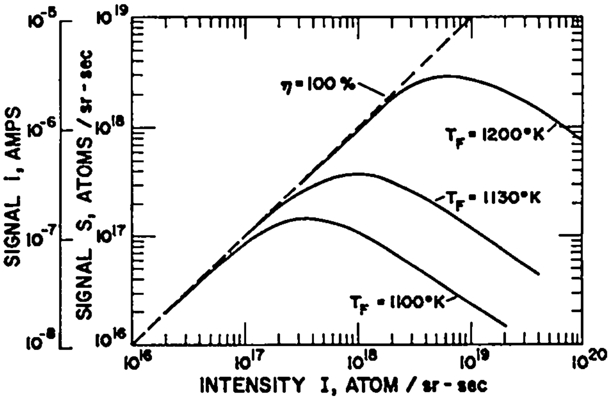

Fig. 88. Detector response

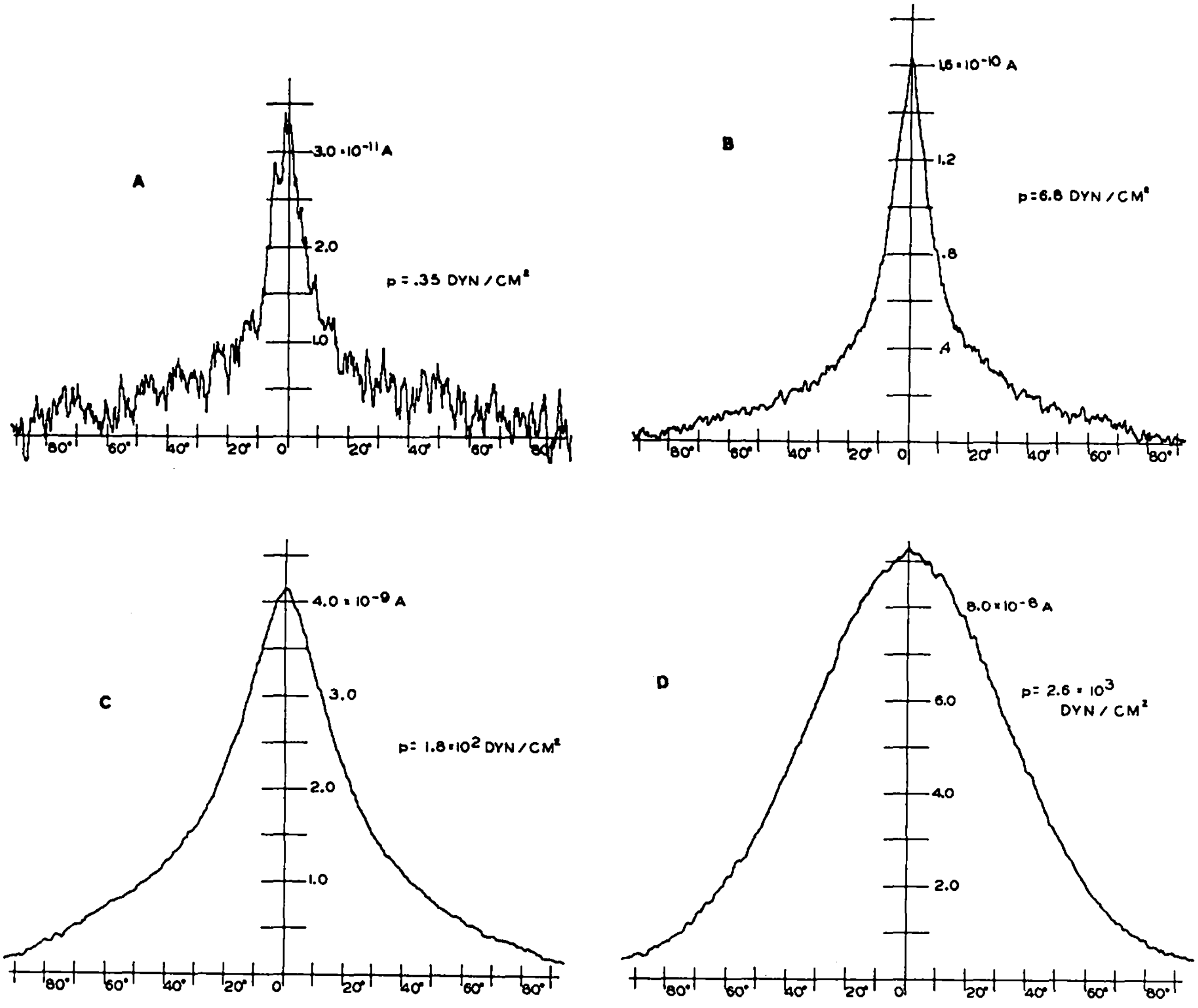

Fig. 89. Raw data: intensity signal vs angle.

report empirical results in terms of a cesium reservoir temperature.

We define an equivalent reservoir temperature to be that for which $n\bar{c}/4$ equals the flux incident upon the filament. The result is the response characteristic plotted in Fig. 88. Data may show a hollow core, due to this nonmonotone response. While inversion is possible, via Fig. 88, it is not very accurate because of the strong dependence of cesium coating upon the filament temperature. For this reason we work in the linear range ($i \propto I$).

Four x-y traces of the intensity signal i(1 amp = .95 x 10^{24} atoms/st. rad.-sec), versus angle θ, for different cesium pressures are shown in Fig. 89 for a nozzle 0.81-mm diam by 5.94-mm long. The pressure p is computed from the oven temperature, T_0, by the vapor pressure equation,

$$p = 10^{10.06-3830.}/T_0 \text{ dynes/cm}^2. \tag{1}$$

The lock-in amplifier was operated with two stages (12db/octave) of output filtering at an RC of 3 sec. Thus we have a ramp response delay of 2 x 3 = 6 sec. Each trace was scanned over 180° in 1200 sec. Thus the response delay is equivalent to (180°/1200 sec) x 6 sec = 0.9°. This does introduce some small distortion to the data; all the scans shown were taken left-to-right. We have not yet decided whether to adjust the apparatus or the data to correct this.

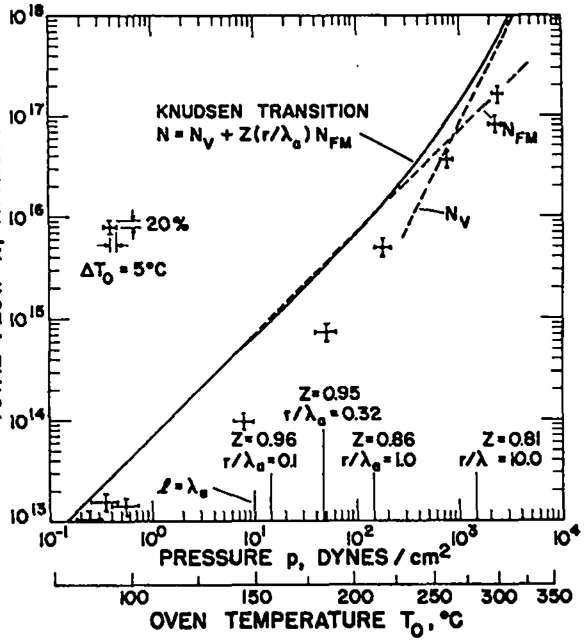

Fig. 90. Total flow vs pressure.

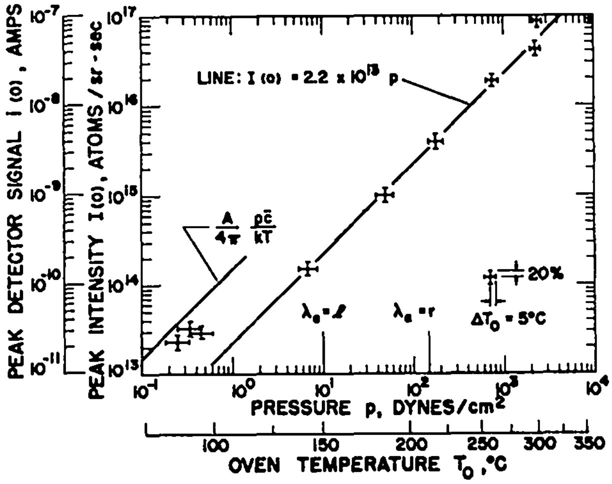

Fig. 91. Peak intensity vs pressure.

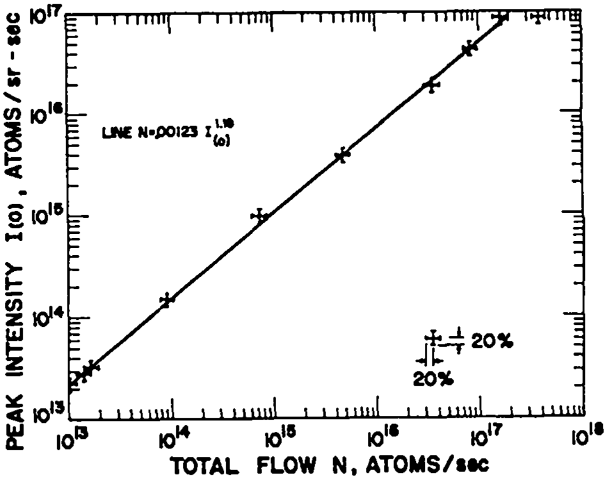

Fig. 92. Peak intensity vs total flow.

We have integrated the data to obtain the total flow, assuming axial symmetry. The total flow is somewhat lower than expected from standard flow theory, as shown in Fig. 90. In computing the theoretical curves, we take the pressure behind the nozzle to be vapor pressure in the oven as found by Eq. (1). The temperature is taken to be that of the nozzle, which is somewhat hotter than the oven. We compute the flow from the usual expression.[2] At low densities we have free molecular flow, giving a total flow of

$$N_{FM} = \frac{n\bar{c}}{4} \cdot A \cdot K(\ell/r),$$

where $K \approx K' = (1 + 3\ell/8r)^{-1}$, ℓ is length, r is radius, n is density behind the nozzle $= p/kT$, $\bar{c}$ is thermal speed $= (8\,kT/\pi m)^{\frac{1}{2}}$, and A is area $= \pi r^2$. At high densities we have

$$N_V = \frac{\pi r^4}{16\eta kT} \frac{p^2}{\ell} \quad .$$

For the viscosity η, we extrapolate the fit which Weaver and Todd[3] make to their data taken over the range 1000 to 2400°K,

$$\eta = 1.35 \times 10^{-7}\, T^{1.06} \text{ g/cm-sec.}$$

In the transition range we use the form

$$N = N_V + Z(r/\lambda_a) \cdot N_{FM},$$

where Z is an empirical form found by Knudsen[4] and the average mean free path is that deduced from the average pressure p_a $(= p/2)$ and the viscosity through the Enskog formula,

$$\lambda_a = \eta kT/(.499\, m\, \bar{c}\, p_a).$$

From Fig. 91 one sees that the intensity and curve widths increase with increasing pressure as is expected. The plot of peak intensity I(0) vs total flow, Fig. 92, shows a remarkably good fit to our data by the simple power law:

$$N = .00123 \times I_{(0)}^{1.19} \quad .$$

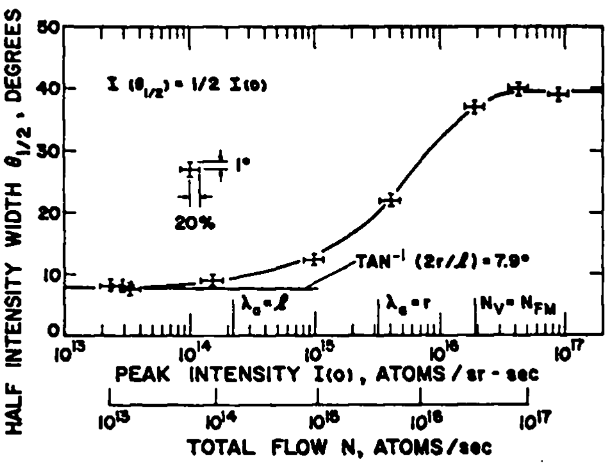

Fig. 93. Half width vs peak intensity.

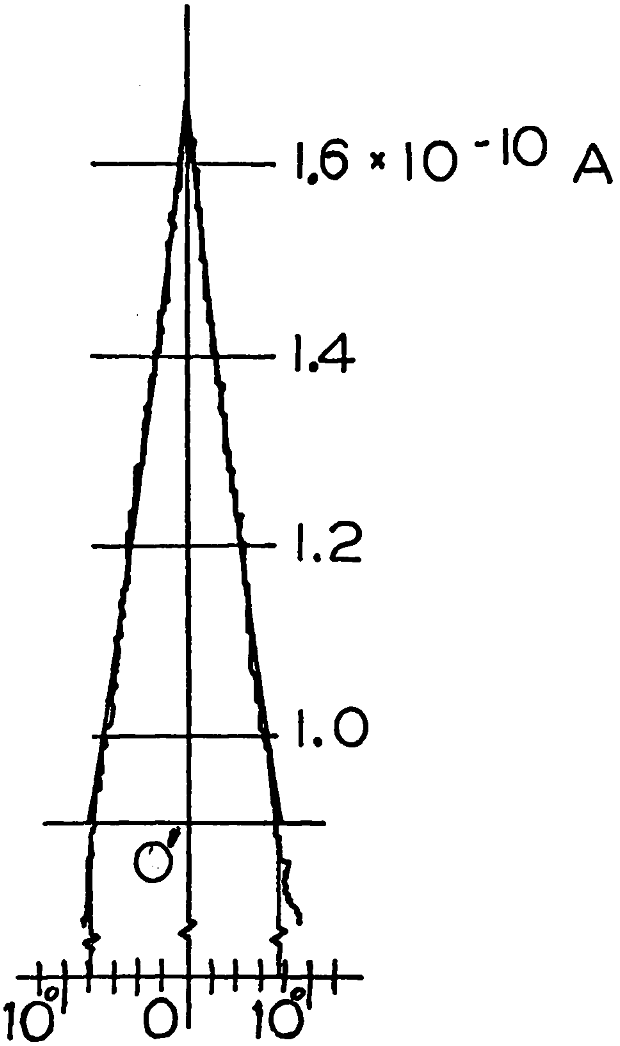

Fig. 94. Data and theory

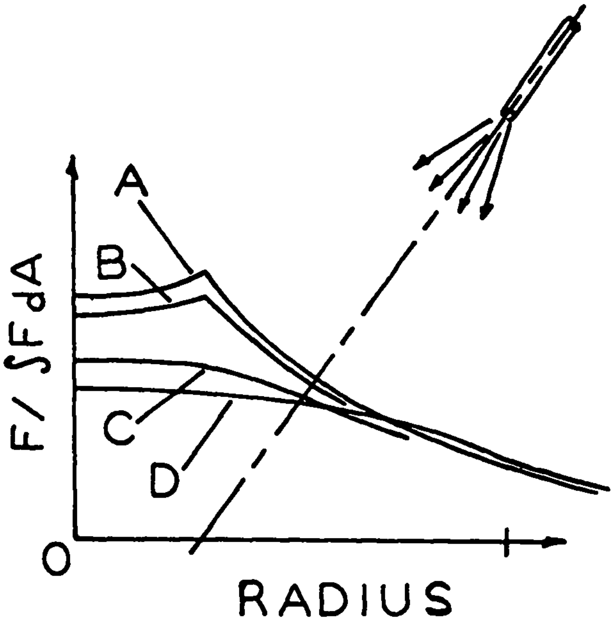

Fig. 95. Flux on hot plate.

This empirical fit is used to provide the second ordinate scale in Fig. 93, which indicates how the efflux distribution changes in shape. We see clearly that there are two asymptotic limits corresponding to the free molecular and viscous flow regimes.

Finally we note that we may account for the cusp-like peaks on the low pressure data in Fig. 89. By associating these peaks with atoms which flow through the nozzle making no collisions with other atoms or the walls, we have, as for a simple baffle,

$$I_{(\theta)} \propto \cos\theta \left\{ 1 - \frac{2}{\pi} \left(\beta\sqrt{1 - \beta^2} + \sin^{-1}\beta \right) \right\} ,$$

where $\beta \equiv (\ell/d)\tan\theta$. In Fig. 94 we superimpose this shape with an arbitrary intensity upon the peak of the p = 6.8 dynes/cm^2 curve from Fig. 89. The agreement is quite good.

The $I_{(\theta)}$ vs θ data permits us to compute the atomic flux incident upon a hot plate for various arrangements of nozzles. As an illustration of this computation Fig. 95 shows the normalized profiles of flux incident upon a hot plate using the data of the four cases shown in Fig. 89. In this computation the nozzles were arranged into a ring of radius equal to their distance from the plate. They are aimed at points three-tenths of this distance out from the center. $I_{(\theta)}$ data for various nozzle dimensions will enable us to design an array of nozzles to best approximate any desired distribution of flux onto the hot plate and to predict the flux profile as a function of total flux.

References

1. I. Langmuir and K. Kingdon, Proc. Roy. Soc. (London), 107 61 (1925).
2. S. Dushman and J. Lafferty, Scientific Foundations of Vacuum Technique, (Wiley: New York 1949).
3. C. Weaver and J. Todd, Proc. IEEE Thermionic Conversion Specialist Conf., 1967, p. 236.
4. As reported in Dushman, ibid., p. 256.

DEVELOPMENT OF A SECOND GENERATION QUIESCENT PLASMA SOURCE: THE ECH Q-MACHINE

(D. Michael, J. McLeod, and H. Dreicer)

Experiments are under way on a plasma column which, instead of a hot plate, utilizes a modest amount of microwave power at or near electron cyclotron resonance to ionize hydrogen gas and heat the electrons. Our motivation is the need for a plasma that--unlike the conventional Q-machine plasma--is not restricted to 0.25 eV particle energies and to alkali ions, and yet possesses a reasonable degree of quiescence. A theoretical analysis of the conditions under which such a plasma column could be maintained was presented by us in an earlier report.[1] For the sake of completeness some of these notions are repeated here before the experimental results are presented.

Analysis of Operating Conditions

A cylindrical magnetized plasma column which terminates on metallic floating end plates is maintained against continuous loss of particles to these end plates by electron ionization of neutrals. Even if the average electron travels many times the length of the column before making such an ionizing collision with a neutral, it must make exactly one during its lifetime in the machine to maintain steady state. This fact determines the neutral gas density required. For if the principal loss is collisionless ambipolar streaming along the magnetic lines to the end wall intersecting the column, then

$$n_e \bar{\nu}_i V = JA, \qquad (1)$$

where n_e = electron density, $\bar{\nu}_i$ = average ionization frequency per electron, V = plasma volume, J = ion end-wall particle current density, and A = plasma cross sectional area.

The ion end-wall current along the magnetic field can be determined approximately from the argument that most of the electrons must be reflected by a sheath which accelerates the ions and retards those electrons which reach the wall. Such a sheath is usually characterized by a potential drop of several times kT_e, where $\frac{3}{2}kT_e$ equals the average electron energy. Thus the ions gain energy $\frac{1}{2} M\bar{v}_i^2 \approx 5kT_e$ by the time they strike the wall. The electric field of such a sheath extends deep into the plasma and accelerates the ions toward the end wall so that the ion velocities are not really random.

Maintenance of a steady state requires exact balance between ionization and the loss of ions out the ends of the column. In the collisionless limit of free ion streaming, the average ionization rate per electron needed to produce this balance can be shown to be[2]

$$\bar{\nu}_i = (.8092/L)\sqrt{2kT_e/M_i} \text{ (cgs units)}, \qquad (2)$$

where L is the length of the plasma column. The effect of ion-neutral collisions or magnetic mirrors would be to make the required rate smaller.

By assuming a Maxwellian velocity distribution we have computed[1] the values of $\bar{\nu}_i/\nu_e$, listed in Table I, for molecular hydrogen. Here $\bar{u}$ is the average electron energy and ν_e, the electron-neutral elastic collision rate for momentum transfer, is given by $\nu_e = 6 \times 10^9\ p\ \text{sec}^{-1}$ where p is the gas pressure in Torr. When the computed values for $\bar{\nu}_i/\nu_e$ are substituted into Eq. (2) we have the following expression for the

Table I

$\bar{u}$ (eV)	$\bar{\nu}_i/\nu_e$	u* (eV)
4	1.6×10^{-4}	330
6	1.5×10^{-3}	100
10	1.1×10^{-2}	65
16	3.8×10^{-2}	80
25	9×10^{-2}	110
40	0.20	170
60	0.35	250

hydrogen gas pressure required for steady state operation,

$$p = \frac{(1.3 \times 10^{-4})\sqrt{T_e}}{(\bar{\nu}_i/\nu_e)\, L}, \qquad (3)$$

Here L has the units of cm and T_e is the electron temperature in eV. The necessity of meeting this balance exactly provides, for any particular gas, a unique relationship between electron temperature and neutral pressure which is independent of microwave power or plasma density. Figure 96 shows this relationship for the case of hydrogen and a one-meter long plasma column. The evaluation of $\bar{\nu}_i/\nu_e$ immediately clarifies another facet of the problem. Since $\bar{\nu}_i/\nu_e < 1$ over the entire energy range considered in Table I, it follows that, for these cases, the average electron will make at least a few and, depending on $\bar{u}$, possibly a large number of elastic collisions with neutrals during its lifetime. Qualitatively speaking it is clear then that such elastic collisions occur frequently enough to insure the high degree of isotropy in f required to avoid instabilities of the anisotropy and loss-cone type even though the electron mean free path may exceed the machine length.

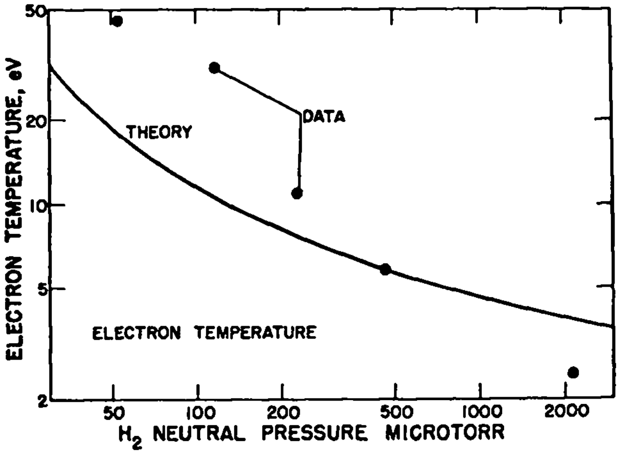

Fig. 96. Comparison between computed and measured average electron energy as a function of H_2 gas pressure.

The foregoing arguments have been based upon an ionization rate calculated for a Maxwellian distribution. However, the conclusion about isotropy in f will not be altered by more exact distributions. This is true at low average electron energies, because only the few electrons in the tail of f can ionize, whereas all electrons in the distribution make elastic encounters. For higher average electron energies, such that $\bar{u} \geq u_i$, $\bar{\nu}_i$ should become relatively insensitive to the exact form for f since in this case most electrons in the distribution can ionize. The maintaining pressure given in Eq. (3), on the other hand, can be expected to depend quite sensitively on an exact knowledge of f for low average electron energies.

The energy input, u*, required to replace an electron lost from the plasma includes the energy required to produce a new ionization and the kinetic energy carried off by the electron. The latter is much more than the average electron kinetic energy since only very energetic electrons can penetrate the sheaths at the ends of the column.

The sheath reduces the electron current by a factor of the square root of the ratio of electron-to-ion mass. Thus the threshold energy for escape is 5.12 T_e in hydrogen where this mass factor is 60.

The average energy of electrons capable of escaping is

$$\int_{5.12\, T_e}^{\infty} u f(u) du = 5.50\; T_e. \qquad (4)$$

Therefore

$$u^* = \frac{P_x}{n_e e \bar{\nu}_i} + 5.50\; T_e, \qquad (5)$$

where P_x is the power dissipated in inelastic collisions. Values for P_x, which includes vibrational, rotational, electronic excitation, and electronic ionization, have been computed for hydrogen, and u* is listed in Table I as a function of $\bar{u}$. For low $\bar{u}$ inelastic losses dominate u*. For large $\bar{u}$, the contribution to u* is mainly the kinetic lost with the escaping electron. It is important to note that, through its dependence on $\bar{u}$, the quantity u* is determined by the neutral gas density.

The power required to maintain the plasma in steady state is the product of the electron loss rate and the energy, u*, lost with each electron. In hydrogen the latter has a minimum of 66 eV at an average electron energy of about 10 eV. If the loss rate is dominated by ambipolar streaming-out at the ends, then the minimum power requirement is

$$P = 2S_o h_o n \sqrt{\frac{2kT_e}{M_i}}\ Au^* = (2.26 \times 10^{-11})\, nA, \qquad (6)$$

where n is in cm^{-3}, and S_o and h_o are as defined earlier.[2] The quantities u* and T_e are determined by the neutral gas density. Thus the absorbed microwave power will determine only the plasma density.

At the average energies shown in Table I, the electron-electron mean free collision time is too long to ensure the development of a Maxwellian distribution function unless the density is larger than 10^{12} cm^{-3}. There are two other effects, however, which should at least ensure that the distribution functions have the general appearance of a Maxwellian and be free of a second hump. The first one is that the microwave heating power is present in only a small part of the plasma, which a typical electron will enter and leave many times with random phase. The second is the presence of inelastic electron-neutral collisions with rates that rise monotonically with energy throughout the energy range of interest, thereby cooling fast electrons preferentially. This effect is probably somewhat stronger than needed to prevent runaway electrons so that it probably also cuts off the tail of the distribution. Nevertheless, a Maxwellian distribution has been assumed in calculating Fig. 96 and Table I.

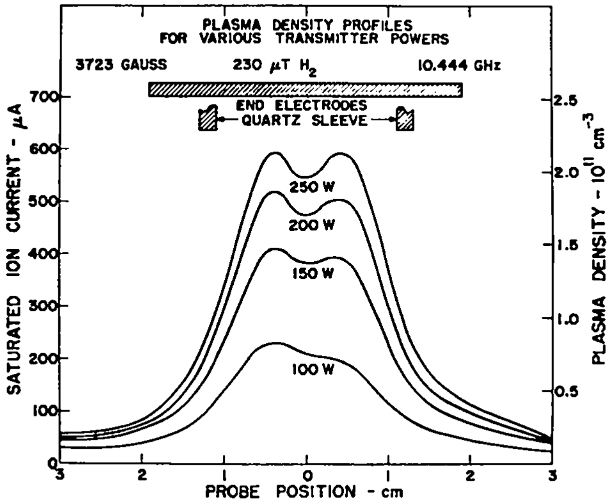

Fig. 97. Density profile measured with incident microwave power as a parameter.

Experimental Arrangement and Results

Our ECH plasma has proved to be an efficient absorber of microwave power. Since only about 100 eV is required per particle during its 50-μsec computed lifetime, the large electric fields produced in resonant coupling structures are not required. The nonresonant structure that we are using was inspired by that of Lisitano,[3] but considerable simplification of the standard Lisitano coil is made possible at 10.4 GHz where waveguide techniques are possible. The structure used in our experiment has been described elsewhere.[4]

The theoretical analysis of plasma parameters given above is based on a one-dimensional model, in which variations were allowed only in the direction along the magnetic field lines. In actual practice, the plasma must have a finite radial extent. A class of density profiles obtained in our plasma with a motor-driven Langmuir probe movable in a plane perpendicular to the plasma is shown in Fig. 97. Here incident (not absorbed) microwave power plays the role of a parameter. The hydrogen gas pressure was 230 μTorr. Nuclear magnetometer measurements showed that the magnetic field was uniform to 1.5% over the 100-cm distance between end plates, and uniform to 0.02% within the microwave structure. The conversion from ion saturation current to plasma density is tentative since the probe theory used is based upon a Maxwellian ion velocity distribution. The distribution must actually be strongly anisotropic due to the acceleration in the deeply penetrating sheath. Moreover probe theory involves the ion mass and our assumption that we are dealing with H_2^+ rather than H^+ requires corroboration. Furthermore, it also ignores particles trapped near the probe, and assumes a simple probe geometry.

In those parts of the profile which are concave downwards, the effective diffusion coefficient is negative, which can only mean that ion production locally exceeds direct end losses by free streaming and the surplus is diffusing across the magnetic field to stream out along some other field line. The average electron energy in this region must therefore be greater than the steady state value computed in the one-dimensional case. Where the curve is concave upwards, ion production locally fails to balance ion end losses and the deficit must be made up by cross-field diffusion. Here the average electron energy must be less than the steady state value predicted for the one-dimensional case. This argument makes it possible to identify the regions in which microwave heating occurs. These heating regions are surprisingly far in from the inside of the coupling structure. In this situation, the ratio of the cross-field diffusion coefficient to the net rate of ion production per electron above ion end losses appears as an intimate combination so that neither can be evaluated independently.

A contour map of ion saturation current is shown in Fig. 98. The data on which it is based were taken some months later than the data shown in Fig. 97. The highly symmetric double humped profile in Fig. 97 has not been reproduced lately, and Fig. 98 is measured on a less symmetric column.

A plot of plasma density vs magnetic field is shown in Fig. 99 and of reflected microwave power vs magnetic field in Fig. 100. Neither the structure of these curves nor the effect of

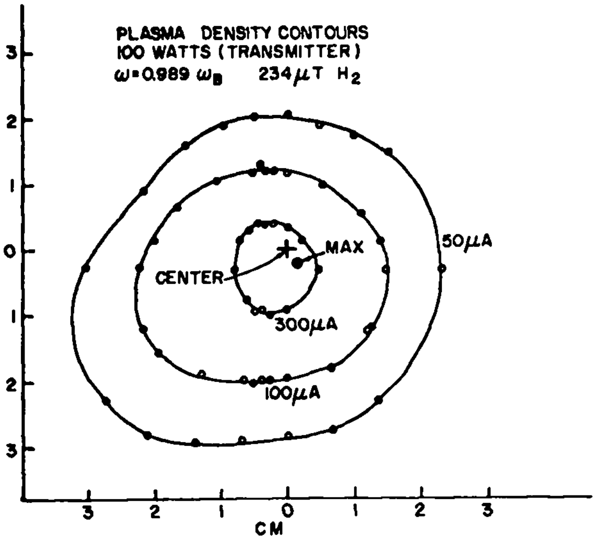

Fig. 98. Contours of constant ion saturation current measured in a plane perpendicular to the applied magnetic field.

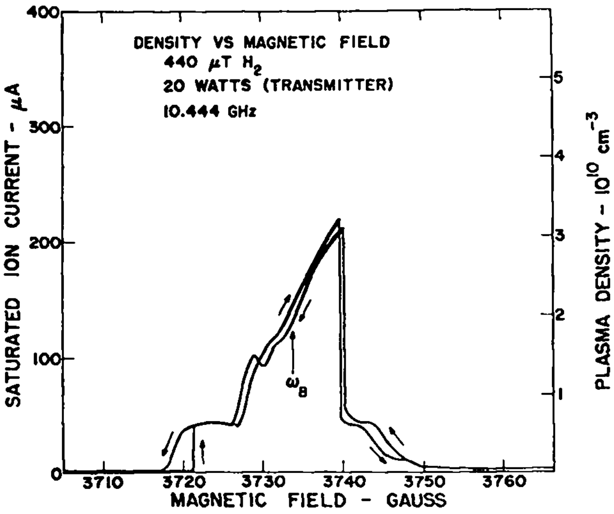

Fig. 99. Plasma density measured as a function of applied magnetic field.

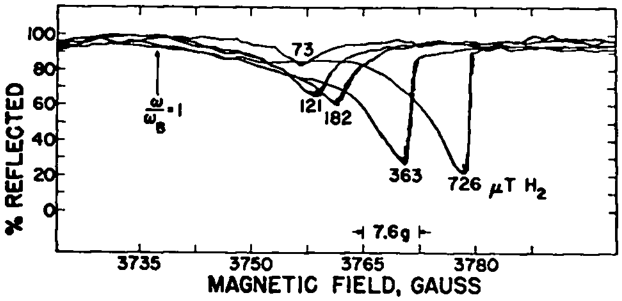

Fig. 100. Percentage of microwave power reflected by the microwave coupling structure and plasma as a function of magnetic field with gas pressure as a parameter.

pressure is understood. The shape of the density curve has the wrong sense to be related with the upper hybrid resonance. The peak of this curve, i.e., the portion just to the left of the abrupt cut-off, is hard to reproduce and is sometimes almost absent. In this region the appearance of the plasma is appreciably delayed following microwave turn-on; the delay exceeds a millisecond at the edge of the precipice. This effect was discovered when the ordinary c.w.-microwave operation was replaced by audio-frequency amplitude-modulation of the klystron source in order to measure the plasma diamagnetism.

A large diamagnetic pickup coil which links the entire column has been installed for the purpose of measuring the average transverse electron energy. The microwave power is chopped at an audio frequency and a phase-locked detector is used to separate the resulting diamagnetic signal (≈ 50 microgauss) from the fluctuations in magnetic field which would otherwise hide it. Since the diamagnetic coil senses the product of density and transverse energy, the resulting transverse energy is no more accurate than the interpretation of the density measurement for which, as mentioned above, we have had tentatively to rely on standard probe theory.

Electron temperatures obtained by this technique range from 2.5 to 46 eV and are shown in Fig. 96 together with the theoretical relation between neutral gas pressure and electron temperature described by Eq. (3). In view of all the difficulties in both theory and experiment, the agreement is encouragingly close.

The data in Fig. 96 were obtained at one microwave power level. Recently obtained data, shown in Fig. 101 and provisional in nature, appear to verify the prediction that the electron temperature does not depend on absorbed microwave power. The same figure also indicates that the measured electron density and line density deduced from an integration over the measured density profile increases with absorbed power as predicted by Eq. (6).

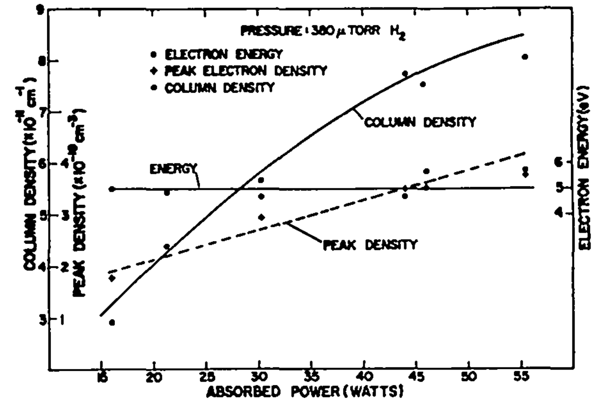

Fig. 101. Peak plasma density, line density, and average electron energy measured as a function of microwave power absorbed by the plasma.

This equation shows that the power required to maintain the plasma is proportional to nA. Thus, to compare theory and experiment it is useful to define a specific power as

$$P^* = P/2\pi \int_0^\infty n(r)\, r dr \approx P/nA. \tag{7}$$

Measured values of this quantity are shown in Fig. 102 together with the theoretical prediction. The accuracy of the data does not really warrant much speculation, but the insensitivity of the observed specific power to electron temperature is puzzling.

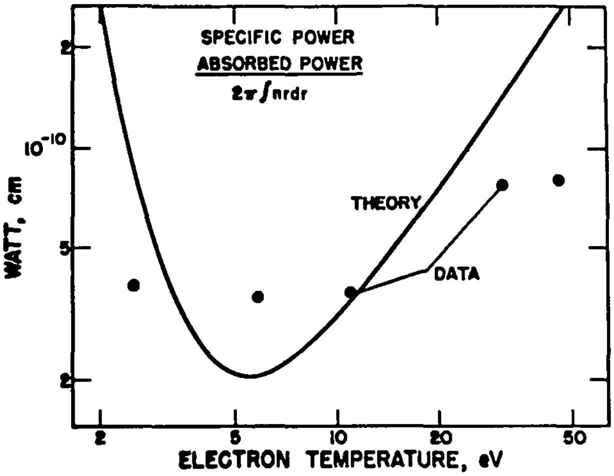

Fig. 102. Specific power measured as a function of average electron energy.

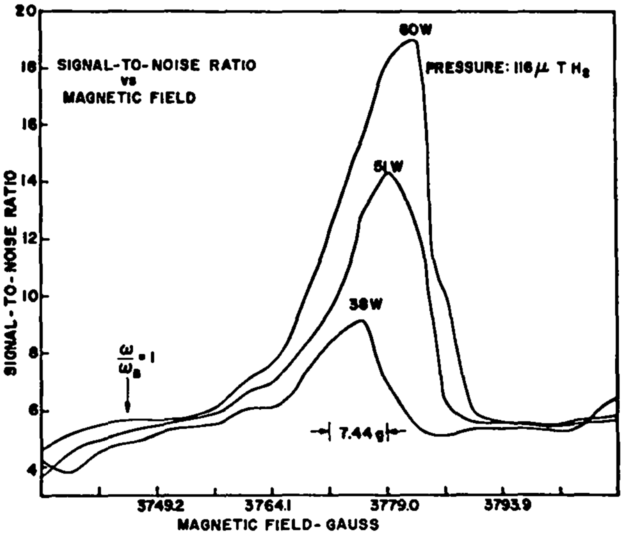

Fig. 103. Signal-to-noise ratio measured as a function of magnetic field with peak absorbed microwave power as a parameter.

The ratio of the time average of the ion saturation current to the rms of fluctuations in the ion saturation current collected by a single Langmuir probe is shown in Fig. 103, plotted against the magnetic field. The value of the peak absorbed power is shown beside each curve. One is tempted to suppose that the fluctuations in ion saturation current represent fluctuations in the plasma density even though presently available probe theory is unconvincing in this respect. If this connection is made, then the ratio of ion saturation current to fluctuations in this current is a measure of the degree of quiescence.

Note the surprising result that the quiescence of the plasma improves with increasing power. The bandwidth of the fluctuation recorder was tested with an oscillator and found to be 1.0 MHz. We have found it necessary to be very careful with the probe bias supply to avoid introducing stray reactances which affect this bandwidth. Spectrum analysis indicates that most of the fluctuation power lies below 1.0 MHz where the spectral density has dropped 30 db below its low-frequency value. Whether this cutoff is a property of the probe sheath or a property of the main plasma is not known. The possibility that the fluctuations are a probe-sheath phenomenon have also not yet been ruled out.

We have also measured the quiescence resulting from a different gas-feed system which produces a strong maximum in the neutral gas pressure near the microwave coupling structure to restrict the outward flow of gas introduced within it. The change to this arrangement did not have a significant effect on the measured degree of quiescence.

References

1. H. Dreicer and J. McLeod, LA-3831-MS, p. 21. See also J. McLeod and H. Dreicer, Bull. Am. Phys. Soc., Ser. 2, 13, 289 (1968).
2. L. Tonks and I. Langmuir, Phys. Rev. 34, 876-922 (1929).
3. G. Lisitano, Proceedings of the Seventh International Conference on Ionization Phenomena in Gases, Vol. 1, 464-467 (1966).
4. H. Dreicer, J. McLeod, D. E. Michael, LA-4075-MS, p. 97.

DESIGN OF ELECTRON INJECTOR FOR SYNCHROTRON RADIATION STUDIES

(D. Ignat, H. Dreicer)

For the purpose of studying synchrotron radiation it is desirable to have a slowly drifting, spatially localized, low density electron beam which has a large amount of energy perpendicular to an externally imposed magnetic field and has a thermal spread which is small compared to the beam energy. To produce such a beam we have considered a microwave cavity, oscillating near cyclotron resonance, to supply transverse energy to a beam emanating from a conventional electron gun. Our tentative conclusion, based on single particle calculations, is that such a procedure will work if sufficient care is exercised in selecting the various parameters.

The configuration we envision is a right circular cylindrical cavity operating in the TE_{111} mode with electrons injected along the axis of symmetry (z axis), which is also parallel to a uniform applied static magnetic field B_o. Full

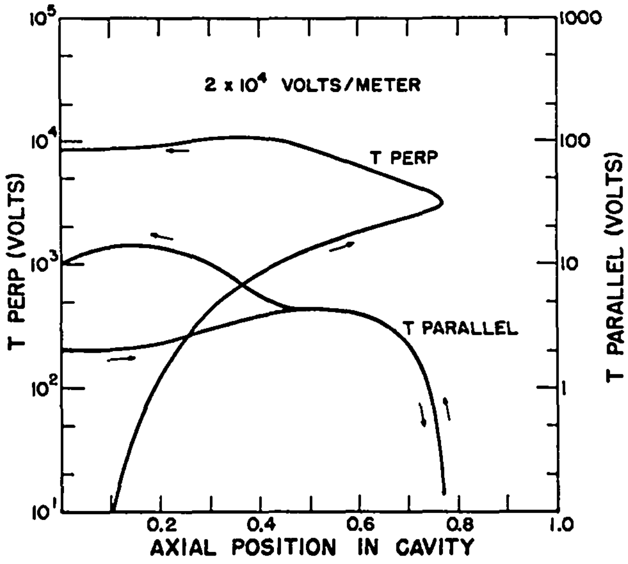

Fig. 104a. An example of an electron being reflected.

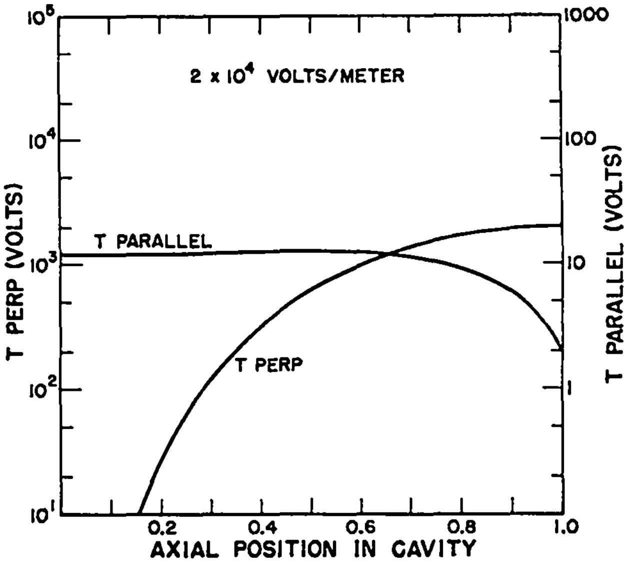

Fig. 104b. The final longitudinal energy is very small.

account was taken of the effect of the microwave magnetic field and the relativistic change in mass of the high energy electrons in calculating the resultant trajectory in configuration and velocity space. Inclusion of these effects leads to a set of three coupled nonlinear second order ordinary differential equations which are simplified by the requirement that the electron is always very near the cavity axis, and that the cavity electric field, E, is in the x direction on the z axis.

The resulting equations have been programmed for the CDC 6600 and many specific cases have been examined. The calculation was set up in the following way. A cavity of specific dimensions and therefore of a specific resonant frequency is chosen. A frequency difference $\Delta\omega$ between the cavity frequency ω and the cyclotron frequency ω_B is selected, and the cyclotron frequency is adjusted as follows: $\omega_B = \omega \pm \Delta\omega$. The quantity $\Delta\omega$ can be imagined to correspond to the Doppler shift associated with some axial energy T_z, when

$$\Delta\omega = k_{\parallel}\sqrt{2T_z/m} \quad .$$

Since the cavity standing wave fields can be decomposed into oppositely directed travelling waves, we might imagine that the case $\omega_B = \omega + \Delta\omega$ corresponds to a strong interaction between a particle of axial energy T_z and the travelling wave component coming toward the particle. The actual computations show that no such simple decomposition is possible. Nevertheless we use it as a guide to the range of injection energies that will cause strong interactions between the fields and the particle.

Trajectories are calculated for a variety of injection energies and electromagnetic field strengths. Graphic output is in the form of energy (in eV) parallel and perpendicular to the magnetic field as a function of position in the cavity.

In the following we illustrate some properties of a 10-cm diam, 6.15-cm long cavity injector which has a resonant frequency of 3.0 GHz. We choose two field strengths: 2 x 10^4 volts/meter, which corresponds to a power flow of 0.2 watt for a Q of about 3500, and 5 x 10^4 volts/meter corresponding to a power of about 1 watt. The quantity $\Delta\omega$ is about 2π x 21 MHz/sec. This assigns to the equivalent axial energy T_z, for which strong interaction might naively be expected, the value of 20 volts. Figures 104a and b show results for the lower field strength with $\omega_B = \omega + \Delta\omega$ at two actual axial injection energies. Note that in both instances the electron is accelerated in the z direction toward higher field strengths after

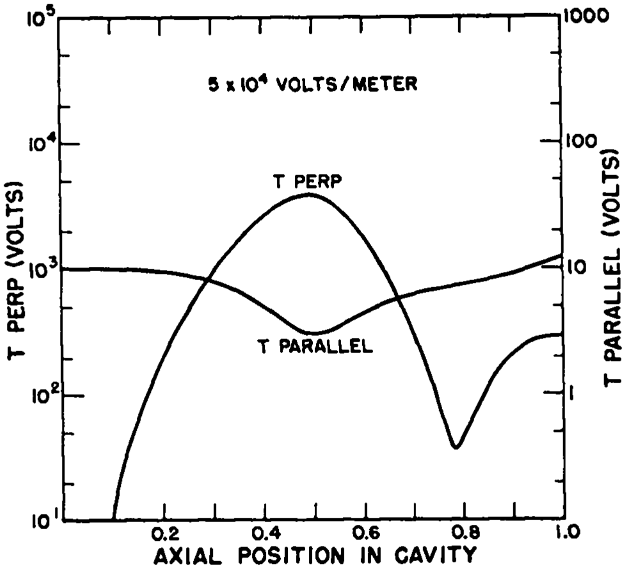

Fig. 105a. An example of a severe loss of the energy gained.

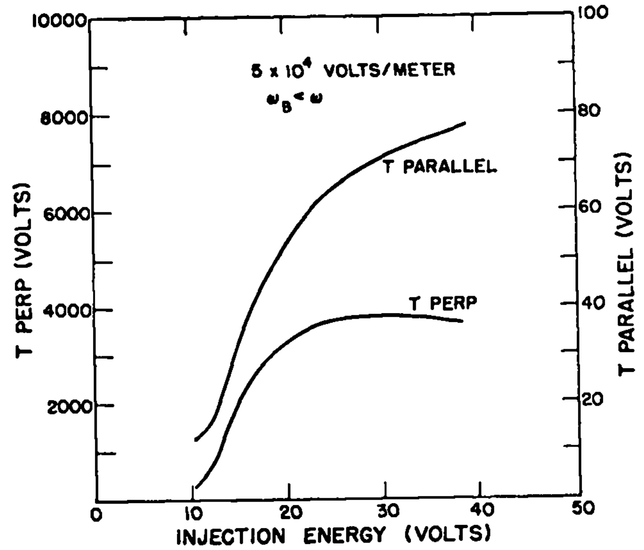

Fig. 105c. Particle energy after leaving the cavity vs longitudinal energy at injection.

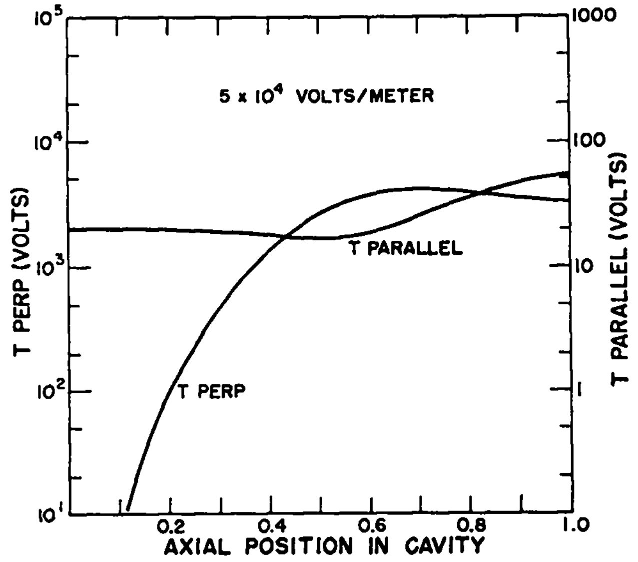

Fig. 105b. A reasonably steady energy gain with a small loss before exiting.

entry. In Fig. 104a, for 2 eV of parallel injection energy this effect causes reflection about $\frac{3}{4}$ of the way through the cavity, but after passing the cavity center on its return it is accelerated to lower field strengths briefly, violating the well-known but approximate rule[1] that the electron will be accelerated toward regions of high field strength for $\omega_B > \omega$ and toward regions of low field strength if $\omega_B < \omega$. Such behavior cannot be satisfactorily understood by using the fact that ω_B is a function of energy. This case, and most others, do not lend themselves well to analysis in terms of this simple rule. At the 12-volt injection energy used to compute the results in Fig. 104b, the particle is first accelerated by a small amount and then decelerated in the z-direction and arrives at the output with a parallel energy of only 2 volts. However, by this time it has gained a transverse energy of 2 keV. In this case longitudinal acceleration is always to regions of higher field strengths. Figures 105 and 106 are illustrations using the higher field strength. In Fig. 105, $\omega_B < \omega$ and the axial acceleration is generally towards low field strength regions. In Fig. 105a, for 10 eV of parallel injected energy we have an example of a serious loss of transverse energy. In Fig. 105b, where the parallel injected energy was increased to 20 eV the transverse energy merely levels off. Figure 105c is a summary of the results for this class of parameters. Here final transverse energy (left scale) and final parallel energy (right scale) are plotted vs injection energy. For injection energies lower than 10 volts, the particle is reflected from the cavity by the electromagnetic force. Note that the maximum perpendicular energy in this figure is about 4 keV. The data in

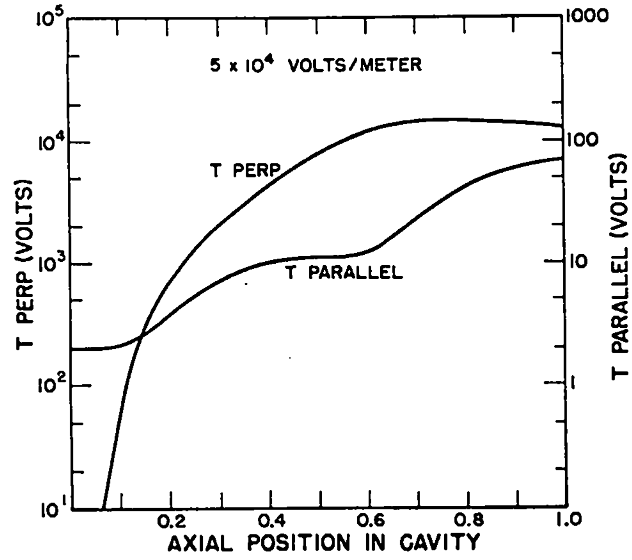

Fig. 106a. A transverse energy gain over 12 keV.

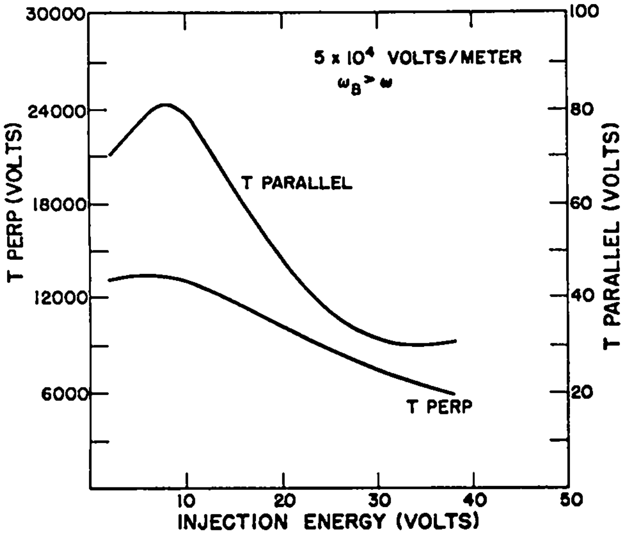

Fig. 106b. Particle energy after leaving cavity vs longitudinal energy at injection.

Fig. 106 also represent the higher field strength, but with $\omega_B > \omega$. For this combination of parameters all the cases examined are well behaved. Figure 106a gives the energy as a function of axial position for a particle with 2 volts at injection. Figure 106b summarizes the results for many different injection energies. Here a peak transverse energy output of about 13 keV is obtained. The effects of switching from $\omega_B < \omega$ to $\omega_B > \omega$ is to increase the maximum possible perpendicular energy by a factor of four.

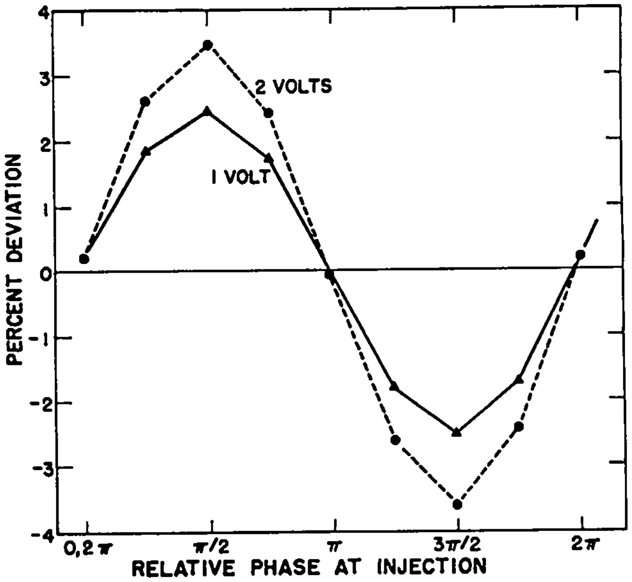

Fig. 107. The effect of a small amount of perpendicular energy at injection on the perpendicular energy at exit.

The possibility that small amounts of perpendicular energy present at injection may have a drastic influence on the results was investigated for several cases, and was found not to be a serious limitation. A summary of results for one specific case is given in Fig. 107. The field strength is 5 x 10⁴ volts/meter, the parallel injection energy is 18 volts, and $\omega_B > \omega$. In the figure we have plotted the percentage change in final perpendicular energy as a function of initial phase angle for two initial perpendicular energies. The zero in the ordinate corresponds to the results obtained when no initial perpendicular energy exists.

These computations indicate the feasibility of producing an electron beam with a large ratio of transverse to longitudinal energy, although the question of space charge effects remains to be resolved. Such space charge effects are intimately connected with the question of injecting the electron beam into a plasma which may provide an adequate density of positive ions for space charge neutralization. To utilize the proposed injector to the fullest requires the design of a particle energy analyzer which can determine both transverse and longitudinal electron velocity distributions. When this question is resolved, we expect to consider ways of injecting such an electron beam into a plasma for synchrotron radiation studies.

Reference

1. The effect of time averaged electromagnetic forces on charged particles is reviewed in the following: H. Motz and C.J. Watson, "The Radio Frequency Confinement and Acceleration of Plasmas," in Advances in Electronics and Electron Physics, Vol. 23, L. Martin ed., Academic Press (1967).

MAGNET CURRENT REGULATIONS

(J. McLeod)

The research program of the Fundamental Plasma Physics Group requires that both of the large magnet power supplies available, a 500-kW motor generator and a 2.5-MW rectifier power supply, have their current stability improved to 0.01%. The basic concept of the improvement has been discussed earlier.[1] The key regulation component is a series control element, consisting of many power transistors in parallel, which passes the entire output current, but drops only a few volts. The maximum current is 2.4 kA for the 0.5-MW motor-generator and is 18 kA for the 2.5-MW rectifier. These transistor banks have been designed by John Rand (ENG-7) who is also the only person devoting full time to their installation and testing.

The transistor regulator (see reference 1 for a photograph of this unit) which is in series with the 0.5-MW motor-generator has been in service for over a year regulating the magnet used for the ECH plasma experiment.[2] Although this service requires excellent regulation, it demands only 380 A and is therefore not a test of the operation of the regulator at its full design current of 2.4 kA. Considerable difficulty has been encountered in designing a single regulation loop suitable for a wide range of currents because of a severe change in the small-signal transfer impedance of the three-stage transistor amplifier as a function of its operating current. This problem has been solved in principle by the insertion of a compensating network of resistors and Zener diodes at a low current level just prior to the antepenultimate stage of current gain. Cooling the ultimate-stage transistors has proved more difficult than had been expected. Fortunately it was possible to reduce their operating voltage to accommodate the required reduction in transistor power. This change has led to confusion in the implementation of the network to compensate for gain change. Completion and final testing have been delayed primarily because the unit is in regular use, but also because a full-power load is presently unavailable.

Progress on the larger transistor bank to be used in series with the 2.5-MW rectifier has been slowed by numerous engineering difficulties. The most important of these was the result of arc breakdown in the 13.2 kV ac switchgear. Sufficient energy was released on these occasions to blow the doors off the switchgear cabinets. This problem is now understood, but implementation of the solution awaits delivery of components. In spite of these delays, the new control package on the old IVR has been installed and tested and meets the specified voltage regulation of ± $\frac{1}{4}$% of full scale.

Current has been run through the larger transistor banks and a preliminary feedback loop has been constructed that provides some degree of regulation at currents up to 1 kA (design current = 18 kA maximum). Considerable progress has been made toward splitting the 2.5-MW supply into two 1.25-MW supplies which can be used separately when required. This portion of the work should be completed soon.

The completion of this entire project has been seriously delayed by the limited manpower available. Although presently behind schedule, we believe this work will eventually provide us with the power supply stability required for sophisticated plasma-wave studies.

References

1. J. McLeod, LA-4075-MS, 1968, p. 105.

2. J. McLeod and J. L. Rand, "Precise Regulation of a 500 kW dc Generator with a 2500 Ampere Series-Pass Transistor Bank". To be published in LA-4250.

REACTOR BLANKET CALCULATIONS
(T-DOT)

Tritium from Thermonuclear Reactors

(G. I. Bell)

The tritium breeding potentials of various neutron blankets surrounding a pulsed thermonuclear reactor have been calculated using multigroup methods.[1,2] A basic lithium blanket containing up to 15 volume percent niobium (required for structural purposes) was found to give marginal breeding. For such niobium concentrations the neutron flux depression at niobium resonances must be taken into account in devising multigroup cross sections; this resonance self-shielding increases the triton production by ~ 10% in the basic blanket.

Several modifications of the basic design were found to give improved breeding, in which the ratio of tritons produced to tritons burned in making 14 MeV neutrons is equal to or greater than 1.20. These include (a) replacement of niobium by molybdenum and zirconium, (b) use of lithium enriched in ^{6}Li, and (c) addition of hydrogen to the blanket. A particularly promising design involves the use of a solid Mo shell to provide structural support to a copper coil (which carries the electrical currents to provide the magnetic fields to contain the plasma); the blanket is then not required to have structural strength and can consist of lithium metal with a small amount of zirconium channeling material. The displacement of lithium by beryllium does not appear attractive. Thus, a variety of options are available to obtain satisfactory breeding from a lithium blanket containing substantial amounts of structural material.

References

1. G. I. Bell, LASL Report LA-4131-MS (1969).
2. G. I. Bell, W. H. Borkenhagen and F. L., Ribe, Paper 33, Culham Conference Proceedings (1968).

Heating in Tritium Breeders

(G. I. Bell)

Calculations have been made of the heating of some possible blankets of pulsed thermonuclear reactors due to the absorption and scattering of γ rays. The γ rays are produced by nonelastic scattering of neutrons (mainly inelastic scattering of 14 MeV neutrons by copper and molybdenum) and by the capture of moderated neutrons by copper, molybdenum, and zirconium. The blankets which were considered had a shell of copper, 3 cm in thickness, surrounding a cylindrical plasma region; the copper carries the electrical currents which produce the magnetic field to contain the plasma. Outside the copper is a large heterogeneous region containing molybdenum for structural strength, lithium for triton breeding, and zirconium for channeling the flow of the lithium. The main interest in these calculations was in determining the heat deposition in the copper shell which will, in turn, affect the cooling requirements of the shell.

S_n calculations were first made of the neutron fluxes in the blanket, and from these the sources of γ rays were computed. The transport of the gamma rays was then followed with a Monte Carlo code. For a typical blanket it was concluded that about 3 MeV of γ energy is deposited in the copper shell, per 14 MeV neutron produced in the plasma. About 90% of this energy comes from gamma rays produced in the copper while the remaining 10% is a contribution from gamma rays produced in the molybdenum and zirconium of the main blanket. The latter small contribution is sometimes called "backshine." When the molybdenum is in the form of a shell adjacent to the copper, γ rays originating in the molybdenum contribute about 12% of the heating in the copper which amounts to about 3.4 MeV γ energy per 14 MeV neutron.

PUBLICATIONS

Armstrong, T. P. and Freidberg, P., "Nonlinear Development of the Two Stream Instability," Bull. Am. Phys. Soc., Ser.2, 13, 1528 (1968) (Abstract).

Armstrong, T. P. and Freidberg, J. P., "Persistently Recurring Nonlinear Waves Arising from the Two Stream Instability," ibid., Ser.2, 13, 1745 (1968).

Baker, D. A. and Mann, L. W., "High Beta MHD Equilibrium and Stability of Multipoles," ibid., Ser.2, 14, 1051 (1969) (Abstract).

Baker, D.A., MacRoberts, M.D.J., and Mann, L.W., "Calculations of Pressure Effects and Plasma Diffusion in a Quadrupole," ibid., Ser.2, 13, 1526 (1968) (Abstract).

Baker, D.A. and Mann, L.W., "Curves for Predicting Stresses in Controlled Fusion Pulsed Magnetic Field Systems," LA-4186 (1969).

Bell, G.I., "Neutron Blanket Calculations for Thermonuclear Reactors, II," LA-4131-MS (1969).

Boicourt, G., "Problems in the Design and Manufacture of Energy Storage Capacitors," LA-4142-MS (1970).

Bottoms, P.J., Carpenter, J.P., Mather, J.W., Ware, K.D., and Williams, A.H., "X-Ray Measurements on the Dense Plasma Focus," Bull. Am. Phys. Soc., Ser.2, 13, 1543 (1968) (Abstract).

Bottoms, P.J., Mather, J.W., Carpenter, J.P., Williams, A.H., and Ware, K.D., "Stabilizing Effects of a DC Magnetic Field on the Dense Plasma Focus," ibid., Ser.2, 14, 547 (1969) (Abstract).

Bottoms, P.J., Mather, J.W., Carpenter, J.P., Ware, K.D., and Williams, A.H., "X-Ray Measurements on Plasma Focus," ibid., Ser. 2, 14, 1013 (1969) (Abstract).

Burkhardt, L.C., DiMarco, J.N., and Karr, H.J., "Plasma Injection and Trapping in a Caulked Stuffed Cusp Magnetic Field," Phys. Fluids, 12, 1894 (1969).

Butler, T.D., Henins, I., Jahoda, F.C., Marshall, J., and Morse, R.L., "Coaxial Snowplow Discharge," ibid., 12, 1904 (1969).

Butler, T.D. and Cook, J.L., "Numerical Analysis of a Coaxial Accelerator," ibid., 11, 2286 (1968).

Butler, T.D., Cook, J.L., and Morse, R.L., "MHD Simulation of Coaxial Plasma Flow," APS Topical Conference on Numerical Simulation of Plasma. Abstract in Bull. Am. Phys. Soc., Ser. 2, 13, 1746 (1968).

Daehler, M., Sawyer, G.A., and Thomas, K.S., "Coordinated Measurements of Plasma Density and Cooperative Light Scattering in a Theta-Pinch Plasma," Phys. Fluids, 12, 225 (1969). Abstract in Bull. Am. Phys. Soc., Ser. 2, 13, 877 (1968).

Dickman, D. O., Morse, R.L., and Nielson, C.W., "Numerical Simulation of Axi-Symmetric, Collisionless, Finite Beta Plasma," ibid., 12, 1708 (1969). Abstract in Bull. Am. Phys. Soc., Ser. 2, 13, 1746 (1968).

DiMarco, J.N., and Burkhardt, L.C., "Investigation of Z-Pinch Heating by Strong Shocks using Magnetic Energy Storage," Bull. Am. Phys. Soc., Ser. 2, 13, 1551 (1968)(Abstract).

DiMarco, J.N., and Burkhardt, L.C., "Fast Z-Pinch," ibid., Ser. 2, 14, 1015 (1969) (Abstract).

Dreicer, H., "Microwave Emission by Upper Hybrid Resonance Electrons," ibid., Ser. 2, 13, 1534 (1968) (Abstract).

Dreicer, H., Henderson, D.B., Mosher, D., Wittman, F. E., and Wolfsberg, K., "Measurement of the Resonant Charge Exchange Cross-Section in a Potassium Q-Machine Plasma Column," ibid., Ser. 2, 14, 1056 (1969) (Abstract).

Enoch, J., "Structure of and Particle Orbits in Neutral Plasma Sheaths," Phys. Fluids, 12, 1294 (1969).

Forman, P.R., "Dynamic Stabilization of Z-Pinches," Bull. Am. Phys. Soc., Ser. 2, 14, 829 (1969) (Abstract).

Forman, P.R., Haberstich, A., Karr, H. J., Phillips, J.A., and Schofield, A.E., "First Half Cycle Operation of the Columba Experiment," ibid., Ser. 2, 13, 1489 (1968)(Abstract).

Fowler, C. M., Thomson, D.B., Caird, R.S., Ewing, K.J., and Garn, W.B., "Explosive Generator Power Supply for Driving a Plasma Gun," ibid., Ser. 2, 14, 1061 (1969)(Abstract).

Freidberg, J.P., Morse, R.L., and Nielson, C. W., "Numerical Method for Studying Linear Stability of Highly Inhomogeneous Plasmas," ibid., Ser. 2, 14, 1077 (1969)(Abstract).

Freidberg, J.P., "Magnetohydrodynamic Stability of a Diffuse Screw Pinch," ibid., Ser. 2, 14, 1031 (1969)(Abstract).

Freidberg, J.P.and Morse, R.L., "Collisionless Tearing Mode Instabilities in a High Beta Theta Pinch," Phys. Fluids, 12, 887 (1969).

Freidberg, J.P and Morse, R.L., "Stability of a High Beta Theta Pinch," Bull. Am. Phys. Soc., Ser. 2, 13, 1552 (1968)(Abstract).

Freidberg, J.P. and Armstrong, T.P., "Nonlinear Development of the Two-Stream Instability," Phys. Fluids, 11, 2669 (1968).

Freidberg, J.P., "High Beta Mirror Instabilities," ibid., 12, 1112 (1969).

Gribble, R.F. and Ribe, F.L., "Low-Compression Theta Pinch With Separated Shock Heating," LA-4194-MS (1969).

Gribble, R.F., "Improved Spark Gap and Trigger System for Theta-Pinch Experiments," Bull. Am. Phys. Soc., Ser. 2, 13, 1491 (1968)(Abstract).

Gribble, R.F., Little, E.M., Quinn, W.E., Ribe, F.L., Sawyer, G.A., Thomas, K.S., and Weldon, D.M., "Dynamic Stabilization and Turbulence Experiments on Theta-Pinch Plasmas," Controlled Fusion and Plasma Physics. 3rd European Conference, Utrecht. Contributions, p. 39. Wolters-Noordhoff Publishing (1969).

Haberstich, A. and Forman, P.R., "Radial Stability of the Pinch in the Columba Experiments," Bull. Am. Phys. Soc., Ser. 2, 13, 1489 (1968) (Abstract).

Hammel, J.E., Baker, D.A., Burkhardt, L.C., DiMarco, J.N., Henson, R.M., Karr, H.J., and Marshall, J., "Dipole Current Lead for a Plasma Containment Device," U.S. Patent 3,441,775.

Hammel, J.E. and Kewish, R.W., "Plasma Stream Interactions Through Polarization Electric Fields," LA-3994 (1969).

Henderson, D.B., "Angular Distribution of Efflux from an Atomic Beam Nozzle," Bull. Am. Phys. Soc., Ser. 2, 14, 1056 (1969) (Abstract).

Henderson, D.B., Wittman, F.E., and Dreicer, H., "Control of Hot Plate Temperature Profiles," ibid., Ser. 2, 13, 1557 (1968) (Abstract).

Henins, I., Jeffries, R.A., Kerr, D.M., Marshall, J., and Ingraham, J.C., "Explosive Generator Driven Coaxial Plasma Gun," ibid., Ser. 2, 14, 1061 (1969)(Abstract).

Herold, H.G., "Development of a Low-Density Plasma Halo in a Theta Pinch," ibid., Ser. 2, 13, 1489 (1968)(Abstract).

Herold, H.G. and Jahoda, F.C., "Carbon Dioxide Laser Interferometer for the Measurement of Transient Low-Density Plasmas," Rev. Sci. Instr., 40, 145 (1969).

Karr, H. J., Forman, P.R., and Phillips, J.A., "Dynamic Stabilization of the Z-Pinch by Linear Multiple Fields. I," Bull. Am. Phys. Soc., Ser. 2, 14, 1051 (1969)(Abstract).

Little, E.M., Newton, A.A., Quinn, W.E., and Ribe, F.L., "Linear Theta-Pinch Experiments Related to the Stability of a Toroidal Theta-Pinch of Large Aspect Ratio," Plasma Physics and Controlled Nuclear Fusion Research. 3rd Conf., Novosibirsk. USSR. Paper K-2, IAEA (1968).

Mather, J.W., Ware, K.D., Williams, A.H., Bottoms, P.J., and Carpenter, J.P., "Angular Distribution of Neutron Velocity and Intensity from the Dense Plasma Focus," Bull. Am. Phys. Soc., Ser. 2, 13, 1542 (1968)(Abstract).

Mather, J.W., Bottoms, P.J., Carpenter, J.P., Williams, A.H., and Ware, K. D., "Stability of the Dense Plasma Focus," LA-4088 (1969).

McLeod, J.J., Michael, D.E., and Dreicer, H., "Measurements of ECH Q-Machine Plasma Properties," Bull. Am. Phys. Soc., Ser. 2, 14, 1056 (1969).

Morse, R. L., and Nielson, C.W., "Numerical Simulation of Beam-Plasma Interactions Using the Particle-in-Cell Method," Controlled Fusion and Plasma Physics. 3rd European Conference, Utrecht, p. 39. Wolters-Noordhoff Publishing (1969).

Morse, R.L., "Equilibria of Collisionless Plasma," Part II," LA-3844-MS Part II (1969).

Morse, Richard L., "Instability of Low Beta Magnetic Flute Modes Caused by Transverse Anisotropy," Phys. Fluids, 12, 1483 (1969). Abstract published in Bull. Am. Phys. Soc., Ser. 2, 13, 1504 (1968).

Morse, R.L., Comp. "Proceedings of APS Topical Conference on Numerical Simulation of Plasma," Los Alamos Scientific Laboratory of the University of California, Los Alamos, New Mexico, Sep. 18-20, 1968. LA-3990 (1969).

Morse, R.L. and Nielson, C.W., "Numerical Simulation of Warm Two-Beam Plasma," Phys. Fluids, 12, 2418 (1969). Abstract published in Bull. Am. Phys. Soc., Ser. 2, 13, 1774 (1968).

Morse, R.L., and Nielson, C.W., "One, Two and Three Dimensional Numerical Simulation of Two-Beam Plasmas," Phys. Rev. Letters, 23, 1087 (1969).

Newton, A.A., Marshall, J., and Henins, I., "Continuous Pinch Operation of the Coaxial Gun," Bull. Am. Phys. Soc., Ser. 2, 13, 1544 (1968) (Abstract).

Oliphant, T.A., "Alpha Particle Heating in a Model Thermonuclear Reactor," ibid., Ser. 2, 13, 1546 (1968)(Abstract)

Palsedge, J.A., "Stability of a Rotating Theta-Pinch Plasma," Phys. Fluids, 12, 336 (1969). Abstract published in Bull. Am. Phys. Soc., Ser. 2, 13, 599 (1968).

Phillips, J.A., Forman, P.R., Haberstich, A., Karr, H. J., and Schofield, A.E., "Trapped Reverse Magnetic Field Operation in the Columba Experiment," Bull. Am. Phys. Soc., Ser. 2, 13, 1489 (1968)(Abstract).

Phillips, J.A., Forman, P.R., Haberstich, A., Karr, H. J., and Schofield, A.E., "Dynamic Stabilization of the Z-Pinch by Linear Multiple Fields. II," ibid., Ser. 2, 14, 1051 (1969) (Abstract).

Quinn, W.E., Little, E.M., and Ribe, F.L., "Effect of Oscillating Longitudinal Currents on a One-Meter Theta-Pinch Plasma Column," ibid., Ser. 2, 13,1556 (1968). (Abstract).

Quinn, W. E., Gribble, R.F., and Little, E.M., "Experiments on a Three-Meter Collisionless Plasma Column," ibid., Ser. 2, 14, 1050 (1969) (Abstract).

Ribe, F.L., "Effect of an Oscillating Quadrupole Field on the Kink Modes of a Screw Pinch," LA-4081-MS (1969).

Ribe, F. L., "Free-Boundary Solutions for High-Beta Stellarators of Large Aspect Ratio," LA-4098 (1969).

Ribe, F. L., "Feedback Stabilization of m = 1 Long-Wavelength Modes on a Theta-Pinch Plasma Column," LA-4196-MS (1969).

Ribe, F.L. and Riesenfeld, W. B., "Dynamic Stabilization of the m = 1 Mode on a Bumpy Theta-Pinch Plasma Column," Bull. Am. Phys. Soc., Ser. 2, 13, 599 (1968).

Ribe, F.L., Quinn, W. E., and Riesenfeld, W.B., "Plasma Turbulence Interpretation of the Resistance of a Theta-Pinch Column to Oscillating Longitudinal Currents," Bull. Am. Phys. Soc., Ser. 2, 13, 1566 (1968).

Ribe, F. L., "High-Beta Compression Systems," Perspectives on Controlled Thermonuclear Research: Report on the 3rd IAEA Conf. at Novosibirsk, Aug. 1968, p. 26. TID-2 4804 (1968).

Shonk, C.R. and Morse, R.L., "Two-Dimensional Two-Species PIC Simulations of Collisionless Shocks," Bull. Am. Phys. Soc., Ser. 2, 14, 1058 (1969) (Abstract).

Shonk, C.R. and Morse, R.L., "Two Dimensional Simulation of Shock Waves in Collisionless Plasmas," APS Topical Conference on Numerical Simulation of Plasma, 1968. Abstract published in Bull. Am. Phys. Soc., Ser. 2, 13, 1746 (1968).

Shonk, C.R. and Morse, R.L., "Numerical Simulation of Collisionless Shocks," Bull. Am. Phys. Soc., Ser. 2, 13 ; 1556 (1968).

Suydam, B. R., "Kelvin-Helmholtz Instability in a Flowing Plasma," LA-4107-MS (1969).

Thomas, K.S., "Measurement of Shorting Currents from a Theta-Pinch Plasma," Phys. Rev. Letters, 23, 746 (1969). Abstract published in Bull. Am. Phys. Soc., Ser. 2, 14, 1050 (1969).

Thomas, K.S., Sawyer, G.A., and Weldon, D.M., "Z-Current Experiments on a 150 kJ Theta Pinch," Bull. Am. Phys. Soc., Ser. 2, 13, 1489 (1968) (Abstract).

Tuck, J.L., "Monte Carlo and Computer Plasma Simulation Studies of the Inhibition of End Loss from a Theta-Pinch by Nonadiabatic 'Rough' Magnetic Walls," Plasma Physics and Controlled Nuclear Fusion Research. 3rd Conf., Novosibirsk, USSR. Paper K-5. IAEA, 1968.

Ware, K.D., Mather, J.W., Bottoms, P. J., Carpenter, J.P., and Williams, A.H., "Voltage Scaling for Megajoule Plasma Focus Systems," Bull. Am. Phys. Soc., Ser. 2, 14, 1014 (1969).

Bottoms, P.J., Carpenter, J.P., Mather, J.W., Ware, Kenneth D., and Williams, A.H., "On the Mechanism of Neutron Production from the Dense Plasma Focus," Plasma Physics and Controlled Nuclear Fusion Research. 3rd Conf., Novosibirsk, USSR. Paper G-5, IAEA (1968).

Ware, K.D., Mather, J.W., Bottoms, P.J., Carpenter, J.P., and Williams, A.H., "Plasma Focus Development at Voltages Greater than 25 kV," Bull. Am. Phys. Soc., Ser. 2, 14, 828 (1969) (Abstract).

Williams, A.H., Ware, Kenneth D., Mather, J.P., and Bottoms, P.J., "Characteristics of a 50 kV-10 kJ Vacuum Switch Module," ibid., Ser. 2, 13, 1491 (1968). (Abstract).

Williams, A.H., Carpenter, J.P., Bottoms, P.J., Ware, K.D., and Mather, J.W., "Calorimetric Measurement of X-Ray Flux from Plasma Focus," ibid., Ser. 2, 14, 1013 (1969) (Abstract).